

Mémoire d'Habilitation à Diriger des Recherches
MÉCANIQUE

UNIVERSITÉ PIERRE ET MARIE CURIE

**STOCHASTIC SPECTRAL APPROACH TO
UNCERTAINTY QUANTIFICATION OF
COMPUTATIONAL FLUID DYNAMICS**

DIDIER LUCOR

Defense date/place: December 1st 2011 at UPMC, Paris

JURY

PRESIDENT

Patrick Bontoux

CNRS Research Director, Aix-Marseille Université

REVIEWERS

Rémi Abgrall

Mathématiques de Bordeaux

Professor, INRIA Bordeaux Sud-Ouest & Institut de

Roger Ghanem

Gianluca Iaccarino

Professor, University of Southern California, Los Angeles

Assistant Professor, Stanford University

EXAMINERS

Bruno Després

Pierre Sagaut

Professor, Université Pierre et Marie Curie, Paris

Professor, Université Pierre et Marie Curie, Paris

To Claire & Swann

Abstract

Computational Fluid Dynamics (CFD) has established itself as a valuable computer tool to simulate and analyze fluid flow problems. CFD technologies are nowadays routinely employed as a design and research tool in numerous physical sciences and directly benefits from the fast development of numerical methods/algorithms and computers/supercomputers technology. Despite being a somewhat mature discipline, the question of the reliability and usefulness of computer predictions to practical applications demonstrates that *confidence* in CFD simulations must be *quantitatively* assessed.

An answer lies in probabilistic mechanics, which is complementary to the Verification and Validation (V&V) process in scientific computing and aim at taking into account various system *uncertainties* in order to predict their impact onto the resulting stochastic model response.

The resolution of the stochastic partial differential equations (SPDE) requires: – the *characterization* of all input sources of uncertainty – the *propagation* of this uncertainty through the computational model – the *quantification* of the uncertainty on the response metrics of interest. These main components form what is called *Uncertainty Quantification* (UQ) in computational mechanics.

This manuscript reports on parametric mechanical uncertainties defined by *probability* theory. It focus on UQ tackled by *stochastic spectral* methods (SSM) that seem well-suited to solve SPDE driven by *colored* noise. These methods are grounded in strong mathematical bases and provide a rich probabilistic characterization of the system response thanks to a suitable functional approximation. Some recent developments and possible improvements of SSM are proposed and the numerical techniques are applied to the UQ of various fluid flows, with a particular emphasis on incompressible shear flows and shock-dominated compressible flows.

Mathematical concepts and key ingredients of the spectral representation of stochastic processes in numerical mechanics are outlined in Chapter I. Two classes of representation are presented: the Karhunen-Loève expansion and the (generalized) Polynomial Chaos expansions with a discussion on the appropriate choice of approximation space. Then, the stochastic representation is introduced into the physical deterministic system and different approaches are discussed to propagate this uncertainty to the numerical solution. Finally, some emphasis is given to the evolution of more recent adaptive approaches.

Chapter II introduces the application of stochastic spectral methods to the uncertainty quantification of incompressible parallel sheared flows, which are known to be prone to instabilities and often sensitive to external noise. The focus is mainly on the physical mechanisms and effects induced by colored random inflow or base flow disturbances. Two different physical systems: a Couette flow and a spatially developing mixing layer are considered. While the underlying deterministic models retained for these two flows encompass the entire spectrum of numerical approaches, from linear stability theory to direct numerical simulation, the selected stochastic projection method is the same for both cases and does not require any changes to the existing solvers. Chapter III deals with the class of stochastic compressible flows and more generally with the problem of shock-dominated responses such as the ones obtained for nonlinear hyperbolic systems. A review of the application of spectral Galerkin methods to these kind of systems is given first, with applications to compressible gas dynamics, followed by a section presenting the stochastic investigation of uncertain transonic aerodynamics about several airfoils. The numerical probabilistic representations are general enough to be applied to a wide class of fluid mechanics problems.

Short highlights of current or recent scientific studies, including: quantification of errors in turbulence modeling and nonlinear stochastic aeroelasticity, are introduced in Chapter IV.

Lastly, the final section concludes with some remarks on the work presented and related open questions and adds some perspectives to the discussion. Most of the detailed results presented in the manuscript (i.e. mainly in Chapters II & III and to some extent in Chapter IV), stems from collaborative works conducted with Ph.D. students I have (co-)supervised.

Contents

Abstract	3
Contents	7
Introduction: uncertainty, computational science and fluid dynamics	11
I Stochastic Spectral Methods for uncertainty propagation and quantification	23
1 Probabilistic framework for the discretization of stochastic processes	23
2 Spectral expansions	25
3 Resolution schemes	34
4 Spectral statistics	42
5 Adaptive approaches for error vs. cost control	44
II Shear-dominated convective flows	55
1 Effects of base flow uncertainty on linear shear flow stability	56
2 Sensitivity of mixing layer DNS to random inflow perturbation	65
III Shock-dominated compressible flows	83
1 Galerkin-type method for uncertainty quantification of hyperbolic systems of conservation laws	85
2 Stochastic investigation of uncertain transonic aerodynamics	109
IV Ongoing research interests	127
1 Quantification of errors in turbulence modeling	127
2 Subsonic and supersonic nonlinear stochastic aeroelastic flutter	133
Concluding remarks and some perspectives	139
A Spectral/<i>hp</i> element DNS solver for deterministic incompressible Navier-Stokes equations	147
1 Incompressible Navier-Stokes equations	147
2 Weak form, time integration splitting scheme and spatial discretization	147
B Multidimensional numerical integration	153
1 Stochastic integration techniques	153
2 Deterministic integration techniques	155
C Lagrangian-GAIA solver for deterministic Euler systems	167
1 Lagrange-remap schemes	167
2 Godunov Acoustic Invariant Advection (GAIA) numerical flux	169
3 Numerical flux limiters	170
4 Directional splitting	171
Bibliography	173

Introduction: uncertainty, computational science and fluid dynamics

The computational engineering and science discipline is considered one of the most important scientific advances and achievements in human history. As the speed and power of computer systems continue to grow, it is obvious that the expectations of computer users in *decision-making* and *risk analysis* related to human activities as important as health, displacement/transportation, environment impact, climate change, security, economy, ... continue to grow in parallel. Accurate computer predictions of physical events can be of tremendous importance for our societies. One of the branches related to computational physics, mathematics and mechanics is named Computational Fluid Dynamics (CFD) and predicts the behavior of fluids¹. Started in the early 1970's, CFD has since established itself as a valuable computer tool to simulate and analyze fluid flow problems. It is by essence a multidisciplinary science which lies at the intersection between physical modeling, numerical mathematics and computer science², and directly benefits from the development of numerical methods and algorithms and from the fast evolution of computers and supercomputers technology. Moreover, CFD is in general a more cost-effective and less time-consuming approach than experiments that may be prohibitive (e.g. extensive airplane flight tests). In fact, CFD technologies are now routinely employed as a design tool for engineering as well as a substantial research tool in numerous physical sciences.

Nevertheless, despite being a somewhat mature discipline, the question of the *reliability* and *usefulness* of computer predictions/simulations to practical applications is crucial to a society driven by performance estimation, reduced environmental impact, safety assessment along with technical innovation and economy. A natural answer was to focus on the *accuracy* of the predicted solution by comparing it to experimental measurements [354], in order to reduce and control modeling and numerical errors (e.g. turbulence model, discretization error). More specifically, this is the subject of the *Verification* and *Validation* (V&V) process in scientific computing [353]. The validation process addresses the quality and relevance of the mathematical model \mathcal{M} chosen to represent the physical event while the verification process consists in determining if the computational model (i.e. $\mathcal{N} + \mathcal{C}$) can be used to represent the mathematical model of the event with sufficient accuracy. The verification process involves two steps: the code verification (\rightarrow software engineering) and the solution verification (\rightarrow *a posteriori* error estimation) [412] and it must be carried out prior to the validation [19]. The validation process *corroborates* the accuracy of the verified computational simulation by direct comparison with the “real world”, i.e. *experimental data*. The procedure becomes very tricky in CFD as experimental data for the application conditions of interest are not always (or partially) available and are at best *statistical* in nature, generally given in terms of a significance level [355]. Moreover, it only makes sense to validate the computation with respect to specific *tolerances* for specific quantities of interest [19].

Stimulated by the pioneering work of early advocates of V&V [311, 406, 451, 179], more recent approaches have embraced the concepts while trying to extend the perspective to CFD *uncertainty* in a broader sense [174, 455, 198], reorienting the question of the CFD reliability to the following one:

“How should *confidence* in CFD simulations be *quantitatively* assessed?”

In order to answer this question, one has to go back to the classification and description of uncertainties. *Aleatory* uncertainty³ is uncertainty due to inherent variation or randomness, possibly combined with spatial and/or temporal variations. This type of uncertainty is generally *probabilistically* characterized by a (or a set of) *random variable* (RV) with its *probability density function* (pdf). *Epistemic* uncertainty⁴ is uncertainty due

1. The term “fluids” is taken here in a broad sense and covers as many topics as hydrodynamics, aerodynamics, high-speed and physical gas dynamics, turbulence, multiphase flow, fluid-structure interaction, rheology,...

2. In the following, we refer to \mathcal{M} for the *physical model* (i.e. mathematical/PDE model that provide abstractions of a physical event consistent with a scientific theory proposed to cover that event), \mathcal{N} for the *numerical method* (i.e. the discretized version of a mathematical model) and \mathcal{C} the *computer code* (computer program designed to implement a numerical method), to ease comprehension.

3. Aleatory uncertainty is also called variability, irreducible uncertainty or stochastic uncertainty.

4. Epistemic uncertainty is also called reducible uncertainty or ignorance uncertainty.

to a lack of knowledge. If more information is added (through experiments, improved numerical approximations, expert opinion, higher fidelity physics modeling,...) then this uncertainty may be reduced. This type of uncertainty is generally represented as an *interval* (with no associated pdf) or a pdf which represents *degree of belief* of the analyst⁵. The *Bayesian* approach to uncertainty characterizes epistemic uncertainty as a pdf that represents the degree of belief of the true value on the part of the analyst [147]. Sometimes, the uncertainty maybe too complex to define and is likely to be the result of a mixed between aleatory and epistemic uncertainties. These uncertainties may potentially affect all the stages of a CFD numerical prediction. One can categorized the different sources of uncertainty as occurring in the computational model (i.e. $\mathcal{NC} \equiv \mathcal{N} + \mathcal{C}$) or the physical/mathematical model (\mathcal{M}). Uncertainties in \mathcal{M} results from all abstractions, conceptualizations and mathematical formulations and are by nature epistemic [127]⁶. Sources of uncertainty in the computational model \mathcal{NC} may affect the numerical approximation itself or the inputs to the model:

1. Numerical approximation (nature: some debate about aleatory or epistemic uncertainty):
 - discretization errors
 - round-off errors (finite precision arithmetic)
 - iterative convergence errors
 - coding errors (bugs)
2. Model inputs (aleatory, epistemic or mixed uncertainty):
 - physical/constitutive modeling parameters
 - computational domain (geometry)
 - boundary/initial conditions
 - external forcing / system excitation

These uncertainties may be defined by different theories including *probability* [126], *fuzzy set* [542], *possibility* and *evidence* theory [438]... In a probabilistic framework, our fluid flow problem is now governed by *stochastic* partial differential equations (SPDE). SPDE may be driven by uncertainty modeled as (Gaussian)⁷ *white noise*, that is a random process (RP) with zero mean and constant spectral density [190, 358]. Although such a process does not exist in the conventional sense, it is a very useful mathematical idealization for describing random influence that fluctuates rapidly. Because the use of traditional approximation methods for solving SPDE driven by white noise is limited by the high dimensionality of the problem, only Monte-Carlo simulation techniques or stochastic calculus (Itô/Stratonovich) are quite successful in this case. In this manuscript, we will consider SPDE driven by “colored noise”, i.e. uncertainty that can be modeled by spatial, temporal or spatial-temporal random processes and are characterized by their bounded correlation function [244]. From a practical point of view, the solution of the SPDE is a *random process* (RP) that requires three successive steps to be solved: – the *characterization* of all input sources of uncertainty – the *propagation* of this uncertainty through the computational model – the *quantification* of the uncertainty on the response metrics of interest. These three main components form what is nowadays called *Uncertainty Quantification* (UQ). A last step may be added in order to rank the sources of uncertainty in terms of their influence on the solution uncertainty/variability. This type of study is named *Sensitivity Analysis* (SA). In the following, we will briefly survey different classes of numerical methods used for UQ with an emphasis on the propagation and quantification steps retained for CFD.

The “structures” community and “dynamics/control” discipline have a long history in uncertainty analysis (e.g. for risk-based design methods) whereas the contemporary CFD community is a newcomer to this area (mainly due to the high cost of CFD simulations). Beyond the customary “statistical” vs. “non-statistical” probabilistic methods point of view, three main classes of numerical methods that may be suitable to UQ in CFD, may be singled out: – the *sampling* methods [129, 413], – the *perturbation/sensitivity/adjoint* methods [228, 205, 57], and – the *surrogate model* methods [47, 425, 123, 181], some of them being originally developed in a deterministic context. We will shortly introduce the first two classes and present in more details some of the surrogate models as they have been the preferred choice in recent studies.

The Monte-Carlo (MC) simulation method is based on *statistical* sampling and is now ubiquitous in UQ in science, engineering, finance, industry,... Recent decades have seen many improvements in MC methods. Much of the progress has been in quasi-MC (QMC) sampling and in Markov Chain MC (MCMC). QMC methods improve the accuracy and MCMC greatly extends the range of problems that can be handled by MC. We refer the reader to the first part of the Appendix A for some details and references. Despite the high robustness of the random sampling methods (even for nonlinear problems) and the fact that they are often easy to parallelize, their convergence remains often too slow and their computational cost prohibitively expensive for

5. A common practice when no trends or experimental evidence are available is to consider a *uniform* distribution.

6. They will not be treated in this manuscript.

7. Gaussian white noise is a good approximation of many real-world situations, but one may consider Poisson or Cauchy white noise as well.

high-dimensional CFD problems. This explains the scarce literature on the subject [141, 42, 519].

The idea of the second class of methods (i.e. perturbation/sensitivity/adjoint methods) is to take advantage of the computation of partial *derivatives* of the field variables with respect to the uncertain parameters, in order to lower the problem of dimensionality and associated cost. This approach often accelerates the convergence of the MC method, for instance in calculating tail probabilities for estimating margins and risk [502]. But in general, these methods are restricted to second order statistics and are not sufficient for meaningful risk assessment and failure analysis. These methods were originally designed for deterministic applications with parameters considered as *design* parameters. For instance, deterministic sensitivity analysis, when coupled with CFD, has obvious applications related to design and flow analysis as it provides some insights on how design parameters affect a given flow field [447, 177]. In this case, the computation of the derivatives of flow quantities (e.g. aerodynamic coefficients), often related to both the fluid and the geometry, with respect to geometrical or physical parameters are key to the gradient-based *optimization* of a physical system [205, 343, 369]. Several computational approaches, such as: finite differences methods [401], (discrete or continuous) adjoint methods [133, 402, 381, 204], complex-step methods, software (automatic) differentiation [440], provide the solution gradients with different efficiencies and accuracies. Nevertheless, sensitivity analysis provides a useful tool to link input uncertainty to the subsequent propagation of uncertainty into the CFD simulations results. Along these lines, the following papers apply the propagation of uncertainty through gradient-based design optimization schemes using sensitivity derivatives to various flow problems [393, 466, 481, 293, 227, 206]. Another widely used *non-statistical* method in the framework of finite elements [162] is the *perturbation method*, where input random fields are represented as infinite perturbation expansions of fluctuations around their mean fields (via Taylor series) [228]. In practical applications, at most *second-order* expansions are employed [483, 268, 267, 541]⁸ and an accurate representation of the response pdf is out of reach. A related approach is based on manipulation of the stochastic operators. Such methods include the *Neumann* expansion [162], which is based on expanding the inverse of the stochastic operator in a Neumann series [534, 442, 540, 300], and the weighted integral method [102, 103]. More recently, the work of [18] proposed a perturbation method with successive approximations. They show that uniform coercivity of the diffusion coefficient is sufficient for the convergence of the method. Other perturbation approaches are discussed in [511, 272]. In conclusion, the drawback of perturbation/sensitivity/adjoint methods is their necessary conditions for convergence. In most of the cases the expansions are formal and rely on the assumption of *small* uncertainties.

Most realistic (3D) CFD simulations remain computationally too costly to be run many times (i.e. > several thousands times) in the context of UQ involving a large number of uncertain parameters. One way of alleviating this burden is by constructing approximation models, known as surrogate models⁹ (SM), that mimic the behavior of the simulation model as closely as possible while being computationally cheap(er) to evaluate [123, 181]. The challenge resides in the generation of a SM as accurate as possible, using as few simulation evaluations (i.e. *data*) as possible. The procedure is based on three major steps (which may be iteratively interleaved if the process is made adaptive): – the sample selection, – the construction of the SM (i.e. by some optimization of the model parameters) and finally – some type of *a posteriori* evaluation of the accuracy of the surrogate. Once the SM of the physical quantity of interest is considered accurate enough, its entire structure may be explored at (almost) no computational cost and solution predictions, rare events, statistics and sensitivity become readily available to the analyst.

They are numerous deterministic and stochastic surrogate models, starting with simple linear (least squares) or nonlinear regression [181], moving to the well-known Response Surface Methods (RSM), such as low order polynomial approximations [47, 338], and to more sophisticated techniques such as: Multivariate Adaptive Regression Splines (MARS) [74], Radial Basis Functions (RBF) [392, 359], Artificial Neural Networks [37, 405], Support Vector Regression (SVR) [484, 445]. The model choice depends on many aspects of the problem. For instance, simple linear or polynomial approximations are known to produce inaccurate results to model highly nonlinear or irregular functional behaviors, despite their smoothing capability allowing quick convergence.

The SM known as *Kriging* (Kr) or *Gaussian Process* regression (GPr) is a valuable technique, particularly attractive for global (multidisciplinary) optimization of expensive “black-box” functions [211], as well as for visualization and tradeoff analysis. As it is rooted in a statistical framework, it is sometimes compared with the stochastic spectral approximations introduced in this manuscript. Developed in the mathematical geology literature in the early 1960s [240], tailored to spatial statistics [88, 454] and later adapted to computational simulations [416, 425]¹⁰, Kr first purpose is to fit a stochastic process to the available data, in order to quantify the confidence associated to the numerical predictions of the model. In the classical approach, any output $y(\mathbf{x}) \in \mathbb{R}$ (here scalar) of the simulation is considered a realization of a *Gaussian* RP indexed on the *deterministic*

8. This approach is often named *Second Moment Analysis*.

9. also named *metamodels*, *response surface* models or *emulators*.

10. Kr may also be interpreted as Bayesian modeling, cf. [396].

space of the input variables $\mathbf{x} \in \mathbb{R}^N$, and may be viewed as:

$$Y(\mathbf{x}) = m(\mathbf{x}) + Z(\mathbf{x}),$$

where $m(\mathbf{x}) \equiv \mathbf{F}(\mathbf{x})\boldsymbol{\beta}$ ¹¹ is a deterministic quantity (or *regression* part) representing the “average”¹² computational model response and $Z(\mathbf{x})$ is the centered random component modeling the residual errors. Kr assumes these errors to be somewhat *correlated* (instead of independent) for different \mathbf{x} . Moreover it assumes that $Z(\mathbf{x})$ is *normally* distributed and *stationary* with mean zero and satisfies some generic correlation matrix [181] controlled by a set of *hyperparameters*: σ^2 (variance of Z), $\boldsymbol{\theta}$ (scaling parameter) and \mathbf{p} (shape parameter) accounting for the variability, the anisotropy and the regularity of the correlation decay response. The correlation depends upon distances between the sample points and should reflect the characteristics of the computer-code output. Under these assumptions the $2N + 1$ parameters and the regression coefficients of $\boldsymbol{\beta}$ are the unknown of the model. In practice, those parameters are estimated so as to *maximize* the *likelihood* of some n samples \mathbf{Y}^n (*training set* of data), [211].

The estimates $\hat{\boldsymbol{\beta}}$ and $\hat{\sigma}^2$ that maximize the likelihood depend on $(\boldsymbol{\theta}, \mathbf{p})$ [211]. Once injected into the likelihood function, we must solve a multi-dimensional optimization problem for the estimate $(\hat{\boldsymbol{\theta}}, \hat{\mathbf{p}})$. Once this search is appropriately done (cf. remarks hereafter), one can derive the *best linear unbiased predictor*¹³ of Y at a new point \mathbf{x}^* [416]:

$$\hat{Y}(\mathbf{x}^*) = \mathbf{F}(\mathbf{x}^*)\hat{\boldsymbol{\beta}} + \mathbf{r}(\mathbf{x}^*)^t \mathbf{R}_{\hat{\boldsymbol{\theta}}, \hat{\mathbf{p}}}^{-1} \left(\mathbf{Y}^n - \mathbf{F}_n \hat{\boldsymbol{\beta}} \right),$$

where \mathbf{R} is the $(n \times n)$ correlation matrix, \mathbf{r} denotes the vector of correlations between the error terms at \mathbf{x}^* and at the previously sampled points and $\mathbf{F}_n = [\mathbf{F}(\mathbf{x}^1)^t, \dots, \mathbf{F}(\mathbf{x}^n)^t]^t$.

The Kr predictor bears some nice properties: – it is an *interpolant* SM, – fast and cheap to evaluate and – it provides a *mean square error* of the prediction accuracy that is useful for the implementation of dynamic sampling [428, 506], quantiles estimation [352], optimization problems [211].

At the practical level, Kr may be challenging because of some implementation issues. For high-dimensional problems, the global optimization required to find the correlation hyperparameters poses a major difficulty as the likelihood surfaces tend to have many local maxima and/or flat surfaces. Here are a few algorithms at use: Nelder-Mead *simplex* algorithm [243], branch and bound algorithms [211], *Subplex* method and stochastic algorithms [404]. Another drawback is the poorly-conditioned correlation matrix \mathbf{R} depending on the system size, choice of covariance family and the sampling design. Finally, a very influential component of the predictive scheme is the choice of the initial “experimental design” (also called *Design of Experiments* (DoE)), i.e. the selection of the variable inputs at which to compute the computer experiment outputs [47, 13]. This aspect is related to the sampling methods mentioned hereinbefore. We make the distinction between *space-filling* and *criterion-based* DoE [425]. Space-filling designs seem to have the favor of Kr users and account for designs based on random samples: i.e. Latin Hypercube Designs (LHD) [506], based on measures of distance, or combined design criteria.

Numerous works propose some kind of improvements over Kr. The improved versions are labelled *coKriging* (coKr) and often make use of secondary function values. Among them the Gradient Enhanced Kriging (GEK) seems promising as it takes advantage of gradient information at the sampling points [256, 79]. These advances are nowadays combined with global optimization algorithms resulting in active research since the paper by Sacks *et al.* [416]. Often applied to *deterministic* shape optimization and aerodynamic global optimization, Kr methods and variants have flourished in the CFD community [212, 132, 420]. Nevertheless, when used for UQ of flow dynamics the concept is quite ambiguously stretched to account for inputs uncertainty. The Kr SM is first built independently of the input random parameters distributions, i.e. just taking into account their supports. Once the SM is obtained, the UQ is conducted by sampling the model (statistically, cf. Appendix A.1 or deterministically Appendix A.2). Dwight & Han [113] compared the efficiency of GEK to other methods for the UQ of a compressible NS flow around a parametrized random geometry. Meldi [314] compared Kriging and Polynomial Chaos techniques for the quantification of LES errors in the simulation of spatially developing three-dimensional mixing layers. Others proposed a simultaneous Kriging-based sampling for optimization and uncertainty propagation [207]. There is in fact a very limited amount of papers devoted to the development of GPr SM *explicitly* accounting for uncertain inputs. In the Ph.D. of Girard [172], the uncertainty on the inputs is propagated to the predictive (conditional) mean and covariance from a Bayesian perspective. The predictive mean and variance at uncertain points and also the predictive mean and covariance of conditional GPr for uncertain inputs are obtained for the case of Gaussian kernels and normally and independently distributed noise on the input parameters. The results are applied to multi-step ahead time series analysis and control of nonlinear dynamic systems [173].

11. $\boldsymbol{\beta}$ are the *regression parameters* vector and $\mathbf{F}(\mathbf{x}) = (1, x_1, \dots, x_N)$.

12. There is some debate about the type of approximation basis to use for the regression (e.g. constant vs. polynomial,...).

13. i.e. the value of the function that is most consistent with the typical behavior of the function as evidenced in our training sample.

Since the early 1990's, there has been a growing interest for UQ in numerical mechanics and more particularly to what is nowadays called *stochastic spectral methods* (SSM) and is well-suited to solve SPDE driven by colored noise. This appeal sparked from the work of Spanos & Ghanem [162] who pioneered the computational use of these methods, grounded in strong mathematical bases and derived from the “*Homogeneous Chaos*” (HC) theory of Wiener [508]. We refer the reader to these books on spectral methods suitable for uncertainty quantification [162, 532, 250].

The probabilistic framework chosen in this work normally requires defining *a priori* an infinite dimensional probability space. However, in a computational environment, it is crucial to represent a RP with a *finite* set of RV, thereby discretizing the process¹⁴. Moreover, it would be convenient to represent the RP by another one analytically more tractable. These important steps will allow the construction of a finite dimensional probability space of approximation. The Karhunen-Loève (KL) is a spectral decomposition technique that serves this purpose [216, 269, 287]. The KL representation of a RP with finite variance is an infinite Fourier-type series based on a spectral decomposition of its *covariance* function, thanks to Mercer's theorem [239]. It is well suited for computational purposes since it is optimal, (mean-square) convergent and involves a denumerable set of N *uncorrelated* RV, e.g. $\Theta = \{\Theta_j(\omega)\}_{j=1}^N$. Nevertheless, it requires the specification of the covariance function of the stochastic process to be represented, so that in practice, it is often used in a *truncated* form to characterize *input* sources of uncertainty of the system.

A particular class of problems, including numerous physical applications, involve random quantities with *finite* variance. The mathematical description of these quantities is facilitated by introducing the space of square integrable RV, $L^2(\Omega^{(N)}, \mathcal{B}^{(N)}, P_{\Theta})$. This vector space together with an *inner product* and an associated L^2 -norm, defined with the probability measure dP_{Θ} , becomes an *Hilbert space* \mathcal{H} .

Under these assumptions, it is possible to design functional representation approximations based on classical results from functional analysis and approximation theory. The concept of HC was first introduced by Wiener [508] when he was working on nonlinear functionals of the Brownian motion. It is an extension to Volterra's work on generalizing Taylor series to functionals [489]. It is also called the *Wiener Polynomial Chaos*, or *Wiener Chaos*, or more simply *Polynomial Chaos* (PC). The latter is the denomination that we adopt in this manuscript. Convergence was proved and according to the Cameron–Martin theorem [59]: “any nonlinear functional of a Brownian motion can be represented with mean-square convergence as a Wiener-Hermite series”¹⁵.

More recently, the *generalized Polynomial Chaos* (gPC) method was introduced [523] as a direct generalization of the PC expansion to non-Gaussian random processes, which may improve the convergence and accuracy of the representation.

The search for the *functional* representation of the stochastic problem solution $U \equiv U(\Theta)$, or of a derived quantity of interest $\psi(U(\Theta); \Theta)$, under the form of a generic expansion in terms of basis Φ_{α} *orthogonal* in the space of RV with respect to the dP_{Θ} measure, i.e.:

$$\psi(U(\Theta); \Theta) = \sum_{\alpha \in \mathcal{J}} \psi_{\alpha} \Phi_{\alpha}(\Theta),$$

is at the core of these methods. The deterministic coefficients ψ_{α} (sometimes called *modes*) are to be determined and \mathcal{J} is a set of multi-indices that are sequences of non-negative integers with only finitely many non-zero elements. When the development is accurate, the user holds an explicit functional form representation. It is then very easy to generate a large set of realizations according to the initial random discretization Θ . This information may then be condensed into some more global quantities of interest (e.g. probabilities, statistical moments, pdf, marginal pdf, sensitivity coefficients, quantiles,...) either via sampling or analytically [162].

It is worth mentioning that depending on the probability distributions at hand and the regularity of the system response, the optimal basis choice remains an open question. Indeed the type of distribution of the solution of the SPDE is not known most of the time. In particular, for nonlinear problems, it is not clear that an optimal representation of the inputs is necessarily optimal for the entire problem. Several choices of multivariate spaces (mostly polynomials) have been proposed in the literature: Hermite polynomials for Gaussian probability measures for the standard PC [162], polynomials from the Askey scheme [431] for non-Gaussian probability measures for the gPC [523] but also Lagrange polynomials [465], piecewise polynomials [97, 494], Gegenbauer polynomial [520], wavelets [248], trigonometric functions [330], splines [331],...

Several resolution schemes are available to solve for the unknown coefficients ψ_{α} . Two classes of schemes may be distinguished: – 1. the *stochastic Galerkin* approaches rely on a similar mathematical framework as deterministic Galerkin methods [97, 16, 135]. They have been developed together with the PC approximation and used first in the literature [162, 523, 99]. They define an approximation of the stochastic solution, via an

14. This is very similar to the deterministic case whereby functions are represented by a denumerable set of parameters at some discrete nodal locations (e.g. functions values for the finite element method).

15. The importance of this theorem is that it extends obvious results from finite-dimensional approximations (where various polynomials are complete with respect to their respective measures), to an infinite-dimensional context (Brownian motion instead of a finite set of random variables). Except for the Poisson and binomial measure [431], there is no parallel result for general measures.

approximation basis combined with the weak formulation of the stochastic problem. – 2. *direct methods* are affiliated to MC methods and rely on the resolution of a *set of decoupled deterministic* problems, corresponding to a set of realizations of Θ . Therefore, it only relies on the deterministic model solver (“*black-box solver*”) that is repeatedly called. The advantage of this approach is that it does not require any *a priori* code adaptation. Mainly three different approaches appeared in this order: the interpolation/collocation approach [465, 297], the projection approach [166] and the regression/least squares approach [75, 35]. The superiority of any of the two schemes in terms of accuracy and cost is often problem dependent while direct methods are often easier to implement in a computer code.

While it is manifest that stochastic spectral methods benefit from numerous advantages : e.g. method not limited to small uncertainties with Gaussian distributions, convergence rate, richness of the information, mathematical background... they also suffers major drawbacks: – 1. computational cost due to the “Curse of dimensionality”, i.e. that the number of degrees of freedom of the discretized stochastic problem increases exponentially with the number of RV, which is very bad news for CFD simulations that are known to be computationally costly for any realistic problem with complex geometry. This implies the resolution of very large system of equations or equivalently countless calls to the deterministic CFD solver. This brings the question of what is the effective dimensionality of the solution? – 2. lack of robustness and accuracy for strongly nonlinear systems. Indeed, non-smooth response surfaces are common in fluid dynamics where the nonlinearity often “translates” to the random space. Therefore stochastic global approximations are not well suited to capture solution local parametric front/shocks/gradients. This brings the question of the adaptivity of the approximation basis to the solution probabilistic sudden changes.

Some works address the first limitation by proposing *model reduction* techniques that rely on the concept of *reduced basis* for the stochastic Galerkin formulation. The ingenious idea is to take advantage of the structure of the full approximation (deterministic + stochastic) space $\mathcal{V}_{\text{det}} \otimes \mathcal{S}_{\text{sto}}$ combined together with an optimality criterion depending (if possible) on the model but not on the solution, e.g. the *generalized spectral decomposition* of Nouy [349, 350] or the works of others [415, 48]. Other researchers also propose “Time-dependent” gPC basis [153] or “stochastic POD” [202, 485]. Finally, there exists attempts to unify POD & gPC representations: e.g. “dynamically orthogonal field representation” [427] or “nonlinear biorthogonal decomposition” [487]. Other works show how to reduce the number of deterministic samples required by the direct methods layout while keeping the approximation accurate. This can be achieved by designing *regression-based sparse PC expansion* [40], using *sparse grid-based methods* for (adaptive) stochastic collocation [155, 320, 229, 138, 345, 346, 289] or rely on *ANOVA-type decomposition*, [394, 130].

Most of the studies addressing the second limitation propose *adaptive model refinement* techniques thereby increasing the robustness and/or the level of resolution/details of the approximation to capture nonlinearities. This may be achieved by *multiresolution/multiscale* schemes (e.g. multi-wavelets) [248], binary trees [478], or hierarchical sparse grid collocation [289], *nonlinear Galerkin-type* projection [384, 386], *hybrid* or *iterative gPC projection methods* [387], random [494] (with a *posteriori* heuristic convergence criteria) or random/spatial spaces partitioning [299, 499] (with dual-based error estimation techniques). But a lot of questions remain open: e.g. what type of refinement must be performed? elemental partitioning vs polynomial enrichment?

In contrast to the expansion of numerous literature reviews in computational stochastic solid mechanics [434, 433, 221, 347], there has been very few paper reviews about UQ of CFD simulations, and more specifically dedicated to spectral methods. We refer the reader to [230, 341, 250] for general reviews and briefly introduce in the following some of the accomplishments of this approach in the fields of heat transfer and thermofluidics, porous media flows, incompressible and reacting flows, flow-structure interactions, flows in random geometries and, turbulence and uncertain unsteady dynamics.

There has been a growing interest in quantifying uncertainties in *heat-transfer* in solid mechanics since the beginning of the 1990’s [122, 184] and spectral methods were soon introduced to transient heat conduction [157, 526]. This trend was then impeded to the CFD community. Le Maître *et al.* [247] studied uncertain thermofluid channel flow with temperature-dependent viscosity. They later applied the numerical method to modeling natural convection in a differentially heated cavity with stochastic temperature boundary conditions at the side walls in the Boussinesq limit [249]. Le Maître *et al.* [291] extended this study to the non-Boussinesq limit, implementing the full variable-density low-Mach-number equations. Le Maître *et al.* [248], Asokan & Zabarar [10] and Venturi *et al.* [486] have studied the standard problem of Rayleigh-Bénard flow instability in the Boussinesq limit using polynomial chaos. In this context, they considered a cavity with a stochastically heated bottom wall. Above a critical Rayleigh number, the system transitions from a conductive to a convective heat-transfer mode, as the instability of the flow leads to convective motion. Both teams had to develop a local robust and accurate approximation in order to capture the stochastic bifurcation corresponding to the critical Rayleigh number.

More recently, Wan & Karniadakis [497] have developed an adaptive stochastic spectral method to tackle the problem of subcritical resonant heat-transfer in a heated grooved channel flow subject to external stochastic excitations. Other researchers proposed new coupled methods for computing approximate statistics of the

stochastic temperature field [86].

Stochastic spectral methods dedicated to UQ of fluid flows were first applied to flows through *porous media* which are prone to uncertainties [536, 78] due to spatial heterogeneities of geological materials and temporal variations of the internal and external input flow rates [163, 158, 302]. More recent papers show that spectral UQ is still beneficial to this area [537, 463, 139, 288, 140, 263]. Increasing the level of complexity to *incompressible flows*, Le Maître *et al.* have derived and implemented a stochastic Navier–Stokes PC solver using finite-differences to investigate laminar fluid-flow and transport problems [247, 249]. In [285], the authors have generalized the approach to other non-gaussian types of randomness and polynomials [523], and have applied it to incompressible 2D flows [525] discretized with spectral/*hp* element methods. Lucor has used the same approach to study 3D flows as well [274]. More recently, Asokan & Zabaras [11] have developed a 2D stabilised finite-element stochastic formulation by considering an extension of the deterministic variational multi-scale approach with algebraic subgrid-scale modeling for the stochastic advection and the incompressible stochastic Navier–Stokes equations, and applied it to natural convection problems [10]. Where most of the PC-based studies have dealt with stochastic input generated by a finite number of random variables, Hou *et al.* [195] have considered 2D Navier–Stokes equations (in a stream function-vorticity formulation) driven by Gaussian Brownian motion and advecting a temperature field. They have introduced a compression technique to handle the constant flux of new random variables due to the Brownian motion. While the majority of these studies rely on intrusive techniques, where the weak form of the flow SPDE are derived and solved via a Galerkin-type projection, another choice consists in solving the flow system non-intrusively via probabilistic collocation or spectral projection [232, 236].

Uncertainties are certainly important for the simulation of *reacting flows* but they present serious challenges to spectral UQ. High dimensionality associated with numerous uncertain parameters (e.g. chemical parameters) and the strong nonlinearity of chemical reactions (e.g. threshold behavior) deteriorates the efficiency of the method. Despite these difficulties, several studies have been pursued. Phenix *et al.* [378] first used probabilistic collocation for isothermal chemical ignition in their deterministic equivalent modeling–method approach, focusing on supercritical water oxidation. With this chemical model, Reagan *et al.* [231] employed spectral projection with LHS design in ignition and 1D flames. Later, they computed uncertain sensitivity coefficients from the results [398]. They have also highlighted the need for high stochastic approximation order to ensure species concentration positivity and to maintain stability under fast rates of amplification of uncertainty [397]. Debusschere *et al.* [98] also investigated protein-labeling into electrochemical reacting microchannels flows. Najm and coworkers demonstrated the use of multiwavelet spectral PC techniques for UQ in non-isothermal ignition of a methane–air system while employing Bayesian inference to characterize uncertain parameters [340]. Finally, a stochastic optimization framework combining stochastic surrogate model representation and optimization algorithm was proposed by Lucor *et al.* [275] who applied it to a multi-layer reacting flow device.

Another interesting and relevant topic for the UQ of CFD is the one concerned with the development of tools for efficient simulations of *flow-structure interactions* (FSI) that account for random excitation and uncertain inputs [274]. External loading on structures from environmental sources such as fluid flow is often modeled as a temporal or spatio-temporal stochastic process, cf. the stochastic oscillators study in [282, 278]. In addition, material properties of a structure may vary from point to point in the material [131]. The problem is complex when the flow-structure coupling is nonlinear as in the unsteady case of Vortex-Induced Vibrations (VIV) [283]. Oscillatory vortex shedding behind a stationary [530] and moving circular cylinder [280, 279] with a stochastic Galerkin method coupled to a spectral/*hp* deterministic discretization. Despite these results, heavy three-dimensional DNS or LES flow-structure interaction studies are still out of reach for UQ. A branch of FSI that has been more thoroughly investigated is the field of stochastic *aeroelasticity*. The reason is that the flow excitation is often modeled instead of fully computed, resulting in more manageable CPU times. The prediction of the flutter onset speed is of great importance in aeroelasticity [374]. When nonlinearities are present into the structural or aerodynamic operator, the growth in the amplitude of the response is stabilized to limit cycle oscillations (LCO) which are inherently sensitive to small variations of both the structural parameters and initial conditions [32]. Several stochastic methodologies have been developed in order to gain more insights into the physical flutter mechanism and LCO [330, 516, 513, 512, 514, 312, 71] with affordable computational requirements.

The previous field of application naturally brings the question of how the uncertainty propagation relates to *geometric uncertainty*. For instance, in engineering design a particular attention must be paid to geometric irregularities, caused by manufacturing tolerances that can significantly affect the performance of the mechanical component. This is a very challenging topic and very few papers propose some methodologies [531, 63, 365, 333, 348, 73].

Uncertainty quantification certainly applies to describing deficiencies in *turbulence* modeling. There have been several attempts to apply a PC-based approach to turbulence. In fact, this approach was suggested in the early works of Wiener in 1939, but the idea lay dormant for twenty years. During the 1960’s, several proposals have suggested developing a theory of turbulence involving a truncated Wiener–Hermite expansion of the velocity field [310, 360, 309, 90, 61, 77]. Unfortunately, all these works failed in the sense that the *finite* Hermite

polynomial approximation yielded non-physical kinetic energy spectra. The main reason was that, due to the non local and nonlinear character of turbulence, a truncated polynomial expansion was not able to account for *long-term dynamics* of the kinetic energy transfers among modes and their correlations.

This drawback is associated with a well-known difficulty in the UQ of uncertain dynamical systems over long times. In this case, the parametric uncertainty directly affects the system phase velocity which translates in a broadening spectral content of the solution with time, precluding accurate approximations using usual discretization techniques based on fixed-order stochastic polynomial bases. Some authors proposed some method adaptations to improve the approximation accuracy to later times [377, 32, 498, 495, 512, 153]. Nevertheless, it seems that the failure of the stochastic approximation is delayed but not remedied. Concerning stochastic turbulent flows, the direct decomposition of the instantaneous turbulent field onto a PC approach can not presently be considered as an efficient way to address the issue of the sensitivity of a simulated turbulent flow. Instead the statistical moments of the simulated turbulence field (or related quantities such as the kinetic energy spectrum) may be successfully approximated as functions of the uncertain parameters [281, 316].

The stochastic studies presented in this manuscript cover CFD simulations of fluid flows that have not been extensively investigated in the UQ literature: namely, incompressible shear flows and compressible flows dominated by shock waves. These type of flows are very interesting and relevant in terms of their high sensitivity to parametric uncertainty and random disturbances.

One of the key issues in the study of incompressible sheared flows, which are known to be prone to instabilities and sometimes sensitive to external noise, is the understanding of the flow *transition* from laminar to turbulent state [430]. Both inviscid and viscous theories of hydrodynamic stability has been devoted to the topic of parallel shear flows in a large body of work [65]. Common practice in stability studies is to consider a simple *basic* or *mean* shear flow configuration and add slight deterministic disturbances. While, the assumption of a regular base flow greatly simplifies the analysis, it introduces a limitation that misrepresents realistic configurations [43]. In this work, we propose to generalize the approach by considering shear flow stability with internal uncertainty and covariance dynamics, i.e. stochastic effects that stem from uncertainties in the operator itself.

Another intriguing question, considering the simple form of its *free* shear flow, is the case of the mixing layer that forms between merging fluid streams of differing velocity. Indeed, there is no particular consensus that defines the best inflow condition with which the mixing layer flow simulation should be initialized [307]. In general, special attention is paid to the effects of forcing amplitude and relative phase shift between forcing frequencies onto the growth of the coherent vortex structures. In this work, we treat the problem under a stochastic prism and address the sensitivity of a spatially developing mixing layer to some uncertainties present in the magnitude of various disturbance modes imposed on the shear velocity profile at the upstream boundary. The quest for high-order methods for use in ever more complex compressible flow simulations has led to the emergence of modern shock-capturing numerical methods. Nevertheless, numerical predictions of realistic flows involving complex pattern of interacting shock waves remains often overwhelmed by abundant errors and uncertainties : physical and computational domain/geometry, initial/operating conditions, physical/turbulence models, mathematical model assumptions/simplifications, discretization and numerical algorithmic errors. The application of UQ to compressible flows will certainly have a strong impact but remains nowadays very challenging. In particular, the stochastic approximation of *nonlinear* hyperbolic systems of conservation laws is very hard because they promote discontinuous spatial solutions in finite time, i.e. shock waves and contact discontinuities; the uncertainty slipping into the propagation speeds and in the physical fluxes, it induces in turn discontinuous solutions in the stochastic space and severe Gibbs-like oscillations ineluctably appear. In this manuscript different solutions are investigated, i.e. both Galerkin-type and direct methods relying on gPC approximation are examined. The proposed numerical schemes are then applied to the resolution of nonlinear hyperbolic systems with different levels of regularity, dimensionality and complexity. Finally, a stochastic direct method is coupled to RANS simulations to investigate uncertain transonic aerodynamics.

This manuscript consists of four main chapters with two more in-depth chapters (i.e. Chapters 2 & 3), focussing on the collaborative work conducted with two PhD students I have supervised and a more synthetic chapter (i.e. Chapter 4) gathering brief descriptions of my other current scientific projects. Mathematical probabilistic framework and fundamentals concepts and properties of stochastic spectral methods for uncertainty quantification in numerical mechanics are outlined in the first chapter. Some emphasis is given to the description of more recent adaptive approaches toward the end of the chapter and some paths are suggested for nonlinear model refinement. The second chapter is devoted to the adaptation of these methods to the uncertainty quantification of incompressible parallel shear-dominated flows. More specifically, the study of the effects of base flow uncertainty on the linear stability of a planar Couette flow is considered first, followed by the case of the sensitivity of a spatially developing mixing layer to random inflow disturbances, i.e. a closed and an open shear flow. The focus is mainly on the physical mechanisms and effects induced by colored random inflow or base flow disturbances. The third chapter deals with the class of stochastic compressible flows and more generally with the problem of shock-dominated responses such as the ones obtained for nonlinear hyperbolic

systems. A quite theoretical review of the application of spectral Galerkin methods to these kind of systems is given first, followed by a more applied section presenting the stochastic investigation of uncertain transonic aerodynamics about several airfoils. The next chapter provides short summaries and/or references of my other current or recent scientific interests. Lastly, the final section concludes with some considerations about open questions and adds some perspectives to the discussion.

Chapter I

Stochastic Spectral Methods for uncertainty propagation and quantification in numerical mechanics

The purpose of this introductory chapter is to outline the main mathematical concepts and key ingredients necessary to apprehend the spectral representation of stochastic processes in numerical mechanics. We focus more specifically on continuous stochastic processes in L^2 . Two classes of representation are introduced: the Karhunen-Loeve and the (generalized) Polynomial Chaos expansions, with a discussion on the available choice of approximation space. Then, we explain how the stochastic representation may be introduced into the physical deterministic system and what are the different approaches to propagate this uncertainty to the numerical solution. Finally, some emphasis is given to the evolution of more recent adaptive approaches toward the end of the chapter. We refer the reader to the following literature books for more details [162, 250, 532].

Sommaire

1	Probabilistic framework for the discretization of stochastic processes	23
1.1	Continuous random variables and stochastic processes	23
1.2	Finite-dimensional noise assumption	24
1.3	L^2 Hilbert space of second-order random variable	24
2	Spectral expansions	25
2.1	Karhunen-Loève representation	25
2.2	Polynomial Chaos and generalized Polynomial Chaos expansions	27
2.3	Choice of spaces	31
3	Resolution schemes	34
3.1	Galerkin methods	34
3.2	Direct methods	40
4	Spectral statistics	42
4.1	Statistical moments	42
4.2	Probability distribution functions	43
4.3	Sensitivity coefficients	43
5	Adaptive approaches for error vs. cost control	44
5.1	Model reduction	45
5.2	Model refinement	45

1 Probabilistic framework for the discretization of stochastic processes

1.1 Continuous random variables and stochastic processes

We first recall the notion of *random variable* (RV). If we consider a probability space (Ω, \mathcal{F}, P) where Ω is the sample space, $\mathcal{F} \subset 2^\Omega$ the σ -algebra and P the probability measure and a function X (i.e. a mapping) $X : \Omega \mapsto \mathcal{D} \subset \mathbb{R}$ measurable from (Ω, \mathcal{F}) to $(\mathcal{D}, \mathcal{B}(\mathcal{D}))$, then X is called a \mathcal{D} -valued RV. $X \equiv X(\omega)$ is fully determined by its *cumulative distribution function* (cdf) F_X :

$$F_X(a) = P(X \leq a) = P(\{\omega : X(\omega) \leq a\}) \quad (1.1)$$

and

$$f_X(a) = \frac{d}{da} F_X(a) \quad (1.2)$$

is the *probability density function* (pdf) of X , so $F_X(a) = \int_{-\infty}^a f_X(x) dx$.

This definition can be extended to $\mathcal{D}^N \subset \mathbb{R}^N$ -valued function \mathbf{X} measurable from (Ω, \mathcal{F}) to $(\mathcal{D}^N, \mathcal{B}(\mathcal{D}^N))$. In this case, if all coordinates of \mathbf{X} are RV, then \mathbf{X} is called a *random array* (RA) or random vector.

In the following, we consider a bounded spatial domain $\mathcal{D} \subset \mathbb{R}^d$ (but all definitions can be extended to a time interval).

Let us now consider a function X (respectively \mathbf{X}) : $(\mathbf{x}, \omega) \in \mathcal{D} \times \Omega \mapsto X(\mathbf{x}, \omega)$ (respectively $\mathbf{X}(\mathbf{x}, \omega) \in \mathbb{R}$ (respectively \mathbb{R}^N), depending if X is a scalar or \mathbf{X} a \mathbb{R}^N -valued.

If $X(\mathbf{x})$ (respectively $\mathbf{X}(\mathbf{x})$) is a \mathbb{R} -valued RV (respectively \mathbb{R}^N -valued RA) on the probability space (Ω, \mathcal{F}, P) for all \mathbf{x} , then X (respectively \mathbf{X}) is called a \mathbb{R} -valued (respectively \mathbb{R}^N -valued) *stochastic process* (SP) or *random field* (RF) (respectively vector SP).

The function $X(\cdot, \omega)$ (respectively $\mathbf{X}(\cdot, \omega)$) for a given event $\omega \in \Omega$ is called a *realization* of X (respectively \mathbf{X}) (or a *sample path* in the case of time dependency).

Finally, space and time definitions can be combined to describe a space-time SP.

The probabilistic representation of a SP may be connected to the probabilistic characterization of a collection of RV. Without loss of generality, let us consider now the case where $N = 1$ and $\mathbf{x} = x_1, x_2, \dots, x_M$ is a vector of members of \mathcal{D} that corresponds to M distinct points in space. The vector $(X_{x_1}, X_{x_2}, \dots, X_{x_M})$ has joint distribution $F_{\mathbf{x}} : \mathbb{R}^N \rightarrow [0, 1]$ given by

$$F_{\mathbf{x}}(\mathbf{a}) = P\{X_{x_1} \leq a_1, \dots, X_{x_M} \leq a_M\}; \quad x_i \in \mathcal{D}. \quad (1.3)$$

The collection $\{F_{\mathbf{x}}\}$ as \mathbf{x} ranges over all position vectors of any length is called the collection of *finite dimensional distributions* (fdd) of X , and it contains all the information which is available about X from the distributions of its component variables X_x .

1.2 Finite-dimensional noise assumption

In order to perform a stochastic discretization, we need to reduce the infinite-dimensional (Ω, \mathcal{F}, P) to a finite-dimensional probability space. This can be accomplished by characterizing the probability space with a *countable* number N of mutually independent random variables forming a RV that we call $\Theta = \{\Theta_j(\omega)\}_{j=1}^N$, $N \in \mathbb{N}$ on the probability space with probability distribution $P_{\Theta}(d\theta)$, where $d\theta = d\theta_1 \dots d\theta_N$ is the Lebesgue measure on \mathbb{R}^N . We note the finite-dimensional space $(\Omega^{(N)}, \mathcal{B}^{(N)}, P_{\Theta})$ where $\Omega^{(N)} = \Omega_1 \times \dots \times \Omega_N \subset \mathbb{R}^N$, with $\Omega_j := \text{range}(\Theta_j) = \Theta_j(\Omega)$, $\mathcal{B}^{(N)}$ is the Borel σ -algebra of $\Omega^{(N)}$ and P_{Θ} is the probability distribution of the RA Θ .

Such a procedure, sometimes called the “finite-dimensional noise assumption“, is often achieved via a certain type of decomposition which can approximate the target random process with desired accuracy. One of the choices is the Karhunen–Loève type expansion (cf. next section). Once the random field has been represented in a finite number of independent random variables, it may be seen as a function on a high dimensional space. The independence of the underlying RV allows to see each of them as the axis of a coordinate system. This is asserted by the Doob-Dynkin lemma [358].

The SP U that we seek can now be written: $U(\mathbf{x}, \omega) \approx U(\mathbf{x}, \Theta_1, \Theta_2, \dots, \Theta_N) = h(\mathbf{x}, \Theta)$, where $h : \theta \mapsto h(\theta)$ is a measurable mapping from $\mathbb{R}^N \mapsto \mathbb{R}$.

1.3 L^2 Hilbert space of second-order random variable

A particular class of problems, including numerous physical applications, involve random quantities with *finite* variance. The mathematical description of these quantities is facilitated by introducing the L^2 space of *second-order* RV, i.e. $L^2(\Omega^{(N)}, \mathcal{B}^{(N)}, P_{\Theta})$:

$$L^2(\Omega^{(N)}, \mathcal{B}^{(N)}, P_{\Theta}) = \{U : \Theta \in \Omega^{(N)} \mapsto U(\Theta) \in \mathbb{R} / \mathbb{E}[U^2] < +\infty\} \quad (1.4)$$

with,

$$\mathbb{E}[U^2] = \mathbb{E}[h(\Theta)^2] := \int_{\Omega^{(N)}} h(\Theta)^2 P_{\Theta}(d\theta) = \int_{\Theta(\Omega)} h(\theta)^2 f_{\Theta}(\theta) d\theta, \quad (1.5)$$

where \mathbb{E} denotes the expectation and f_{Θ} the pdf of Θ . This vector space together with an *inner product*:

$$\begin{aligned} \langle U, V \rangle &= \mathbb{E}[UV] = \int_{\Theta(\Omega)} U(\Theta)V(\Theta)P_{\Theta}(d\theta), \\ &\text{with } (U, V) \in L^2(\Omega^{(N)}, \mathcal{B}^{(N)}, P_{\Theta}), \end{aligned} \quad (1.6)$$

and the associated L^2 -norm:

$$\|U\|_2 = \|U\|_{L^2(\Omega^{(N)}, \mathcal{B}^{(N)}, P_{\Theta})} = \mathbb{E}[U^2]^{\frac{1}{2}}, \quad (1.7)$$

becomes an *Hilbert* space \mathcal{H} . It is sometimes referred as a *separable* Hilbert space, which means that it has a *countable* orthonormal basis of RV.

2 Spectral expansions

2.1 Karhunen-Loève representation

The Karhunen-Loève representation [216, 269] of a SP with finite variance is an infinite Fourier-type series based on a spectral decomposition of its *covariance* function. It is closely related to similar decomposition techniques such as Proper Orthogonal Decomposition (POD), Principal Component Analysis (PCA) or Singular Value Decomposition (SVD). The Karhunen-Loève (KL) expansion is very useful for representing physical quantities modeled as SP with finite variance and *known* correlation functions. In particular, the decomposition is very convenient for Gaussian SP. The efficiency of the method is related to the truncation error which should be adjusted depending on the regularity of the covariance function. Numerical techniques have been developed to tackle non-Gaussian and non-stationary stochastic processes with KL [422, 380]. While this decomposition is straightforward for the representation of random inputs some techniques have been proposed to approximate the decomposition when the correlation function is not known *a priori* (e.g. for the solution of the problem), see for instance [107].

2.1.1 From an eigenvalue problem to an infinite series expansion

We consider a *second-order* SP: $R(\mathbf{x}, \omega) \in L^2(\mathcal{D}) \times L^2(\Omega, P)$ and its covariance (or autocovariance to be more specific) function:

$$\text{cov}_R : (\mathbf{x}_1, \mathbf{x}_2) \in \mathcal{D} \times \mathcal{D} \mapsto \text{cov}_R(\mathbf{x}_1, \mathbf{x}_2) = \mathbb{E}[(R(\mathbf{x}_1, \omega) - \mu_R(\mathbf{x}_1))(R(\mathbf{x}_2, \omega) - \mu_R(\mathbf{x}_2))] \in L^2(\mathcal{D}),$$

with $\mu_R(\mathbf{x}_1) = \mathbb{E}[R(\mathbf{x}_1, \omega)]$ and $\mu_R(\mathbf{x}_2) = \mathbb{E}[R(\mathbf{x}_2, \omega)]$.

We can define a covariance operator such that:

$$T_R : q \in L^2(\mathcal{D}) \mapsto T_R(q) := \int_{\mathcal{D}} \text{cov}_R(\cdot, \mathbf{x}_2) q(\mathbf{x}_2) d\mathbf{x}_2 \quad (1.8)$$

If cov_R is continuous and bounded on $\mathcal{D} \times \mathcal{D}$, the covariance operator is *real*, *symmetric* and *positive-definite* and has a countable sequence of eigenpairs $(\lambda_i, r_i) \in \mathbb{R}^+ \times L^2(\mathcal{D})$, satisfying an eigenvalue problem described by a Fredholm equation of the second-kind:

$$\int_{\mathcal{D}} \text{cov}_R(\mathbf{x}_1, \mathbf{x}_2) r_i(\mathbf{x}_2) d\mathbf{x}_2 = \lambda_i r_i(\mathbf{x}_1) \quad \text{with} \quad \int_{\mathcal{D}} r_i(\mathbf{x}) r_j(\mathbf{x}) d\mathbf{x} = \delta_{ij}, \quad (1.9)$$

and the eigenfunctions form a complete Hilbertian orthogonal basis of $L^2(\mathcal{D})$. with: eigenvalues $\{\lambda_i\} \subset \mathbb{R}_+$ and *orthogonal* eigenfunctions $\phi_i(x)$ (complete basis).

We can represent the covariance kernel spectrally as,

$$\text{cov}_R(\mathbf{x}_1, \mathbf{x}_2) = \sum_{i=1}^{\infty} \lambda_i r_i(\mathbf{x}_1) r_i(\mathbf{x}_2). \quad (1.10)$$

The Karhunen-Loève representation of $R(\mathbf{x}, \omega)$ is:

$$R(\mathbf{x}, \omega) = \mu_R(\mathbf{x}) + \sigma_u \sum_{i=1}^{\infty} \sqrt{\lambda_i} r_i(\mathbf{x}) \zeta_i(\omega), \quad (1.11)$$

where:

$$\zeta_i(\omega) = \frac{1}{\lambda_i} \int_{\mathcal{D}} (R(\mathbf{x}, \omega) - \mu_R(\mathbf{x})) r_i(\mathbf{x}) d\mathbf{x}, \quad (1.12)$$

are mutually *uncorrelated* RV with zero mean and unit variance and the λ_i are real, ordered, positive eigenvalues. The equality holds as long as we have an infinite sum. People sometimes refer to Eq. (1.11) as a *bi-orthogonal* decomposition as both eigenfunctions r_i and RV ζ_i are orthogonal.

Practically, we can only deal with finite representation and the KL expansion has to be truncated:

$$R(\mathbf{x}, \omega) \approx R^N(\mathbf{x}, \omega) = \mu_R(\mathbf{x}) + \sum_{i=1}^N \sqrt{\lambda_i} r_i(\mathbf{x}) \zeta_i(\omega), \quad (1.13)$$

2.1.2 Properties

The approximation of the covariance function, $\text{cov}_R^N(\mathbf{x}_1, \mathbf{x}_2) = \sum_{i=1}^N \lambda_i r_i(\mathbf{x}_1) r_i(\mathbf{x}_2)$ converges absolutely and uniformly to $\text{cov}_R(\mathbf{x}_1, \mathbf{x}_2)$ on $\mathcal{D} \times \mathcal{D}$ by Mercer's theorem [239].

The series (1.13) is an optimal *linear* approximation of R in the sense that it converges *uniformly* in $L^2(\mathcal{D}) \times L^2(\Omega, P)$:

$$\|R - R^N\|^2 = \|R - \mu_R\|^2 - \sum_{i=1}^N \lambda_i \longrightarrow 0, \quad \text{as } N \rightarrow \infty. \quad (1.14)$$

This means that there is no other *linear* representation with N terms that has a smaller mean square quadratic error. The truncation error decreases monotonically with the number of terms in the expansion. The convergence is inversely proportional to the *correlation length* and depends on the regularity of the covariance kernel [135], cf. Fig. 1.1.

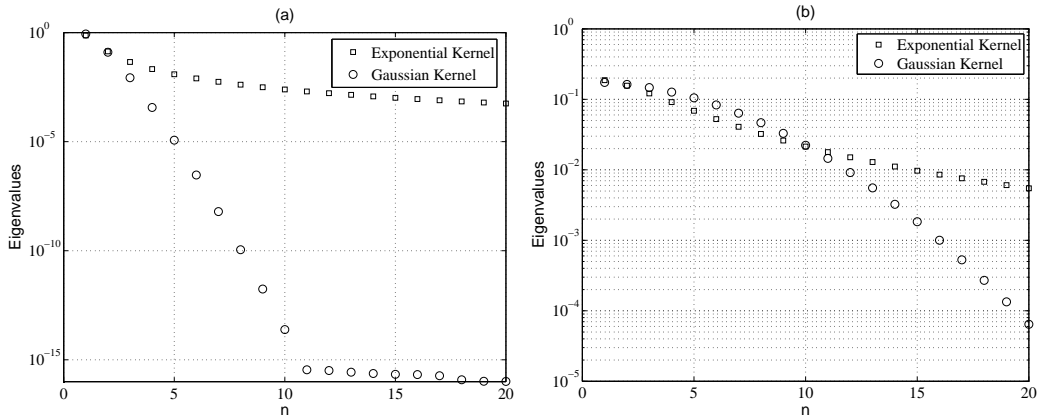


Figure 1.1 – Eigenvalue spectrum convergence comparison between exponential and Gaussian covariance kernels for different correlation length; (a): $C_l = 1.0$, (b): $C_l = 0.1$.

Remark 1.1

A very convenient case is the one where the SP to represent is a Gaussian SP. In this case, the ζ_i RV involved in the Karhunen-Loève representation are Gaussian RV and therefore are independent and easy to manipulate. The task of numerically representing continuous non-Gaussian random fields via a Karhunen-Loève decomposition is not a trivial task. We remark that it is possible to construct multidimensional functional spaces based on finite number of dependent random variables [449]. However, such a construction does not, in its current form, allow straightforward numerical implementations.

A generalization of the KL approach named Hilbert-Karhunen-Loève [255, 107] provides an optimal decomposition of a SP $R \in \mathcal{H} \times L^2(\Omega, P)$, where \mathcal{H} is an Hilbert space of functions defined on \mathcal{D} and the norm is a different one from the L^2 norm. In this case, once the inner product:

$$\langle \cdot, \cdot \rangle_{\mathcal{H} \times L^2(\Omega, P)} = \mathbb{E}[\langle \cdot, \cdot \rangle_{\mathcal{H}}] \quad (1.15)$$

has been defined, the formulation is very similar to the one exposed previously.

2.1.3 Practical numerical resolution

In practice, an approximation of the kernel function cov_R may be constructed from repetitive observations of the process [300]. Such measurement procedure can be costly, and for numerical simulations one often assumes

instead the form of the covariance function. We may distinguish among two classes of SP, whether they bear a rational or non-rational spectrum.

If we consider SP with a rational spectrum, they are stationary output of linear filters to white noise excitation, they have a spectral density that takes the general form:

$$S(\omega) = \frac{N(f^2)}{D(f^2)}, \quad (1.16)$$

where N and D are polynomials of the frequency f of order n and d respectively. The nice property is that the Fredholm equation can be transformed in this case into a second order homogeneous differential equation. There exists in fact some analytic or semi-analytic solutions for a few spectrums [162]. If we consider for instance, the first-order stationary Markovian process in one-dimensional space (or in time) with exponential correlation function defined as

$$\text{cov}_R(x_1, x_2) = \sigma_R^2 e^{-|x_2 - x_1|/C_l} \quad \forall (x_1, x_2) \subset \mathcal{D} \times \mathcal{D}, \quad (1.17)$$

where σ_R^2 is the SP variance, C_l is the correlation length (or correlation time) and $\mathcal{D} = [-L/2, L/2] \in \mathbb{R}$. Then, the SP $R(x, \omega)$ is the stationary solution of the differential equation:

$$\dot{R}(x) = -\frac{1}{C_l} R(x) + \sigma_R \sqrt{\frac{2}{C_l}} W(x), \quad (1.18)$$

in which $W(x)$ is the zero-mean stationary white noise with covariance function $\delta(x)$. It has been shown that higher order Markovian kernels may be expressed as linear combinations of first order ones. This model is widely used in the literature and semi-analytic eigenpair solutions exist [162]. Nevertheless, the suitability of this kernel to model random fields (especially with more than one spatial variability) is questionable due to its one-sided memory effect [507, 458]. That is why it may be preferable to use it to model random time series instead.

It becomes much more difficult to derive the solution of non-rational spectra. It may still be possible to derive an ordinary differential equation and its solution from the Fredholm integral equation, but only for a few specific SP (e.g. triangular kernel, uniformly modulated nonstationary process and band-limited white noise process [162]). This approach becomes intractable in multi-dimensions and/or for complex geometry. In this case, one has to rely on numerical solution and the Fredholm integral equation can be solved by standard techniques [14]. Most of the time, it is done by means of a variational formulation or some Galerkin-type approaches. Once the equation has been discretized, and the eigenfunctions decomposed onto an approximation finite-dimensional space (e.g. finite element shape functions [223]), the equation can be written in a matrix form and it becomes an eigenvalue problem with a stiffness matrix (usually dense) depending on the covariance kernel and approximation basis and a mass matrix (usually sparse) depending on the approximation basis. The numerical resolution of such an eigenvalue problem can be quite challenging. On one hand, the size of those matrices can be large for random processes with short correlation length where a lot of approximation bases are needed. On the other hand, the sparsity of the stiffness matrix becomes poor for strongly correlated processes, which is a severe handicap for standard iterative eigenvalue problem solvers. As we will mention later, there are several techniques, such as the fast multipole method, that alleviates the cost of the KL decomposition, in $\mathcal{D} \subset \mathbb{R}^3$ for instance.

In the following, we consider a smooth kernel: the Gaussian kernel. It takes the following form [135]:

$$\text{cov}_R(x_1, x_2) = \sigma_R^2 e^{-\frac{(x_2 - x_1)^2}{L^2 C_l^2}} \quad \forall (x_1, x_2) \subset \mathcal{D} \times \mathcal{D}, \quad (1.19)$$

where L is the diameter of the domain \mathcal{D} . The associated process is mean-square differentiable of any order. There are no analytical solutions to the Fredholm integral problem for this kernel. Here, the eigenpairs are solve numerically with a spectral collocation method based on Chebyshev polynomials [49]. We use 100 collocation points along the domain \mathcal{D} . The eigenvalue results for two different correlation lengths are displayed in Fig. 1.1. The Karhunen-Loève numerical approximation of the Gaussian kernel with $N = 4$ terms is shown in Fig. 1.2 along with its error surface.

2.2 Polynomial Chaos and generalized Polynomial Chaos expansions

Let us consider the Hilbert space of scalar-valued functions built with a RA $\Theta = \{\Theta_j(\omega)\}_{j=1}^N, N \in \mathbb{N}$, and introduced at the end of Section 1.3. We call $\{\Phi_\alpha\}_{\alpha \in \mathcal{J}}$ a Hilbertian basis of $L^2(\Omega^{(N)}, \mathcal{B}^{(N)}, P_\Theta)$, i.e. a complete *orthonormal*¹ family of functions such that:

$$\mathbb{E}[\Phi_\alpha, \Phi_\beta] = \delta_{\alpha\beta}, \quad (1.20)$$

1. in fact orthogonal is enough here, but we choose the normalized version to simplify the notations.

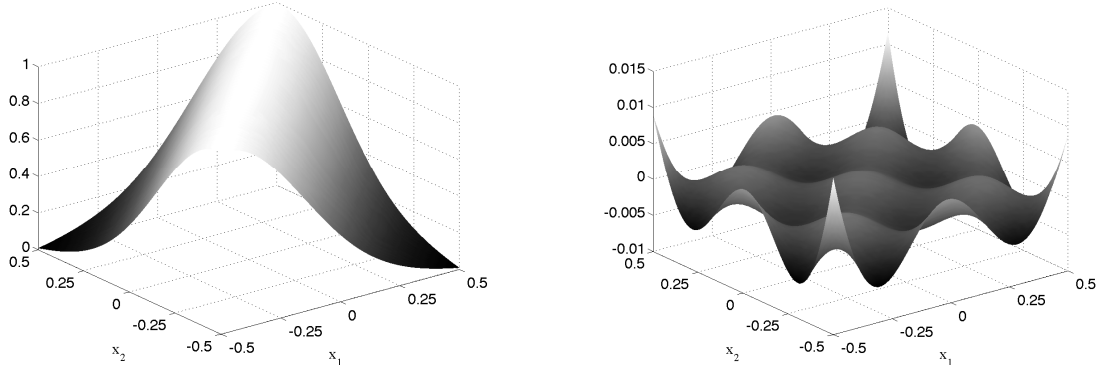


Figure 1.2 – The 4-term Karhunen-Loève approximation of the *Gaussian* covariance kernel (left), and the corresponding relative error surface (right); $C_l = L/2$ and $L = 1$.

and that the representation of a function $V \in L^2(\Omega^{(N)}, \mathcal{B}^{(N)}, P_{\Theta})$ is unique:

$$V = \sum_{\alpha \in \mathcal{J}} V_{\alpha} \Phi_{\alpha}, \quad \text{with} \quad V_{\alpha} = \mathbb{E}[V \Phi_{\alpha}]. \quad (1.21)$$

2.2.1 Case of independent random variables

In the case, where those RV are *independent* with associated marginal PDF $f_{\Theta_j}(\theta_j)$, then the joint PDF of Θ may be written:

$$f_{\Theta}(\boldsymbol{\theta}) = \prod_{j=1}^N f_{\Theta_j}(\theta_j). \quad (1.22)$$

The construction of the multi-dimensional Hilbert bases is obtained from *tensorisation* of one-dimensional basis. We have:

$$\Phi_{\alpha}(\boldsymbol{\theta}) = \prod_{j=1}^N \Phi_{\alpha_j}^{(j)}(\theta_j), \quad (1.23)$$

where $\{\Phi_k^{(j)}\}_{k \in \mathcal{J}^{(j)}}$ is the basis of $L^2(\Omega^{(j)}, \mathcal{B}^{(j)}, P_{\Theta_j})$ and the multi-index $\alpha = (\alpha_1, \dots, \alpha_N) \in \mathcal{J} = \mathcal{J}^{(1)} \times \dots \times \mathcal{J}^{(N)} \subset \mathbb{N}^N$.

2.2.2 Case of dependent random variables

In the case, where the RV are now mutually *dependent*, equality (1.22) does not hold anymore and the multi-dimensional basis may be written instead [449]:

$$\Psi_{\alpha}(\boldsymbol{\theta}) = \left[\frac{\prod_{j=1}^N f_{\Theta_j}(\theta_j)}{f_{\Theta}(\boldsymbol{\theta})} \right]^{1/2} \Phi_{\alpha}(\boldsymbol{\theta}), \quad (1.24)$$

with the same notation for the multi-indices as previously. We notice that if $\{\Phi_{\alpha_j}^{(j)}\}$ are orthonormal then Ψ_{α} is orthonormal. However if $\{\Phi_{\alpha_j}^{(j)}\}$ are polynomial basis (cf. next section), Ψ_{α} are not polynomial for general joint densities. Therefore, the construction of an optimal basis of representation for general probability laws is complex and may require heavy numerical procedures.

2.2.3 Polynomial Chaos expansion

In the following we discuss Polynomial Chaos and generalized Polynomial Chaos expansions that rely on the use of polynomial approximation and the ideas introduced hereinbefore. The concept of *Homogeneous Chaos* (HC) was first introduced by Wiener [508] when he was working on non-linear functionals of the Brownian motion. It is an extension to Volterra's work on generalizing Taylor series to functionals [489]. It is also called the *Wiener Polynomial Chaos*, or *Wiener Chaos*, or more simply *Polynomial Chaos* (PC). The latter is the denomination that we adopt in this manuscript.

Later, Ghanem & Spanos [450] have pioneered the computational use of the (PC) expansion. More recently, the *generalised Polynomial Chaos* (gPC) method was introduced [523] as a direct generalization of the PC expansion to non-Gaussian random processes, which may improve the convergence and accuracy of the representation.

In the following, we consider a separable Hilbert space $L^2(\Omega^{(N)}, \mathcal{B}^{(N)}, P_{\Theta})$ (cf. section 1.3). We define the space \mathbb{P}_p^N of all N -variate *polynomials* of degree p by:

$$\mathbb{P}_p^N(\Theta) := \{\mathcal{P}(\boldsymbol{\theta}) \mid \mathcal{P} \text{ is polynomial of degree } p; \boldsymbol{\theta} \in \Theta, N < \infty\}. \quad (1.25)$$

The space of all polynomials is called $\mathbb{P}(\Theta) := \bigcup_{p=0}^{\infty} \mathbb{P}_p^N(\Theta)$. We denote by $\bar{\mathbb{P}}_p^N$ the closure with respect to the L^2 measure and define:

$$\begin{aligned} \mathbb{H}_0^N &:= \bar{\mathbb{P}}_0^N, \\ \mathbb{H}_p^N &:= \bar{\mathbb{P}}_p^N \ominus \bar{\mathbb{P}}_{p-1}^N, \quad \text{for } l \in \mathbb{N}, \end{aligned} \quad (1.26)$$

then \mathbb{H}_p^N is the orthogonal complement of $\bar{\mathbb{P}}_{p-1}^N$ in $\bar{\mathbb{P}}_p^N$.

Then we call \mathbb{H}_p^N the HC of order p and $\mathbb{H}_{\leq p}^N := \bigcup_{k=0}^p \mathbb{H}_k^N$ the PC of order p . This ‘‘total degree’’ polynomial space is commonly used for stochastic spectral methods but we will see in the following sections (cf. Section 2.3.1) that different polynomial basis choices exist depending on the prevalence of accuracy versus efficiency.

Finally our L^2 space bears the following orthogonal polynomial decomposition:

$$L^2(\Omega^{(N)}, \mathcal{B}^{(N)}, P_{\Theta}) = \bigoplus_{p=0}^{\infty} \mathbb{H}_p^N, \quad (1.27)$$

and is called the *PC decomposition* of $L^2(\Omega^{(N)}, \mathcal{B}^{(N)}, P_{\Theta})$.

An orthogonal basis of the PC may explicitly be constructed by multivariate polynomials $\mathbb{H}_{\boldsymbol{\alpha}}^N(\mathbf{x})$ that are tensor-products of univariate polynomials $\mathbb{H}_{\alpha_j}^1(x_j)$. The entire family of polynomials can be written in a more compact fashion by means of *multi-indices*. These multi-indices $\boldsymbol{\alpha} = (\alpha_i)_{i \in \mathbb{N}}$ are sequences of non-negative integers with only finitely many non-zero elements. We can write:

$$\mathbb{H}_{\boldsymbol{\alpha}}^N(\mathbf{x}) = \left\{ \prod_{j=1}^N \mathbb{H}_{\alpha_j}^1(x_j); \boldsymbol{\alpha} \in \mathbb{N}^N; |\boldsymbol{\alpha}| = p \right\} \quad (1.28)$$

The theorem of Cameron & Martin [60] shows that, based on the previous PC decomposition, any $\mathcal{B}(\Theta)$ -measurable RV on Ω (not necessarily Gaussian!) with *finite variance* has a L^2 convergent approximation in the multivariate *Hermite* polynomial space of *Gaussian* random variables (cf. Fig. 1.3 – top left – for an example of two-dimensional Hermite polynomials).

The PC decomposition of a RV U is then represented in terms of *orthonormal Hermite* polynomials $\mathbb{H}_{\boldsymbol{\alpha}}^N \equiv H_{\boldsymbol{\alpha}}$ of independent standard *Gaussian* RVs $\mathbf{X} = \{X_j(\omega)\}_{j=1}^N$ (cf. Table 1.1):

$$U = \sum_{|\boldsymbol{\alpha}|=0}^{\infty} U_{\boldsymbol{\alpha}} H_{\boldsymbol{\alpha}}(\mathbf{X}), \quad (1.29)$$

where the *deterministic* coefficients $U_{\boldsymbol{\alpha}}$ are defined as:

$$U_{\boldsymbol{\alpha}} = \mathbb{E}[U H_{\boldsymbol{\alpha}}], \quad (1.30)$$

and the polynomials must satisfy a zero mean and orthogonality conditions:

$$\mathbb{E}[H_i] = 0 \quad \text{and} \quad \mathbb{E}[H_i H_j] = \delta_{ij}. \quad (1.31)$$

In practice, due to the tensor form construction of the multi-dimensional basis, an expansion in N dimensions with highest order P has a total number of terms $(M + 1)$ such that:

$$\dim(\mathbb{H}_{\leq P}^N) = M + 1 = \binom{P + N}{N}. \quad (1.32)$$

It is sometimes more convenient to map the multi-index $\boldsymbol{\alpha}$ to a single index $0 \leq k \leq M$ and the expansion becomes:

$$U(\omega) \approx U_P(\mathbf{X}(\omega)) = \sum_{k=0}^M U_k H_k(\mathbf{X}(\omega)). \quad (1.33)$$

For a fixed number N of RV, it shows the very fast increase, even exponential, in the total number of expansion terms with increasing P . This effect is known as the *curse of dimensionality*.

2.2.4 Generalized Polynomial Chaos expansion

The Cameron-Martin theory was generalized to other random processes, such as Poisson processes [357] and general independent-increment processes [435] but the generalization is not straightforward for non Wiener processes. The connections between stochastic processes and orthogonal polynomials are summarized in [432]. Xiu & Karniadakis [523] generalized the concept to non-Gaussian discrete and continuous RV by employing the *Askey* scheme of hypergeometric orthogonal polynomials. The approximation essentially bears the same form as 1.33. If we consider a RA $\Theta = \{\Theta_j(\omega)\}_{j=1}^N$, $N \in \mathbb{N}$ of *known* joint probability density function $f_{\Theta}(\theta)$, the gPC representation of a random functional $V(\Theta)$ of $L^2(\Omega, \mathcal{F}, P)$ reads:

$$V(\Theta) = \sum_{|\alpha|=0}^{\infty} V_{\alpha} \Phi_{\alpha}(\Theta), \quad (1.34)$$

where $\Phi_{\alpha}(\Theta)$ denotes the gPC basis of degree $|\alpha| = p$ in terms of the random variable Θ . The family of polynomials is obtained as a tensor product of one-dimensional basis $\{\Phi_{\alpha_k}(\Theta_k)\}$, and is orthogonal with respect to a weight function that is *identical* or *very close* to the pdf $f_{\Theta}(\theta)$ of Θ (cf. Table 1.1), with orthogonality relation:

$$\mathbb{E}[\Phi_{\alpha} \Phi_{\beta}] = \mathbb{E}[\Phi_{\alpha}^2] \delta_{\alpha\beta}. \quad (1.35)$$

Moreover, the gPC expansion $V_P(\Theta(\omega)) = \sum_{k=0}^M V_k \Phi_k(\Theta(\omega))$ will converge to V in the L^2 sense:

$$\mathbb{E}[(V - V_P)^2] \rightarrow 0, \quad \text{as } M \rightarrow \infty. \quad (1.36)$$

Table 1.1 – Correspondence between a few continuous probability densities and one-dimensional orthogonal polynomials.

Distribution	$f_X(x)$	Polynomials	Support
Gaussian	$\frac{1}{\sqrt{2\pi}} \exp^{-x^2/2}$	Hermite $H_k(x)$	$(-\infty, \infty)$
Gamma	$\frac{x^{\alpha} \exp^{-x/\beta}}{\Gamma(\alpha+1) \beta^{\alpha+1}}$	generalized Laguerre $L_k^{(\alpha)}(x)$	$[0, \infty)$
Exponential	\exp^{-x}	Laguerre $L_k(x)$	$[0, \infty)$
Beta	$\frac{(1+x)^{\alpha-1} (1-x)^{\beta-1}}{2^{\alpha+\beta-1} B(\alpha, \beta)}$	Jacobi $P_k^{(\alpha, \beta)}(x)$	$[-1, 1]$
Uniform	$1/2$	Legendre $P_k(x)$	$[-1, 1]$

We mention in Table 1.1 a few classic probability density functions with their corresponding one-dimensional orthogonal polynomials². All of these polynomials satisfy three-terms recurrence relations [5]. For arbitrary probability measures, the construction of the orthogonal polynomials must be numerically enforced.

Fig. 1.3 represent examples of different two-dimensional ($N = 2$) orthogonal polynomials (i.e. Hermite, Legendre, generalized Laguerre and Jacobi polynomials), for the particular choice of a polynomial of cubic order in its first dimension and a quadratic order in its second dimension, i.e. $\alpha = (3, 2)$.

Even if the gPC method does not provide a perfectly rigorous probabilistic framework to extend Wiener's theory to general measures (indeed there is no general proof of exponential convergence for orthogonal polynomials with arbitrary measures), it has been successfully used to solve stochastic differential equations relying on finite-dimensional approximations and appears to exhibit spectral convergence in many cases [523]. For instance, some results hold for the approximation of a smooth functional via Legendre-chaos polynomial space. If one considers the approximation $V_p(\Theta)$ of a functional $V(\omega)$ over a N -dimensional hypercube $\Omega^{(N)} = (-1, 1)^N$ via Legendre-chaos of highest degree p , the following convergence can be proven [493]:

$$\|V - V_p\|_2 \leq Cp^{-m} \|V\|_{H^m(\Omega^{(N)})}, \quad \text{with } m \geq 0, \quad (1.37)$$

where $\|\cdot\|_2$ is the norm defined in Eq. 1.7, and:

$$\|V\|_{H^m(\Omega^{(N)})} = \left(\int_{\Omega^{(N)}} \sum_{|r| \leq m} (\partial_{\Theta}^r V(\Theta))^2 d\Theta \right)^{1/2}, \quad (1.38)$$

with Θ RA with uniform distribution. So we see that the regularity of the functional with respect to Θ plays an important role (via the parameter m) and that spectral p -type convergence is obtained for smooth functionals.

2. Chebychev or Gegenbauer polynomials are particular case of Jacobi polynomials.

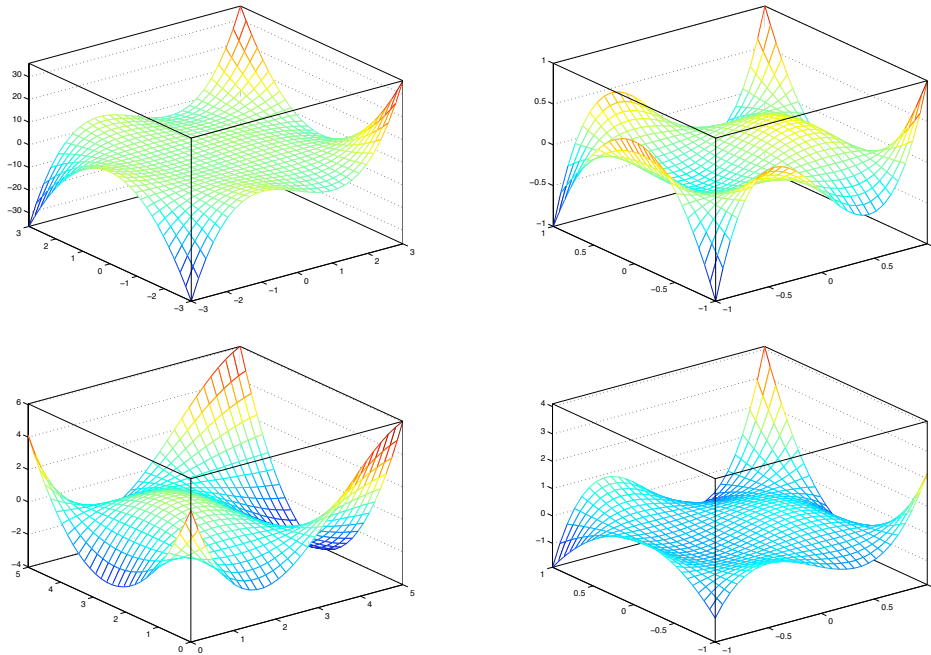


Figure 1.3 – Two-dimensional ($N = 2$) polynomials with $\alpha = (3, 2)$ for different types of distributions; Hermite-Gaussian H_α (top left), Legendre-uniform P_α (top right), Laguerre-Gamma $L_\alpha^{(1/2)}$ (bottom left) and Jacobi-Beta $P_\alpha^{(1/2, 0)}$ (bottom right).

2.3 Choice of spaces

It is worth mentioning that the optimal basis choice remains an open question for the representations of complex and highly nonlinear processes. Indeed the type of distribution of the solution of the SPDE is not known most of the time. When the complete random input distribution is known (i.e. density, joint-density or full set of marginal densities), one can build the corresponding polynomial basis from the Askey family. We emphasize that this choice is not indisputable as the optimality is only guaranteed for the stochastic inputs. For non-linear problems, it is not clear that an optimal representation of the inputs is necessarily optimal for the entire problem as spectral decomposition of the solution in terms of global basis sometimes exhibits severe limitations.

In the following, we briefly review several choices of multivariate spaces. We emphasize that the space choice is critical when the stochastic solution does not depend smoothly and continuously on the random inputs or when the number of input random variables is large, since the number of stochastic degrees of freedom might grow very fast (e.g. long-time integration of stochastic systems characterized by a limit-cycle oscillation response).

2.3.1 Global polynomial spaces

In the following, we review the possible options for the multivariate polynomial basis that will be chosen as approximation spaces for our stochastic spectral methods. In this section, we consider only *global* polynomial spaces, which means that they span the entire image of their underlying distribution supports. Piecewise polynomial spaces will be introduced in the next section. While all those multivariate polynomials are constructed based on tensor-products of univariate polynomials (orthogonal with respect to the underlying distribution), depending whether *full* or *sparse* tensor-products are employed, will strongly impact the dimensionality of the basis.

Getting back to the space notation of Section 2.2.3, we consider the multivariate polynomial space $\mathbb{H}_{\mathbf{\Lambda}(l)}^N(\Omega^{(N)})$ of increasing level of approximation (represented by the index set $\mathbf{\Lambda}(l)$ ³), up to level of approximation $l \in \mathbb{N}$. Different approximations are possible:

- (a) full tensor-product polynomial space of maximum degree l :

$$\mathbf{\Lambda}(l) = \{\alpha \in \mathbb{N}^N : \max_{k=1, \dots, N} \alpha_k \leq l\}$$

3. The sequence of increasing index sets $\mathbf{\Lambda}(l)$ is such that $\mathbf{\Lambda}(0) = \{(0, \dots, 0)\}$ and $\mathbf{\Lambda}(l) \subseteq \mathbf{\Lambda}(l+1)$, for $l \geq 0$.

(b) "full" tensor-product polynomial space of total degree l :

$$\Lambda(l) = \{\boldsymbol{\alpha} \in \mathbb{N}^N : \sum_{k=1}^N \alpha_k \leq l\}$$

(c) Hyperbolic cross space:

$$\Lambda(l) = \{\boldsymbol{\alpha} \in \mathbb{N}^N : \prod_{k=1}^N (\alpha_k + 1) \leq l + 1\}$$

(d) Smolyak polynomial space:

$$\Lambda(l) = \{\boldsymbol{\alpha} \in \mathbb{N}^N : \sum_{k=1}^N h(\alpha_k) \leq h(l)\}, \text{ with } h(\alpha) = \begin{cases} 0, & \alpha = 0 \\ 1, & \alpha = 1 \\ \lceil \log_2(\alpha) \rceil, & \alpha \geq 2. \end{cases}$$

Choice (b) is the most common choice in the literature so far, as it offers a reduced curse of dimensionality compared to option (a). Hyperbolic cross spaces (c) have been used to solve elliptic PDEs in high dimensions [439]. Smolyak spaces are not very common but inherit similar properties as Smolyak-based sparse cubature grids (cf. Section 2.2.2). There exists some similarities between (c) and (d) [20]. Other sparse polynomial spaces have been introduced in [473].

It is also possible to introduce anisotropic versions of these global spaces [20], by weighting appropriately the indices in order to account for different solution regularities along the stochastic dimensions.

2.3.2 Piecewise polynomial spaces

Although global gPC approximation can achieve exponential convergence for smooth problems [523], it may converge slowly or fail to converge in case of discontinuities (such as strong shocks) or steep fronts in random space [384]. In order to mitigate these problems, several numerical methods introduced in [97, 248, 494] consider piecewise local approximations on a partition of $\Omega^{(N)}$, that is eventually *adaptively* refined. In [97], Deb *et al.* extend classic finite-element-type method to the parametric space and obtained the same h -convergence rate as in the deterministic finite element methods. In [248], a multi-wavelet representation is proposed in the case of an hypercube domain $[0, 1]^N$ with uniform distributions. A binary partition is introduced in the one-dimensional case and the polynomial spaces are then tensorized to get a multivariate *multi-scale* approximation. In the following, we closely follow in more details the mathematical framework proposed by Wan and Karniadakis [494] to overcome these limitations. We outline a *piecewise* polynomial approximation, sometimes referred as multi-elements generalized Polynomial Chaos (ME-gPC) method, that consists in introducing a partition of the random space and constructing local orthogonal polynomials.

Here the stochastic solution is expressed in a *partitioned* random space. To this end, we construct a piecewise polynomial basis $\Phi_{\boldsymbol{\alpha}}$, orthogonal in each element with respect to the local probability distribution. We consider a partition \mathbf{D} of $\Omega^{(N)}$ with N_e non-overlapping elements B_l :

$$\mathbf{D} = \begin{cases} B_l = (a_1^l, b_1^l) \times (a_2^l, b_2^l) \times \cdots \times (a_N^l, b_N^l), \\ \bar{B} = \bigcup_{l=1}^{N_e} \bar{B}_l, \\ B_{l_1} \cap B_{l_2} = \emptyset, \text{ if } l_1 \neq l_2, \end{cases} \quad (1.39)$$

where $l, l_1, l_2 = 1, 2, \dots, N_e$, and a_i and b_i are finite (or infinite) in \mathbb{R} . Fig. 1.4 shows some examples of partitions of bounded stochastic domains in two and three dimensions.

Next, we must define *indicator* random variables I_{B_l} , such that in each element:

$$I_{B_l}(\boldsymbol{\Theta}) = \begin{cases} 1 & \text{if } \boldsymbol{\Theta} \in B_l, \\ 0 & \text{otherwise,} \end{cases}$$

and such that $\bar{\Omega}^{(N)} = \bigcup_{l=1}^{N_e} \overline{I_{B_l}^{-1}(1)}$ is a decomposition of the sample space $\Omega^{(N)}$ into the N_e elements. Based on Bayes' rule, we then define a new \mathbb{R}^N -valued *local* random vector $\boldsymbol{\Theta}^l = (\Theta_1^l, \dots, \Theta_i^l, \dots, \Theta_N^l): I_{B_l}^{-1}(1) \rightarrow B_l$ on the space $(I_{B_l}^{-1}(1), \mathcal{F}^{(N)} \cap I_{B_l}^{-1}, P(\cdot | I_{B_l} = 1))$ subject to a conditional *pdf*:

$$\hat{f}_{\boldsymbol{\Theta}^l}(\boldsymbol{\theta}^l | I_{B_l}(\boldsymbol{\Theta}) = 1) = \frac{f_{\boldsymbol{\Theta}}(\boldsymbol{\theta}^l)}{\Pr(I_{B_l}(\boldsymbol{\Theta}) = 1)},$$

where $\Pr(I_{B_l}(\Theta) = 1) = \int_{B_l} f_{\Theta}(\theta) d\theta > 0$. The piecewise polynomial spectral approximation $U_p(\Theta)$ of the solution $U(\Theta)$ now reads:

$$\begin{aligned} U(\Theta) \approx U_p(\Theta) &= \sum_{l=1}^{N_e} \Pr(I_{B_l}(\Theta) = 1) U_l(\Theta^l(\Theta)) \\ &= \sum_{l=1}^{N_e} \Pr(I_{B_l}(\Theta) = 1) \sum_{|\alpha| < P} U_{l,\alpha} \Phi_{l,\alpha}(\Theta^l(\Theta)), \end{aligned} \quad (1.40)$$

with polynomial basis $\Phi_{l,\alpha}$ orthogonal in each element B_l with respect to the local probability measure \hat{f}_{Θ^l} . For most input distributions, the orthogonal polynomials have to be numerically constructed based on recurrence relations [498]. However, due to the nice properties of *uniform* distribution (constant *pdf*), the orthogonality of Legendre-chaos can be naturally inherited in the decomposition of random space, which means that the polynomial construction is unnecessary for the *uniform* distribution.

The representation of Eq. 1.40 converges to $U(\Theta)$ in the L_2 sense [494] but remains only practicable in the context of adaptivity that will be presented further.

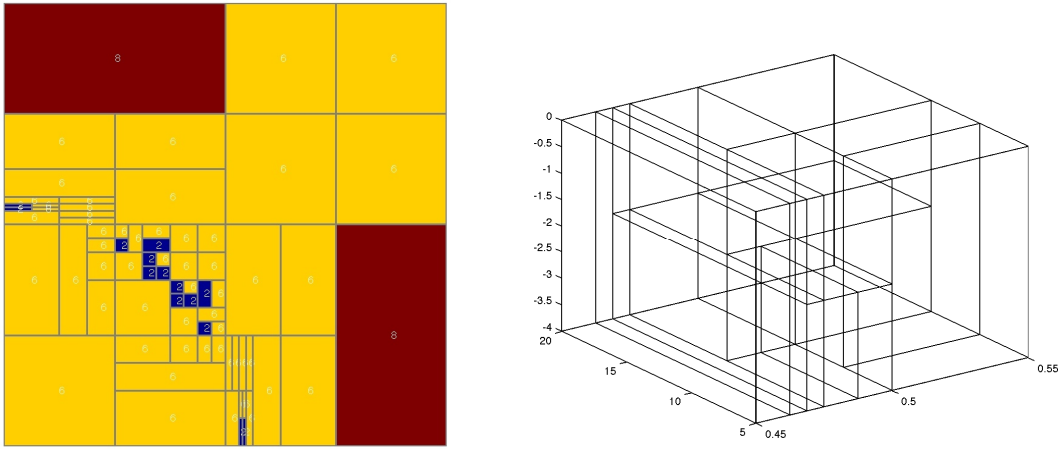


Figure 1.4 – Examples of two-dimensional (left) and three-dimensional (right) stochastic partitions.

We take the opportunity to briefly recall some approximation error results.

Some hp convergence results

Some hp -convergence results (where h denotes the side length of a typical random element and p the polynomial order) have been established for Legendre-chaos expansion with *uniform* distributions.

If one considers the *piecewise* Legendre-chaos approximation (of highest degree p): $V_p(\Theta)$ of a functional $V(\omega)$ over a N -dimensional hypercube $\Omega^{(N)} = [-1, 1]^N$ decomposed in a *regular* partition \mathbf{D} of N_e^N elements, the following convergence can be proven [493]:

$$\|V - V_p\|_2 \leq Cp^{-m} N_e^{-m} |V|_{H^m(\Omega^{(N)})}, \quad \text{with } m \geq 0, \quad (1.41)$$

where $\|\cdot\|_2$ is the norm defined in Eq. 1.7, and the semi-norm:

$$|V|_{H^m(\Omega^{(N)})} = \left(\sum_{|r| \leq m} \int_{\Omega^{(N)}} |\partial_{\Theta}^r V(\Theta)|^2 d\Theta \right)^{1/2}, \quad (1.42)$$

with Θ RA with uniform distribution. C is a constant.

If we take $m = p + 1$ and consider the error of the second-order moment we recover a h -convergence rate [97, 494]:

$$|\mathbb{E}[V^2] - \mathbb{E}[V_p^2]| \leq C(p) N_e^{-2(p+1)}, \quad N_e \sim 1/h. \quad (1.43)$$

It is interesting to notice the similarity of the convergence rate in Eq. 1.41 with the one for a *deterministic* hp polynomial approximation:

$$\|V - V_p\|_2 \leq Cp^{-m} h^{\mu} \|V\|_{H^m}, \quad \text{with } \mu = \min(p + 1, m), \quad (1.44)$$

and h is the maximum size of the mesh elements in the physical space.⁴

4. Say something about the choice btw h & p to make the solution converge.

2.3.3 Lagrange interpolant spaces

Stochastic *interpolant* spaces are involved in the (probabilistic) collocation method, cf. Section 3.2.3 and [154, 26, 155, 54, 533, 345]. While it benefits from the well-established theory of one-dimensional Lagrange interpolation, multivariate polynomial interpolation is more complicated as one has to identify the set of points and polynomial subspaces for which the interpolation problem can be solved. So in practice, although the approach seems very similar to Monte-Carlo technique, the “sample points” are often chosen deterministically in order to get good approximation properties.

Interpolation is closely tied to numerical integration, cf. Appendix B. For each random dimension $k = 1, \dots, N$ let Θ_{k,j_k} with $1 \leq j_k \leq n_k + 1$ be the $n_k + 1$ collocation points chosen along that direction. To any vector of indexes $[j_1, \dots, j_N]$ we may associate the global index $j = j_1 + n_1(j_2 - 1) + n_1 n_2(j_3 - 1) + \dots$. We then denote by Θ_j the point $[\Theta_{1,j_1}, \dots, \Theta_{N,j_N}] \in \Omega^{(N)}$. Based on those points, we can now define an interpolating space $\mathcal{P}_n(\Omega^{(N)})$ which is the span of tensor product polynomials with degree at most $n = (n_1, \dots, n_N)$ i.e. $\mathcal{P}_n(\Omega^{(N)}) = \bigotimes_{k=1}^N \mathcal{P}_{n_k}(\Omega_k)$ [15].

We also introduce, for each dimension $k = 1, \dots, N$, the Lagrange basis: $\{l_{k,i}\}_{i=1}^{n_k+1}$ of the space \mathcal{P}_{n_k} :

$$l_{k,i} \in \mathcal{P}_{n_k}(\Omega_k); \quad l_{k,i}(\Theta_{k,m}) = \delta_{i,m}, \quad i, m = 1, \dots, n_k + 1. \quad (1.45)$$

The generic form of the N_q -point Lagrange interpolation of a functional u is then:

$$u_I(\Theta) = \sum_{k=1}^{N_q} u^{(k)} \mathcal{L}_k(\Theta), \quad (1.46)$$

where $\mathcal{L}_k(\Theta) = \prod_{k=1}^N l_{k,j_k}(\Theta_k)$ and $u^{(k)} \equiv u(\Theta^{(k)})$.

Multidimensional – full, sparse or dimension-adaptive – interpolant spaces (respectively formula) are constructed, similarly to numerical grids (respectively quadratures), from standard one-dimensional interpolants that may be tensorized in different fashions (e.g. via Smolyak algorithm [446]).

Very similarly to Eq. (B.24) in Appendix B, the sparse interpolation of level ν is made of linear combinations of tensor-products which use a small number of evaluations:

$$\mathcal{M}_\nu^N[u] = \sum_{\mathbf{k} \in \mathcal{K}(\nu, N)} (-1)^{\nu + N - |\mathbf{k}|_1 - 1} \binom{N-1}{|\mathbf{k}|_1 - \nu} \cdot (\mathcal{M}_{k_1}^1 \otimes \dots \otimes \mathcal{M}_{k_N}^1) u,$$

where $\mathcal{K}(\nu, N) = \{\mathbf{k} \in \mathbb{N}_+^N, \mathbf{k} > 0 : \nu - N \leq g(\mathbf{k}) \leq \nu - 1\}$ and the strictly increasing function g characterizes the set of multi-indices used to construct the sparse interpolation, e.g. $g : \mathbb{N}_+^N \rightarrow \mathbb{N}_+ \mid g(\mathbf{k}) = \sum_{n=1}^N (k_n - 1)$. It is proved that this scheme is interpolant if the underlying one-dimensional approximations are *interpolant* and corresponding grids have *nested* points [26]. Fig. 1.5 shows some examples of two-dimensional Lagrange interpolant polynomials constructed for isotropic sparse interpolation of random functionals in $\Omega^{(N)} = [0, 1]^2$ and based on sparse Clenshaw-Curtis 13-points grid (top row) and Kronrod-Patterson 17-points grid (bottom row). We refer the reader to the Section 2.1 of Appendix B for the details about the grids.

In higher dimensions, it is possible to reduce the overall computational cost by constructing interpolation spaces based on *adaptive anisotropic* sparse grid scheme [155, 346, 229].

3 Resolution schemes

In this section, we introduce the different numerical methods deployed to compute the deterministic polynomial chaos coefficients. These methods may be categorized in two large classes of “intrusive” or “non-intrusive” techniques. The former consists of Galerkin methods which are based on a weighted residual formulation to establish system of equations for the spectral unknown coefficients. The latter consists of direct methods which do not require any modification of the deterministic model used a number of times as a black-box solver. Both classes are subject to the curse of dimensionality. Which of the considered techniques is the most efficient is a very problem-dependent question that depends on the random dimensions, on the spatial discretization and deterministic solvers at hand and on properties of the solution, i.e. its regularity in the stochastic space.

3.1 Galerkin methods

The Galerkin formulation is often used for solving deterministic spectral problems [49] in fluid flows [62, 219]. Stochastic Galerkin approaches rely on a similar mathematical framework [97, 16, 135]. They have been used and developed together with the Polynomial Chaos approximation [162, 523, 99]. They define an approximation of the stochastic solution, via an approximation basis combined with the weak formulation of the stochastic problem. These techniques have been applied to numerous fluid engineering problems [529, 247, 286, 249, 525].

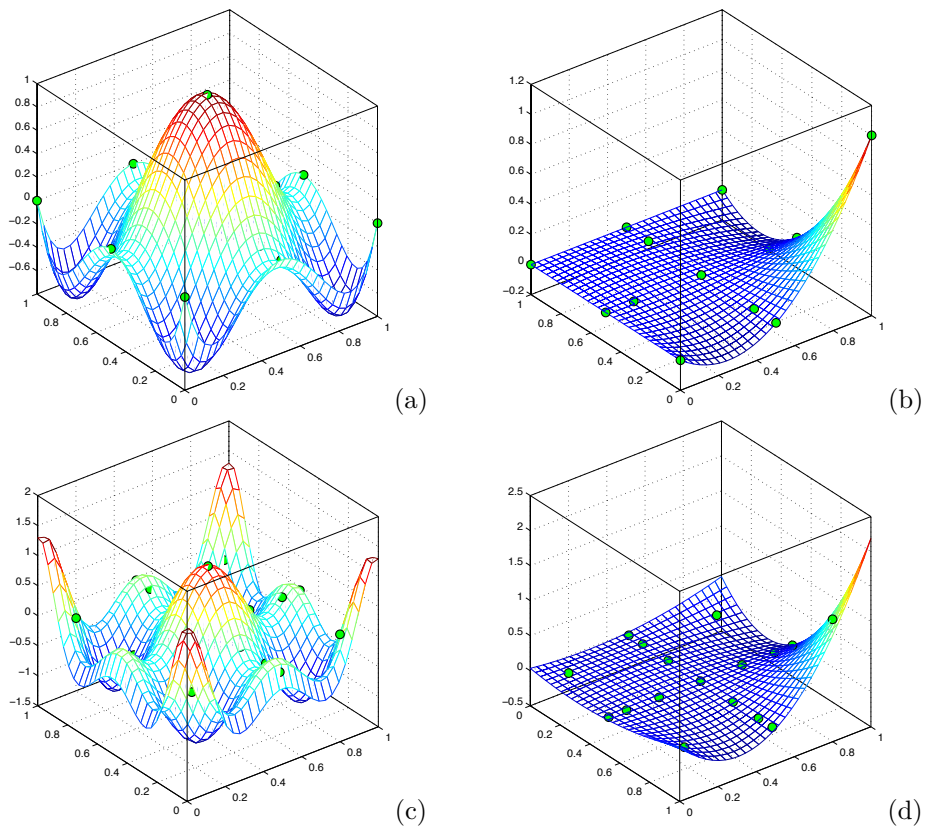


Figure 1.5 – Examples of two-dimensional ($N = 2$) interpolating Lagrange polynomials on $\Omega^{(N)} = [0, 1]^2$ based on sparse Clenshaw-Curtis 13-points grid (top row) and Kronrod-Patterson 17-points grid (bottom row). Grid point locations are represented by spherical green markers. (a): $\alpha = (3, 3)$ (b): $\alpha = (5, 1)$ (c): $\alpha = (3, 3)$ (d): $\alpha = (7, 1)$.

3.1.1 Stochastic problem and weak forms:

We consider a well-posed deterministic model that relates the solution $\mathbf{u}(\mathbf{x}, t)$ to a certain set of parameters (or data) $\mathbf{q}(\mathbf{x}, t)$ and some sources $\mathcal{B}(\mathbf{x}, t)$:

$$\mathcal{A}(\mathbf{u}(\mathbf{x}, t); \mathbf{q}(\mathbf{x}, t), \mathbf{x}, t) = \mathcal{B}(\mathbf{x}, t), \quad (1.47)$$

where \mathcal{A} may be a linear (or non-linear) differential operator and also includes initial and boundary conditions, constraints,...

Let us assume now that the set of parameters and/or the sources bear some level of uncertainty that will affect the solution of the model, but keeps the problem well posed. We indicate the dependence of the parameters (respectively the sources) to the random event $\omega \in \Omega$ by $\mathbf{q}(\mathbf{x}, t, \omega)$ (respectively $\mathcal{B}(\mathbf{x}, t, \omega)$) and assume that the set of random parameters is well represented by a stochastic process on the probability space (Ω, \mathcal{F}, P) . The problem becomes *stochastic* and its *strong* form is written as:

$$\mathcal{A}(\mathbf{u}(\mathbf{x}, t, \omega); \mathbf{q}(\mathbf{x}, t, \omega), \mathbf{x}, t, \omega) = \mathcal{B}(\mathbf{x}, t, \omega). \quad (1.48)$$

In the following, we will drop the spatial and temporal dependency (\mathbf{x}, t) in the notation for conveniency.

Weak form at the deterministic level

The weak form of the *deterministic* aspect of the problem, consists in finding a random solution \mathbf{u} in a suitable functional Hilbert space \mathcal{V} such:

$$a(\mathbf{u}(\omega), \mathbf{v}; \omega) = b(\mathbf{v}; \omega), \quad \forall \mathbf{v} \in \mathcal{V}, \quad (1.49)$$

where $a(\cdot, \cdot; \omega)$ and $b(\cdot; \omega)$ are the continuous bilinear forms on $\mathcal{V} \times \mathcal{V}$ and \mathcal{V} , respectively. It will be assumed in the following that \mathcal{V} is independent of the random event, so that we call it the deterministic space.

Weak form at the stochastic level

Let us consider that the random quantities involved in Eq. (1.48) are second-order ones and let us consider the Hilbert space of scalar-valued functions. We call $\mathcal{S} = L^2(\Omega, \mathcal{F}, P)$, the stochastic space of approximation, and we now seek the solution \mathbf{u} of Eq. (1.49) in the $\mathcal{V} \otimes \mathcal{S}$ space.

The weak formulation is now to find $\mathbf{u} \in \mathcal{V} \otimes \mathcal{S}$ such:

$$A(\mathbf{u}, \mathbf{v}) = B(\mathbf{v}), \quad \forall \mathbf{v} \in \mathcal{V} \otimes \mathcal{S}, \quad (1.50)$$

where

$$\begin{aligned} A(\mathbf{u}, \mathbf{v}) &= \mathbb{E}[a(\mathbf{u}(\omega), \mathbf{v}; \omega)], \\ B(\mathbf{v}) &= \mathbb{E}[b(\mathbf{v}; \omega)]. \end{aligned} \quad (1.51)$$

Eq. (1.50) and (1.51) show that the interpretation of the stochastic problem is in the *mean sense*.

Remarks:

1. The assumption of independence between the deterministic and the stochastic space (with the use of the tensor product) has very important consequences. It requires to use the same deterministic space for all realizations of the data and implies that the deterministic discretization level is fine enough to capture all possible realization scales. This limitation may cause severe difficulties if the uncertainty is such that it may cause changes in the nature of the model equations. This is obviously the case when the physical geometry of the problem is random, or when the uncertainty induces random modifications to the physical geometry through the fluid interaction, e.g. fluid-structure interaction problems.
2. The problem as well as the corresponding operators considered in Eq. (1.48), were described as continuous. However, one may want/need to start from a discrete deterministic problem. In this case, classical Galerkin formulations (for finite elements methods, spectral methods,...) are often encountered. They are constructed with a discrete space of approximation $\mathcal{V}^\delta \subset \mathcal{V}$ of finite dimension n . If we denote the approximation space by $\mathcal{V}^\delta = \text{span}\{\phi_1, \dots, \phi_n\}$ where $\phi = \{\phi_k\}_{k=1}^{k=n}$ form a basis, then the Galerkin approximation of the random function $\mathbf{u}^\delta(\omega) \in \mathcal{V}^\delta$ must almost surely satisfy:

$$a(\mathbf{u}^\delta(\omega), \mathbf{v}^\delta; \omega) = b(\mathbf{v}^\delta; \omega), \quad \forall \mathbf{v}^\delta \in \mathcal{V}^\delta. \quad (1.52)$$

The discretized version is written:

$$A(\mathbf{U}; \omega)_k = a(\mathbf{u}^\delta, \phi_k; \omega) \text{ and } B(\omega)_k = b(\phi_k; \omega), \text{ for } k = 1 \dots n. \quad (1.53)$$

where we approximate the discrete solution $\mathbf{u}^\delta = \mathbf{U} \cdot \phi^T$ with $\mathbf{U} = (\mathbf{u}_k)_{k=1}^n$.

3.1.2 Stochastic Galerkin approximation:

In the following, we assume that the discretization at the deterministic level has already been performed. The next step is to propose a stochastic discretization of the weak form of Eq. (1.50). Again, we parametrize the randomness with a finite set of scalar-valued functions built with a RA $\Theta = \{\Theta_j(\omega)\}_{j=1}^N$, $N \in \mathbb{N}$, and introduced at the end of Section 1.3. We assume moreover that the RV are independent and with known distribution 1.22. The stochastic solution is then sought in an approximate space $\mathcal{S}_M \subset L^2(\Omega^{(N)}, \mathcal{B}^{(N)}, P_\Theta)$ 1.4 of finite dimension. We call $\{\Phi_k\}_{k=0}^\infty$ a Hilbertian basis of \mathcal{S} , and restrain to truncated basis $\{\Phi_k\}_{k=0}^M$ for the representation of \mathcal{S}_M . This basis can be a global PC or gPC basis 2.2 but other choices of approximation spaces are possible, cf. Section 2.3, as long as it forms a complete *orthonormal* family of functions such that the representation of a function $V \in \mathcal{S}_M$ is unique:

$$V = \sum_{k=0}^M V_k \Phi_k, \quad \text{with} \quad V_k = \mathbb{E}[V \Phi_k]. \quad (1.54)$$

The parametrization is carried on for the random inputs (i.e. the parameters $\mathbf{q}(\omega) \equiv \mathbf{q}(\Theta(\omega))$) and the sources $\mathcal{B}(\omega) \equiv \mathcal{B}(\Theta(\omega))$) as well as for the solution itself, cf. 1.34. The difference between the two groups of variables resides in the fact that the modal coefficients of the solution approximation are *unknown*.

Projection and stochastic residual

Now, we enter the core part of the Galerkin method where the stochastic expansions for the solution and the inputs are first injected into the weak form of the stochastic problem. Next, the resulting stochastic equation is projected onto the expansion basis to yield a set of generally coupled deterministic problems for the stochastic modes of the solution.

The weak formulation derived from the semi-discretized version of Eq. (1.50) is now to find $\mathbf{u}_M^\delta \in \mathcal{V}^\delta \otimes \mathcal{S}_M$, that is find the $\{\mathbf{u}_k\}_{k=0}^M \in \mathcal{V}^\delta$, such that:

$$A \left(\sum_{k=0}^M \mathbf{u}_k \Phi_k(\Theta), \mathbf{v}^\delta \right) = B(\mathbf{v}^\delta), \quad \forall \mathbf{v}^\delta \in \mathcal{V}^\delta \otimes \mathcal{S}, \quad (1.55)$$

which using the definitions of A and B is equivalent to:

$$\mathbb{E} \left[\mathbf{v}^\delta \text{Res} \left(\sum_{k=0}^M \mathbf{u}_k \Phi_k(\Theta); \Theta \right) \right] = 0, \quad \forall \mathbf{v}^\delta \in \mathcal{V}^\delta \otimes \mathcal{S}, \quad (1.56)$$

$$\text{with} \quad \text{Res}(\mathbf{u}(\Theta); \Theta) = b(\Theta) - A(\mathbf{u}(\Theta); \Theta).$$

In the final step, the Galerkin method leads to a choice of the test functions \mathbf{v}^δ from the same space \mathcal{S}_M as the trial functions $\{\Phi_k\}_{k=0}^M$. We obtain the following system of $(n \times M)$ linear or non-linear equations for the stochastic modes $\{\mathbf{u}_k\}_{k=0}^M \in \mathcal{V}^\delta$ of the solution:

$$\mathbb{E} \left[\Phi_k(\Theta) A \left(\sum_{i=0}^M \mathbf{u}_i \Phi_i(\Theta); \Theta \right) \right] = \mathbb{E}[B(\Theta) \Phi_k(\Theta)], \quad \forall k \in \{0, \dots, M\}. \quad (1.57)$$

3.1.3 Convergence rates

A *a priori* error analysis of the stochastic Galerkin method may be obtained if the regularity of the solution is known (i.e. expressing the regularity by specifying a suitable subspace in which the solution is contained). Additionally, the error in the gPC approximations for functions from this space must be specified as well [223]. A large body of work has been devoted to the case of *elliptic* problems with random coefficients [160], see for instance [97, 300, 17, 135, 473]. Deb *et al.* [97], Babuška *et al.* [17] and Frauenfelder *et al.* [135] use finite elements to approximate the noise dependence of the solution.

Babuška *et al.* consider the *hp*-version of the FEM formulation and moreover assume the solution to be smooth in the stochastic parameters. They prove that the method provides an *exponential* rate of convergence with respect to the degree of the polynomials used for the approximation, for a fixed number of random dimensions. They also derived error estimation of the expected value of the solution. In [135], Frauenfelder *et al.* treat the case of stochastic elliptic problems with random diffusion coefficients whose spatial correlations are known explicitly and represented as a Karhunen-Loève series. Analyticity of the solution in the stochastic variables with sharp bounds for the domain of analyticity are used to prescribe a PC expansion with *variable* stochastic polynomial degree for the approximate solution. Numerical examples show that the number of stochastic dimensions depends on the spatial correlation length of the random diffusion coefficient. Sparse polynomial

chaos bases were investigated in [473] based on explicit constructions of finite element spaces in the parametric variables, which were not of tensor-product type, and for which optimal convergence rates of the corresponding Galerkin or Collocation approximations were shown.

The work of Benth & Gjerde on convergence rates for finite element approximations of SPDEs in *general* probability spaces (i.e. not finite-dimensional probability spaces) should also be mentioned [30].

3.1.4 Numerical resolution

We briefly review the numerical methods/solvers employed for the resolution of the large system of equations resulting from the application of PC Galerkin discretization to linear or nonlinear SPDEs.

Linear case

Good reviews of numerical methods for linear SPDEs are given in [223, 250]. The tensor product structure of the Galerkin formulation leads to a large system of block equations. A good strategy is to try to take advantage of the sparsity block structure in order to store and solve efficiently these very large systems. In fact, even for linear problems, the resolution by direct inversion is generally too costly and the assembly of the matrix is often impossible, so it is more advantageous to solve the linear block system by iterative solvers.

Krylov-type iterative solvers, such as preconditioned gradient techniques [161, 368, 300] may be preferred. However these schemes still require a great computational cost as well as important memory requirements and require efficient block preconditioners (such as block-Jacobi preconditioners, block diagonal preconditioner based on the operator expectation [161, 368] or block diagonal preconditioners adapted to the underlying deterministic model [116]). A complementary approach is to resort to parallel computing, see [223, 222].

Multigrid (or multilevel) solvers are also used for the large systems resulting from the Galerkin discretization of parabolic and elliptic SPDEs [303, 292].

Other alternative approaches exist for linear models: – the subspace methods proposed by Nair & Keane [339], in which the solution is sought in a subspace of random vectors (which is different from the Krylov space previously mentioned and spanned by deterministic vectors); – the generalized spectral decomposition method proposed by Nouy [349] where the solution is sought in the dominant subspace of the stochastic operator. We refer the reader to Section 5.1 for model reduction techniques.

Nonlinear case

Most of realistic mechanical engineering systems are nonlinear by nature. We emphasize that the accurate treatment of nonlinearities in stochastic Galerkin methods is key to the success of the approach. Unfortunately, there are no standard techniques to project nonlinear *nonpolynomial* functions onto the expansion basis and one must have recourse to Taylor series, integration, nonlinear projection involving minimization or other numerical “tricks” to approximate those functions, see for instance [99].

Iterative Newton or quasi-Newton methods may then be used to solve the resulting nonlinear system of equations [223]. The latter seems more attractive if one wants to avoid the costly linearization and subsequent resolution of new linear system at each iteration. In any case, the residual has to be evaluated at least once in each iteration, which means that complex integral must be repeatedly computed [301]. In general this can not be done analytically (as before in the case of linear equations), and one has to resort to numerical quadrature rules instead.

A Newton method has been proposed in [290] for the resolution of the stochastic incompressible *steady* Navier-Stokes equations. It is a direct extension of techniques developed for deterministic problems. It uses the unsteady equations to derive a linear equation for the stochastic Newton increments. The method leads to matrix-free strategies, where Newton increments are successively computed by solving a series of spectral problems consisting in pseudo-time integration of the linearized unsteady stochastic flow equations. The method is applied to the case of a flow ($\overline{Re} = 60$) around a circular cylinder with random viscosity with a lognormal distribution.

3.1.5 Application to incompressible Navier-Stokes equations

In this section we sketch the main steps of the derivation of the Galerkin formulation for stochastic two-dimensional incompressible Navier-Stokes equations driven by *colored* noise. The stochastic scheme is coupled to a spectral/*hp* element solver used for direct numerical simulation of turbulent flow. We refer to the valuable theoretical work of Mikulevicius *et al.* for the Wiener chaos treatment of two-dimensional stochastic Navier-Stokes system driven by *white noise* [327].

Deterministic problem

The governing equations are the incompressible Navier-Stokes equations, written here with a primitive-variable formulation and in convective form in a rectangular domain $\mathcal{D} \subset \mathbb{R}^2$ with boundary $\partial\mathcal{D} = \Gamma_d \cup \Gamma_n$. We

refer to the diffusive time L^2/ν and normalize the pressure with respect to the viscous stress $\mu U/L$, in order to get the dimensionless form:

$$\frac{\partial \mathbf{u}}{\partial t} + (\mathbf{u} \cdot \nabla \mathbf{u}) = -\nabla p + Re^{-1} \nabla^2 \mathbf{u} + \mathbf{f} \quad \text{in } \mathcal{D}, \quad \text{and} \quad (1.58)$$

$$\nabla \cdot \mathbf{u} = 0 \quad \text{in } \mathcal{D}, \quad \text{for } t \geq 0, \quad (1.59)$$

where the Reynolds number is $Re = UL/\nu$ and \mathbf{f} is an external body force and $\mathbf{f} \in L^2(\mathcal{D})^2$. We consider homogeneous Dirichlet and Neumann boundary conditions over the respective portions of the domain boundary. They are:

$$\mathbf{u} = 0 \text{ (wall) or } 1 \text{ (inflow) on } \Gamma_d \quad \text{and} \quad \frac{\partial \mathbf{u}}{\partial n} = 0 \text{ on } \Gamma_n, \quad \text{for } t \geq 0. \quad (1.60)$$

The DNS spectral/ hp element deterministic solver is presented in more details (variational formulation, time integration, spatial discretization and approximation space) in Appendix A.

Stochastic problem

We consider that there is now some uncertainty in the system, for instance in the upstream inflow boundary condition which is function of a random event ω from the sample space Ω of a probability space (Ω, \mathcal{F}, P) . We now deal with a system of stochastic Navier-Stokes equations whose solution satisfies almost surely the following stochastic problem:

$$\begin{aligned} \mathbf{u}_t(\mathbf{x}, t, \omega) + (\mathbf{u}(\mathbf{x}, t, \omega) \cdot \nabla \mathbf{u}(\mathbf{x}, t, \omega)) &= -\nabla p(\mathbf{x}, t, \omega) + Re^{-1} \nabla^2 \mathbf{u}(\mathbf{x}, t, \omega) \quad \text{in } \mathcal{D}, \quad \text{and} \\ \nabla \cdot \mathbf{u}(\mathbf{x}, t, \omega) &= 0 \quad \text{in } \mathcal{D}, \\ \mathbf{u}(\mathbf{x}, t, \omega) &= \mathbf{g}(\mathbf{x}, t, \omega), \quad \mathbf{x} \in \Gamma_d \\ \mathbf{u}_n(\mathbf{x}, t, \omega) &= 0, \quad \mathbf{x} \in \Gamma_n, \quad \text{for } t \geq 0, \end{aligned} \quad (1.61)$$

where \mathbf{g} is a smooth function (random variable or stochastic process) of the random event. In order to simplify the problem, we will consider random fields for \mathbf{g} , i.e. $\mathbf{u}(\mathbf{x}, \omega) = \mathbf{g}(\mathbf{x}, \omega)$ at the inflow.

Stochastic discretization

We assume that the uncertainty is correctly approximated with a finite set of independent RVs forming a random array $\Theta = \{\Theta_j(\omega)\}_{j=1}^N, N \in \mathbb{N}$, cf. Section 1.3. We call $\{\Phi_\alpha\}_{\alpha \in \beta}$ a Hilbertian basis of $L^2(\Omega^{(N)}, \mathcal{B}^{(N)}, P_\Theta)$, i.e. a complete orthonormal family of functions such that:

$$\mathbb{E}[\Phi_\alpha, \Phi_\beta] = \delta_{\alpha\beta}, \quad (1.62)$$

and the representation of the source of uncertainty, velocity and pressure fields in $\mathcal{S} = L^2(\Omega^{(N)}, \mathcal{B}^{(N)}, P_\Theta)$ is unique. For practical computations, the gPC expansions are truncated to $(M+1)$ terms, i.e. with finite polynomial order and the approximation space is defined as: $\mathcal{S}_M \equiv \text{span}\{\Phi_0, \dots, \Phi_M\} \subset \mathcal{S}$.

The truncated gPC representations of all field variables, including velocity and pressure fields, are introduced:

$$\begin{aligned} \mathbf{u}(\mathbf{x}, \Theta) &= \sum_{k=0}^M \mathbf{g}_k(\mathbf{x}) \Phi_k(\Theta), \quad \mathbf{x} \in \Gamma_d \\ \mathbf{u}(\mathbf{x}, t, \Theta) &= \sum_{k=0}^M \mathbf{u}_k^\delta(\mathbf{x}, t) \Phi_k(\Theta), \\ p(\mathbf{x}, t, \Theta) &= \sum_{k=0}^M p_k^\delta(\mathbf{x}, t) \Phi_k(\Theta), \quad \mathbf{x} \in \mathcal{D}, \quad \text{for } t \geq 0, \end{aligned} \quad (1.63)$$

with the deterministic coefficients $(\mathbf{u}_k^\delta, p_k^\delta)$ being themselves expanded in each spectral element according to the approximation of Eq. (A.25), cf. Appendix A.

After injection of the expansions in the system weak form followed by a Galerkin projection and making use of orthogonality relations, the problem results in seeking a solution in $\mathcal{V}^\delta \otimes \mathcal{S}_M$ of the following system of *deterministic* governing equations:

$$\begin{aligned} \frac{\partial \mathbf{u}_k^\delta}{\partial t} + \sum_{i=0}^M \sum_{j=0}^M \varepsilon_{ijk} (\mathbf{u}_i^\delta \cdot \nabla \mathbf{u}_j^\delta) &= -\nabla p_k^\delta + Re^{-1} \nabla^2 \mathbf{u}_k^\delta \quad \text{in } \mathcal{D}, \\ \nabla \cdot \mathbf{u}_k^\delta &= 0 \quad \text{in } \mathcal{D}, \quad \text{for } t \geq 0, \\ \mathbf{u}_k^\delta &= \mathbf{g}_k(\mathbf{x}) \quad \text{on } \Gamma_d, \\ \mathbf{u}_{k_n}^\delta &= 0 \quad \text{on } \Gamma_n, \quad \text{for } k = 0, 1, \dots, M, \end{aligned} \quad (1.64)$$

with $\varepsilon_{ijk} = \mathbb{E}[\Phi_i \Phi_j \Phi_k]$ are known tabulated quantities once the polynomial basis is chosen.

It can be observed that the system bears a very similar form to the original Navier-Stokes equation. The difference resides in its size: $(M + 1)$ -times larger than the corresponding deterministic system and in the coupling of the stochastic modes in the nonlinear convective term. We also notice that the velocity divergence constraints are decoupled.

We recall the main steps of the time integration splitting scheme that has to be carried out for each random modes $k = 0, \dots, M$ (we drop the δ superscript for ease of notation):

$$\frac{\hat{\mathbf{u}}_k - \sum_{q=0}^{J_i-1} \alpha_q \mathbf{u}_k^{n-q}}{\Delta t} = - \sum_{q=0}^{J_e-1} \beta_q \left[\sum_{i=0}^M \sum_{j=0}^M \varepsilon_{ijk} (\mathbf{u}_i \cdot \nabla \mathbf{u}_j) \right]^{n-q} \quad (1.65)$$

$$\frac{\hat{\hat{\mathbf{u}}}_k - \hat{\mathbf{u}}_k}{\Delta t} = -\nabla p_k^{n+1} \quad (1.66)$$

$$\frac{\gamma_0 \mathbf{u}_k^{n+1} - \hat{\hat{\mathbf{u}}}_k}{\Delta t} = Re^{-1} \nabla^2 \mathbf{u}_k^{n+1}. \quad (1.67)$$

Then, assuming the intermediate field $\hat{\mathbf{u}}_k$ is *divergence-free* and taking the derivative of the second equation, the problem can be recast as an elliptic *Poisson* equation:

$$\nabla^2 p_k^{n+1} = \Delta t^{-1} \nabla \cdot \hat{\mathbf{u}}_k, \quad \text{for } k = 0, \dots, M, \quad (1.68)$$

with consistent Neumann boundary conditions derived from the normal component of the momentum equations:

$$\frac{\partial p_k^{n+1}}{\partial \mathbf{n}} = - \left[\frac{\hat{\mathbf{u}}_k^{n+1}}{\Delta t} + Re^{-1} \sum_{q=0}^{J_p-1} \beta_q (\nabla \times \boldsymbol{\omega}_k)^{n-q} \right] \cdot \mathbf{n}, \quad \text{for } k = 0, \dots, M, \quad (1.69)$$

where \mathbf{n} is the outward unit normal vector along the boundary, and $\boldsymbol{\omega}_k = \nabla \times \mathbf{u}_k$ is the vorticity.

Because the divergence constraints are decoupled, this approach results in a set of $(M + 1)$ decoupled pressure projection steps. Since these steps typically account for the bulk of the computational effort, the solution comes to a cost of about $(M + 1)$ deterministic solutions. The numerical method is easily parallelizable on $(M + 1)$ processors as only the nonlinear term in Eq. (1.65) exhibits a stochastic modes coupling which is treated explicitly with this approach [274].

Application to noisy inflow past an oscillating cylinder

The computational approach is applied to the case of an incompressible laminar flow past an oscillating cylinder. The uncertainty is in the upstream velocity boundary condition with a 30% coefficient of variation compared to the deterministic case. The average Reynolds number is $Re = 140$. The goal is in the quantification of the effect of the noise on the vortex formation behind the crossflow oscillating cylinder.

Fig. 1.6 shows the instantaneous spatial distribution of vorticity *rms* values in the wake of the two-dimensional cylinder forced to oscillate in some harmonic motion along the vertical direction. For particular values of cylinder motion amplitude and frequency, it was found that the inflow variability triggers shedding-mode switching in the vortices of the wake [279].

3.2 Direct methods

Let us assume that we seek the approximation of a quantity of interest $J(\omega) \equiv J(u(\boldsymbol{\Theta}); \boldsymbol{\Theta})$, where u is the stochastic solution, that depends on random data parametrized by a finite set of random variables $\boldsymbol{\Theta} \equiv \boldsymbol{\Theta}(\omega)$, under the generic form:

$$J(u(\boldsymbol{\Theta}); \boldsymbol{\Theta}) = \sum_{\alpha \in \mathcal{J}} J_\alpha \Phi_\alpha(\boldsymbol{\Theta}), \quad (1.70)$$

where $\boldsymbol{\Theta}$ is defined on the probability space (Ω, \mathcal{F}, P) with pdf $f_{\boldsymbol{\Theta}}(\boldsymbol{\theta})$. For simplicity, we assume in the following that $\boldsymbol{\Theta}$ has independent RV (cf. Eq. (1.22)). Direct stochastic methods rely on the resolution of a *set of decoupled deterministic* problems, corresponding to a set of realizations of $\boldsymbol{\Theta}$, to build the approximation, which can be apprehended as a response surface in terms of a basis of orthogonal random functionals. Therefore, it only relies on the deterministic model solver (also called *black-box* solver) that is repeatedly called in order to associate to each input parameters realization a model output. The advantage of this approach is that it does not require any *a priori* code adaptation. Moreover, it is easy to parallelize and can be exploited for complex problems involving multiphysics, coupled or highly nonlinear models. The drawback resides in the computational effort which is intensive as it scales with the number of deterministic simulations. That is why direct methods are particularly

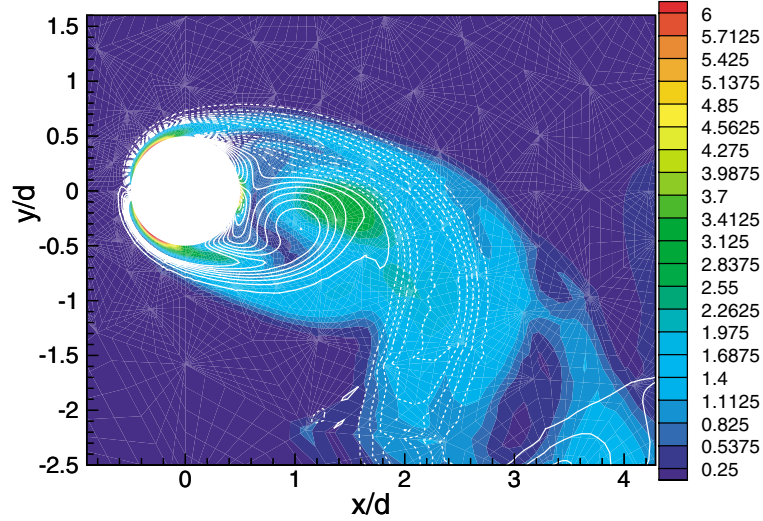


Figure 1.6 – Effect of upstream velocity parametric uncertainty on the laminar wake of a cylinder forced to oscillate in the crossflow direction. Comparison of instantaneous *rms* values (multicolor flood) and deterministic values (white isocontour lines) of vorticity at identical time.

costly if the underlying deterministic model is expensive to solve on its own. Consequently, improvement of direct methods by reduction of the number of deterministic simulations necessary to reach a reasonable accuracy is the focus of many ongoing efforts. We will review next three different direct (or *non-intrusive*) approaches.

3.2.1 Projection approach

The spectral projection approach was first introduced in [166] and has been used since for many different applications, among others [128, 249, 236]. This approach consists in defining the approximation J_P (here P refers to the Projection) of J as a projection onto the L^2 space (defined in Eq. (1.4–1.5) with associated inner product and norm defined in Eq. (1.6–1.7) span by the $\{\Phi_\alpha\}_{\alpha \in \mathcal{J}}$ basis (e.g. Eq. (1.27)). In this case:

$$J(u(\Theta); \Theta) \approx J_P = \sum_{\alpha \in \mathcal{J}} J_\alpha \Phi_\alpha(\Theta), \quad (1.71)$$

and the coefficients J_α are obtained, thanks to the orthogonality of the basis:

$$J_\alpha = \mathbb{E}[J(u(\Theta); \Theta) \Phi_\alpha(\Theta)] / \mathbb{E}[\Phi_\alpha^2(\Theta)]. \quad (1.72)$$

If the members of the basis are orthonormal, the expression of the coefficients is even simpler:

$$J_\alpha = \mathbb{E}[J(u(\Theta); \Theta) \Phi_\alpha(\Theta)] = \int_{\Theta(\Omega)} J(u(\theta); \theta) \Phi_\alpha(\theta) f_\Theta(\theta) d\theta. \quad (1.73)$$

Each coefficient J_α can be seen as the correlation between the functional of interest J and the α -th basis function $\Phi_\alpha(\Theta)$. We notice that the dimensionality of the coefficient does not depend on the total number of members in the basis. Moreover its determination does not depend on the other coefficients (i.e. the expansion coefficients are here not coupled).

Different techniques have been proposed in order to evaluate the N -dimensional integrals appearing in the right hand side of Eq. (1.73). These techniques involving sampling strategies or quadrature/cubature methods are detailed in Appendix B. The computational cost of these methods will be high for large N (due to the lack of knowledge of the functional regularity) and will require the use of adaptive algorithms.

3.2.2 Regression/Least squares approach

Regressions and least squares fits have been used to build response surfaces based on available data sets [226, 181]. Finding an optimal data set (or *experimental design*) has received recent attention [13, 338]. The application of these concepts in the context of stochastic finite element has been investigated in [75, 34, 35]. The idea can be summarized with the following optimization problem to approximate the expansion coefficients $\mathbf{J} \equiv \{J_\alpha\}_{\alpha \in \mathcal{J}}$ of the approximation: $J(u(\Theta); \Theta) \approx J_R = \sum_{\alpha \in \mathcal{J}} J_\alpha \Phi_\alpha(\Theta)$:

$$\hat{\mathbf{J}} = \arg \min_{\mathbf{J}} \sum_{k=1}^{N_q} w_k \left(J(u(\Theta^{(k)}); \Theta^{(k)}) - \sum_{\alpha \in \mathcal{J}} \hat{J}_\alpha \Phi_\alpha(\Theta^{(k)}) \right)^2, \quad (1.74)$$

where the $\Theta^{(k)}$ and w_k are the minimization points (or realizations) and associated weights and N_q is the total number of points.

This minimization is equivalent to solving a linear system, where the solution is expressed as:

$$\hat{\mathbf{J}} = \mathbf{A}^{-1}\mathbf{B}, \quad \text{with} \quad (\mathbf{A})_{\alpha\beta} = \sum_{k=1}^{N_q} w_k \Phi_{\alpha}(\Theta^{(k)}) \Phi_{\beta}(\Theta^{(k)}) \quad (1.75)$$

$$\text{and} \quad (\mathbf{B})_{\alpha} = \sum_{k=1}^{N_q} w_k \Phi_{\alpha}(\Theta^{(k)}) J(u(\Theta^{(k)}); \Theta^{(k)}).$$

While the method seems natural and flexible, the choice of the minimization points and weights is crucial but complex because the regularity of the functional J is not known *a priori*. Several choices have been proposed based on sampling techniques: MC, LHS or QMC methods or numerical quadrature techniques: such as Gauss cubature (cf. Appendix B). If the quadrature used satisfy the orthogonality relation of the basis $\{\Phi_{\alpha}\}_{\alpha \in \mathcal{J}}$ in the sense of the numerical inner product $\langle u, v \rangle_{N_q} = \sum_{k=1}^{N_q} u(\Theta^{(k)})v(\Theta^{(k)})$, it can be shown that the regression approach is *equivalent* to the L^2 projection of the previous section.

Berveiller [34] concludes from the study of various problems that $N_q \sim (N-1) \times p$ is an optimal size for the experimental design. Adaptive approaches have been proposed in this context [40, 38].

3.2.3 Interpolation/Collocation approach

Stochastic (or also called *probabilistic*) collocation method was first introduced by Tatang [465, 464] with later important developments [297, 533, 15]. The method considers, for the approximation space Φ_{α} , *interpolating* polynomials that are associated to a nodal set of points (or realizations) $\{\Theta^{(k)}\}_{k=1 \dots N_q}$. By choosing a set of nodes based on the theory of multivariate polynomial interpolations, this approach retains the accuracy and fast convergence of the other methods previously mentioned. The coefficients of the expansion are this time the deterministic solutions of the problem associated to the realizations:

$$J(u(\Theta); \Theta) \approx J_C = \sum_{k=1}^{N_q} J(u(\Theta^{(k)}); \Theta^{(k)}) \Phi_k(\Theta). \quad (1.76)$$

A convenient choice to build the polynomials $\Phi_k(\Theta)$ is to express them by means of Lagrange polynomials $\mathcal{L}_k(\Theta)$, that satisfy $\mathcal{L}_i(\Theta^{(j)}) = \delta_{ij}$ with $1 \leq i, j \leq N_q$, but other basis have been considered as well, e.g. piecewise linear functions [229] or radial basis functions [305]. The extension of the Lagrange polynomials to the N -dimensional space uses tensorized grids, in a similar way as for the integration. Again, we recall that the complexity of this approach is directly linked to the number of interpolation points and computational cost obviously becomes an issue with the increase of stochastic dimensions N . A way to decrease the total number of deterministic simulations is to use sparse tensor products for the grids [182, 26] such as the one introduced in the Smolyak's algorithm [533, 345, 138]. Adaptive sparse grid techniques were recently considered [346, 289]. Probabilistic collocations in the context of stochastic piecewise polynomial approximation were first developed in [130] and later adapted to an ANOVA-type decomposition for dealing with problems of high random dimensions [130].

4 Spectral statistics

Once the Polynomial Chaos-type (i.e. PC or gPC) spectral approximation of the second-order RV (cf. relation (1.4)) $U(\Theta)$ (or SP, e.g. $U(\mathbf{x}, \Theta)$) under consideration has been obtained, the user holds an explicit functional form representation. It is then very easy to generate a large set of realizations of this RV (or RP for fixed time or/and space coordinates), according to the random discretization Θ of the input data. Nevertheless this information is often too large and must be condensed into some more global quantities of interest (e.g. probabilities, statistical moments, pdf, marginal pdf, sensitivity coefficients, quantiles,...) either via sampling or analytically as we will see next.

4.1 Statistical moments

Due to the orthogonality of the hierarchical approximation basis, any statistical moment may be expressed analytically. For instance, let us consider the M -terms approximation of the RP $U(\mathbf{x}, \Theta)$, this is its *mean* value:

$$\mu_U = \mathbb{E}[U(\mathbf{x}, \Theta)] = U_0(\mathbf{x}), \quad (1.77)$$

and its *variance*:

$$\sigma_U^{2;M} = \mathbb{E} \left[(U(\mathbf{x}, \Theta) - \mu_U)^2 \right] = \sum_{k=1}^M U_k^2(\mathbf{x}) \mathbb{E} [\Phi_k^2]. \quad (1.78)$$

The coefficient of variation $c_v \equiv \frac{\sigma_U^M}{\mu_U}$ is a non-dimensional number and is a measure of the *dispersion* of a probability distribution. Its approximation is expressed as:

$$c_v^M = \frac{1}{U_0(\mathbf{x})} \left(\sum_{k=1}^M U_k^2(\mathbf{x}) \mathbb{E} [\Phi_k^2] \right)^{\frac{1}{2}}. \quad (1.79)$$

In a similar fashion, the *skewness* writes:

$$\delta_U^M = \frac{1}{\sigma_U^{3;M}} \mathbb{E} \left[(U(\mathbf{x}, \Theta) - \mu_U^M)^3 \right] = \frac{1}{\sigma_U^{3;M}} \sum_{i=1}^M \sum_{j=1}^M \sum_{k=1}^M U_i(\mathbf{x}) U_j(\mathbf{x}) U_k(\mathbf{x}) \mathbb{E} [\Phi_i \Phi_j \Phi_k], \quad (1.80)$$

and the *kurtosis*:

$$\kappa_U^M = \frac{1}{\sigma_U^{4;M}} \mathbb{E} \left[(U(\mathbf{x}, \Theta) - \mu_U^M)^4 \right] = \frac{1}{\sigma_U^{4;M}} \sum_{i=1}^M \sum_{j=1}^M \sum_{k=1}^M \sum_{l=1}^M U_i(\mathbf{x}) U_j(\mathbf{x}) U_k(\mathbf{x}) U_l(\mathbf{x}) \mathbb{E} [\Phi_i \Phi_j \Phi_k \Phi_l]. \quad (1.81)$$

We notice that the computational cost increases with the moment order. Nonetheless, the expectation of the polynomial products has a very sparse structure and maybe stored beforehand. In practice, for a fixed dimensionality M , lower statistical moments should be more accurate than higher order moments.

Spatial statistics are also readily available: e.g. *covariance* between two fields $U(\mathbf{x}, \Theta)$ and $V(\mathbf{x}, \Theta)$:

$$\begin{aligned} R_{UV}^M(\mathbf{x}_1, \mathbf{x}_2) &= \mathbb{E} \left[(U(\mathbf{x}_1, \Theta) - \mu_U^M) \cdot (V(\mathbf{x}_2, \Theta) - \mu_V^M) \right] \\ &= \sum_{k=1}^M U_k(\mathbf{x}_1) V_k(\mathbf{x}_2) \mathbb{E} [\Phi_k^2], \end{aligned}$$

and *auto-correlation*:

$$\begin{aligned} R_U(\mathbf{x}_1, \mathbf{x}_2) &= \mathbb{E} [U(\mathbf{x}_1, \Theta) \cdot U(\mathbf{x}_2, \Theta)], \\ &= \sum_{k=0}^M U_k(\mathbf{x}_1) U_k(\mathbf{x}_2) \mathbb{E} [\Phi_k^2]. \end{aligned}$$

4.2 Probability distribution functions

Concerning the computation of pdfs, except for low dimensional toy problems solved with low polynomial order approximations and for which analytical expressions may be derived, several numerical approaches are conceivable for practical applications. One simple way to proceed is to generate a large population sample, using MC methods or variants, cf. Appendix B: Sections 1.1 and 1.2, since the gPC expansion involves only algebraic evaluations with little computational cost. An histogram of these data can then be built. A variant that produces smoother distributions is the kernel-smoothing density estimate with an optimal bandwidth [500, 181].

Moreover, owing to the hierarchical and ordered nature of the gPC series, the computation of marginal densities remains tractable.

4.3 Sensitivity coefficients

In the following, let us consider a *second-order* RV U belonging to $L^2(\Omega^{(N)}, \mathcal{B}^{(N)}, P_{\Theta})$ space, cf. Eq. (1.4).

Global variance-based sensitivity analysis may be performed in order to quantify, via correlation ratios, the relative importance of each (or a group of) random input parameter to the uncertainty response of the system. The Sobol' functional decomposition (or ANOVA decomposition) of $U = h(\Theta)$ is unique and hierarchic. We have:

$$U = h(\Theta) = \sum_{s \subseteq \{1,2,\dots,N\}} h_s(\Theta_s), \quad (1.82)$$

where s is a set of integers such that $\Theta_s = (\Theta_{s_1}, \dots, \Theta_{s_N})$, with $N = \text{card}(s) = |s|$ and $h_\emptyset = h_0$. In this way, the variance of the solution can be derived from Eq. (1.82) and decomposed accordingly [114]:

$$\sigma_U^2 = \sum_{s \subseteq \{1,2,\dots,N\}} \sigma_s^2, \quad \text{with} \quad \sigma_s^2 = \mathbb{V}[\mathbb{E}[U|\Theta_s]] - \sum_{\substack{t \subseteq s \\ t \neq \emptyset}} \sigma_t^2, \quad (1.83)$$

where \mathbb{V} is the variance operator. The Sobol' indices [448] S_s are defined as:

$$S_s \equiv \frac{\sigma_s^2}{\sigma_U^2} \quad \text{and} \quad \sum_{\substack{s \subseteq \{1,2,\dots,N\} \\ s \neq \emptyset}} S_s = 1, \quad (1.84)$$

which measure the sensitivity of the variance of U due to the interaction between the variables Θ_s , without taking into account the effect of the variables Θ_t (for $t \subsetneq s$).

The *total* Sobol' indices [192] S_i^t are defined as:

$$S_i^t = \sum_{k \# i} S_k, \quad (1.85)$$

which expresses the total sensitivity of the variance of U due to the variable Θ_i , and where $\#i$ corresponds to all indices subsets containing i .

Those indices are trivial to compute when the stochastic solution is *globally* decomposed onto its associated gPC basis. In this case the hierarchical nature of the gPC representation in the domain is the key to an easy evaluation.

However, fast and direct evaluation of the Sobol' indices from the *local* gPC coefficients in the context of piecewise polynomial approximation (cf. Section 2.3.2) is not straightforward but provides good results [71]. In this case, we may rely on MC-like techniques [192] where we sample the gPC expansion (cf. Eq. (1.40)) *a posteriori* to compute the indices. With this approach, we make use of two independent sample sets $\{\Theta^{(k)}\}_{k=1}^{N_{MC}}$ and $\{\Xi^{(k)}\}_{k=1}^{N_{MC}}$, and the MC sample estimate of the partial variance in (1.84) becomes:

$$\hat{\sigma}_s^2 = \frac{1}{N_{MC}} \sum_{k=1}^{N_{MC}} h(\Theta^{(k)})h(\tilde{\Theta}_s^{(k)}) - \sum_{t \subsetneq s} \hat{\sigma}_t^2, \quad (1.86)$$

where

$$(\tilde{\Theta}_j)_s^{(i)} = \begin{cases} \Theta_j^{(i)} & \text{if } j \in s, \\ \Xi_j^{(i)} & \text{otherwise.} \end{cases} \quad (1.87)$$

Therefore, the evaluation of all of the $(2^N - 1)$ sensitivity coefficients S_s requires $\mathcal{O}(N_{MC} \cdot 2^N)$ evaluations of h .

5 Adaptive approaches for error vs. cost control

While it is manifest that standard stochastic spectral methods benefit from numerous advantages, they also present some limitations for complex engineering applications with realistic uncertainty conditions: – 1. computational cost due to the “curse of dimensionality” (e.g. relates to the correlation length of the process), which translates into the resolution of very large system of equations or equivalently countless calls to the deterministic solver. This brings the question of what is the effective dimensionality of the solution? – 2. lack of robustness and accuracy for strongly nonlinear systems for which stochastic global approximations are not well suited to capture solution local parametric front/shocks/gradients. This raises the question of the adaptivity of the approximation basis to the solution probabilistic sudden changes? – 3. “long-term integration”: problem of the time-integration of dynamical systems involving random coefficients (e.g. random frequency) due to the broadening of the solution spectrum as time evolves (e.g. method loses p -convergence after a finite time). This difficulty is somewhat related to point 1. Obviously, points 1. & 2. are often intricately connected for most nonlinear engineering multiphysics systems.

A natural approach consists in trying to reduce the computational cost while improving or at least maintaining the quality of the stochastic representation. Some early attempts [258, 278] showed through a *a posteriori* analysis of the stochastic approximation spectrum that it was often possible to lower the effective dimensionality of the system. Some works address the first limitation by proposing *model reduction* techniques that rely on the concept of *reduced basis* for the stochastic Galerkin formulation.

5.1 Model reduction

The ingenious idea is to take advantage of the structure of the full approximation (deterministic + stochastic) space $\mathcal{V}_{\text{det}} \otimes \mathcal{S}_{\text{sto}}$ and improve the basis by reducing its size:

Find optimal $\mathcal{V}_M = \text{span}\{r_k\}_{k=1}^M \subset \mathcal{V}$ & $\mathcal{S}_M = \text{span}\{\psi_k\}_{k=1}^M \subset \mathcal{S}$ such that:

$$u(\mathbf{x}, \Theta) \approx u_M(\mathbf{x}, \Theta) = \sum_{k=1}^M r_k(\mathbf{x}) \psi_k(\Theta) \quad \text{with } M \text{ small.}$$

But, how to define and build these reduced basis? and what is the right *optimality* criterion?

If u is (partially) known, the optimal decomposition can be defined via the classical inner product:

$$\|u - u_M\|^2 = \min_{\substack{r_1 \dots r_M \in \mathcal{V} \\ \psi_1 \dots \psi_M \in \mathcal{S}}} \left\| u - \sum_{k=1}^M r_k \psi_k \right\|^2, \quad \|u\|^2 = \mathbb{E}[\langle u, u \rangle_{\mathcal{V}}]$$

In this case, the standard *spectral decomposition* or KL representation is recovered. It is sometimes referred as an *a posteriori* model reduction [300, 6, 107].

The technique becomes more general and is referred as an *a priori* model reduction when the *reduced basis* for the stochastic Galerkin formulation is combined together with an optimality criterion depending on the model but not on the solution, e.g. the *generalized spectral decomposition* of Nouy [349, 350] or the works of others [415, 48].

$$u(\Theta) \approx u_M(\Theta) = \mathbf{R} \Psi \quad \text{with}$$

$$\mathbf{R} = (r_k)_{k=1}^M \in \mathcal{V}_M \quad \& \quad \Psi = (\psi_k)_{k=1}^M \in \mathcal{S}_M$$

$$\begin{array}{ll} \text{Simultaneous} & \text{Progressive} \\ \forall \mathbf{v}_M \in \mathcal{V}_M \otimes \mathcal{S} + \mathcal{V} \otimes \mathcal{S}_M & \forall \mathbf{v} \in \{r\} \otimes \mathcal{S} + \mathcal{V} \otimes \{\psi\} \end{array}$$

$$\begin{array}{ll} \text{Galerkin} & \langle \langle \mathbf{v}, \mathcal{A}(\mathbf{u}_M) - \mathcal{B} \rangle \rangle = 0 \quad \langle \langle \mathbf{v}, \mathcal{A}(\mathbf{u}_m + \psi r) - \mathcal{B} \rangle \rangle = 0 \\ \text{Minimal residual} & \langle \langle \mathcal{A}(\mathbf{v}), \mathcal{A}(\mathbf{u}_M) - \mathcal{B} \rangle \rangle = 0 \quad \langle \langle \mathcal{A}(\mathbf{v}), \mathcal{A}(\mathbf{u}_m + \psi r) - \mathcal{B} \rangle \rangle = 0, \end{array}$$

which are interpreted as pseudo-eigenproblems that may be solved with different algorithms variants:

- Progressive definition \rightarrow power iterations
- Simultaneous definition (optimal) \rightarrow subspace iterations [349]
- Approximation of the optimal \rightarrow Arnoldi [349]

Other researchers propose to overcome the curse of dimensionality with a low-rank *separated approximation* of the solution, obtained using an alternating least-squares (ALS) scheme [108]. They show in some cases that the computational cost of the proposed algorithm grows linearly with respect to the dimension of the underlying probability space of the system.

Some researchers propose “time-dependent” gPC basis [153] or “stochastic POD” [202, 485]. Finally, there exists attempts to unify POD & gPC representations: e.g. “dynamically orthogonal field representation” [427] or “nonlinear biorthogonal decomposition” [487].

Other works show how to reduce the number of deterministic samples required by the direct methods layout while keeping the approximation accurate. This may be achieved by designing *regression-based sparse* PC expansion [40], using *sparse grid-based* methods for (adaptive) stochastic collocation [155, 320, 229, 138, 345, 346, 289] or rely on *ANOVA-type decomposition*, [394, 130].

Most of the studies addressing the second limitation propose *adaptive model refinement* techniques thereby increasing the robustness and/or the level of resolution/details of the approximation to capture nonlinearities.

5.2 Model refinement

The first attempt of model adaptation was achieved by *multiresolution/multiscale* schemes (e.g. wavelets and multi-wavelets) [248], soon followed by random *partitioning* with *a posteriori* heuristic convergence criteria [494]. Later, complementary approaches were proposed with random/spatial spaces *partitioning* [223, 299, 499] (with dual-based error estimation techniques to improve global error estimation) or *hierarchical sparse grid collocation* [289] and more recently, *binary trees* [478].

We also proposed original adaptive approaches such as *hp*-adaptive piecewise gPC representation [251], *non-linear Galerkin-type* formulation [384, 386], *hybrid* [387, 385] or *iterative gPC-based spectral projection* methods [388]. In the following we will present the key ingredients of the first and last latter methods while the nonlinear Galerkin method is detailed in Section 1.4 of Chapter III.

5.2.1 *hp*-adaptive formulation for piecewise gPC stochastic approximation

The piecewise polynomial spaces framework introduced in subsections 2.3.2 & 2.3.2 from Section 2.2.4 is very useful for improving the local resolution of the stochastic representation. Nevertheless, a uniform or brute-force refinement over the entire space is very likely to overwhelm the available CPU resources. Therefore one must look for an adaptive (often *iterative*) procedure that will *automatically* perform refinement *locally* where it is needed. Similarly to deterministic spectral element methods [490], the refinement maybe performed in terms of the size of the piecewise polynomial support or in terms of the expansion order itself, or a combination of both.

Provided a stochastic partition of the parametric domain, cf. Eq. (1.39), the adaptive formulation uses an *a posteriori* heuristic based on the *local* convergence of the solution *variance* within each element of the partition. An assumption is that the same polynomial order P is used within the entire partition which implies that the adaptive procedure only relies on element size refinements. The notation M_P emphasizes the relationship between the number of degrees of freedom M for a given polynomial order P . The local solution variance within element B_l is derived, thanks to the polynomial basis orthogonality:

$$\sigma_{l,P}^2 = \sum_{j=1}^{M_P-1} u_{l,j}^2 \mathbb{E}[\Phi_{l,j}^2], \quad (1.88)$$

while the approximate *global* mean \bar{u} and variance σ^2 of the solution can be expressed as:

$$\mu \approx \sum_{l=1}^{N_e} u_{l,0} \Pr(I_{B_l} = 1), \quad \sigma^2 \approx \sum_{l=1}^{N_e} \left(\sigma_l^2 + (u_{l,0} - \mu)^2 \right) \Pr(I_{B_l} = 1), \quad (1.89)$$

where N_e is the number of elements in the partition. We associate the decay rate of the representation to the variance relative error in each element. Based on multiple levels of p_k of approximations, we introduce

$$\eta_{l,P} = \sum_{i=M_{P-1}}^{M_P-1} u_{l,i}^2 \mathbb{E}[\Phi_{l,i}^2] / \sigma_{l,P}^2$$

which represents the contribution of the order- P gPC terms to the local variance

and we define the following criterion:

$$\eta_{l,P}^\gamma \Pr(I_{B_l} = 1) \leq \epsilon_1, \quad 0 < \gamma < 1, \quad (1.90)$$

where γ and ϵ_1 are prescribed constant parameters.

1. If this criterion is satisfied, the element and its inner approximation remain the same,
2. otherwise, the element under consideration needs refinement.

The first choice is to check if we can perform a p -refinement:

p -refinement

If the response is smooth in the element, we can check if the convergence of the spectrum is close to a spectral form: $\eta_{l,k} \approx \eta_{l,k}^* = a_{l,k} \times \exp(-b_{l,k} p_{l,k})$ where $(a_{l,k}, b_{l,k})$ are some constants. This may be easily verified using a least square fit of the difference $q_{l,k} \equiv |\eta_{l,k} - \eta_{l,k}^*|$ at the data points. We then introduce another criterion:

$$\|q_{l,k}\|_2 \leq \epsilon_3. \quad (1.91)$$

1. If the criterion is satisfied, it means that the response in element B_l is smooth enough to lower the error further by increasing the polynomial order at the next iteration: i.e. $p_{l,k} \leftarrow p_{l,k+1}$ and the quadrature grid is updated as well. The polynomial order increment between two consecutive iterations may be arbitrary,
2. otherwise, we perform a h -refinement instead.

h -refinement

In this case the element will be split in the next iteration. However, due to dimensionality and in order to keep an affordable number of elements, we consider only the most sensitive random dimensions based on the following *anisotropic* criterion [494]:

$$r_i = \frac{u_{i,P}^2 \mathbb{E}[\Phi_{i,P}^2]}{\sum_{j=Q_{P-1}}^{Q_P-1} u_j^2 \mathbb{E}[\Phi_j^2]}, \quad i = 1, 2, \dots, N \quad (1.92)$$

where we drop the subscript l for clarity and the subscript $\cdot_{i,P}$ denotes the mode consisting only of random dimension Θ_i with polynomial order P . For each element, the random dimensions which satisfy $r_i \geq \epsilon_2 \cdot \max_{k=1, \dots, N} r_k$, will be split into two parts in the next step while all other random dimensions remain unchanged.

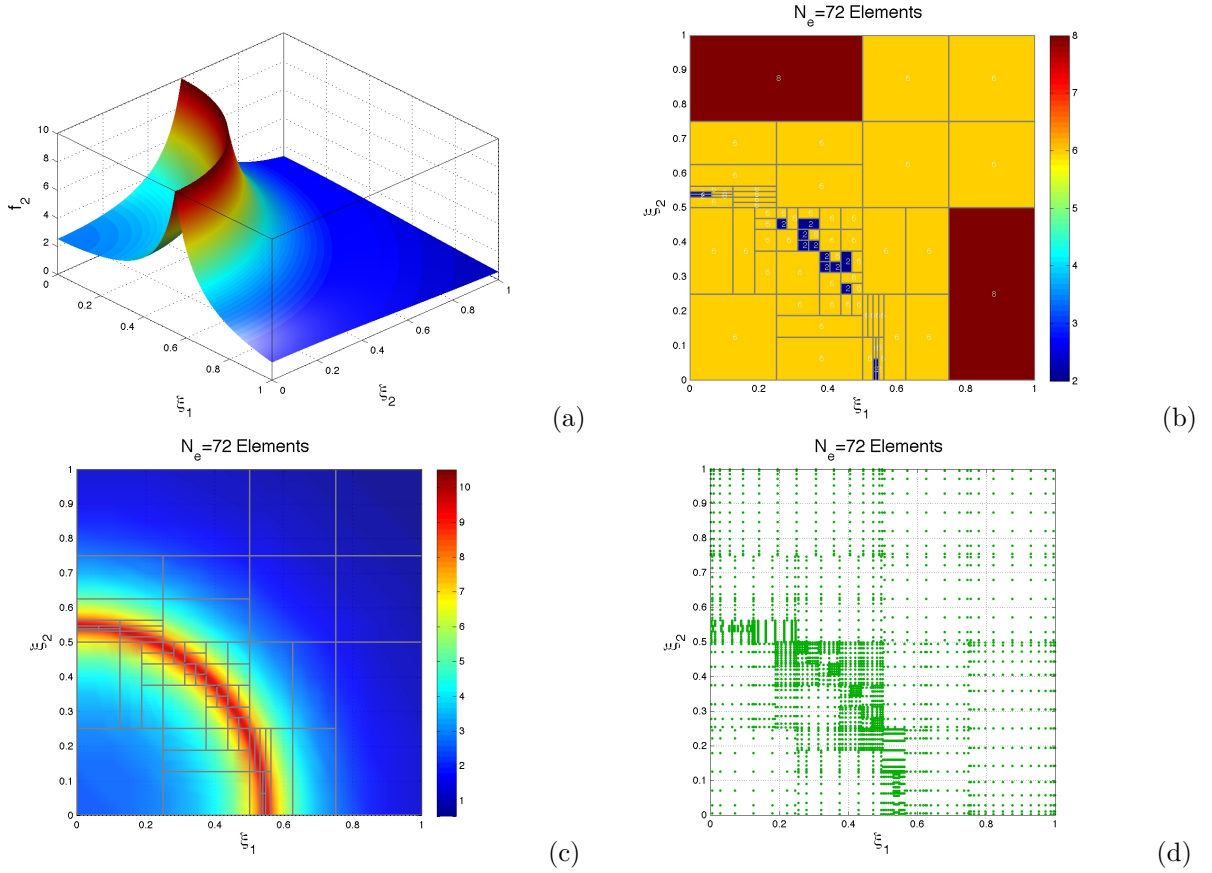


Figure 1.7 – Exact (a) and piecewise hp -adaptive approximation (c) of non-smooth & non-polynomial functional with regularized line singularity: $f_2(\xi_1, \xi_2) = \frac{1}{|0.3 - \xi_1^2 - \xi_2^2| + \delta}$ with $\delta = 10^{-1}$ and (ξ_1, ξ_2) are *uniform* i.i.d RV [289]; Legendre polynomial order distribution: 3 different p -enrichment levels are allowed i.e. $p = (2, 6, 8)$ (b) and corresponding quadrature points (d).

In the following, we show how the method performs for a nonlinear test function and for a problem of nonlinear stochastic aeroelasticity, cf. also Section 2 of Chapter IV.

Fig. 1.7 shows that the decomposition adapts very well to the difficult case of the curved ridge that is progressively misaligned to the main directions. Only the final partition required for a converged approximation is represented. As expected, low polynomial order is employed along the ridge region and higher polynomial orders are retained away from the singularity where the function is smoother. The quadrature used relies on a full Kronrod-Patterson grid which is conveniently nested so that previous computations can be re-used, cf. Section 2.1.3 of Appendix B.

Fig. 1.8 displays illustrative examples of a parametric grid- and polynomial order-refinement process for the pitch response surface of a subsonic two degrees-of-freedom pitch-and-plunge airfoil with *uniformly* distributed linear and cubic torsional stiffness. For the chosen flow speed and structural range of parameters, the response is characterized by the presence of a supercritical branch of flutter instability that is brutally triggered by a small parametric change (cf. the 2 distinct regions in the figures). The adaptive approach is able to sense automatically the location of the front, to refine the size of the elements along the right direction in its vicinity and to increase the polynomial order where the response surface is smooth although slightly bent.

5.2.2 Iterative Galerkin-based spectral projection method

Here we propose a new *iterative* approach for Galerkin-based spectral projection methods, which we call *iterative-gPC* (i-gPC), that is more accurate than the classical approach with the same level of approximation. Moreover, the accuracy of the representation improves no matter the regularity of the random variable of interest. Therefore, it is particularly well suited when nonlinear transformations of random variables are in play, as in the case of compressible gas dynamics for instance.

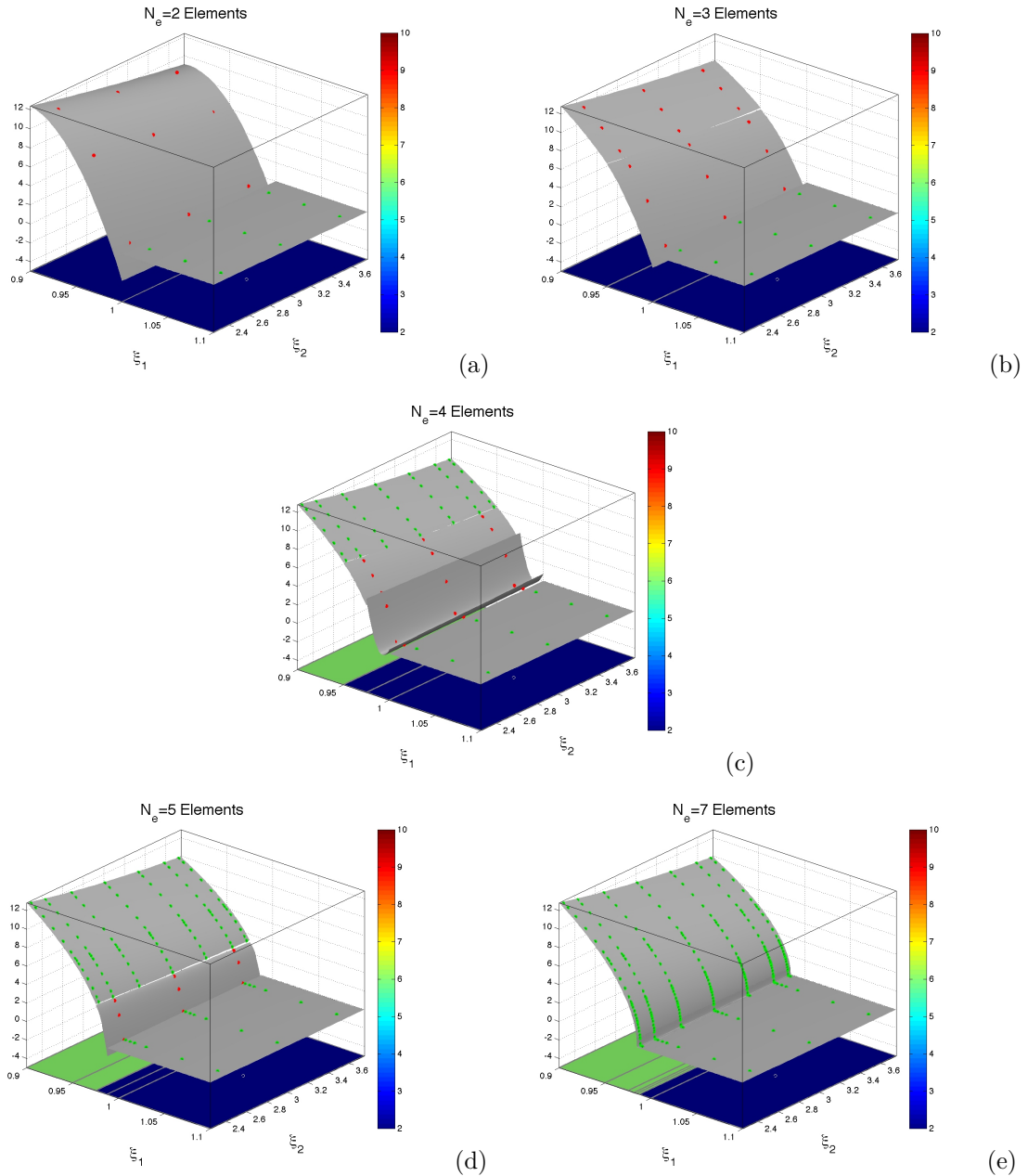


Figure 1.8 – hp -adaptive pitch flutter response of a subsonic pitch-and-plunge airfoil with *uniformly* distributed linear and cubic torsional stiffness [313, 251, 70]. Not all iterations are displayed (iterations 1 & 6 are missing). Red quadrature points indicate that the local convergence criterion is not satisfied in the random element of interest, and that refinement needs to be performed. Isocolors in the horizontal plane refer to polynomial order; 2 different p -enrichment levels are allowed $p = (2, 6)$. The scheme allows h - and p -refinement in different elements during the same iteration, e.g. change from (b) to (c).

Suppose X denotes our input RV, here $X \in \mathbb{R}^n$ denotes a random vector with independent components. We suppose its pdf f_X – it is a product of the probability measure of the independent components of the RV X – is known together with its optimal *orthonormal* gPC basis $(\phi_k^X)_{k \in \mathbb{N}}$ i.e. such that $\forall(k, t) \in \mathbb{N}^2$,

$$\mathbb{E}[\phi_k^X(X)\phi_t^X(X)] = \int \phi_k^X(x)\phi_t^X(x)f_X(x)dx = \delta_{k,t}. \quad (1.93)$$

Now suppose one wants to approximate a RV: $Y = u(X)$ where u is a (possibly nonlinear) transformation⁵ of X .

The initial step of our algorithm consists of the application of the gPC formalism: we define the moments of Y in the P -truncated basis $(\phi_k^X)_{k \in \{0, \dots, P\}}$ by

$$y_k^X = \mathbb{E}[u(X)\phi_k^X(X)], \forall k \in \{0, \dots, P\}, \quad (1.94)$$

so that

$$Y \approx y_X^P(X) = \sum_{k=0}^P y_k^X \phi_k^X(X). \quad (1.95)$$

Note that $P = P(Q, n)$ depends on the dimension of the RV $X \in \mathbb{R}^n$ and the truncation order of the gPC representation in each dimensions Q . For example, for full tensorized product $P = Q^n$, for triangular product $P = \frac{(Q+n)!}{Q!n!}$. In the following, the dependence of P with respect to Q and n is recalled only if necessary.

Next, we look for a $L^2(\Omega)$ basis orthonormal with respect to the numerical approximation distribution. If we denote by $(\phi_k^Z)_{k \in \mathbb{N}}$ this basis, and f_Z the associated measure, they must satisfy $\forall(k, t) \in \mathbb{N}^2$,

$$\mathbb{E}[\phi_k^Z(Z)\phi_t^Z(Z)] = \int \phi_k^Z(x)\phi_t^Z(x)f_Z(x)dx = \delta_{k,t}. \quad (1.96)$$

In order to build this basis without evaluating directly the probability measure, we suggest using Christoffel formulae, see [459]. We call $(s_i^Z)_{i \in \mathbb{N}}$ the i^{th} statistical moments of Z :

$$s_i^Z = \mathbb{E}[Z^i] = \int x^i f_Z(x)dx, \forall i \in \mathbb{N}, \quad (1.97)$$

and the orthonormal basis is given by (see Christoffel's formulae [459]), $\forall n \in \mathbb{N}$,

$$\phi_n^Z(x) = \frac{1}{\sqrt{D_{n-1}D_n}} \begin{vmatrix} s_0 & s_1 & \dots & s_n \\ \vdots & \vdots & \vdots & \vdots \\ s_k & s_{k+1} & \dots & s_{n+k} \\ \vdots & \vdots & \vdots & \vdots \\ 1 & x^1 & \dots & x^n \end{vmatrix}, \quad (1.98)$$

where $|\cdot|$ refers to a matrix determinant and D_{n-1} , respectively D_n , is the determinant of the matrix of general term $\{s_{i+j}\}_{(i,j) \in \{0, \dots, n-1\}^2}$, respectively $\{s_{i+j}\}_{(i,j) \in \{0, \dots, n\}^2}$.

In a second step, we seek the gPC development of $Y = u(X)$ in the new orthogonal basis $(\phi_k^Z)_{k \in \mathbb{N}}$, now optimal with respect to the RV Z . We consider the transformation F that relates the RVs X and Z . We have $X = F(Z) = F_X^{-1}(F_Z(Z))$, where F_X and F_Z are the cdf of X and Z , respectively.

Note that in practice, we never look for F (this is explicit in equation (1.99)). In the new basis, the gPC coefficients are expressed as

$$\begin{aligned} y_k^Z &= \mathbb{E}[u(F(Z))\phi_k^Z(Z)] = \int u(F(x))\phi_k^Z(x)f_Z(x)dx, \\ y_k^Z &= \mathbb{E} \left[u(X)\phi_k^Z \left(\sum_{l=0}^P y_l^X \phi_l^X(X) \right) \right], \\ &= \int u(x)\phi_k^Z \left(\sum_{l=0}^P y_l^X \phi_l^X(x) \right) f_X(x)dx, \forall k \in \{0, \dots, Q\}. \end{aligned} \quad (1.99)$$

Here, we arbitrarily made the choice of using the same polynomial order as in each stochastic dimension Q for the new approximation basis. In practice, when using quadrature rules in order to compute the $(y_k^Z)_{k \in \{0, \dots, Q\}}$,

5. Transformation in a broad sense i.e. Y can be the output of a code etc.

the last formulae of (1.99) is used so that we do not need to look for F . We then build the gPC development of $Y = u(X)$ in the new gPC basis $(\phi_k^Z)_{k \in \{0, \dots, Q\}}$:

$$\begin{aligned} Y \approx y_Z^P &= \sum_{l=0}^Q y_l^Z \phi_l^Z(Z), \\ Y \approx y_Z^P &= \sum_{l=0}^Q y_l^Z \phi_l^Z \left(\sum_{k=0}^P y_k^X \phi_k^X(X) \right). \end{aligned} \quad (1.100)$$

In [388], we prove the $L^2(\Omega)$ convergence and accuracy of the approximation with the new basis.

We apply the new method to several test cases with different levels of regularity, dimensionality and complexity, and compare it in terms of computational cost with the classical approach.

One dimensional test case: discontinuous solution (piecewise constant function)

Let us first consider that $P = Q$ in all this paragraph. In this section, we assume X follows a *uniform* distribution in $[-1, 1]$ and $Y = u(X)$ where

$$u(x) = \mathbb{I}_{]-\infty, -\frac{1}{2}]}(x) = \begin{cases} 1 & \text{if } x \leq -\frac{1}{2}, \\ 0 & \text{elsewhere.} \end{cases} \quad (1.101)$$

The location of discontinuity is here arbitrary and does not affect the conclusion of this exercise. From a statistical point of view, a continuous RV X is here transformed into a discrete RV Y having each different optimal basis (Legendre for X and Krawtchouk for Y , cf. [431]). Besides, the oscillations appearing in the gPC approximations in this section are known in the literature as the Gibbs phenomenon and are relevant to PDEs (e.g. Euler system) that develop discontinuous solutions in finite time (see [436] for example).

We first apply the classical gPC approach to this problem with the choice of a Legendre basis, optimal for the representation of the input X . The nonlinear transformation of Eq. (1.101) obviously makes the Legendre basis unadapted to the output Y leading to an oscillating approximation (Gibbs phenomenon and induces an artificial spread of the pdf, see [382]).

We now apply i-gPC to this same test case in the same conditions. Figure 1.9 shows the approximations obtained for the first four iterations: we recall that iteration $m = 0$ corresponds to the gPC approximation on a Legendre basis hereinbefore mentioned.

With increasing number of iterations, more oscillations appears close to the discontinuity but their amplitudes are bounded and decrease significantly. Meanwhile, the position of the discontinuity is better captured.

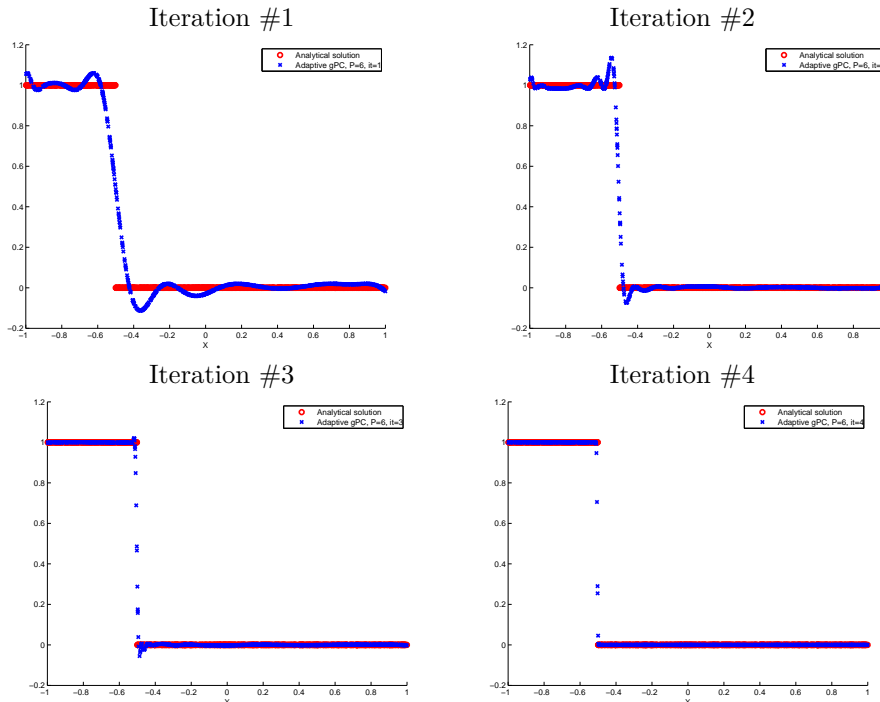


Figure 1.9 – Evolution of the approximation in the random space with respect to the iteration number.

Figure 1.10 (left) compares the analytical pdf with the i-gPC solution (here: $P = 6$, level 7 of CC quadrature, $m = 5$ iterations). The histograms match after the fourth iteration and the approximated solution does not oscillate anymore.

Figure 1.10 (right) presents a convergence study with respect to both the polynomial order P and the number of iterations. We verify that the errors for the classical approach remain important whatever the order P used. We notice that for all cases the error norm eventually reaches machine accuracy ($\sim < 10^{-15}$), which is quite

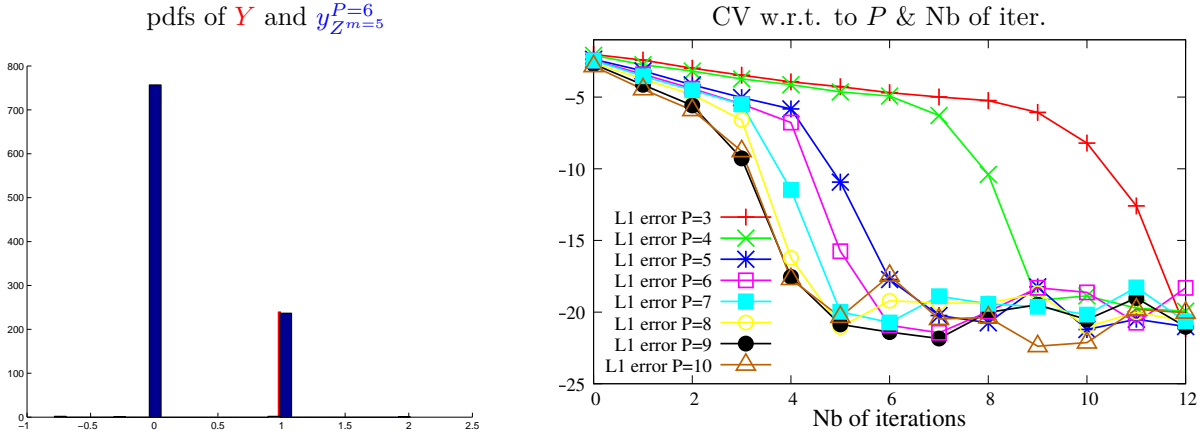


Figure 1.10 – Left: exact and approximated pdfs for $P = 6$ and 5 iterations. Right: Convergence of i-gPC on the discontinuous test-case. Each curve represent the logarithm of the $L_1(\Omega)$ -error for one polynomial order P with respect to the number of iterations.

remarkable for this problem. The cases with higher polynomial approximation order converge faster in terms of number of iterations of the algorithm. We also observe that the convergence rate for each curve seems to be made of two regimes: a first one that is quite linear – in this semi-logarithmic plot – and is shorter while steeper for higher P –case, followed by another very fast convergence regime that only necessitate 2 to 3 iterations to reach machine accuracy and does not depend on P .

Moreover, we recall that our approach only consists in post-processing of a fixed number of deterministic solution evaluations. Therefore, the CPU cost dedicated to the iterative procedure is negligible compared to the CPU cost of the deterministic simulations.

One question may be the relevance of i-gPC to different type of input distributions. In [388], we show that the approach still converges for a Gaussian RV.

High dimensional test problem: g -function of Sobol': 5 – D stochastic

In this section, we apply the i-gPC algorithm on high dimensional stochastic problems. In [388], we apply it to a discontinuous 2 – D stochastic test-case based on the analytical solution of Burgers equation, see [382]. Here, we test a 5 – D stochastic problem, the g -function of Sobol', suggested in [423] and used in several benchmark works, see [39, 38, 232]. The model is:

$$Y = \prod_{i=1}^D \frac{|X_i| + a_i}{1 + a_i}, \quad \text{with } \forall i \in \{1, \dots, D\}, a_i \geq 0, \quad (1.102)$$

where the $(X_i)_{i \in \{1, \dots, D\}}$ are independent identically distributed uniform random variables. For this model, the mean and variance can be evaluated exactly:

$$\begin{cases} \bar{Y} &= 1, \\ \text{var}(Y) &= \prod_{i=1}^D \left(\frac{1}{3(1 + a_i)^2} \right) - 1. \end{cases} \quad (1.103)$$

We emphasize that the parameter a_i controls the stiffness of the model: lower values of a_i have the tendency to increase the discontinuity jump of the absolute value derivative profile, while higher values tend to decrease it. We decide to test both isotropic and anisotropic cases. For the first (isotropic) case, $\vec{a} = (a_1, a_2, a_3, a_4, a_5) = (0.5, 0.5, 0.5, 0.5, 0.5)$ and for the second (anisotropic) case, $\vec{a} = (0.5, 1, 2, 4, 8)$, i.e. $a_{i+1} = 2 \times a_i$ with $a_1 = 0.5$ and the higher dimensions become less and less predominant.

Figure 1.11 compares the pdf profiles for each case – (a): isotropic and (b): anisotropic – in linear and semi-logarithmic vertical scales. The comparison is between MC, classical gPC and i-gPC (after one iteration). Both

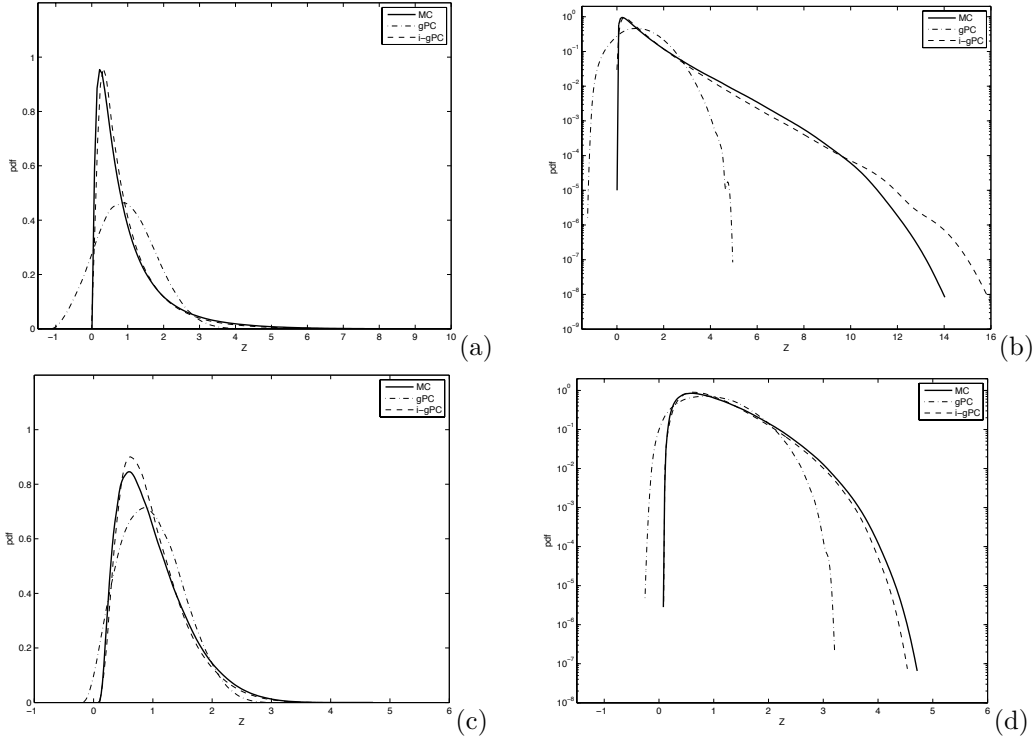


Figure 1.11 – Comparison between MC, gPC and i-gPC (after one iteration) pdfs profiles of Sobol' 5D g -functions, (a-b): isotropic function and (c-d): anisotropic function in linear (left column) and semi-logarithmic (right column) vertical scales.

gPC computations are carried out with a polynomial order 3 and $1M$ samples are drawn to evaluate each pdf with a kernel smoothing density technique.

We notice a very substantial improvement of the pdfs derived from the i-gPC approximation (after only one iteration) compared to the classical approach (which does not even preserve positivity of the approximation). The effect is weakened in the anisotropic case. Here a low polynomial order of degree 3 is used to test the robustness of the method in this context of moderate dimensionality. The number of degrees of freedom of the optimal reconstructed basis is lowered by more than one order of magnitude compared to the original gPC basis.

In summary, the new *iterative* approach for Galerkin-based spectral projection methods increases the accuracy of the spectral approximation independently of the regularity of the random variable of interest and at *no significant additional cost*. The method is particularly well suited when non linear transformations of random variables are in play. The new iterative approach allows to recover the same bounds of error in the vicinity of discontinuities as in the vicinities of smoother regions with no need for polynomial order refinement (i.e. no impact on the corresponding number of deterministic simulations).

In conclusion, there is a real need for efficient/robust error control at lowest computational cost and adaptive approaches seem to be the key. Ultimately, one would like to control the error both at deterministic and stochastic levels. However, an optimal approach is difficult to design because of the interaction between spatial and stochastic discretizations. At the deterministic level, the user may benefit *a priori* from the CFD community experience or his own physical intuition, e.g. it is often easy to apprehend the region of the flow with strong spatial gradient. However, it is very difficult to predict the parameter range and distribution for which the system will turn out to be the most sensitive. Therefore, a lot of questions remain open at a stochastic level: e.g. what type of refinement must be performed? elemental partitioning vs polynomial enrichment? along which dimensions? In this context, sound numerical methods and corresponding algorithms must be designed in order to perform *automatic* refinement.

Chapter II

Application to shear-dominated convective flows

This chapter introduces the application of stochastic spectral methods to the uncertainty quantification of incompressible parallel sheared flows, which are known to be prone to instabilities and often sensitive to external noise. The focus is mainly on the physical mechanisms and effects induced by colored random inflow or base flow disturbances. Two different physical systems: a plane Couette flow and a spatially developing mixing layer are considered, i.e. a closed and an open shear flow. While the underlying deterministic models retained for these two flows encompass the entire spectrum of numerical approaches, from linear stability theory to direct numerical simulation, the selected stochastic method is the same for both cases and does not require any changes to the existing solvers. This work has been communicated in the following journal publications and proceedings [233, 236, 234, 235, 237].

Sommaire

1	Effects of base flow uncertainty on linear shear flow stability	56
1.1	Linear stability of planar Couette flow with stochastic base flow	57
1.2	Numerical methods	59
1.3	Results	60
1.4	Concluding remarks	63
2	Sensitivity of mixing layer DNS to random inflow perturbation	65
2.1	Spatially developing mixing layers with random inflow disturbances	66
2.2	Numerical Method	69
2.3	Results	72
2.4	Perspectives on three-dimensional mixing layers	80
2.5	Concluding remarks	80

Canonical shear flows: e.g. Poiseuille flow, Couette flow, Hagen-Poiseuille flow, square duct flow, Blasius boundary layer,... despite of being of simple appearance are of tremendous importance in engineering (mechanical, aeronautics, chemical, materials, civil,...), in numerous scientific disciplines (aerodynamics, environmental fluid dynamics, atmospheric, meteorology, oceanography, geophysics, astrophysics,...) and turbulence, transport and mixing processes in general. A key issue in the study of these flows is the understanding of the *transition* of the flow from a laminar to a turbulent state when fluid velocity increases.

Despite remarkable results such as the formulation of the viscous stability problem for parallel shear flows by Orr & Sommerfeld for instance, there are still some unanswered questions including the discrepancy between the computed critical Reynolds number and the observed transitional Reynolds number. Indeed, many shear-induced flows are in fact *subcritical* transitional flows, i.e. excursions away from the laminar state can happen despite the linear stability of the underlying base flow. In fact, the assumption of a simple and regular base flow greatly simplifies stability analysis, but at the same time introduces a limitation that misrepresents many realistic configurations. For example, the base flow may be influenced by small fluctuations, thus compromising the assumption of a regular base profile. In this work, we propose to generalize the approach by considering internal uncertainty and covariance dynamics, i.e. stochastic effects that stem from uncertainties in the operator itself.

Another intriguing question, considering the simple form of its *free* shear flow, is the case of the mixing layer that forms between merging fluid streams of differing velocity. The correlation between the presence of quasi-two-dimensional coherent structures, found in the turbulent region of the flow, and the effects of inflow conditions

upon the growth rate of the layer is not well understood. The controlled environment that numerical deterministic simulations offer should provide some answer. In practice, this is often made difficult due to the sensitivity of the mixing layer to upstream perturbations in addition to the challenge of the validation of those numerical results against experiments. Moreover, there is no particular consensus that defines the best inflow condition with which the mixing layer flow simulation should be initialized. In general, special attention is paid to the effects of forcing amplitude and relative phase shift between forcing frequencies onto the growth of the coherent vortex structures in the early stages of the development. In this work, we will address the sensitivity of a spatially developing mixing layer to some uncertainties present in the magnitude of various disturbance modes imposed on the shear velocity profile at the upstream boundary.

1 Effects of base flow uncertainty on linear shear flow stability

One of the key issues in the study of sheared flows is the understanding of the flow *transition* from a laminar (“simple”) to a turbulent (“very complex”) state when fluid velocity increases. When an infinitesimal perturbation is introduced to a laminar shear flow, the disturbance either decays to return the flow to its original state or grows until the flow evolves into a different (possibly turbulent) state. The evolution of such perturbation can be numerically examined with the linear stability theory (LST) that focus on studying the *asymptotic* ($t \rightarrow \infty$) system stability [430] under the assumption of possible exponential time dependence of some growing normal modes. The numerical method predicts the critical Reynolds number at which instability occurs as well as the type of flow structures causing transition. In reality, while classical LST is successful for many problems (e.g. Taylor-Couette flow, Rayleigh-Benard convection), it fails badly for numerous shear flows. For instance, for plane Couette flows, the LST theory predicts *unconditional* stability although experimental results [44, 92, 470] observe turbulence at Reynolds number as low as $Re = U_{\text{wall}} H/\nu = 350$ [471]. In fact, the transition for many shear flows occurs for lower Re numbers than predicted by the theory. Moreover, the theory sometimes predicts erroneous type of flow structures, e.g. in the boundary layer, it predicts traveling Tollmien-Schlichting (TS) waves instead of turbulent spots or streaks as evidenced by experiments. It turns out that experimental critical Re numbers and transitions in general are very sensitive to background disturbances/noise: e.g. surface/wall roughness, thermal fluctuations, free-stream or pressure gradient fluctuations, wall vibrations, acoustic noise...

Since the beginning of the nineties, a *nonmodal* more “modern” approach to transition in shear flows, including nonmodal *transient growth*, *optimal perturbations* and *pseudospectra* has been followed by some researchers [56, 400, 476, 7, 430, 273, 429] in order to explain LST failures. This research was motivated by the fact that the linearized Navier-Stokes (NS) operator applied to most wall-bounded shear flows is *nonnormal*. The objective was to develop numerical techniques able to capture *short-term* perturbation dynamics and understand their impact on the transition scenarios. It was shown that for a sufficiently large disturbance amplitude, *algebraic* nonmodal growth could lead to the so-called *bypass-transition*, not associated with exponential instabilities. A concomitant task was the prediction of the disturbance that grows the most in a short time scale (which is often very different from the least stable mode predicted by LST!). With these new advances, the researchers have redefined stability and transition in a broader sense, considering the response of the linearized NS system to general input variables such as initial conditions, external (deterministic or random) forcing or *internal* perturbations.

In particular, several scenarios consider the influence of small defects¹ on the onset of instability [254, 110], which defects may distort the mean flow in subcritical conditions. Using a variational technique, Bottaro *et al.* have shown that small *base flow* variations can displace the eigenvalues of a planar Couette flow towards the unstable region [43] and the work was extended to the spatial frame for Hagen-Poiseuille flow [143]. While the effects of deterministic disturbances have recently received much attention [22, 43, 36], we wish to broaden this approach by treating shear flow sensitivity and stability through the prism of an UQ *stochastic* framework [236]. If the nature of the disturbances is viewed as stochastic, two leads may be considered: - the response of the deterministic linearized operator subject to *external* stochastic excitations [125, 21, 225]; - the response of the deterministic LST operator perturbed by *internal* stochastic processes (e.g. incomplete knowledge of the mean state). For both cases, due to the non-normality of the dynamical system, the input stochastic excitation may possibly induce a transfer of background flow energy to the perturbation field, with a level of variance far exceeding that resulting from the energy accumulation from the forcing. In the second case, the problem may be seen as the determination of the stability of an *uncertain* operator. Farrell & Ioannou obtained dynamical equations of the mean and second moment quantities for systems with stochastic operator due to additive Gaussian noise modeled as a *temporal* Markov process with exponential covariance decay [124]. Schmid [429] examined the plane Poiseuille flow response of the optimal growth of a velocity profile subject to four localized random perturbations (with Gaussian peak magnitudes) and governed by a temporal stochastic process. However, the

1. Small defects are here larger than infinitesimal perturbations.

stochastic moments obtained from Monte-Carlo simulations, despite the variation in the energy growth and the strong favoring of streamwise elongated structures, showed that the flow did not become unstable.

A LST analysis of a Couette flow subject to an internal *random* perturbation is carried out via a stochastic spectral projection method. We consider the case of an *uncertain* base flow with *spatial* variability, i.e. the modifications of the mean flow are regarded as part of a spatial *random field*. Such stochastic base flow uncertainties may represent differences or *defects* between the flow in experimental conditions and its ideal numerical counterpart. The *zero-mean* random process modeling the spatial fluctuations is represented via a Karhunen-Loève expansion, cf. Section 2.1 of Chapter 1. The sensitivity of the system response, i.e. the *probability* associated with the occurrence of an instability, due to these uncertainties is quantified via a stochastic spectral projection method 3.2.1 based on a generalized Polynomial Chaos (gPC) representation 2.2. We focus mainly on the sensitivity of the eigenspectrum as well as the maximum possible amplification of the transient growth; those quantities being computed thanks to a linear stability solver relying on a Chebyshev spectral collocation method.

1.1 Linear stability of planar Couette flow with stochastic base flow

1.1.1 Deterministic formulation

Let us consider a parallel incompressible flow between two parallel plates with two homogeneous streamwise x - and spanwise z - and one inhomogeneous vertical y -direction (with $y \in \mathcal{D}_y = [-H, +H]$). An infinitesimal three-dimensional perturbation is added to the Navier-Stokes equations that are linearized around the base flow state $U \equiv U(y) = y$ created by the two walls moving at U_{wall} in opposite directions. A system of ordinary differential equations is obtained for the wall normal velocity \tilde{v} and vorticity $\tilde{\eta}$ amplitudes:

$$\begin{pmatrix} k^2 - D_y^2 & 0 \\ 0 & I \end{pmatrix} \frac{\partial}{\partial t} \begin{pmatrix} \tilde{v} \\ \tilde{\eta} \end{pmatrix} = \begin{pmatrix} \mathbf{L}_{OS} & 0 \\ i\beta U' & \mathbf{L}_{SQ} \end{pmatrix} \begin{pmatrix} \tilde{v} \\ \tilde{\eta} \end{pmatrix}, \quad (\text{II.1})$$

with boundary conditions $\tilde{v} = \tilde{v}_y = \tilde{\eta} = 0$ at the solid walls and $\mathbf{L}_{OS} = i\alpha U(k^2 - D_y^2) + i\alpha U'' + \frac{1}{Re}(k^2 - D_y^2)^2$. \mathbf{L}_{OS} and \mathbf{L}_{SQ} are the Orr-Sommerfeld (OS) and Squire (SQ) operators, D_y is the derivative in the y -direction and I is the identity matrix. Here, we adopt a temporal setting where the disturbances are bounded in space and exponentially decay or grow in time. Thus, normal velocity and vorticity are assumed to have wave-like forms in the homogeneous streamwise and spanwise directions with wavenumbers α and β , respectively (we note $k^2 = \alpha^2 + \beta^2$), and complex frequency $\omega_t = \omega_{t_r} + i\omega_{t_i}$ in time. We define the complex wave speed $c = \omega_t/\alpha$. The system of equations written in a matrix form (including the boundary conditions) comes down to an eigenvalue problem. Its structure shows that the SQ equation is driven by solutions to the OS equation unless $\beta = 0$. In this work, we will adopt a value of $\beta = 0$, which corresponds to the case of two-dimensional disturbances. This assumption is not restrictive as the use of Squire's transformation [430] allows to recover the three-dimensional case. Moreover, since the Squire modes are always damped [430], we only solve the OS eigenvalue problem to study the stability of the system. By solving for the eigenvalues and eigenfunctions of Eq. (II.1), one can determine the most unstable wavenumber and perturbation profiles that leads to an asymptotically unstable state at large t .

However, due to the non-orthogonality of the governing equations, transient growth can occur at small t even when the flow is linearly stable [400]. These transient growths can lead to bypass transition to turbulence through secondary instability mechanisms. In the non-modal analysis of the OS equations, the transient behaviour of the perturbation is an initial value problem where temporal evolution of \mathbf{q}_0 is governed by Eq. (II.1) or $\frac{\partial \mathbf{q}}{\partial t} = \mathbf{M}^{-1} \mathbf{L} \mathbf{q} = \mathbf{L}_1 \mathbf{q}$ where \mathbf{M} and \mathbf{L} are the matrices on the left and right hand sides of Eq. (II.1). The transient behaviour of a disturbance in the form of \mathbf{q} is quantified using an appropriate norm in the form of $G(t)$ where

$$G(t) = \max_{\mathbf{q}_0} \frac{\|\mathbf{q}(t)\|^2}{\|\mathbf{q}_0\|^2} = \max_{\mathbf{q}_0} \frac{\|\mathbf{q}_0 \exp(\mathbf{L}_1 t)\|^2}{\|\mathbf{q}_0\|^2} = \|\exp(\mathbf{L}_1 t)\|^2 \quad (\text{II.2})$$

for a given initial \mathbf{q}_0 . The time distribution of this function represents the maximum possible energy amplification.

1.1.2 Stochastic formulation

Recent works have focused on the non-normality of the underlying differential operator [400, 476]. In this case, applying an *external unstructured* random perturbation $\mathbf{E}(\omega)$ (of magnitude ϵ) to the Fourier transform of the wall normal velocity component of Eq. (II.1) may be written in the generic form:

$$[\mathbf{L}(U(y), \alpha, \beta) + \mathbf{E}(\omega)] \tilde{v} = i\omega_t \mathbf{M} \tilde{v}.$$

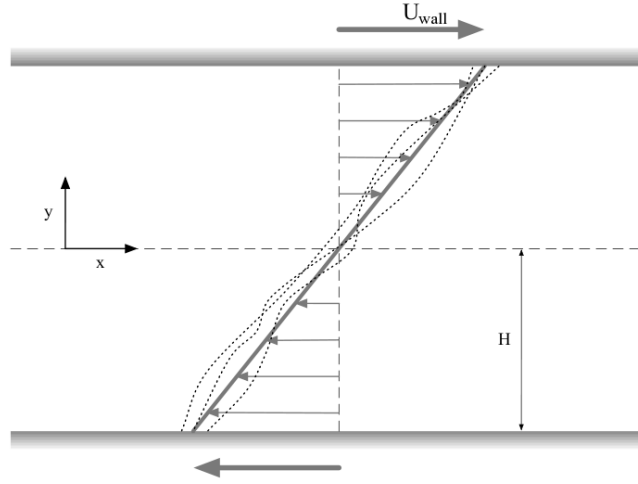


Figure II.1 – Sketch of the canonical Couette flow with examples of randomly perturbed base flow velocity profiles (dashed lines) compared to the ideal base flow *linear* profile (solid line).

The sensitivity of the eigensolutions is related to the condition number of \mathbf{L} and the magnitude ϵ [456]. For highly non-normal \mathbf{L} operators, such as the Couette OS operator, a value of $\epsilon \sim \mathcal{O}(10^{-6})$ is enough to introduce non-negligible variations in the eigensolution due to the large condition number of \mathbf{L} . The effect is especially significant for the eigenvalues located near the intersection of the branches [456]. However, the physical meanings of such external perturbation is unclear and may introduce artificial coupling between eigensolutions [429].

In contrast, an *internal structured* perturbation mimics some defects in the base flow by modifying the velocity profile $U(y)$. Here, we consider the case of an *uncertain* base flow with *spatial* variability, i.e. the modifications of the mean flow are regarded as part of a *spatial random field*. The velocity profile is replaced by a random field $U_S(y, \omega)$ where ω is the random event of a *probability space* $(\Omega, \mathcal{A}, \mathcal{P})$, i.e.

$$[\mathbf{L}(U_S(y, \omega), \alpha, \beta)] \tilde{v} = i\omega_t \mathbf{M} \tilde{v},$$

where

$$U_S(y, \omega) = U(y) + \tilde{U}(y, \omega), \quad (II.3)$$

and the small perturbation $\tilde{U}(y, \omega)$, which need not be infinitesimally small, is a *random field* characterized by a typical magnitude r and correlation length Cl controlling the amount of noise injected into the system. Such stochastic base flow uncertainties may represent differences or *defects* between the flow in experimental conditions and its ideal numerical counterpart. This is illustrated in Fig. II.1, some defects are juxtaposed to the ideal linear Couette base flow velocity profile². In this study, the random process modeling the spatial fluctuations will be represented through a Karhunen-Loève expansion.

In this work, we assume that $\tilde{U}(y, \omega)$ is a *second-order* random field (cf. Section 1.3), accurately discretized with a *finite* set of N independent RVs. We define $\Theta = \{\Theta_j(\omega)\}_{j=1}^N$, $N \in \mathbb{N}$, to be a \mathbb{R}^N -valued random array on a *probability space* $(\Omega, \mathcal{A}, \mathcal{P})$ with probability distribution $P_{\Theta}(d\theta)$ and we have the following approximation: $\tilde{U}(y, \omega) \approx \tilde{U}(y, \Theta)$.

In the following, we will be more specific about our choice of random process for the base flow defects within this stochastic framework.

1.1.3 Choice and representation of the base flow random process

In this work, we make the choice to model the structured random defect $\tilde{U}(y, \omega)$ as a stationary *colored* second-order *Gaussian* stochastic process of some characteristic spatial length scale. This approach models the experimental imperfection more realistically as the defects are unlikely to bear some optimal shape or local Gaussian peaks. The injection of noise in the system is done in a much more controlled and rigorous manner than other studies, where uncorrelated random perturbations are bluntly added at each mesh point, cf. [144]. As we do not want to favor *a priori* any specific spatial regions, we define the model with a mean value $\mathbb{E}\{\tilde{U}(y, \omega)\} = 0$ and a *constant std* $\sigma_{\tilde{U}}$ at all points across the channel. A continuous and bounded Gaussian covariance kernel with spatial correlation length Cl is chosen to characterize the correlation of the random process:

$$C(y_1, y_2) = \mathbb{E}\{\tilde{U}(y_1, \omega) \otimes \tilde{U}(y_2, \omega)\} = \sigma_{\tilde{U}}^2 \exp\left(-\left(\frac{y_1 - y_2}{2H \times Cl}\right)^2\right), \quad \forall (y_1, y_2) \in \mathcal{D}_y \times \mathcal{D}_y, \quad (II.4)$$

2. The amplitude of the base flow perturbations has been voluntarily exaggerated on the figure.

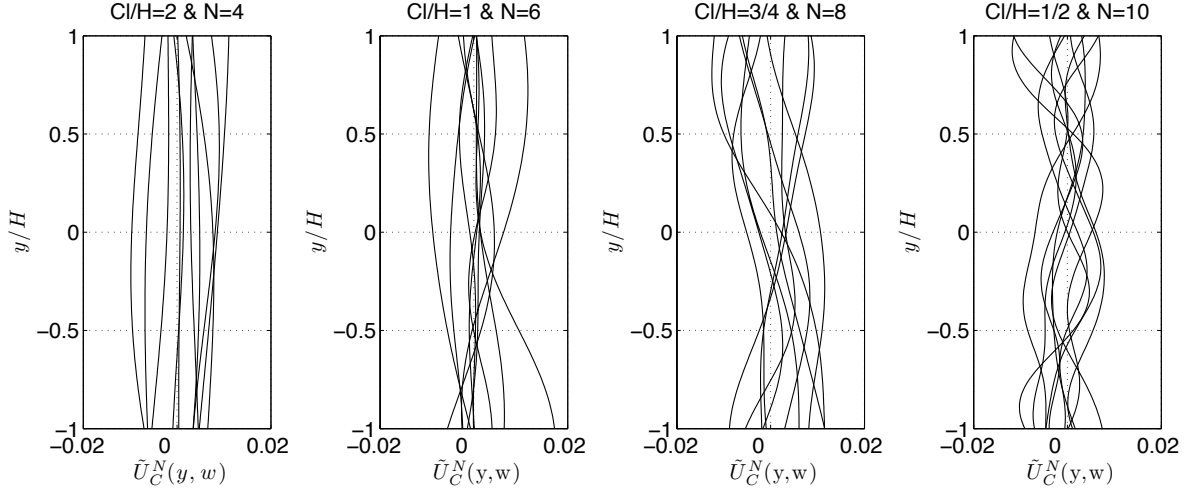


Figure 11.2 – Several realizations of the randomly perturbed profiles added to the Couette linear base flow for four different correlation lengths. Decreasing correlation lengths Cl relative to the half channel height H are from left to right. $\sigma_{\tilde{U}}/U_{\text{wall}} = 1\%$.

where H is the half-channel height. In this paper, we will focus on normalized correlation lengths in the range $2 \leq Cl/H \leq 1/2$. Gaussian kernels are known to bear nice regularity properties that insure reasonably fast convergence of their numerical representation [134]. We can now redefine our notations in order to express the link between the random process and its underlying covariance kernel:

$$U_S(y, \omega) = U(y) + \tilde{U}(y, \omega) = y + \tilde{U}_C(y, \omega) \quad (11.5)$$

The numerical tool used to represent the random process is a N -terms KL expansion, cf. Section 2.1 in Chapter 1:

$$\tilde{U}_C(y, \omega) \approx \tilde{U}_C^N(y, \Theta) = \sum_{i=1}^N \tilde{U}_i(y) \Theta_i(\omega). \quad (11.6)$$

The random array $\Theta = \{\Theta_j(\omega)\}_{j=1}^N$ is in this case a *Gaussian* vector with *uncorrelated* and consequently *independent* Gaussian random variables. Fig. 11.2 shows several realizations of the stochastic base flow defects for different Cl . As the Cl relative to the channel height decreases, the random fluctuations appear more noisy and the total number of inflection points, with relative maxima in vorticity, statistically increases. The location of those inflection points is random and located in regions that spread along the crossflow direction as the correlation length decreases. Such inflection points potentially render the flow unstable through an inviscid mechanism by Fjortoft’s criterion [430]. When Cl is small, a larger number N of random variables are needed to correctly capture the given statistics of the process.

The magnitude $\sigma_{\tilde{U}}$ is chosen based on a energy-like norm criteria r similar to the one introduced in [43]:

$$r = \left(\int_{\Gamma} \int_y (U_S(y, \omega) - U(y))^2 \rho_{\Theta}(\theta) dy d\theta \right)^{1/2} = \left(\int_{\Gamma} \int_y (\tilde{U}_C^N(y, \Theta))^2 \rho_{\Theta}(\theta) dy d\theta \right)^{1/2}, \quad (11.7)$$

with $\Gamma \in \mathbb{R}^N$, where $\Gamma \equiv \prod_{j=1}^N \Gamma_j$, and $\Gamma_j \equiv \theta_j(\Omega)$. In [43], they consider a distortion norm $r \sim \mathcal{O}(10^{-2})$, small but finite, which is similar to the typical scale introduced by the defect D/H (with D : wire radius) of [92, 22].

1.2 Numerical methods

A stochastic spectral projection method, cf. Section 3.2.1 in Chapter 1, is used to study the effect of stochastic base flow defects on the linear stability of Couette flows. This approach involves multi-dimensional numerical integration of the solution over the random domain. The deterministic linear stability solutions are obtained with a Chebyshev spectral collocation solver. Robustness and accuracy of the obtained statistical results should meet requirements as both deterministic and stochastic numerical methods used are fully spectral.

1.2.1 Stochastic discretization and resolution

The *truncated* Karhunen-Loève representation of the random input $\tilde{U}_C(y, \omega)$ writes:

$$\tilde{U}_C(y, \omega) \approx \tilde{U}_C^N(y, \Theta) = \mathbb{E}\{\tilde{U}_C(y, \Theta)\} + \sigma_{\tilde{U}} \sum_{i=1}^N \sqrt{\lambda_i} \varphi_i(y) \Theta_i(\omega). \quad (11.8)$$

Table II.1 – Logarithmic values of L^1 -norm errors of Gauss covariance kernels numerically reconstructed from KL expansions with N terms for different correlation lengths; $H = 1$.

	N=2	N=4	N=6	N=8	N=10
Cl/H=2	-4.416	-10.246	-15.926	-15.979	-15.976
Cl/H=1	-2.565	-5.998	-10.201	-14.942	-17.282
Cl/H=3/4	-2.027	-4.573	-7.797	-11.542	-14.987
Cl/H=1/2	-1.518	-3.111	-5.118	-7.548	-10.340

For our choice of kernel, Eq. (1.9) has to be solved numerically with the projection method outline in [14]. Using a numerical quadrature method, Eq. (1.9) is written as $\mathcal{P}_Z(\lambda - C)\varphi_Z = 0$ where \mathcal{P}_Z is a projection operator with Z collocation points. Representing an approximated solution with Lagrange interpolation polynomials and using numerical quadrature abscissae as the interpolants, \mathcal{P}_Z is determined from the $Z \times Z$ numerical integral matrix. Using estimates from [218], at least $Z = 2 + 2N$ collocation points are used to solve the eigensolutions up to the N -th KL expansion term.

In order to ensure that the stochastic process is well represented, the truncation error in the KL expansion needs to be estimated. Much work had been devoted in this area previously [196, 379, 284, 453]. In this study, the error is estimated by integrating the L^1 -norm error between the exact kernel and the numerical kernel truncated up to N KL terms. This gives an indication of the number of terms, i.e. number of random variables, required to remain within a certain accuracy. The error estimates with different Cl/H and N are listed in Table II.1.

The stochastic response of the eigenspectrum is quantified thanks to the stochastic spectral projection method introduced in great details in Section 3.2.1. The retained approximation space is span by multi-dimensional orthogonal Hermite polynomials. Several authors propose efficient formulations based on the PC expansion to treat the problem of representing random eigenvalues and eigenvectors [168, 159]. The sensitivity analysis is carried out by means of the analysis of the Sobol's coefficients [448], whose computation becomes trivial when the stochastic solution is decomposed onto its associated gPC basis [89, 41].

The gPC coefficients are evaluated through numerical cubatures, cf. Appendix B. For low random dimensions N , full tensor Gauss-Hermite quadratures may be used [232]. For higher dimensions, the exponential growth in quadrature costs may be alleviated by using the sparse Smolyak quadrature [446]. Smolyak type algorithms combined with nested grids are commonly used for bounded support, cf. Section 2.2.2. But, generic 1D nested quadrature rule does not exist for integrals with infinite supports. However, the Kronrod-Patterson (KP) rule turns out to be a very economical choice for Hermite polynomials when correctly adapted [149]. This is the type of cubature that is used in this study. We refer the reader to Section 2.1.3 for more details. Additional information maybe found in [232].

1.2.2 Deterministic Couette LST solver

The solver used to generate the population of stability characteristics for the various perturbed base flows rely on a spectral collocation method based on Chebyshev polynomials to solve the OS-SQ system (II.1). This method is highly accurate and easy to implement. We have used the solver outlined in [430, 475] that we have modified to fit our purpose. The one-dimensional eigenvalue problem to solve contains second- and fourth-order derivatives that are well approximated by the Chebyshev differentiation matrix. The stochastic streamwise base flow velocity profile, U_S , and its second derivative U_S'' complete the inputs and are computed via the KL expansion and the differentiation matrix, respectively. A convergence analysis (not presented here) has determined that $N_y = 100$ collocation points across the channel were enough to compute the first sixty eigenmodes with great accuracy [232]. The modal and non-modal solutions were also validated against several studies [430, 475, 43, 232]

1.3 Results

We present the modal analysis first and then the non-modal results. We are interested by correlation lengths in the range $Cl/H \sim 1$ and perturbation magnitudes close to $r \sim \mathcal{O}(10^{-2})$ [43]. Most of the physical as well as numerical parameters used in this study are listed in Table II.2. The half-channel height is $H = 1$ and $Re = 500$. Appropriate quadrature methods and levels were used to minimize the number of collocation points, N_q , while maintaining a constant polynomial accuracy (here, $P = 19$) for the gPC approximation.

Remark II.1

The Reynolds number $Re = 500$ considered in this study is in the linearly stable regime but above the Re

Table II.2 – Parameters, type of quadrature schemes and number of quadrature points Nq used for the each correlation length case.

Cl/H	N	Quadrature Scheme	Nq	$\sigma_{\tilde{U}}/U_{\text{wall}}$
2	4	Full Hermite	5 000	0.5%, 1%, 2%
1	6	Sparse Hermite-KP	17 679	0.5%, 1%, 2%
3/4	8	Sparse Hermite-KP	116 185	0.5%, 1%, 2%
1/2	10	Sparse Hermite-KP	603 323	0.5%, 1%, 2%

| where turbulence has been experimentally observed.

1.3.1 Modal Analysis

For each eigenspectrum realization obtained from the LST solver for a particular perturbation base flow profile, the first 15 eigenvalues with the largest imaginary parts are retained. From Fig. II.3, we can see that the eigenvalues shift about their corresponding deterministic counterpart but retain a branch structure. The eigenvalues from different realizations, shown as black dots around their corresponding red deterministic values, show significant variations in their location. Due to the use of symmetric quadrature grids, the distribution of the eigenvalue spectrum does not appear fully random. For instance, each eigenvalue has a symmetric eigenvalue (with same imaginary but opposite real part) that corresponds to the *centrosymmetric* variant of the perturbed base flow, see discussion in [22].

The variability of the eigenvalues position relative to the unstable region is then quantified by means of estimation of the variance and *pdf*. In the range of Cl/H and $\sigma_{\tilde{U}}$ investigated, all realizations remain linearly stable although some eigenvalues for small Cl/H are found very near the real axis (for $Cl/H = 1/2$ and $\sigma_{\tilde{U}} = 2\%$). Row-wise, the results show that the eigenvalues are *globally* affected by the change in $\sigma_{\tilde{U}}$. Column-wise, the plots show that changes in Cl/H have a more *local* but stronger influence. As expected from the literature, the eigenvalues located at the intersection of the branches are more sensitive. Large overlap between eigenvalue “clouds” can be observed at small Cl/H . Varying $\sigma_{\tilde{U}}$ does not alter the shape of the stochastic defect profiles but decreasing Cl/H increases the number of inflection points in the profile, leading to significant movements in the eigenvalues, especially in the direction of the imaginary axis and near the intersection of the branches.

When the variance of the eigenvalues is computed, spectral convergences are observed in its real and imaginary parts. The convergence is faster for eigenvalues away from the branch intersection. The normalized *std* values presented in Fig. II.4, respond linearly to $\sigma_{\tilde{U}}$ for large correlation lengths as the collapse of the normalized values shows. Again, we see that the eigenvalues located close to the branch intersection exhibit more variability. For low Cl/H , the response becomes non-linear for modes near the branch intersection, in particular for mode 5 and 7. Eigenvalue *pdf* results (not presented here) show that lowering the correlation length strongly skews the right tail of the *pdf* toward the positive imaginary region, i.e. the unstable domain, cf. [234].

In the following, the most sensitive LST normal velocity mode on the S-branch, i.e. mode 7, is examined in detail. The sensitivity of its eigenfunction, both its magnitude and its phase, is presented in Fig. II.5(a). We notice the high sensitivity of its amplitude in the central region of the flow for decreasing Cl/H . The *std* lobes points to two regions of large variability around the middle point of the domain. In this region, the phase is rapidly changing with a linear variation along the crossflow direction. The randomness of the base flow may shift by some amount the phase speed of the solution but does not affect its linear dependence. Moreover, the decrease of Cl/H has little effect on the phase speed. These characteristics indicate that long elongated streamwise flow structures still dominate despite the uncertainty.

Next, we try to identify the type of base flow perturbation that most affects the mode 7 response. The effect of each base flow perturbation modes (i.e. different terms in the KL expansion) to the solution variance is examined through Sobol’s coefficients [232]. The results (not presented here) confirm that, as the correlation length of the base flow decreases, higher modes contribute to the variability of mode 7 and therefore to the tendency of the flow to tend to instability. In particular, the results indicate that when $Cl/H < 1$, mode 7 becomes insensitive to the odd forcing modes but very sensitive to the even (centrosymmetric) forcing modes, and more specifically to the set $N^* = \{6, 8, 10\}$ of random modes. In this case, the analysis of base flow profiles bearing only those modes, cf. Fig. II.5(b), indicates that the typical perturbation wavelength of the random perturbation is approaching $\lambda_{\tilde{U}N^*}/H \sim 1/2$ as $Cl/H \rightarrow 1/2$. This result puts forward some connections with the results of Bottaro et al. [43] who predict that a centrosymmetric optimal mean flow modification of typical wavelength $\lambda/H \sim 1/2$ is required to push mode 7 toward the unstable region.

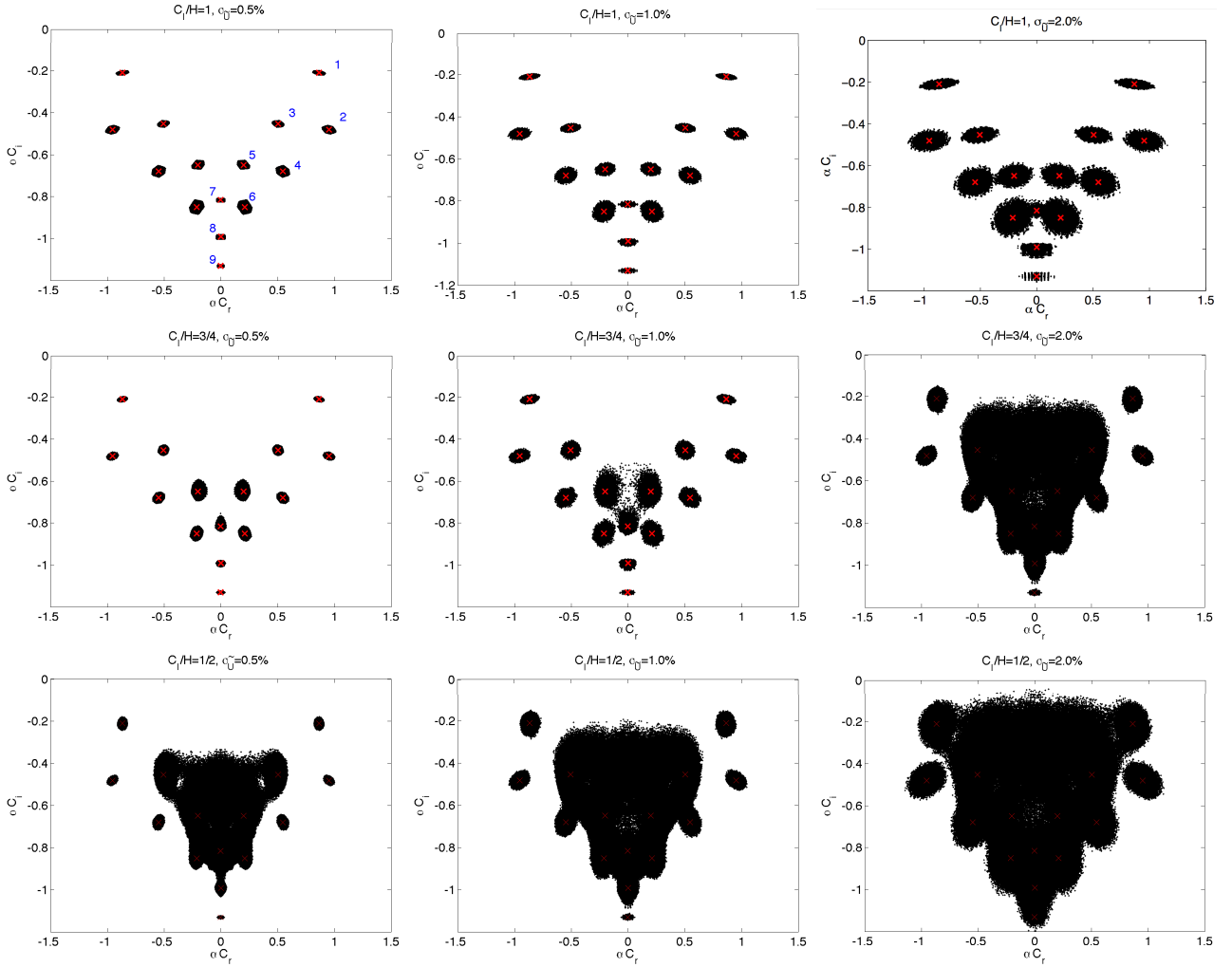


Figure II.3 – Eigenspectrum ensemble realizations for the ideal Couette flow (red crosses) and the Couette-like flow with base flow stochastic defects (black dots) for different Cl/H and $\sigma_{\bar{U}}$ values. Each set of (black dot) eigenvalues correspond to a randomly perturbed base flow determined by its KL realization computed for a set of quadrature points. Deterministic parameters: $H = 1$, $\alpha = 1.5$, $\beta = 0$, $Re = 500$.

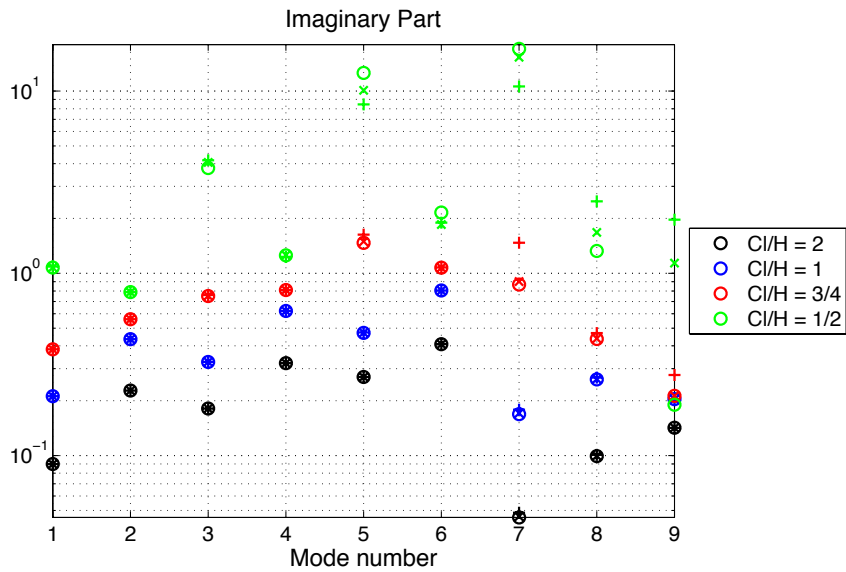


Figure II.4 – $\sigma_{\alpha C_i} / \sigma_{\bar{U}}$: normalized *std* of the OS eigenvalue imaginary parts for four different Cl/H values. The symbols \circ , \times and $+$ refer to $\sigma_{\bar{U}} / U_{\text{wall}} = 0.5\%$, 1% and 2% , respectively.

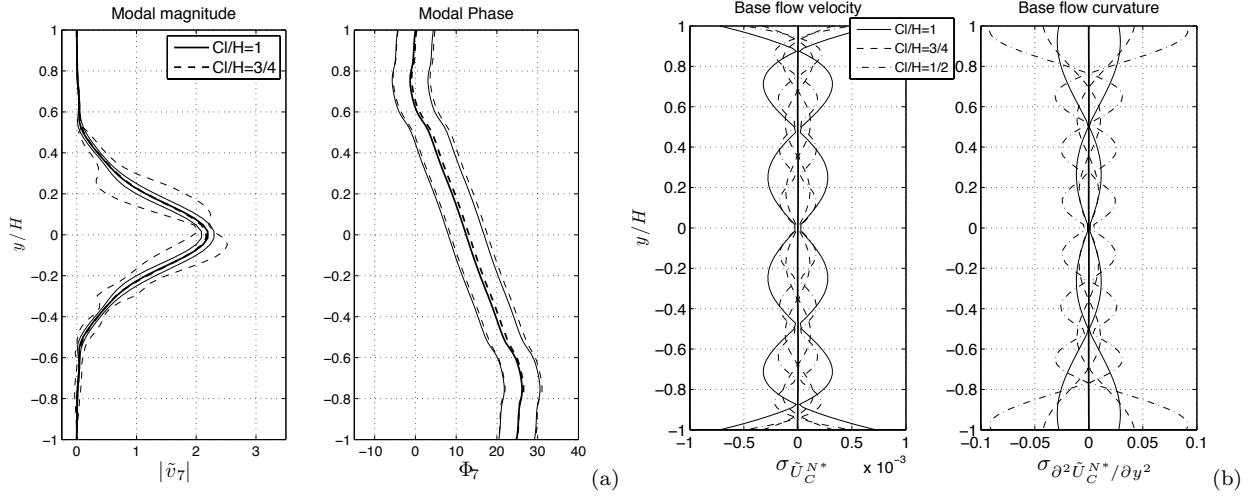


Figure 11.5 – Statistical distributions of mode 7 normal velocity (a) with magnitude (left) and phase (right) and corresponding base flow *dominant* statistics (b) with velocity (left) and curvature (right) profiles for different correlation lengths. Thin lines refer to $\text{mean} \pm 3 \times \text{std}$ (a) or $\text{mean} \pm \text{std}$ (b) envelopes; thick lines refer to mean values; $\sigma_{\tilde{U}}/U_{\text{wall}} = 2\%$.

Some LST preliminary results for $Cl/H \sim 1/3$ (with $\sigma_{\tilde{U}}/U_{\text{wall}} = 2\%$ and $N = 10$) clearly show that a few eigenvalue realizations – with low associated probability – did become unstable.

1.3.2 Non-modal Analysis

The transient growth examines the ensemble behaviour of the flow and the identification of the individual eigenvalues is not necessary. The non-modal analysis was carried out at the same Cl/H values as in the modal-analysis and at $\sigma_{\tilde{U}}/U_{\text{wall}}$ up to 20%. The response of the transient growth of the Couette flow is largely linear to the stochastic base flow defects. The temporal evolutions of the mean and variance of $G(t)$ remain unchanged unless $\sigma_{\tilde{U}}/U_{\text{wall}}$ exceeds large values (i.e. $\sigma_{\tilde{U}}/U_{\text{wall}} > 10\%$). Clearly this is beyond the order of magnitude of the perturbation energy that is of interest to this study.

The influence of the stochastic defects on the maximum Couette flow transient growths in the phase-space is quantified. Instead of a single deterministic isocontour, the classical results of $G_{\text{max}}(t)$ in the phase space from [430] can be better represented with error bars. Here, the mean contour is sandwiched by two contours denoting the standard deviation envelopes. Such a case was examined for $Cl/H = 1$ and $\sigma_{\tilde{U}}/U_{\text{wall}} = 2\%$. As the shapes of the variance envelopes indicate, the stochastic defects have different influence on the maximum growth rate at different streamwise and cross-stream wavenumbers. Near $\beta = 0$, the variance envelopes are narrow and appear to widen monotonically with increasing α and β . As the coupling between the OS and the Squire modes increase with increasing β and as the flow becomes more three-dimensional, the maximum transient growth exhibit stronger dependence on the stochastic defects. In addition, the effect of the stochastic defect is damped for some α - β combinations, as observed in the upper-left corner in Fig. 11.6.

1.4 Concluding remarks

Linear stability analysis of a Couette flow subject to an internal *random* perturbation – here added to the linearly sheared base flow – is carried out via a stochastic spectral projection based on the generalized Polynomial Chaos theory. This approach probabilistically quantifies the stability properties of the system in a stochastic context. The computation of the sensitivity functions does not rely on any linear dependence assumptions of the response to the random perturbation nor it is restricted to small perturbation variations. Such base flow defects may represent differences between experimental flow conditions and their ideal numerical counterparts. A Gaussian random field with a Gaussian covariance kernel of prescribed correlation length and variance is chosen to model the random fluctuations. The eigenmodes close to the branch intersection of the eigenspectrum are shown to be the most sensitive to the uncertainty. Large variability in the normal velocity disturbance is obtained for correlation length lower than half of the channel height. The symmetric modes in the defects mainly influence the phase speed in the streamwise direction, while centrosymmetric components influence the stability of the system. Despite, this variance in the solution, the modal analysis shows that the flow remains linear stable for the range of correlation lengths and perturbation magnitudes investigated. This result may be attributed to the smoothness of the chosen random (Gaussian) perturbation and a correlation length too large to access a critical base flow wavelength of $\lambda/H \sim 1/2$. Nevertheless, some preliminary results at $Cl/H \sim 1/3$

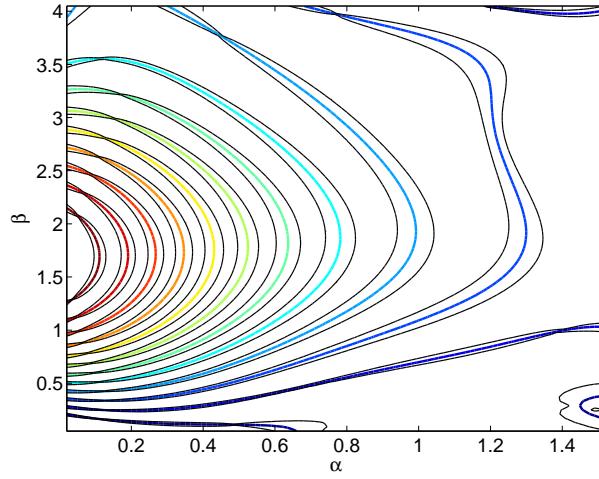


Figure II.6 – The maximum growth contour $G(t)_{\max}$ of the Couette flow subject to randomly perturbed based flow velocity profile with $Cl/H = 1/2$ and $\sigma_{\tilde{U}}/U_{\text{wall}} = 2\%$. The lines in color show the mean $G(t)_{\max}$ and the black lines outline the respective *std* envelope on each level. The successive lines from left to right have the magnitudes $G(t)_{\max} = 275, 250, \dots, 50, 25$

indicate that a few realizations, with low probability, did become unstable. From the non-modal analysis of the transient growth of the system, it seems that the stochastic defects with different correlation lengths and magnitudes have only a linear influence on the transient growth of the flow. However, the effects may be more significant for other combinations of spatial perturbation wavenumbers.

2 Sensitivity of mixing layer DNS to random inflow perturbation

Experimental studies of transport phenomena are often affected by uncertainties in the geometry, the boundary conditions and the fluid properties. However, these uncertainties are ignored in the definition of numerical simulations. Thus, the basis of comparison between simulations and experiments may be tenuous, especially when the experiments are sensitive to the uncertainties mentioned above. Without additional statistical information, the calibration of numerical models against experimental data may lead to erroneous conclusions. One classical case that is “hypersensitive” to experimental conditions is the plane mixing layer induced by the Kelvin-Helmholtz (KH) instability whose large coherent structures and vortex interactions are easily influenced by small changes in the inlet condition [361, 136].

Definition II.2

A plane mixing layer (ML) is formed where vortices grow and interact at the interface of two parallel co-flowing streams with different velocities, cf. Fig. II.7.

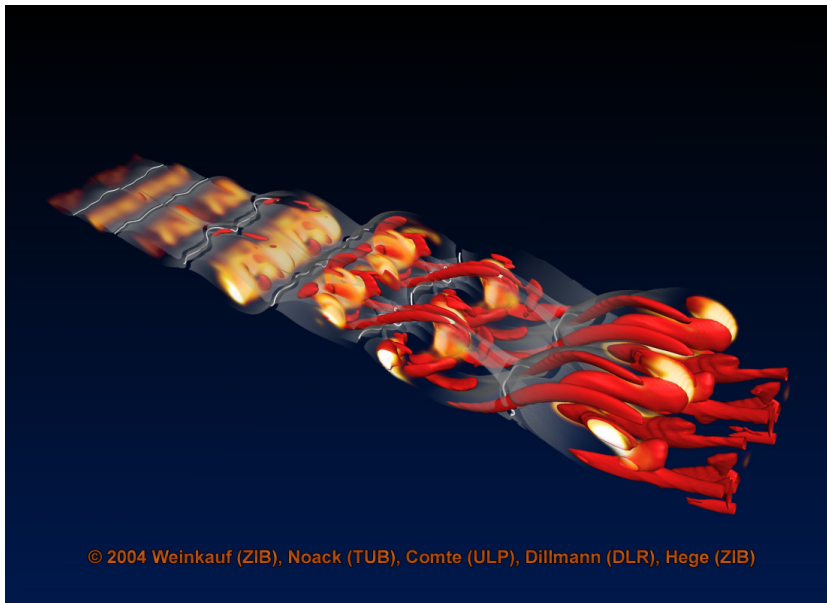


Figure II.7 – Snapshot of 3D mixing layer (at $Re_\theta = 100$) with spatial evolution of Kelvin-Helmholtz vortices, vortex pairing, and formation of spanwise rib vortices near saddle points. Courtesy of [472].

Spatially-developing plane MLs are first examined experimentally by Brown and Roshko [52] and Winant and Browand [510]. They observe vortical structures which exhibit two-dimensional (2D) behavior and amalgamate as they travel downstream, leading to the growth of the ML. In addition, spanwise vortex rollers form and are influenced by the streamwise distribution of the vortices [33, 318].

In the absence of external forcing at the inlet, the vortices form at random downstream positions at a dominant *fundamental* frequency and its associated *subharmonics*. Winant and Browand attribute the growth of the ML to the repeated pairing of the vortices and find the subharmonic mode to be essential in the vortex merging process [510]. When external forcing is imposed on the inflow, the growth of the ML is significantly increased [52]. In addition, the formation and merging of the coherent vortex structures become localized. The location of vortex merging coincides with the position of maximum streamwise energy with the subharmonic frequency, supporting the importance of subharmonic mode in ML growth [188].

Numerically, the forced ML has been extensively studied using both the temporal or the spatial approach [187]. However, it is shown that spatial simulations are preferred to resolve asymmetric entrainment and instability wave dispersion in the vortex interactions [509]. Moreover, in the real ML, the flow is influenced by events taking place downstream, in the form of low-frequency feedback which is better captured by the spatial approach.

Notably, the 2D numerical growth rate and the turbulent kinetic energy production of a ML forced with *discrete* perturbation modes are consistent with 3D experiments in which a broad band of perturbation frequencies is also present [271]. Thus, 2D numerical simulations are relevant in capturing the ML growth, particularly when discrete forcing is applied at the inflow.

Inflow forcing can be designed based on forcing magnitude, phase difference and forcing frequency. They often consist of a summation of temporally oscillatory disturbances added on top of the mean flow. Experimentally, the forcing can be created with active hydrodynamic [186], mechanical [521], or acoustic devices [189]. Some

of these parameters can be more easily controlled than the others. Despite the experimentalists' best effort to define the inflow forcing parameters *a priori*, the inherent uncertainties of the system do not allow them absolute control over the error associated with the imposed forcing.

The perturbation frequencies have a strong impact on the vortex interaction but can be manipulated experimentally with a high degree of accuracy. Using the linear stability theory (LST), Michalke determines the fundamental perturbation frequency of a ML with a hyperbolic tangent mean velocity profile [324, 325]. Subsequently, a sensitivity study shows that the ML has a maximum amplification rate near the fundamental perturbation frequency [334] and this is confirmed experimentally [186]. Similarly, the phase differences can also be readily controlled. The effect of various discrete phase differences on the behavior of ML vortex interactions is studied numerically with a temporal [366, 403] and spatial [87, 188, 83, 94, 424, 199, 200, 452] approach, and experimentally [188, 538]. The phase difference between two successive modes primarily affects the energy transfer between the modes. The phase lag leads to a shift in the vortex arrangement in the stream. The possible vortex interactions range from vortex merging, when the modes are in phase, to vortex shredding, when the phase difference is $\pi/2$ [403].

In contrast, not only is the perturbation amplitude difficult to control, its definition also varies from study to study. For hydrodynamic, mechanical and acoustic forcing devices mentioned previously, the perturbation magnitude is quantified using flow volume [186], flap vertical displacement [521] or acoustic intensity [189], respectively. The lack of a calibrated perturbation magnitude measure makes the comparison of different experiments difficult. Furthermore, there is no clear correlation between the final perturbation magnitudes and the forcing methods, which makes the definition of the perturbation in numerical models imprecise. The growth of the mixing layer forced with various finite perturbation amplitudes is studied experimentally [186, 539] and numerically [199, 200]. It is reported that a larger forcing magnitude causes the energy associated with the subharmonic frequency to grow faster along the streamwise direction, thus triggering the onset of vortex interaction further upstream towards the inlet. Nevertheless, we believe that the knowledge of the system response at a finite number of isolated points is not satisfactory. The choice of the magnitude of each forcing mode relative to the total perturbation seems to be often unmotivated [199, 96]. A more systematic approach that would consider entire parametric interval ranges is needed. Moreover, we seek an efficient representation that would account for the inherent uncertainties associated with the forcing parameters. In particular, we would like to associate a certain probability distribution to the random forcing parameter under consideration. Then, we would like to propagate it in real time through the system and be able to quantify its effect onto the ML response.

As in the case of forced MLs, there are many sources of uncertainty in fluid flows and the importance to address them in numerical simulations has been recently recognized and has received much attention, among others [195, 535, 281]. To produce the additional statistical information from deterministic numerical models, the Monte Carlo (MC) method can be used. For instance, the linear stability of a Poiseuille flow, with the mean velocity profile perturbed by the four localized Gaussian peaks having random magnitudes, is studied to examine the effect of flow fluctuations [429]. The stochastic mean and variance of the optimal energy growth is calculated from 100 MC simulations and the transient energy growth of the Poiseuille flow is shown to be stable despite the additional perturbations. However, the MC method is costly and inefficient for the sensitivity analysis of ML flow that we wish to pursue here. Alternatively, other more efficient approaches can be taken, especially when the uncertainty level present in the system is moderate. For instance, one can use the gPC method (cf. Section 2.2), which spectrally represents the solution response to system uncertainties. In many cases, it can provide the statistical information at a fraction of the cost of the MC method for a given accuracy. In addition, the solution sensitivity to individual parameter and the overall solution probability density function (PDF) can be ascertained as well.

This study will address the sensitivity of the ML to the uncertainties present in the magnitude of various disturbance modes imposed on the velocity profile at the inlet. We will use the gPC method that allows us to systematically quantify the solution dependence to the random inputs. In particular, the sensitivity of the time-averaged vorticity, vorticity thickness and momentum thickness will be examined. In Section 2.1, we will briefly introduce the spatially developing ML and we will specify the form of the random inflow perturbations. In Section 2.2, we will describe the numerical technique. In Section 2.3, we will discuss the results for the bi- and tri-modal perturbation cases. The applicability of the results to three-dimensional turbulent ML is speculated in Section 2.4 the conclusion in Section 2.5.

2.1 Spatially developing mixing layers with random inflow disturbances

Following the non-dimensional formulation by Monkewitz and Huerre [334], the time-averaged streamwise and cross-stream inlet velocity profiles of a 2D ML are defined respectively as

$$\bar{u}_{\text{in}}^t(y) = 1 + \lambda \tanh(y/2), \quad (\text{II.9})$$

$$\bar{v}_{\text{in}}^t(y) = 0, \quad (\text{II.10})$$

where $\lambda = \Delta U / 2\bar{U}$ is a measure of the magnitude of the velocity difference and y is the cross-stream coordinate. The mean velocity, \bar{U} , and the velocity difference, ΔU , are calculated from the upper and lower streams' velocities, which are U_H and U_L , respectively.

Downstream from the inlet, vortices form due to shear and the ML grows when vortex interaction takes place. The spatial growth of the ML can be quantified by the *vorticity thickness*,

$$\delta_\omega = \frac{\Delta U}{[\partial \bar{u}^t(y) / \partial y]_{\max}}, \quad (\text{II.11})$$

where $\bar{u}^t(y)$ is a time-averaged streamwise velocity profile [52], and the *momentum thickness*,

$$\theta = \frac{-1}{\Delta U^2} \int_{-\infty}^{\infty} (\bar{u}^t(y) - U_H) (\bar{u}^t(y) - U_L) dy. \quad (\text{II.12})$$

The velocity and distance are non-dimensionalized by \bar{U} and θ at the inlet, θ_{in} . In this study, the Reynolds number is defined as

$$Re_\theta = \frac{\bar{U} \theta_{\text{in}}}{\nu}, \quad (\text{II.13})$$

based on the momentum thickness at the inlet, or

$$Re_{\delta_\omega} = \frac{\bar{U} \delta_{\omega_{\text{in}}}}{\nu}, \quad (\text{II.14})$$

based on the vorticity thickness at the inlet. In our case, we have: $Re_{\delta_\omega} = 4Re_\theta$.

A characteristic property of the canonical incompressible ML is that the most unstable mode is expected to be two-dimensional. This, of course, does not imply that the whole transition process is two-dimensional [33]. The most amplified (i.e. *fundamental*) instability wave from linear stability theory (LST) is two-dimensional and can be determined theoretically for the hyperbolic tangent mean flow velocity profile [324, 325].

Numerical simulations of the ML dynamics allow for a sensitivity analysis of the response of the system. Once the computational simulation parameters (e.g. domain size, grid resolution, temporal resolution, ...) have been carefully chosen, sensitivity analysis of the ML to different inflow conditions can be investigated. As often seen in the literature, these forcing inflow conditions consist of perturbation velocity distributions based on LST [509]. In this case, the fundamental perturbation mode can be combined with its associated subharmonic modes to form the inflow forcing. The time-dependent forcing is superimposed on the mean inflow velocity to trigger the vortex formation [509]. The perturbation consists of the summation of *discrete* perturbation modes, each with oscillation frequency, ω_i . Phase difference between perturbation modes, γ_i , can also be defined. Nevertheless, the choice of the relative magnitude of each forcing mode relative to the total perturbation is often arbitrary [199, 96]. The idea here is to generalize this approach by considering *ranges* of forcing magnitudes defined as random quantities. In order to keep the problem well-posed, we choose to represent these uncertainties as independent, *uniformly* distributed, RVs with *bounded* supports.

The time-dependent inflow velocity profiles used in this study are

$$u_{\text{in}}(y, t) = \bar{u}_{\text{in}}^t(y) + \sum_{i=1}^N \epsilon_i [f(y) \sin(\omega_i t) + \gamma_i], \quad (\text{II.15})$$

$$v_{\text{in}}(y, t) = \bar{v}_{\text{in}}^t(y) + \sum_{i=1}^N \frac{\epsilon_i}{i} [g(y) \sin(\omega_i t) + \gamma_i], \quad (\text{II.16})$$

where N is the total number of perturbation modes and ϵ_i quantifies the magnitude of each forcing mode with respect to the total perturbation magnitude.

Remark II.3

| The parameter N , number of perturbation modes of the inflow, is also the number of random dimensions.

Remark II.4

| The perturbation velocity profiles $f(y)$ and $g(y)$ are expressed in a simple way as to mimic the profiles obtained from LST.

We have chosen $f(y) = \cos(n_i y) h(y)$ and $g(y) = \cos(n_i y / 2) h(y)$ which are defined as a product between simple cosine functions and a decaying function $h(y)$. The wavelength parameters n_i and the function h are tuned

according to the LST results [334]. The function h is proportional to the cross-stream derivative of the mean flow and limits the perturbations away from the y -axis. We have

$$h(y) = 1 - \tanh^2(y/2). \quad (\text{II.17})$$

The cross-stream velocity perturbation, Eq. (II.16), is only used for the validation case (cf. Section 2.2.3). Otherwise, the v -component of the forcing and the phase differences γ_i are simplified to be zero in this study.

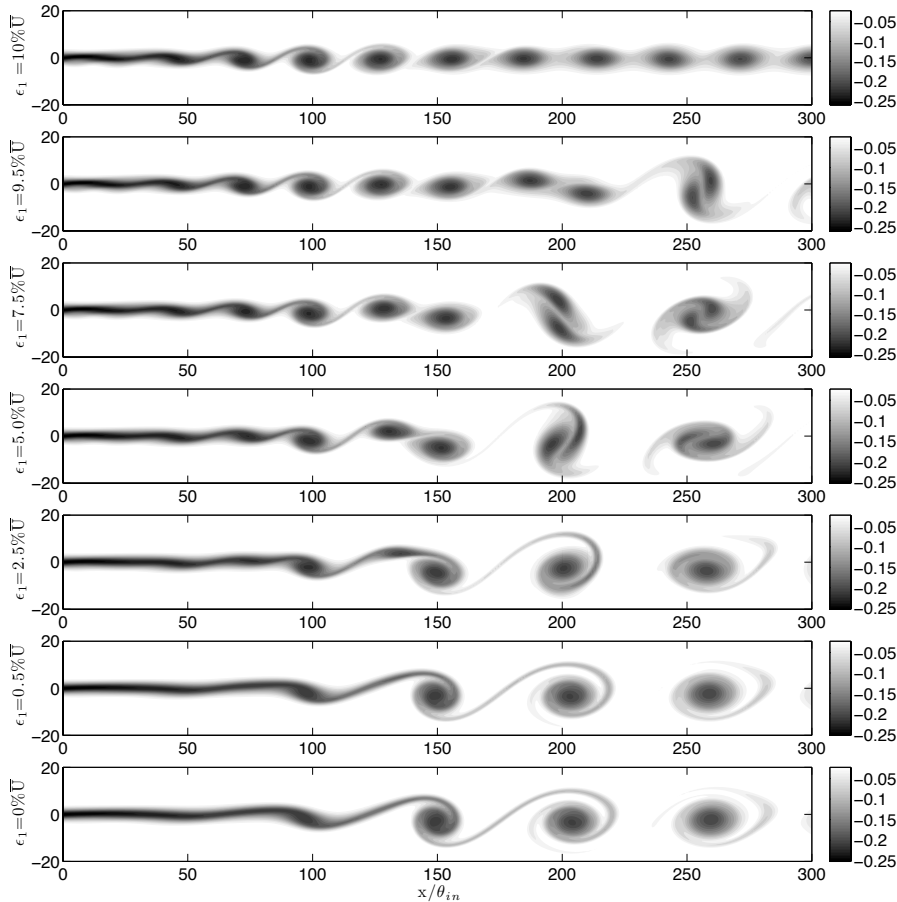


Figure II.8 – DNS instantaneous distributions of vorticity in the 2D mixing layer with bi-modal perturbation forcings. Effect of decreasing the magnitude of the fundamental forcing mode relative to the subharmonic mode.

The possible variation in the relative magnitudes of the perturbation modes has a non-trivial effect on the vortex interactions. Several Direct Numerical Simulations (DNS) bi-modal perturbation simulations are presented here to illustrate this influence (cf. Fig. II.10). Our DNS solver is introduced in more details in Appendix A. For reference, the sum of the fundamental and subharmonic magnitudes is such that $\epsilon_1 + \epsilon_2 = 10\% \bar{U}$. Here and in the remaining part of the study, the Reynolds number is taken to be $Re_\theta = 100$. This value is in the range of previous DNS [410] and LES [96] studies and it also. It facilitates direct comparison with the numerical work of Wilson and Demuren [509].

From Fig. II.10, we clearly notice the presence of large vorticity structures whose pairing process leads to the growth of the shear layer thickness. In the cases where $\epsilon_1 = 0$ or $\epsilon_1 = 10\% \bar{U}$, the vortex roll-ups are visible at regular intervals with the onset of roll-up occurring further downstream for the subharmonic mode (i.e. $\epsilon_1 = 0$). Vortex pairing occurs only when both modes are present. The shift of dominance in the vortex pattern from the fundamental to the subharmonic mode is clearly related to the change in the amplitude ratio. The interactions of the two perturbation modes cause a doubling of the vorticity thickness of the shear layer compared to the single fundamental forcing. Those results are in agreement with [539].

The downstream evolutions of time-averaged thickness measures, θ/θ_{in} and $\delta_\omega/\delta_{\omega,in}$, also vary quite significantly for different magnitude ratios (cf. Fig. II.9). Indeed, we expect the variation in the excitation intensities to alter the evolution of the coherent structures and their amalgamations. The growth of θ is comparable for all cases for $x/\theta_{in} \leq 75$. Downstream from this location, the different solutions look very different with the highest value of θ/θ_{in} reaching 3.5. Once again, the inhibition of the θ growth is observed except for the $\epsilon_1 = 10\% \bar{U}$ case.

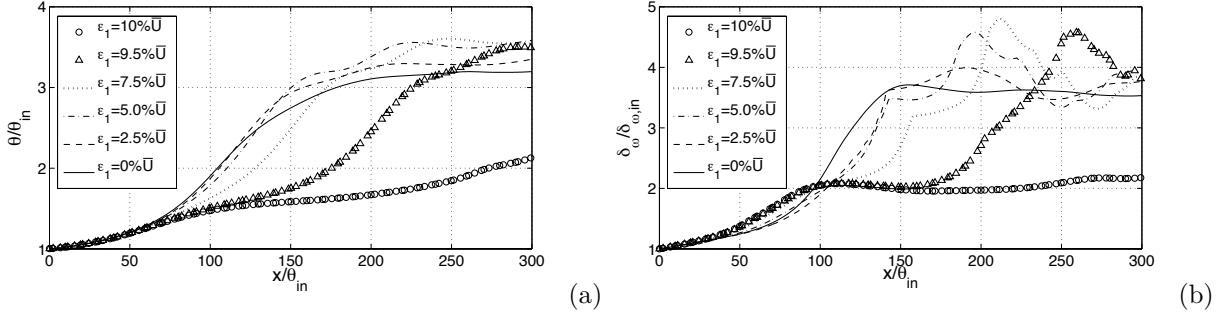


Figure II.9 – Momentum thickness (a) and vorticity thickness (b) distributions for different fundamental to subharmonic forcing modes combinations.

For $\delta_\omega/\delta_{\omega,in}$, the case with $\epsilon_1 = 10\%\bar{U}$ has the fastest growth between the inlet and $x/\theta_{in}=90$; further downstream, $\delta_\omega/\delta_{\omega,in}$ reaches a plateau of $\delta_\omega/\delta_{\omega,in}=2$. The growth when $\epsilon_1 = 0$ is smooth between the inlet and $x/\theta_{in}=150$ and reaches a plateau of $\delta_\omega/\delta_{\omega,in}=3.5$ after $x/\theta_{in}=150$. When combinations of the two perturbation modes are used, the extent of the strong growth is increased and the resulting $\delta_\omega/\delta_{\omega,in}$ profiles exceed the boundaries established by the two aforementioned extreme cases. More specifically, a sharp kink followed by a subsequent peak increase are observed in the $\delta_\omega/\delta_{\omega,in}$ profiles where the vortex pairing process occurs. The inhibition of the $\delta_\omega/\delta_{\omega,in}$ growth follows the second peak. The position of these features gradually move upstream as the magnitude of ϵ_1 decreases.

Upstream of the kink in the $\delta_\omega/\delta_{\omega,in}$ curves, the magnitudes of $\partial u/\partial y$ become different at the ML peripheries with the upper and lower streams. A sudden shift of the maximum magnitude of $\partial u/\partial y$ from the upper-stream side to the lower-stream side leads to the kink observed in the curve. The energy exchange among the coherent structures is evident. In particular, if the subharmonic perturbation mode has a substantial amplitude, it may extract energy from the fundamental mode through some resonance phenomenon [224]. This energy transfer seems to be briefer when the energy content of the fundamental mode is low. The new merged structure then dominates the rate of spread of the ML and exceed the limit of the forced solution with a single subharmonic mode. This explains the presence of the peaks in the curves.

Remark II.5

Although the total perturbation amplitudes are identical in all cases, significant differences are observed depending on the relative magnitude between the fundamental and the subharmonic perturbation modes. Thus sensitivity of pertinent physical measures, such as θ/θ_{in} and $\delta_\omega/\delta_{\omega,in}$, to randomness in perturbation magnitudes needs to be quantified.

In many studies, the different discrete perturbations are assumed to contribute equally to the total forcing and their magnitudes are therefore normalized such that $\epsilon_i \propto \bar{U}/N$. In the present study, ϵ_i are treated as independent and identically distributed (iid) RVs with finite support, i.e.

$$\epsilon_i = \mathbb{E}[\epsilon_i] + \sigma\xi_i, \quad (\text{II.18})$$

where $\xi = \{\xi_i\}_{i=1}^N$ are iid RVs with *uniform* distributions and σ^2 is the variance of the distribution. Here, it is the mean perturbation magnitude, $\mathbb{E}[\epsilon] = \mathbb{E}[\{\epsilon_i\}_{i=1}^N]$, that is proportional to \bar{U}/N .

In the following section, the numerical method used to obtain the stochastic solution and its statistical measures are presented.

2.2 Numerical Method

2.2.1 gPC-based stochastic surrogate model

The random magnitudes of the forcing perturbations are represented by a second-order RA: ξ (cf. Section 1.3) discretizing the probability space with a finite set of N *uniform* RVs: $\xi = \{\xi_j(\omega)\}_{j=1}^N$ with probability distribution $P(d\xi)$. We name the finite-dimensional space $(\Omega^{(N)}, \mathcal{B}^{(N)}, P_\xi)$ where $\Omega^{(N)} = \Omega_1 \times \dots \times \Omega_N \subset \mathbb{R}^N$, with $\Omega_j := \text{range}(\xi_j) = \xi_j(\Omega)$, $\mathcal{B}^{(N)}$ is the Borel σ -algebra of $\Omega^{(N)}$ and P_ξ is the probability distribution of the RA ξ .

A spectral projection approach (cf. details in Section 3.2.1) is retained to compute the stochastic modal response of the physical quantities of interest to the uncertainty. The approach consists in defining the stochastic approximation as a projection onto the L^2 space (defined in Eq. 1.4-1.5 with associated inner product and norm defined in Eq. 1.6-1.7) span by the $\{\Phi_\alpha\}_{\alpha \in \mathcal{J}}$ basis (e.g. Eq. 1.27), here chosen as multi-variate global Legendre polynomials over the supports.

Table II.3 – Geometry and mesh resolution for each deterministic DNS realization.

	Height	Length	Grid cells
bi-modal	$120 \theta_{in}$	$360 \theta_{in}$	24×36 quad. elements
tri-modal	$240 \theta_{in}$	$600 \theta_{in}$	48×60 quad. elements

Simple full Gauss-Legendre cubatures (here $N = \{2, 3\}$) are used to evaluate the integrals of Eq. (I.73) of Chapter I. The minimum number of quadrature points necessary to integrate exactly a polynomial function (of order P^3) along each random dimension is used as the lower bound for the integration, see Appendix B.

The gPC modal coefficients of the primary flow quantities (i.e. velocities and pressure) can be readily calculated. The gPC modal coefficients of the derived flow quantities (i.e. vorticity, vorticity thickness and momentum thicknesses) require more careful handling. For instance, expressing the momentum thickness, defined in Eq. (II.12), with an expanded stochastic flow velocity field $u(\mathbf{x}; \boldsymbol{\xi})$, one obtains

$$\theta(x, \boldsymbol{\xi}) \approx \frac{-1}{\Delta U^2} \int_{-H}^H \left[\left(\sum_{i=0}^M u_i(\mathbf{x}) \phi_i(\boldsymbol{\xi}) - U_H \right) \left(\sum_{i=0}^M u_i(\mathbf{x}) \phi_i(\boldsymbol{\xi}) - U_L \right) \right] dy \quad (\text{II.19})$$

The arithmetic operation with U_H and U_L only affects the constant term in the u expansion (i.e. u_0) and the modal coefficient, θ_m , can be determined by taking the Galerkin projecting on both sides of Eq. (II.19). This gives $(M + 1)$ equations for the modal coefficient of θ which requires the integral evaluation in the cross-stream direction, which is performed using a Gauss-Lobatto/Jacobi numerical quadrature.

A sensitivity analysis of the system can also be carried out by identifying which parameters and corresponding scales are the most influential onto the solution. This is achieved by calculating the Sobol' sensitivity index, cf. Section 4.

Concerning the computation of the PDF of the response, several approaches are conceivable. One simple way to proceed is to generate a large population sample since the gPC expansion involves only algebraic evaluations with little computational cost. An histogram of these data can then be built. A variant that produces smoother distributions is the kernel-smoothing density estimate [500] which is used in this study.

2.2.2 Direct Numerical Simulations

The 2D incompressible Navier-Stokes equations are solved using a DNS solver, *NekTar* [218], cf. Appendix A. This package utilizes hierarchical spectral/ hp expansions on hybrid subdomains. In the current study, quadrilateral elements are used over the entire flow domain and are populated with Jacobi polynomial nodes corresponding to high order 2D mixed weights. The order of the polynomials, P_J , can be spatially adjusted to provide spectral refinement but a constant $P_J = 12$ in each mesh cell is found to be sufficient for all cases.

A Dirichlet time-dependent velocity boundary condition with periodic perturbations is used at the inlet. The streamwise velocity profile is defined by Eq. (II.15). For the validation case treated below, Eq. (II.16) is used for the cross-stream velocity profile. The entire flow domain is initialized with the hyperbolic tangent mean flow without perturbations. Neumann boundary condition is used on the three remaining boundaries. A reasonable grid aspect ratio is used due to the cross-stream growth of the ML in the streamwise direction, following recommendation of Wilson and Demuren [509]. The domain sizes and the mesh resolution are listed in Table II.3. The mesh parameters provide a sufficiently fine mesh resolution for a uniform grid [509, 96]. The Navier-Stokes equations are non-dimensionalized with \bar{U} and θ_{in} . The relevant model parameters are listed in Table II.4. The mean and variance chosen for the ϵ_i are such that the range of variability of each magnitude is in the $[0, 10\% \bar{U}]$ interval. This range of perturbation magnitude will be used in this study unless stated otherwise. The wavenumbers n_i are chosen to best match the LST profiles. That explains why the cross-stream scale is not doubled when the streamwise scale doubles for each subharmonic. The corresponding non-dimensional wavelengths are 5, 6.667 and 10 respectively, when normalized with θ_{in} . From Eq. (II.17), one can see that the effects of the perturbation are reduced by 10%, 1% and 0.1% at cross-stream positions of 2.94, 5.29 and 7.60 θ_{in} . All γ_i in Eq. (II.15) are defined to be zero in this study. Each simulation is run for at least twelve periods of the lowest perturbation mode and flow statistics are collected over the last four periods of the run. This is enough for the time-averaged flow quantities to converge and the transient effects due to the initial conditions to be convected out. The accuracy of the DNS solver and the gPC method are validated in the next section.

3. P is the chosen maximum order of the stochastic polynomial approximation space.

Table II.4 – Numerical parameters used for the bi-modal and tri-modal inflow perturbations. The wavelength, ω_3 , and wave number, n_3 , is only used for the tri-modal perturbation case.

Re_θ	Re_{δ_ω}	λ	$\mathbb{E}[\epsilon_i]$	σ_i	ω_1	ω_2	ω_3	n_1	n_2	n_3
100	400	0.5	$5\% \bar{U}$	$5\% \bar{U}$	0.22	0.11	0.073	0.4π	0.3π	0.2π

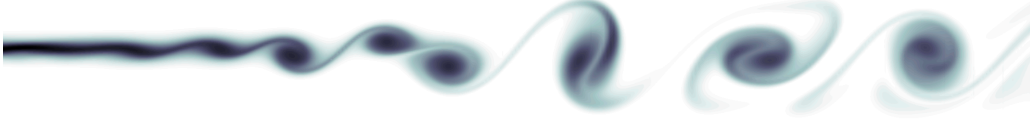


Figure II.10 – Instantaneous planar mixing layer vorticity with bi-modal perturbation forcing computed with spectral elements DNS solver.

2.2.3 Validation and Convergence Study

The continuous stochastic representation involves the computation of multiple deterministic (DNS) fields for a set of parameters. In addition to the deterministic solver, several numerical techniques are used in this study. The gPC method is used to spectrally expand the stochastic solution in the random space and numerical quadratures are used to approximate the multi-dimensional integrals involved in the calculations of the gPC coefficients. The validity of the DNS simulations will be established first, then the quadrature approximation and the gPC method will be validated.

DNS solver

The validation of the DNS solver is performed against the 2D DNS results from Wilson and Demuren [509]. Different mesh refinements and P_J values were tested for the bi- and tri-modal perturbation cases and the final configuration is listed in Table II.3. The deterministic inflow parameters for the bi-modal case are listed in Table II.5. The DNS solver captures well the vortical structure and the momentum thickness growth of the ML when compared to the results in [509] (cf. Fig. II.11.).

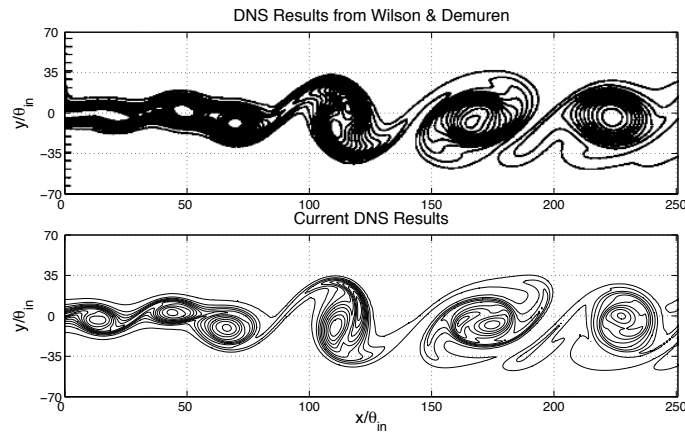


Figure II.11 – Comparison of ML instantaneous vorticity contours (bi-modal forcing case). Top: DNS from Wilson and Demurer [509]; Bottom: current DNS result.

Table II.5 – Validation case: inflow parameters from the Wilson and Demuren study [509].

Re_θ	λ	$\epsilon_{1,2}$	ω_1	ω_2
100	0.538	$2.12\% \bar{U}$	0.22	0.11

It is worth mentioning, that since we did not use the exact LST perturbation modes, as in [509], a spatial delay in the downstream onset of the vortex formation is observed. A delay with a similar order of magnitude is also observed for a case where the LST was not used [96]. In Fig. II.11, the spatial onset of the mixing growth from our DNS has been horizontally aligned to facilitate the comparison. We conclude that despite the lack of exact LST modes, our solver accurately captures the dynamics of the evenly spaced vortical structures connected by braids as seen in [509].

gPC convergence

The quadrature method is validated by examining the convergence of the statistical mean of the gPC solution for different quadrature levels, cf. [232]. Quadrature levels of 9 and 10 (ie. 81 and 1000 quadrature points) were found to be sufficient for $N=2$ and $N=3$ respectively. In the gPC expansion, the spectral convergence was also achieved in the L^2 -norm of the truncation error versus increasing polynomial order P for both $N=2$ and $N=3$. We normalize this error as follows:

$$\frac{|E_T(U)|_2}{|\text{var}(U)|_2} = \sqrt{\frac{\int_{\Omega_P} (\sum_{m=M+1}^{\infty} U_m^2(\mathbf{x}) \phi_m^2(\mathbf{Y}))^2 d\mathbf{x}}{\int_{\Omega_P} (\text{var}(U))^2 d\mathbf{x}}}. \quad (\text{II.20})$$

Here, as no exact solution exists for the variance, the variance computed with our highest quadrature level available is used as the reference solution (cf. Fig. II.12). For $N=2$ case, the reference solution is evaluated with 81 quadrature points while 216 quadrature points are used for the $N=3$ case.

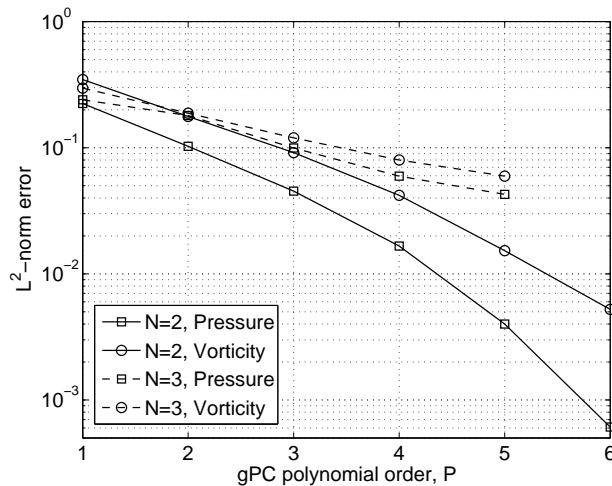


Figure II.12 – Convergence in the L^2 -norm error of the gPC variances of the time-averaged pressure and vorticity for $N=2$ and $N=3$ with increasing gPC polynomial order.

The gPC representation can also predict the solution for some arbitrary point within the support. The accuracy of the prediction can then be compared *a posteriori* to the reference DNS solution evaluated with the same inflow conditions. The following magnitudes $\epsilon/\bar{U}=[7.89\%, 2.11\%]$ and $\epsilon/\bar{U}=[8.55\%, 5\%, 5\%]$ are chosen for the bi-modal and the tri-modal cases, respectively. For the bi-modal perturbation case, excellent agreements are observed in the time-averaged cross-stream vorticity profiles between the prediction and the DNS solution (cf. Fig. II.13(b)). For the tri-modal perturbation case, predicted and DNS vorticity contours show again good agreement as P increases (cf. Fig. II.13(a)). As non-linear interactions develop downstream from the inlet, the prediction of the solution becomes less accurate and a slight disagreement appears in the vorticity profiles (cf. Fig. II.13(c)). Overall, the agreement between the gPC prediction and the DNS solution is still very satisfactory.

2.3 Results

In this section, the results of the forced plane ML subject to bi- and tri-modal random perturbations are presented and discussed. The geometry and the mesh resolution are listed in Table II.3 and the perturbation parameters are listed in Table II.4. The stochastic collocation procedure for the bi-modal case employed a quadrature level $l=9$ (i.e. $N_q=81$ points) and a gPC expansion with $P=7$. The tri-modal results required a level $l=10$ (i.e. $N_q=1000$ points) and $P=8$.

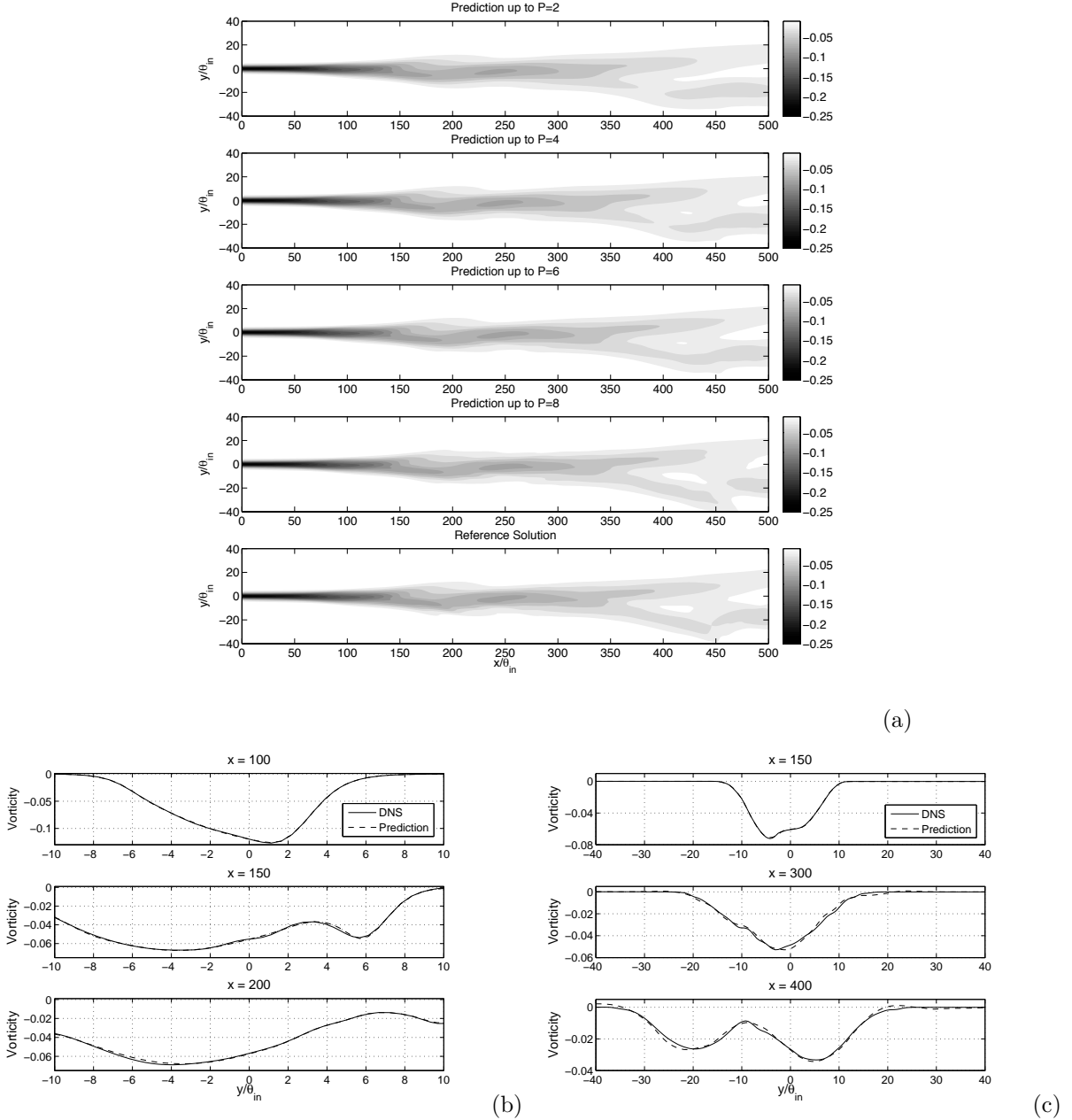


Figure II.13 – (a) Predicted time-averaged vorticity contours for increasing (from top to bottom) levels of resolution P for the tri-modal perturbation case. The last plot is the *reference* deterministic DNS solution. Predictions of time-averaged cross-stream vorticity profiles at different downstream locations are compared against the reference DNS solution for (b) $N=2$ and (c) $N=3$.

2.3.1 Response variability

MLs forced by a few discrete modes usually grow in a stepwise fashion. The layer thickness eventually reaches a plateau as the forcing modes saturate. Changes in the strength of the initial disturbances affects the timing of these saturations and consequently the location where the layer enlargements take place. Previous studies have shown that the perturbation magnitude has a strong influence on the onset of vortex merging [188, 199, 200] but has little effect on the flow near the inlet [361]. A similar interpretation can be made from the analysis of the mean vorticity solution and its variance. For instance, looking at Fig. II.14, one can see that the mean contour remains nearly unchanged from the inlet up to $x/\theta_{in}=50$, i.e. the location of the onset of the shear layer roll-up of the fundamental perturbation mode. The vorticity contour gradually spreads out in the transverse direction as the flow proceeds downstream. The contour ceases to change after $x/\theta_{in}=250$ as most of the vortex interactions are completed. Furthermore, the vorticity variance is large away from the inlet, in the region where vortex pairing is most likely to occur. Since the perturbation magnitudes primarily affect the locations of roll-up and pairing, the variance is concentrated along the x -axis. Then, the dispersive effect of

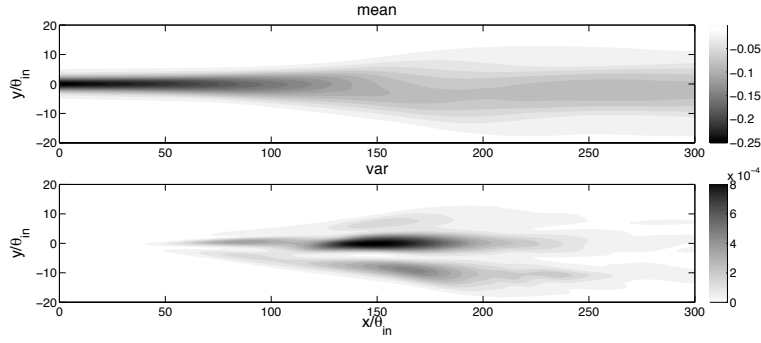


Figure II.14 – Spatial distributions of the mean solution and variance of the time-averaged vorticity in the ML with bi-modal perturbation forcing.

the ML leads to a fan-shaped contour. The vorticity response is sensitive to the variation in the perturbation magnitude with a maximum variance reached around $x/\theta_{in}=150$. This corresponds to a coefficient of variation $c_v = 0.41$.

The mean solutions and standard deviation envelopes of $\delta_\omega/\delta_{\omega,in}$ and θ/θ_{in} are plotted in Fig. II.15. We recall that the standard deviation envelope consists in adding and subtracting one standard deviation unit from the mean value. It spans a 68% confidence interval for a normally distributed population. In our case, it is a rough estimation of the response variability. For more accurate estimations, we refer the reader to the PDF results of section 2.3.3. The mean value of $\delta_\omega/\delta_{\omega,in}$ grows regularly from 1.0 at the inlet to 4.0 around $x/\theta_{in}=200$ and the growth somewhat stagnates after this point (cf. Fig. II.15(a)). The bulge in the width of the standard deviation envelope, particularly near $x/\theta_{in}=140$ and $x/\theta_{in}=180$, shows that there exists a localized region of large variability. The mean momentum thickness grows steadily from 1.0 at the inlet to 3.5 after $x/\theta_{in}=200$ (cf.

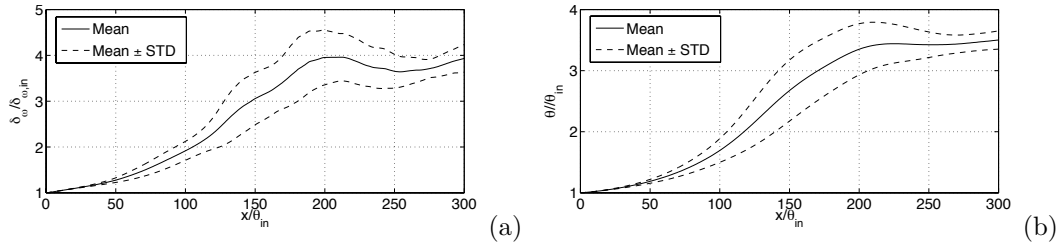


Figure II.15 – Streamwise distributions of the mean solution and standard deviation envelope of (a) $\delta_\omega/\delta_{\omega,in}$ and (b) θ/θ_{in} for the ML with bi-modal perturbation forcing.

Fig. II.15(b)). After this location, the growth stagnates. The θ/θ_{in} variance is significant between $x/\theta_{in}=90$, near the fundamental shear layer roll-up, and $x/\theta_{in}=250$, near the end of the subharmonic pairing, with a peak around $x/\theta_{in}=150$.

We note that while mean values of $\delta_\omega/\delta_{\omega,in}$ and θ/θ_{in} could be quite meaningless in some cases (e.g. stochastic bifurcation between two different states), the determination of the regions where the response variability is large is crucial to the problem. We believe that these regions coincide with streamwise locations where strong physical vortex interactions take place, i.e. vortex pairing (cf. Fig. II.9).

A large variability in the response of the ML subject to the tri-modal forcing is also observed. Two distinct

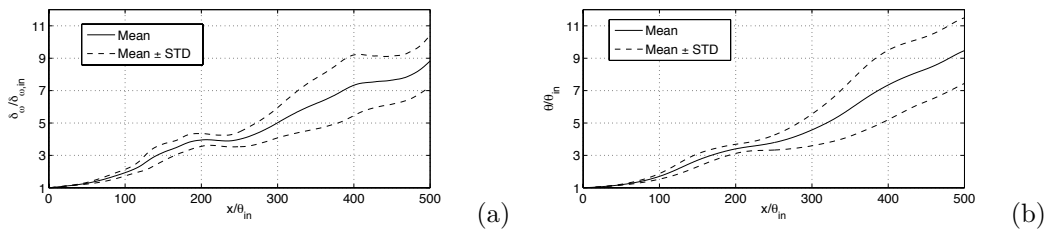


Figure II.16 – Streamwise distributions of the mean solution and standard deviation envelope of (a) $\delta_\omega/\delta_{\omega,in}$ and (b) θ/θ_{in} for the mixing layer with tri-modal perturbation forcing.

stages are observed for the moment distributions $\delta_\omega/\delta_{\omega,in}$ (cf. Fig. II.16(a)). Similar to the bi-modal case,

the growth reaches $\delta_\omega/\delta_{\omega,\text{in}}=4.0$ at $x/\theta_{\text{in}}=200$ after the first vortex pairing sequence. The second plateau at $\delta_\omega/\delta_{\omega,\text{in}}=7.5$ is reached after the second vortex pairing sequence. The variance keeps growing along the stream-wise direction. In the two zones where the vortex pairings are likely to occur, larger variance magnitudes are observed in the variance profiles with local peaks at $x/\theta_{\text{in}}=140$ and $x/\theta_{\text{in}}=390$. The profiles of $\theta/\theta_{\text{in}}$ are shown in Fig. II.16(b). The distribution is similar to that of the bi-modal case, where a value of $\theta/\theta_{\text{in}}=3.5$ is reached near $x/\theta_{\text{in}}=200$. Due to the presence of the second subharmonic mode, the growth continues after $x/\theta_{\text{in}}=250$.

Spatial distributions of the variability of the layer thickness show that the ML is more sensitive during the vortex pairing phases. This is because different combinations of perturbation magnitudes affect the location and extent of the vortex pairings. A more detailed analysis of the solution sensitivity to each forcing mode magnitude is needed. In particular, the question of the predominance of one of the forcing modes over the others has to be addressed. This is the topic of the next section.

2.3.2 Sensitivity analysis

From the spatial distribution of the vorticity sensitivity indices (or partial variances, cf. Eqs. (??)-(??)), we can apprehend the solution sensitivity to each perturbation mode and to their interactions. For the bi-modal case, the total variance is decomposed into three parts, D_1 , D_2 and D_{12} , namely the contributions from ϵ_1 , ϵ_2 and their coupled interaction to the total variance. Here, the contours, normalized against the maximum total variance, are plotted in Fig. II.17 and reveal the localized effect of the individual random input. Large values of D_1 are located around the shear layer roll-up position of the fundamental perturbation mode whereas large values of D_2 are located around that of the subhamornic mode (cf. Fig. II.10). Furthermore, the contour magnitudes clearly indicate that the ML is more sensitive to the variation in the subharmonic mode amplitude. Indeed, the maximum absolute value of D_2 is more than double that of D_1 . The complex contours of D_{12} take place in an intermediate zone between D_1 and D_2 and its magnitude is much smaller.

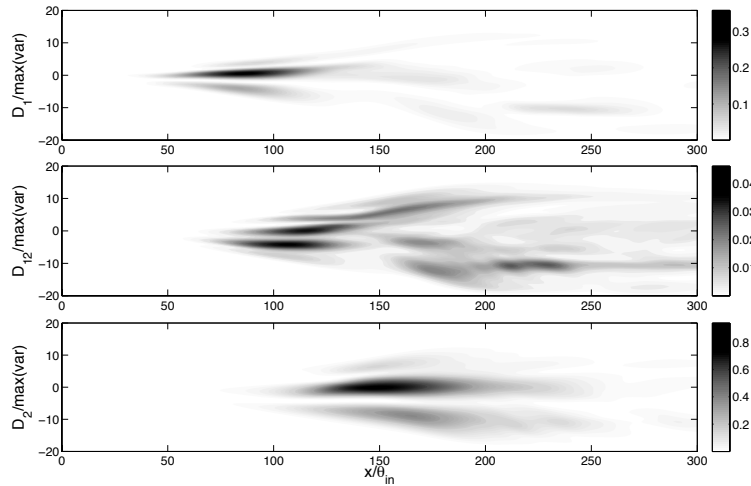


Figure II.17 – Spatial distributions of the sensitivity indices (partial variances) of the time-averaged vorticity in the ML with bi-modal perturbation forcing.

The $\delta_\omega/\delta_{\omega,\text{in}}$ and $\theta/\theta_{\text{in}}$ response surfaces for the bi-modal case are summarized in Fig. II.18 and are constructed at several locations ($x/\theta_{\text{in}}=140$, $x/\theta_{\text{in}}=175$ and $x/\theta_{\text{in}}=240$) but the entire sequence was visualized with computer animations. Near the inlet and up to $x/\theta_{\text{in}}=90$, the responses in both $\theta/\theta_{\text{in}}$ and $\delta_\omega/\delta_{\omega,\text{in}}$ are nearly linear to increasing perturbation magnitudes. The maximum response is obtained for large ϵ_1 and ϵ_2 and the response surfaces show that the solution is not very sensitive to the input uncertainties.

As $\delta_\omega/\delta_{\omega,\text{in}}$ and $\theta/\theta_{\text{in}}$ reach values comparable to the fundamental perturbation length scale, the solution becomes more sensitive to the subharmonic mode than the fundamental mode. Furthermore, due to the kink in the $\delta_\omega/\delta_{\omega,\text{in}}$ curves observed in Fig. II.9(b), the $\delta_\omega/\delta_{\omega,\text{in}}$ growth experiences a brief inhibition, clearly seen in the depression in the upper corner of the response surface at $x/\theta_{\text{in}}=140$ (cf. Fig. II.18(a)). This depression propagates through the response surface at further downstream locations as the low perturbation magnitude cases experience the kink. The $\delta_\omega/\delta_{\omega,\text{in}}$ surface has two flat regions near $\delta_\omega/\delta_{\omega,\text{in}}=2.0$ and $\delta_\omega/\delta_{\omega,\text{in}}=3.5$ and they reflect the two thickness scales that have a high probability of occurrence. After the brief inhibition, the growth of $\delta_\omega/\delta_{\omega,\text{in}}$ resumes until $x/\theta_{\text{in}}=175$. In comparison, the growth of $\theta/\theta_{\text{in}}$ continues until $x/\theta_{\text{in}}=195$. At $x/\theta_{\text{in}}=175$, the larger probable $\delta_\omega/\delta_{\omega,\text{in}}$ thickness scale overcomes the smaller one. Indeed, we observe that flat regions in the $\delta_\omega/\delta_{\omega,\text{in}}$ response surface shifts from $\delta_\omega/\delta_{\omega,\text{in}}=2.0$ to $\delta_\omega/\delta_{\omega,\text{in}}=3.5$ at downstream regions of

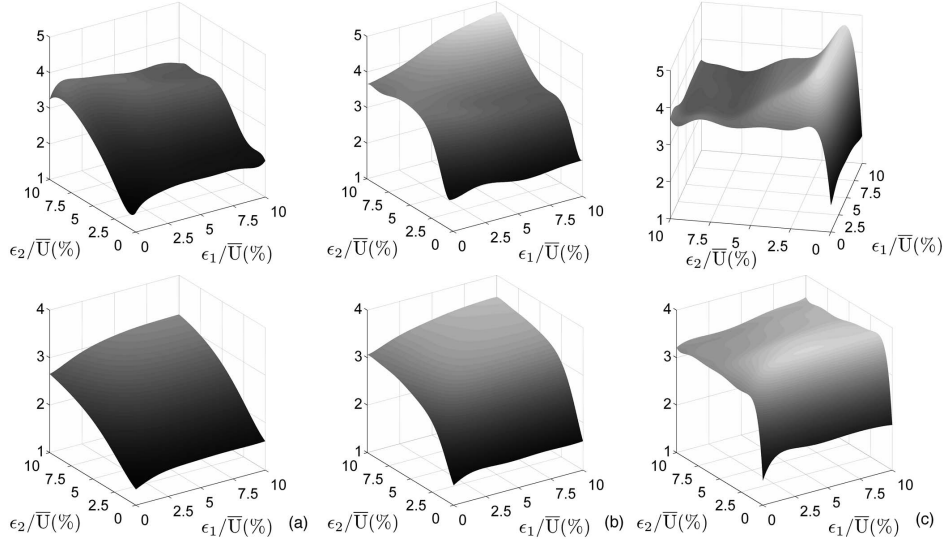


Figure II.18 – Response surfaces of the vorticity thickness $\delta_\omega/\delta_{\omega,\text{in}}$ (top row) and momentum thickness $\theta/\theta_{\text{in}}$ (bottom row) vs. the disturbances strengths, ϵ_1 and ϵ_2 , for the bi-modal perturbation case: (a) $x/\theta_{\text{in}}=140$, (b) $x/\theta_{\text{in}}=175$ and (c) $x/\theta_{\text{in}}=240$.

$x/\theta_{\text{in}}=175$ and $x/\theta_{\text{in}}=240$. Similarly, the state of $\theta/\theta_{\text{in}}=3.5$ also becomes dominant, as seen in the flat region in the $\delta_\omega/\delta_{\omega,\text{in}}$ response surface at $x/\theta_{\text{in}}=240$.

For the tri-modal case, the sensitivity of the solution to the individual perturbation modes is assessed by the study of the sensitivity indices and response surfaces (not presented here) of the time-averaged vorticity and related quantities. A striking feature is the fact that the sensitive regions corresponding to each random disturbances are located in very distinct places in space. Similar to the bi-modal perturbation case, the partial variances D_1 , D_2 and D_3 reach their maximum magnitudes near the shear layer roll-up positions of the respective perturbation modes (cf. Fig. II.19).

The strong influence of the uncertainty in the first subharmonic forcing magnitude is again observed with D_2 values twice as large as those of D_1 and D_3 . The dark contours show the spatial spread of the sensitive regions. In particular, the spread is larger for D_3 than D_2 , and the D_2 spread is in turn larger than of D_1 . The partial variance D_{12} is an indicator of the coupled interaction between the fundamental and the first subharmonic forcing modes. This interaction consists mainly of the extraction of energy from vortical structures with the fundamental length scale to those with the first subharmonic length scale. Indeed the peak of D_{12} occurs in the region between the shear layer roll-up positions associated with the fundamental and the subharmonic modes. It is interesting to notice that the distribution of D_{12} is very similar for the bi-modal perturbation case (cf. Fig. II.17). The energy transfer between vortical structures related to the first and the second subharmonic forcings is quantified by the D_{23} coefficient. The peak of D_{23} occurs in the region between the shear layer roll-up positions associated with the first and the second subharmonic modes. The magnitude of D_{23} is larger than that of D_{12} . In contrast, the interaction between the fundamental and the second subharmonic, i.e. D_{13} , and the interaction amongst all three modes, i.e. D_{123} , are small. This indicates that the energy exchanges between *successive* modes are more significant. These results are consistent with the *resonance* phenomenon described by Kelly [224] who studied analytically the possible interactions of the perturbation modes. Kelly showed that the energy transfer from the fundamental mode is more significant to its first subharmonic than to any other frequencies [224]. This was also observed experimentally [505].

The results show, for both the bi-modal and tri-modal cases, that if the presence of the fundamental mode is crucial to trigger the ML instability, the variability of its amplitude is not influential. This is especially true close to the inlet. The response is much more sensitive to the first subharmonic forcing amplitude, i.e. ϵ_2 . For the tri-modal case, the second subharmonic forcing amplitude becomes very influential in the second half of the computational domain. In this region, the layer thickness grows fast and reaches large values under the influence of ϵ_3 . Moreover, the response is even more sensitive for small values of ϵ_2 combined to ϵ_3 but saturates when the ϵ_2 magnitude becomes too large.

Where non-linear interactions take place, the energy re-distribution affects multiple modes and the effects of the couplings can be seen in the distribution of the second-order sensitivity indices. In conclusion, since the effect of each perturbation mode is localized at different downstream regions, the growth of the ML can be better manipulated by focusing our attention on perturbation modes that are relevant to the downstream

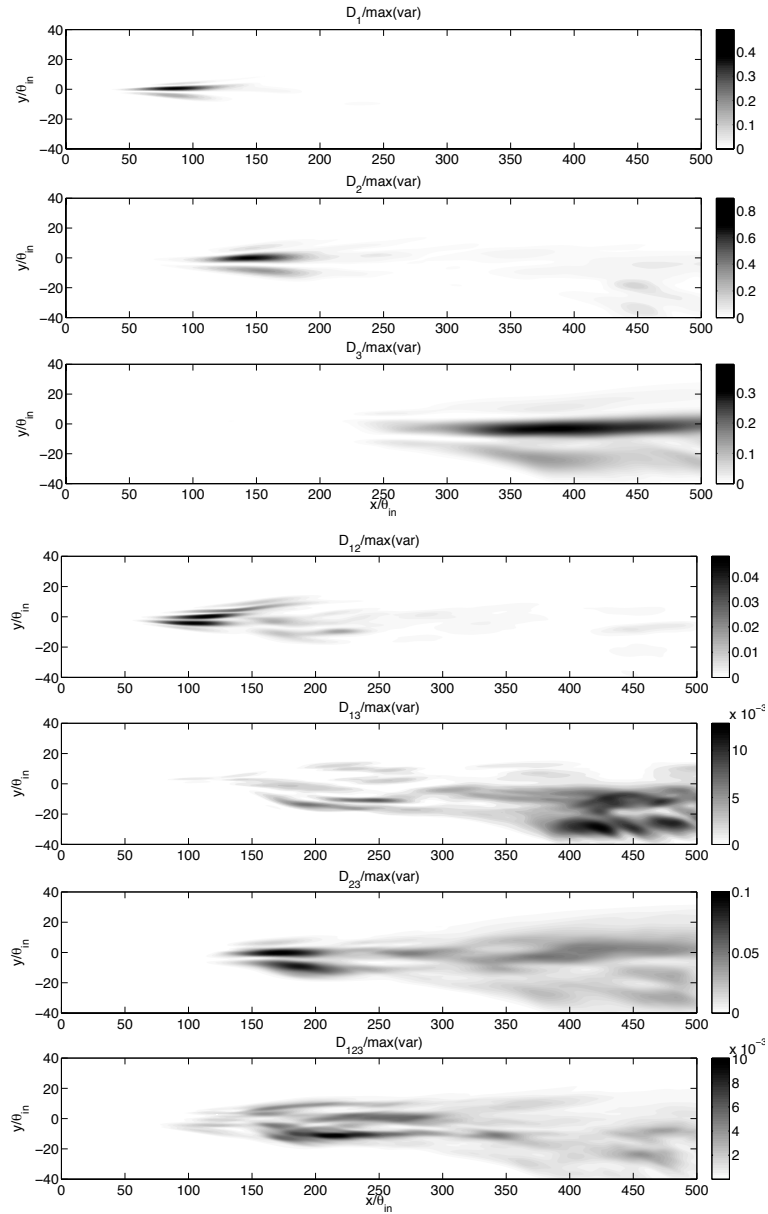


Figure II.19 – Spatial distributions of the sensitivity indices (partial variances) of the time-averaged vorticity in the ML with tri-modal perturbation forcing.

region of interest.

2.3.3 Most probable solution

The PDF of $\delta_\omega/\delta_{\omega,in}$ and θ/θ_{in} are evaluated along the streamwise direction. The density distributions provide very useful information as they give a quantitative estimate of the variability of the response and its bias, and show the path of the most probable solutions.

We use the kernel-smoothing density estimate with a Gaussian kernel and an optimal bandwidth [500]. A sufficient number of samples (4 million for the bi-modal case and 40 million for the tri-modal case) is chosen to obtain accurate distributions. The results are shown in Figs. II.20-II.21 for the bi-modal case and Figs. II.22-II.23 for the tri-modal case. Continuous contours as well as profiles extracted at some specific locations are presented. The contours are normalized at each streamwise location such that the maximum probability density is always unity. This is done because we are more interested in the variability range and locations of the most probable solutions than the exact probability density associated with them.

The first observation is that the ML thicknesses do not bear *uniform* distributions, as seen from the extracted profiles. This disparity with the random inputs distribution confirms that the system response is non-linear. Although the downstream evolution of the $\delta_\omega/\delta_{\omega,in}$ PDF contour is not as smooth and regularly distributed as that of θ/θ_{in} , the interpretation of the results is very similar. Despite a large variability of the support of

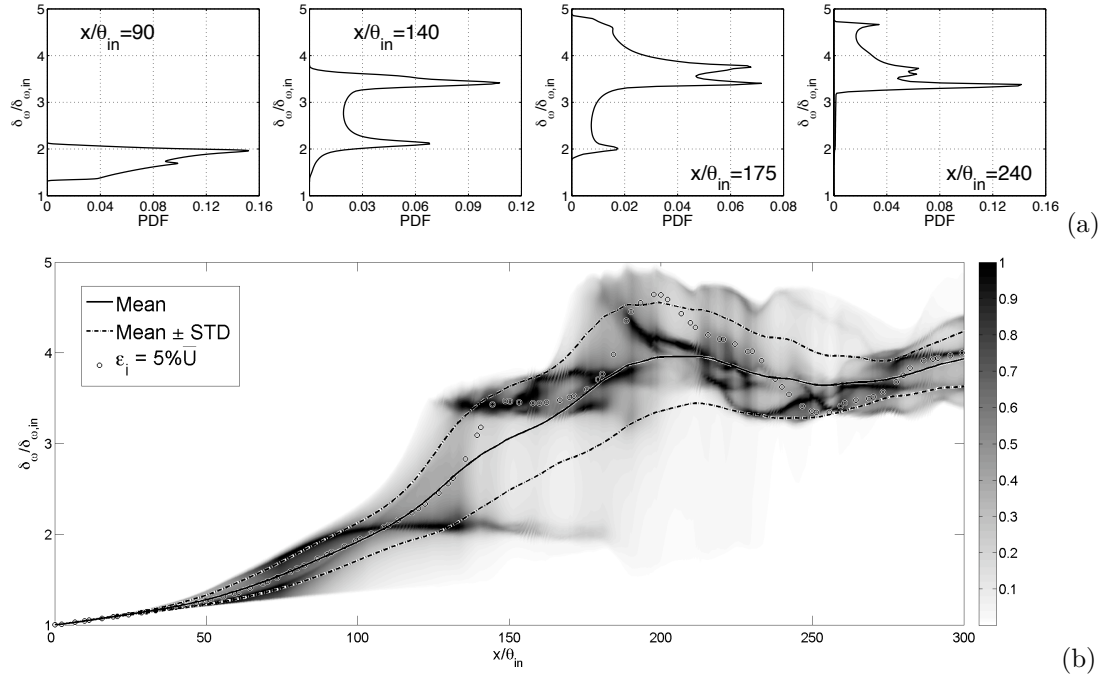


Figure II.20 – PDF of the ML vorticity thickness $\delta_\omega/\delta_{\omega,in}$ for the bi-modal perturbation case. (a) PDF profiles at four downstream locations. (b) Spatial distribution of the normalized PDF contours. Mean and variance, and deterministic solution for the input mean value, are included for comparison.

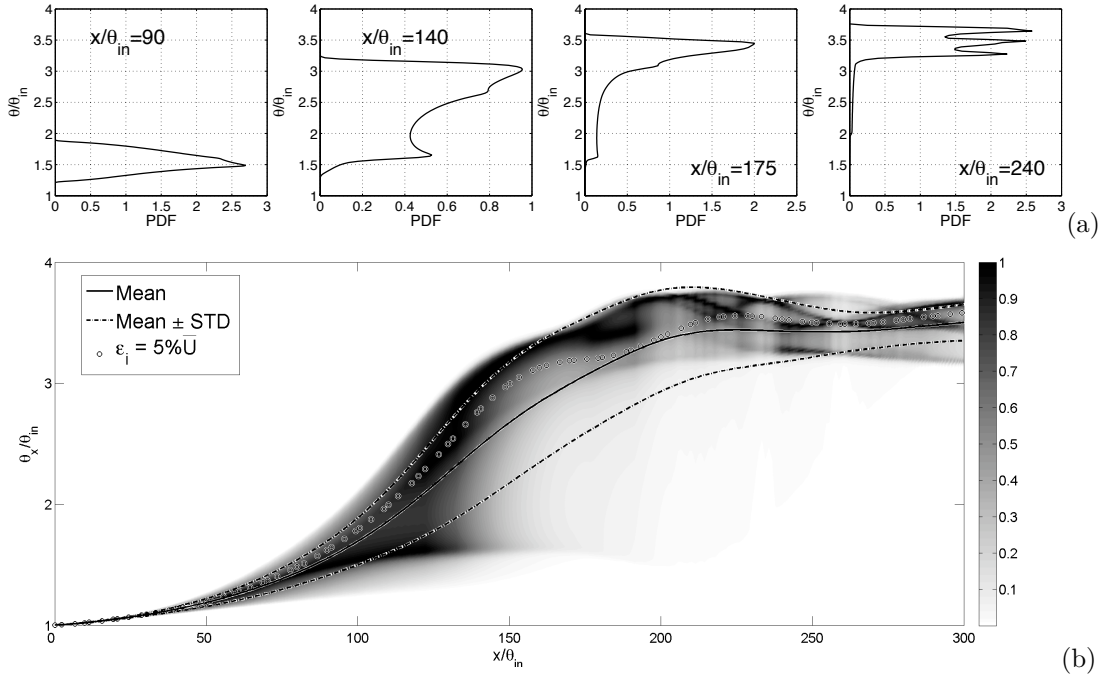


Figure II.21 – PDF of the ML momentum thickness θ/θ_{in} for the bi-modal perturbation case. See Fig. II.20 for detailed caption.

the PDFs along the streamwise direction, we notice the appearance of regions with higher probability densities (darker shades in the contour plots). These regions correspond to peaks in the local PDF profiles and indicate the emergence of distinct probable solutions. Moreover, it appears that these regions of high probability of occurrence are organized in a series of distinct stages presenting rapid changes along the spatial direction. As expected, this feature is more striking in the distribution of $\delta_\omega/\delta_{\omega,in}$ (a cross-flow local quantity) than the distribution of θ/θ_{in} (a cross-flow integral quantity).

The extracted profiles of $\delta_\omega/\delta_{\omega,in}$, for the bi-modal case, show that upstream and up to $x/\theta_{in}=90$ (i.e. the location of the fundamental shear layer roll-up) sharp peaks develop and their magnitudes grow until they reach the typical thickness associated with the fundamental forcing mode alone (cf. Fig. II.9). Therefore, near

the inlet, the most probable ML growth is dictated by the fundamental forcing mode. In this case, the mean solution is closed to the most probable solution and the uncertainty in the disturbances has little effect. Further downstream, we notice the emergence of an additional peak (cf. profiles at $x/\theta_{in}=140$). For instance, two probable solutions for $\delta_\omega/\delta_{\omega,in}$ are visible at $\delta_\omega/\delta_{\omega,in}=2.1$ and $\delta_\omega/\delta_{\omega,in}=3.4$. For the momentum thickness, the second peak is wider and looks more like a narrow-band response. We believe that these second peaks are locked into or around the typical mixing scale imposed by the subharmonic forcing mode (cf. Fig. II.9). Therefore, there exists a competition between these two distinct scales. This duality is at its maximum around a streamwise location that coincide with the onset of the vortex pairing. The mean solution becomes in this case quite meaningless. In the next phase (cf. profiles at $x/\theta_{in}=175$), the solution corresponding to the fundamental forcing dies out as the magnitude of the second peak increases. This transition is fast and the most probable values of the ML thicknesses quickly switch to the larger scale. In fact, the coherent structure associated with the subharmonic forcing extracts energy from the fundamental mode through some resonance phenomenon. The gain in energy further increases the value of the most probable thickness. The variability of the response remains bounded after $x/\theta_{in}=200$. Meanwhile, the complex non-linear interaction between the different flow structures in addition to the randomness effect influence the probability of occurrence of the phenomena. As a consequence, the distribution becomes more chaotic with the presence of new and smaller scales interacting with the large scale imposed by the subharmonic forcing (cf. profiles at $x/\theta_{in}=240$). These complex interactions and intricate redistributions of the probability of occurrence of the layer thickness subsist downstream of the vortex pairing region. Moreover, due to the non-linearity of the system, we notice that the mean solution is very different from the deterministic solution obtained for the mean value of the random inputs. This is true for almost the entire spatial domain for θ/θ_{in} and downstream of $x/\theta_{in}=140$ for $\delta_\omega/\delta_{\omega,in}$.

For the tri-modal case, we observe similar mechanisms with most probable solutions growing in a stepwise fashion (cf. Figs. II.22-II.23).

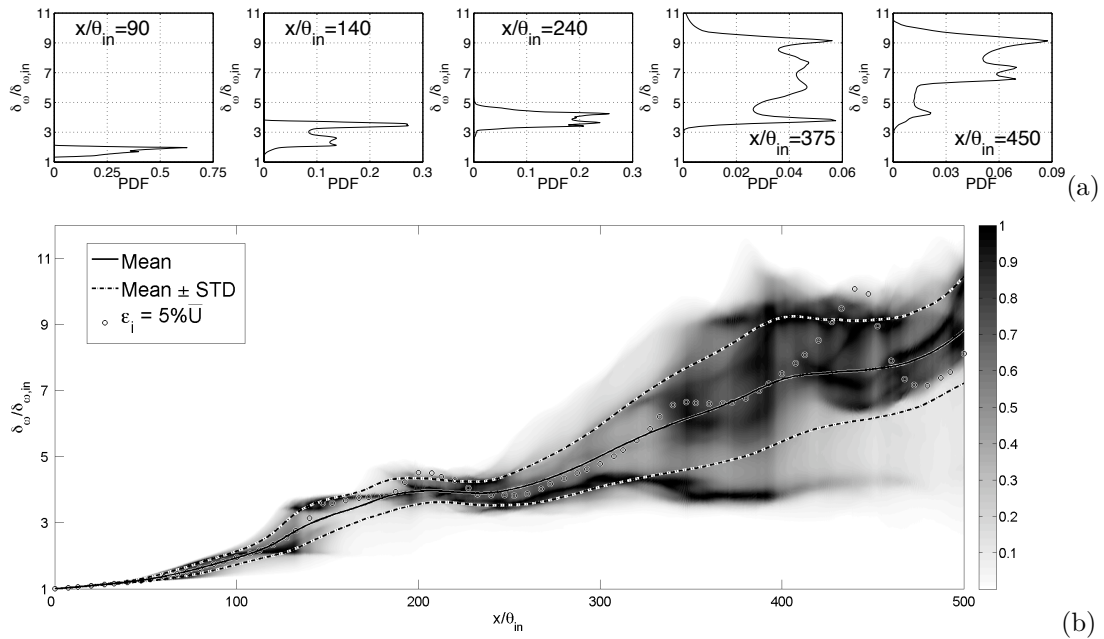


Figure II.22 – PDF of the ML vorticity thickness $\delta_\omega/\delta_{\omega,in}$ for the tri-modal perturbation case. (a) PDF profiles at five downstream locations. (b) Spatial distribution of the normalized PDF contours. Mean and variance, and deterministic solution for the input mean value, are included for comparison.

The PDF studies of $\delta_\omega/\delta_{\omega,in}$ and θ/θ_{in} have shown large variations of the distributions leading to high level of uncertainty in the response. The variability grows along the streamwise spatial direction as the flow progresses and reaches very large values for the tri-modal case. The growth of the layer thickness is therefore irregular along the x -direction. Regions of small variance and low sensitivity alternate with regions of large spectrum spread. The distributions indicate the presence of dominant scales leading to the concept of the *most probable* solutions. The most probable momentum thickness, and vorticity thickness to some extent, evolve in a stepwise fashion with clear jumps along the x -direction. In the regions of small variability, one scale dominates that corresponds to the length scale associated with the forcing disturbance that is the most influential at this location. In the sensitive regions, multiple scales coexist and can dominate but the energy is more spread out. The range of probable ML thickness takes a fan shape. These regions correspond to zones where strong physical interactions (e.g. vortex pairings) are very likely to happen. Therefore, the regions of high uncertainty are representative of the local flow features that are affected mostly by the presence of randomness introduced at

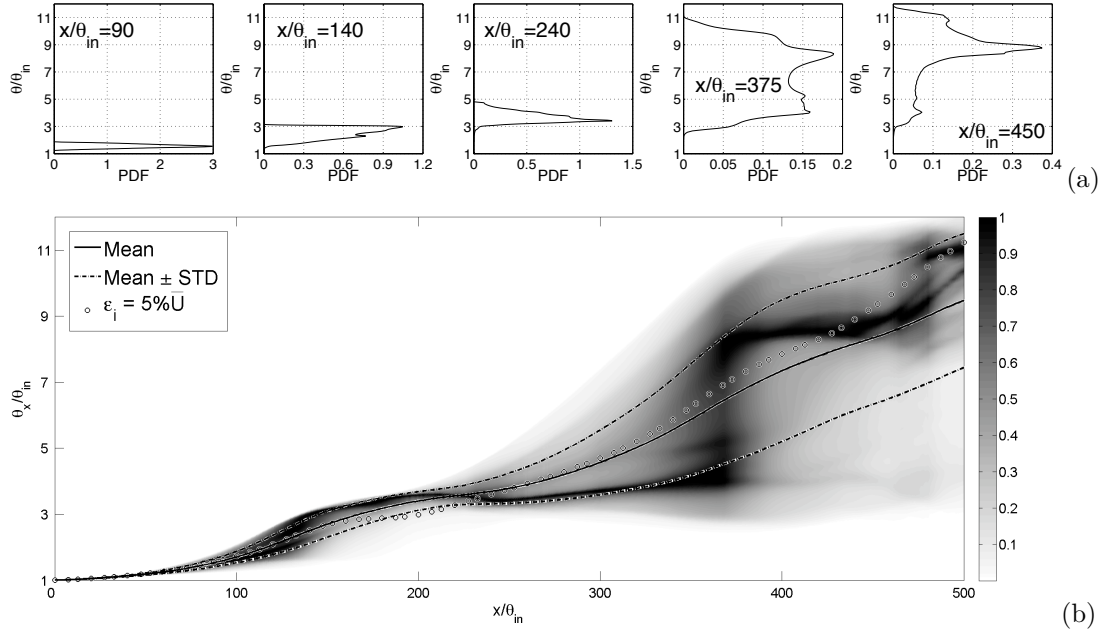


Figure II.23 – PDF of the ML momentum thickness θ/θ_{in} for the tri-modal perturbation case. See Fig. II.22 for detailed caption.

the inflow. Finally, we have seen that the path of the most probable solution is very different from the solution determined from the mean uncertain input. More importantly, the most probable solution is not realizable with any deterministic solutions.

2.4 Perspectives on three-dimensional mixing layers

The flow structure in a 3D plane ML is largely two-dimensional [101] and the streamwise organization of vortices has a strong influence on the spanwise vortex structures [33, 318]. Nevertheless, it is natural to wonder about the impact of three-dimensionality and turbulence level on a more realistic 3D simulation. Indeed, we have seen that the principal mechanism of growth in the 2D plane ML simulation is through the pairing interactions. While, this mechanism dominates the pre-transition region of the 3D ML flow, it does not seem to be the case past the transition region. It is reported that self-similar plane MLs grow linearly, without preferred thickness levels, and therefore seems to be less inclined toward sensitivity to inflow perturbations.

It is very hard to speculate *a priori* on the sensitivity of the 3D results. On one hand, we expect the flow fluctuations to be lower due to the additional spanwise dimension and the subsequent transfer of energy into the flow structures along this direction. On the other hand, the vorticity thickness is known to grow faster in the 3D than the 2D case and could exhibit some sensitivity to certain scales. Without this knowledge, we briefly expose the key-points that would help addressing this issue.

Obviously, the gPC framework as presented here can be used for 3D MLs. Nevertheless, new difficulties will arise from a computational point of view. These issues could be minimized by considering different numerical methods less costly than DNS methods, e.g. large eddy simulations (LES), as long as the accuracy of the simulation is reasonably preserved.

2.5 Concluding remarks

The effect of the inflow uncertainties on the growth of a forced 2D plane ML initiating from laminar conditions has been studied using a stochastic spectral projection method based on a generalized Polynomial Chaos representation. The magnitudes of the discrete forcing modes – composed of a fundamental mode plus one or two subharmonic modes – are treated as iid RVs with uniform distribution, each amplitude amounting at most to 10% of the mean inflow. Stochastic continuous polynomial response surfaces of momentum and vorticity thicknesses are constructed from discrete DNS solution samples. Then, the results are analyzed in terms of response variability and dominance of the most probable ML thickness along the streamwise direction. The sensitivity of the solution versus the different forcing mode amplitudes and their couplings is also investigated.

We have found that uncertainties in the bi-modal and tri-modal perturbation magnitudes have significant effects on the spatial distribution of the ML growth. Furthermore, the ML is more sensitive during the vortex pairing phases. This is because different combinations of perturbation magnitudes affect the location and extent of the vortex interactions.

The study of the sensitivity indices and surface responses of momentum- and vorticity-related quantities shows that it is not sufficient to identify the parameters that are globally influential. Indeed, the influence of each forcing uncertainty is concentrated in a specific spatial downstream region of the domain. Those regions coincide with zones where vortex interactions are most likely to happen. For both the bi-modal and tri-modal cases, the presence of the fundamental mode is crucial to trigger the ML instability but some randomness in its amplitude is not influential. The response is much more sensitive to the first subharmonic forcing amplitude. For the tri-modal case, the second subharmonic forcing amplitude becomes very influential after the first vortex merging. In this region, the layer thickness grows fast and reaches large values.

The probability density functions of the ML thickness have shown large variations of the distributions leading to high level of uncertainty in the response. The variability grows along the streamwise direction as the flow progresses. The growth of the layer thickness is not uniform along the downstream direction. Regions of small variance and low sensitivity alternate with regions of wider spectrum spread indicating high sensitivity of the solution to the input uncertainties. Those regions of high uncertainty are representative of the local flow features that are affected mostly by the existence of randomness introduced at the inflow. The distributions demonstrate the presence of dominant scales leading to the concept of the *most probable* solutions. The most probable layer thicknesses, evolve in a stepwise fashion and almost doubles at each new step. The fundamental mechanism of vortex pairing in a stochastic context takes place once for the bi-modal case and twice for the tri-modal case. It can be briefly described along the stream as follows. The process starts with one leading scale and a small level of uncertainty. As the magnitude of the most dominant scale slowly decreases, a fan shape spread of the PDF solution develops, mainly toward larger layer thickness values. The level of uncertainty grows fast and many length scales of the layer growth are probable. Then, we see the emergence of a new larger flow scale. While the two different flow scales are in competition, there is a sudden switch of the *preferred* layer thickness toward the larger scale and the variance of the response starts decreasing. Next, the inherent non-linear interaction of the coherent structures combined with the uncertainty in the forcing magnitude induce a complex and more chaotic redistribution of the energy in the system. This stage takes place unless another forcing mode (with a longer wavelength) takes over and stabilizes the layer for some distance until the process eventually reiterates, as seen for the tri-modal case.

For both cases, it was found that the mean solution becomes quite meaningless when there exist multiple dominant solutions. There exists a distinct path for the most probable solutions of the vorticity and momentum thicknesses, which are distinct from the deterministic solutions computed based on the mean stochastic inputs. It remains that the knowledge of the most probable numerical solution provides a better comparison for experimentalists than the mean solution or the deterministic solution computed for some empirically chosen input values. The supremacy of the dominant most probable scale depends on the flow streamwise location under consideration. The most probable paths are not realizable through the deterministic simulations but can be determined using the gPC method.

Finally, although it is well known that the ML growth is intricately connected to the inflow perturbation [51, 186], to the best of our knowledge, there has been no detailed measurements on the inflow perturbations. As such, direct comparison with experiments is difficult. However, the gPC variance distributions of vorticity show good qualitative agreement with previous experiments where effects of variation in the inlet condition are observed to be dominant away from the inlet [361, 199]. In addition, the preferential transfer of energy between successive modes, as demonstrated by the partial variance contours, have also been observed experimentally [505]. Therefore, this study discusses an efficient approach to address uncertainties in fluid flows numerical simulations and also raises the significance of better measurements of physical system uncertainties.

Chapter III

Application to shock-dominated compressible flows

In this chapter, both Galerkin-type and direct methods relying on generalized polynomial chaos approximation are examined in conjunction with acknowledged deterministic CFD solvers to improve uncertainty quantification of shock-dominated flows. The first part is devoted to the review and development of Galerkin-type methods for uncertainty quantification of hyperbolic system of conservation laws. A new approach inspired by kinetic theory and akin to nonlinear projections is proposed in this context. The different methods are applied to the resolution of stochastic nonlinear hyperbolic systems (e.g. Burgers' equation or Euler systems). In the second part, non-intrusive approaches such as stochastic spectral projection techniques are adapted to the subject of uncertain transonic aerodynamics. An error analysis of the global representation, based on the number of solution samples and the polynomial order at use, is carried out to better understand the coupling between aliasing, finite-term projection and deterministic numerical errors. This work has been communicated in the following journal publications and proceedings [383, 384, 386, 385, 387, 389, 68, 443, 69].

Sommaire

1	Galerkin-type method for uncertainty quantification of hyperbolic systems of conservation laws	85
1.1	Stochastic hyperbolic equations	85
1.2	Stochastic discretization	86
1.3	Linear Galerkin-type projection	87
1.4	Nonlinear Galerkin-type projection	87
1.5	Numerical and computational aspects	89
1.6	Derivation of the nonlinear Galerkin projection for 2D stochastic Euler equations	91
1.7	Applications	93
1.8	Closing remarks	106
2	Stochastic investigation of uncertain transonic aerodynamics	109
2.1	Stochastic transonic flows past a NACA0012 airfoil	110
2.2	Stochastic transonic flows past a supercritical OAT15A airfoil	117
2.3	Error analysis	120
2.4	Concluding remarks	125

A mature and reliable CFD is indispensable for compressible flow simulations used in experimental design for instance. In fact numerical simulations are the best alternative to the high cost and technical difficulties associated with supersonic or hypersonic experimental facilities. The quest for high-order methods for use in ever more complex physical configurations and multiphysics flows has led to the emergence of modern shock-capturing numerical methods [474, 518]. Nevertheless, numerical predictions of realistic flows involving complex pattern of interacting shock waves remains often overwhelmed by abundant uncertainty and errors. This uncertainty may creep from numerous sources: physical and computational domain/geometry (manufacturing process, roughness, domain size, boundary conditions,...), initial/operating conditions, physical/turbulence models, mathematical model assumptions/simplifications (e.g. linearization, adiabaticity, perfect gas,...), discretization and numerical algorithmic errors (round-off or truncation error, numerical dissipation/dispersion, aliasing,...). The application of uncertainty quantification to compressible flows will impact physically and mathematically fundamental problems (e.g. Riemann problem), classical aerodynamics problems (e.g. the piston problem [260] or [72], the dual-throat nozzle [72, 411]) as well as more realistic engineering problems (e.g. [85]).

Stochastic spectral methods have been recently developed and adapted with success to ordinary differential, elliptic and parabolic equations subject to parametric uncertainties [450, 97, 18, 16, 15, 20, 135, 300, 326, 473, 12, 497, 524, 522, 495].

But the application of those methods to stochastic *hyperbolic* problems is more challenging and the literature devoted to this topic is scarce. When the equations are linear, the situation is already not as straightforward as in its deterministic counterpart. For instance, due to the random change in the direction of the characteristic waves, proper care has to be taken to impose consistent boundary conditions [176, 460]. Nonlinear hyperbolic systems of conservation laws (especially inviscid flows such as Euler systems) are even more challenging: this is because they promote discontinuous spatial solutions in finite time, i.e. shock waves and contact discontinuities. In a stochastic context, because of the uncertainty slipping into the propagation speeds and in the physical fluxes, discontinuous solutions develop in the stochastic space as well. When standard global polynomial approximation spaces are retained, severe Gibbs-like oscillations ineluctably appear close to the solution strong gradients. The situation becomes even more complex when coupled to characteristics-based deterministic solvers.

There are different answers to these obstacles. Mathelin et al.[298] have applied the Galerkin PC representation to quasi-one-dimensional supersonic nozzle flow with uncertainty in inlet conditions and geometry. They have proposed to map their probabilistic space to a substitute space in which they perform a Lagrange interpolation. Some work in the supersonic regime have also been performed by Lin et al.[262] dealing with 2D Euler equations for a stochastic wedge flow (random inflow velocity and random oscillations of the wedge around its apex). They use a piecewise gPC method with Legendre polynomial basis and uniform distributions to solve the two-dimensional stochastic Euler equations. A Galerkin projection is employed in the random space while WENO discretization is used in the physical space. Their analysis shows that the shock wave stochastic response can induce important changes in the mean-flow structure. Interested by the “rough skin” concept for enhanced-lift of high-speed aerodynamic surfaces, they use their technique to study the shock waves scattering due to geometric roughness [264, 261].

Chantramsi *et al.* introduce a novel non-intrusive global stochastic representation based on a Padé-Legendre formalism; in addition, a filtering procedure is developed in order to minimize the errors introduced in the approximation close to the discontinuities [64]. Their numerical examples include a simple dual throat nozzle problem with uncertain initial state, and the turbulent transonic flow over a transonic airfoil with uncertain flight conditions.

Abgrall and coworkers [3] develop an original non-intrusive numerical scheme based on ENO-like reconstructions in the stochastic space for the advection, Burgers, and Euler equations. It is based on a formulation reminiscent of what is done in finite volume schemes to compute a polynomial reconstruction in order to increase the computed flux accuracy via a MUSCL extrapolation [180, 25, 1]. They present three types of reconstructions: first-order, piecewise quadratic and ENO reconstructions. Later on, they propose a semi-intrusive evolution that requires only a limited amount of modification in the deterministic flow solver at hand [4, 2]. Probably inspired by this work, Barth comes up with an intrusive WENO-like adaptive polynomial approximations in order to capture the discontinuous solutions in both physical and stochastic dimensions [24]. Numerical results are presented for inviscid Burgers equation with uncertain initial data as well as the compressible Reynolds-averaged Navier-Stokes equations with uncertain boundary data and turbulence model parameters [24].

Recently, Poëtte et al. [384] have proposed a stochastic intrusive approach to tackle shocks in compressible gas dynamics. Their gPC-based technique relies on the decomposition of the *entropic* variable of the flow and does not require a special discretization of the random space. They apply their technique to the case of the Sod’s shock-tube problem with uncertainty carried on the initial interface position between the light and the heavy fluid. A stochastic optimization framework combining stochastic surrogate model representation and optimization algorithm is proposed by Lucor et al. [275]. The stochastic optimization method is applied to multi-layer reacting flows with random geometry. Very recently, Tryoen et al. [479, 480] consider nonlinear hyperbolic systems of conservation laws. Similarly to [262], they introduce piecewise stochastic subspaces to discretize the random probability space. They perform a standard Galerkin stochastic projection coupled to a finite volume scheme with a Roe-type solver (detailed in the second reference) for discretization in space and time. They apply their method to 1D inviscid Burgers equation with uncertain initial condition and 1D Euler equations with parametric uncertainty in the adiabatic coefficient γ .

Hosder et al.[194] treat the cases of inviscid shock wave and expansion wave problems with geometric uncertainty and the case of a laminar boundary layer flow over a flat plate with uncertain viscosity. In all cases, the uncertainty is modeled as a single Gaussian random variable and Hermite polynomials are chosen for the chaos basis. The accuracy of their point-collocation non-intrusive Polynomial Chaos method applied to multiple uniform random variables is studied in Hosder et al. [193]. Loeven et al. [270] make use of a deterministic compressible Reynolds Averaged Navier Stokes (RANS) code which is coupled to a probabilistic collocation solver to propagate free-stream aerodynamic (Mach number) uncertainty through a subsonic steady flow around an airfoil. Subsequently, Simon et al. [443] and Chassaing et al. [69] conduct deeper investigations of stochastic transonic flows around a OAT15A and NACA0012 airfoils, respectively. They emphasize the stochastic interaction between the stochastic shock and separated shear-layers. The uncertain parameters under consideration in the

numerical simulations are the free-stream Mach number and the angle of attack, with *uniform* and *non-uniform* distributions.

In the remainder, both Galerkin-type and direct methods relying on generalized Polynomial Chaos approximation will be examined in conjunction with acknowledged deterministic CFD solvers. The first section will be devoted to the review and development of Galerkin-type methods for uncertainty quantification of hyperbolic system of conservation laws. The advantages and weaknesses of the standard linear Galerkin projection (such as the loss of hyperbolicity of the numerical system) will be pointed out. Next a new approach inspired by kinetic theory and akin to nonlinear projections will be detailed in this context. Finally, the different methods will be applied to the resolution of nonlinear hyperbolic systems with different levels of regularity, dimensionality and complexity such as Burgers' equation and stochastic Riemann problems governed by Euler systems. In the second section, our discussion will approach more applied topics. In particular, we are interested by uncertain transonic aerodynamics. Our study was carried out with the constraint of using existing or legacy deterministic solvers. This is why we will turn to a non-intrusive approach and use a stochastic spectral projection technique. We will conclude by a careful error analysis of the global representation, based on the number of solution samples and the polynomial order at use, to better understand the coupling between aliasing error, finite-term projection error and the deterministic numerical error.

1 Galerkin-type method for uncertainty quantification of hyperbolic systems of conservation laws

Standard Galerkin-type stochastic projection 3.1 may be performed to transform the original stochastic partial differential equations into a set of deterministic equations that can be readily discretized via standard numerical techniques. Although such a Galerkin approach is effective in many problems, its application to hyperbolic problems is limited. The primary reason is because the properties of the system of equations resulting from the Galerkin projection are not fully understood. Nevertheless, when the direction of the characteristics are not changed due to the uncertainty, the Galerkin system can be shown to be hyperbolic and solved in a straightforward manner [176]. In the following, we will propose a new approach for uncertainty quantification of systems of conservation laws that may be apprehended as a *nonlinear* Galerkin projection and is well suited for shock-dominated compressible flows [384, 386].

1.1 Stochastic hyperbolic equations

We consider a very general stochastic hyperbolic system, written here as a *Conservation Laws* together with its initial condition. For now the boundary conditions are not specified:

$$\begin{aligned} \partial_t u(\mathbf{x}, t, \Xi) + \partial_x f(u(\mathbf{x}, t, \Xi); \Xi) &= 0 \\ u(\mathbf{x}, t = 0, \Xi) &= u^0(\mathbf{x}, \Xi), \end{aligned} \quad (\text{III.1})$$

where $\mathbf{x} \in \mathcal{D} \subset \mathbb{R}^d$ is the spatial domain coordinate, t is the time coordinate and Ξ is the second-order RA (cf. Section 1.3) discretizing the probability space with a finite set of N RVs $\Xi = \{\Xi_j(\omega)\}_{j=1}^N$ with probability distribution $P_\Xi(d\xi)$. We name the finite-dimensional space $(\Omega^{(N)}, \mathcal{B}^{(N)}, P_\Xi)$ where $\Omega^{(N)} = \Omega_1 \times \dots \times \Omega_N \subset \mathbb{R}^N$, with $\Omega_j := \text{range}(\Xi_j) = \Xi_j(\Omega)$, $\mathcal{B}^{(N)}$ is the Borel σ -algebra of $\Omega^{(N)}$ and P_Ξ is the probability distribution of the RA Ξ .

We call $\mathcal{J}_u \subset \mathbb{R}$ the set of admissible values or invariants [45] of the solution u in the case of a scalar hyperbolic equation (e.g. for the inviscid Burgers equation: $\mathcal{J}_u = \mathbb{R}$) and $\mathcal{J}_\mathbf{u} \subset \mathbb{R}^n$ (with $n > 1$) the set of admissible values or invariants of the solution \mathbf{u} in the case of a hyperbolic system of equations (e.g. for Euler equations $\mathcal{J}_\mathbf{u}$ is the ensemble of states with positive density and pressure). In the next sections we will abuse the notations and use u to refer to the solution of either scalar or vectorial equations.

The solution that we seek:

$$u : (\mathbf{x}, t, \Xi) \in \mathcal{D} \times [0, T] \times \Omega^{(N)} \longmapsto u(\mathbf{x}, t, \Xi) \in \mathcal{J}_u \otimes L^2(\Omega^{(N)}, \mathcal{B}^{(N)}, P_\Xi), \quad (\text{III.2})$$

has a given initial condition that is random $u^0(\mathbf{x}, \Xi)$ and also appears in the random flux f :

$$f : (u; \Xi) \in \mathcal{J}_u \otimes L^2(\Omega^{(N)}, \mathcal{B}^{(N)}, P_\Xi) \times \Omega^{(N)} \longmapsto f(u; \Xi) \in \mathbb{R}^n \otimes L^2(\Omega^{(N)}, \mathcal{B}^{(N)}, P_\Xi), \quad (\text{III.3})$$

If the solution u is smooth, the hyperbolic system III.1 may be written in non-conservative (quasi-linear) form:

$$\begin{aligned} \partial_t u(\mathbf{x}, t, \Xi) + A(u; \Xi) \partial_x u(\mathbf{x}, t, \Xi) &= 0 \\ u(\mathbf{x}, t = 0, \Xi) &= u^0(\mathbf{x}, \Xi), \end{aligned} \quad (\text{III.4})$$

where:

$$A(u; \Xi) = \nabla_u f(u; \Xi), \quad (\text{III.5})$$

is the stochastic *Jacobian* matrix of the flux function $f(u)$.

Definition III.1

The functional $s : u(\mathbf{x}, t, \Xi) \in \mathcal{J}_u \otimes L^2(\Omega^{(N)}, \mathcal{B}^{(N)}, P_\Xi) \mapsto s(u) \in \mathbb{R}$ is a mathematical entropy of III.1, if there exists an entropy flux $g : u(\mathbf{x}, t, \Xi) \in \mathcal{J}_u \otimes L^2(\Omega^{(N)}, \mathcal{B}^{(N)}, P_\Xi) \mapsto g(u) \in \mathbb{R}^d$ such that:

$$\partial_t s(u) + \sum_{i=1}^d \partial_{x_i} g_i(u) = 0, \quad \text{for smooth } u, \quad (\text{III.6})$$

If $s(u)$ is strictly convex on $\mathcal{J}_u \otimes L^2(\Omega^{(N)}, \mathcal{B}^{(N)}, P_\Xi)$, then:

$$\partial_t s(u) + \sum_{i=1}^d \partial_{x_i} g_i(u) \leq 0, \quad \text{for discontinuous } u. \quad (\text{III.7})$$

1.1.1 Hyperbolicity

Remark III.2

The stochastic system III.1 is hyperbolic (i.e. mathematically well-posed) for u in the invariant \mathcal{J}_u if for almost every $\Xi \in \Omega^{(N)}$:

- the Jacobian matrix of the flux $A(u; \Xi)$ is \mathbb{R} -diagonalizable in a complete basis of n eigenfunctions, i.e.:

$$R^{-1}(u; \Xi) A(u; \Xi) R(u; \Xi) = D(u; \Xi), \quad (\text{III.8})$$

with diagonal matrix of eigenvalues $D(u; \Xi) = \text{diag}(\lambda_k(u; \Xi))_{k=1 \dots n}$ and complete basis of eigenvectors $R(u; \Xi) = (r_1(u; \Xi), \dots, r_n(u; \Xi))$,

or

- there exists a strictly convex mathematical entropy-entropy flux pair (s, g) , cf. [437, 175], such that:

$$\nabla_{u,u}^2 s(u) > 0 \quad \text{and} \quad \partial_t s(u) + \sum_{i=1}^d \partial_{x_i} g_i(u) \leq 0.$$

1.2 Stochastic discretization

As presented in Section 2.2.4 (or in Section 2.3.2 for the case of a piecewise polynomial Chaos approximation), we make use of a gPC basis, orthogonal with respect to the f_Ξ distribution, to span the $L^2(\Omega^{(N)}, \mathcal{B}^{(N)}, P_\Xi)$ space of approximation. If we build the approximation over global supports, we expand the solution as:

$$u(\mathbf{x}, t, \Xi) = \sum_{\alpha \in \mathbb{N}^N} u_\alpha(\mathbf{x}, t) \Phi_\alpha(\Xi), \quad (\text{III.9})$$

where the deterministic fields $u_\alpha(\mathbf{x}, t)$ are the unknowns and the set \mathcal{A} of multi-indices $\{\alpha \in \mathbb{N}^N\}$ controls the dimensionality of the problem. The approximated solution is sought in a finite dimensional subspace which implies the truncation of the polynomial basis. Therefore $\mathcal{A} \equiv \mathcal{A}^{N,p}$ depends on N and the chosen polynomial order of approximation p , $\mathcal{A}^{N,p} \equiv \{\alpha \in \mathbb{N}^N / \|\alpha\|_1 = |\alpha| \leq p\}$. We note $P \equiv \text{card}(\mathcal{A}^{N,p}) = \binom{p+N}{N}$ the dimensionality of the random space. The expansion may be written with a single index now:

$$u(\mathbf{x}, t, \Xi) \approx u^P(\mathbf{x}, t, \Xi) = \sum_{\beta=0}^P u_\beta(\mathbf{x}, t) \Phi_\beta(\Xi) = (U^P)^T \Phi^P, \quad (\text{III.10})$$

where $U^P = (u_0, \dots, u_\beta, \dots, u_P)^T$, $\Phi^P = (\Phi_0, \dots, \Phi_\beta, \dots, \Phi_P)^T \in \mathbb{R}^{(P+1) \times n}$, and

$$u_\beta(\mathbf{x}, t) = \mathbb{E}[u(\mathbf{x}, t, \Xi) \Phi_\beta(\Xi)], \quad \text{for all } \beta = 0, \dots, P. \quad (\text{III.11})$$

In the following, we will treat parametric uncertainty involving *uniform* distributions and consequently we make the choice of using an *orthonormal* basis of tensorized Legendre polynomials. For similar problems, Lin et al. [262] as well as Tryoen et al. [479] choose a *piecewise* polynomial reconstruction, with tensorized Legendre polynomials, and performed on a dyadically decomposed random space.

1.3 Linear Galerkin-type projection

Set up on the stochastic discretization framework described previously, the classic linear Galerkin-type projection described in Section 3.1 is applied to the system III.1. We obtain the new system which bears a form similar to the original one:

$$\begin{aligned}\partial_t U^P(\mathbf{x}, t) + \partial_x F(U^P(\mathbf{x}, t)) &= 0 \\ U^P(\mathbf{x}, t=0) &= U^{P0}(\mathbf{x}),\end{aligned}\quad (\text{III.12})$$

where $U^P = (u_0, \dots, u_\beta, \dots, u_P)^T$ and $F(U^P) = (F_0(U^P), \dots, F_\beta(U^P), \dots, F_P(U^P))^T$, with $F_\beta(U^P) = \mathbb{E}[f(u^P; \cdot) \Phi_\beta]$, $\forall \beta = 0, \dots, P$ and u^P given by III.10.

If the approximated solution u^P is smooth, the hyperbolic system III.12 may be written in non-conservative form:

$$\begin{aligned}\partial_t U^P(\mathbf{x}, t) + A^P(U^P) \partial_x U^P(\mathbf{x}, t) &= 0 \\ U^P(\mathbf{x}, t=0) &= U^{P0}(\mathbf{x}),\end{aligned}\quad (\text{III.13})$$

where the Galerkin expression of the Jacobian matrix of the flux $A^P(U^P) \in \mathbb{R}^{(P+1) \times n, (P+1) \times n}$ takes the form:

$$\begin{aligned}A^P(U^P) &= \nabla_U F(U^P(\mathbf{x}, t)) \\ &= \mathbb{E}[\nabla_U (f(u^P; \cdot)) \Phi_\beta]_{\beta=0, \dots, P} \\ &= \mathbb{E}[\nabla_U u^P \nabla_u f(u^P; \cdot) \Phi_\beta]_{\beta=0, \dots, P} \\ &= \mathbb{E}[\nabla_u f(u^P; \cdot) \Phi_\alpha \Phi_\beta]_{\alpha, \beta=0, \dots, P}\end{aligned}\quad (\text{III.14})$$

Remark III.3

When a piecewise polynomial approximation space with no overlapping elements (cf. Section 2.3.1) is used to represent the solution, A^P takes a diagonal block structure.

1.3.1 Hyperbolicity of the Galerkin system

Poëtte et al. [384] later followed by Tryoen et al. [479] proved that the Galerkin projection of a *scalar* conservation law always leads to a hyperbolic system. Tryoen et al. [479] also proved that in the *very* particular case where the stochastic Jacobian matrix eigenvectors are independent of the parametric uncertainty, then the Galerkin Jacobian matrix is \mathbb{R} -diagonalizable.

Remark III.4

As we will see later, numerical schemes used to solve the stochastic hyperbolic system often requires some knowledge about the eigenspectrum of the Galerkin stochastic Jacobian matrix. Nevertheless, the study of all eigenvalue–eigenvector couples is difficult due to the stochasticity.

Poëtte [382] uses the example of an hyperbolic P -system in Lagrangian coordinates, which describes the adiabatic evolution of a compressible fluid in its own frame of reference, to study the hyperbolicity of the derived Galerkin system. Considering different closure for the pressure term, different schemes and different levels of polynomial approximation, he shows that a key point is the accurate representation of the nonlinear terms involved in the Jacobian matrix of the flux. He concludes that most of the time, and despite the use of *convergent* approximations, the hyperbolicity of the Galerkin system is not preserved [387]. Després [104] also proves the loss of hyperbolicity of the Galerkin system of Saint-Venant shallow waters equations when using low-order Legendre polynomial chaos approximation.

1.4 Nonlinear Galerkin-type projection

We propose a new closure to our system based on the application of the maximum entropy principle and inspired from kinetic theory and the theory of moments. The idea is to expand an adjoint (or entropic) variable (related to the solution u) on the polynomial chaos basis, instead of expanding the variable u itself.

Introducing the *closure entropy* $\theta : u \mapsto \theta(u) \in \mathbb{R}$, a strictly *convex* functional of u , i.e. $\nabla_{u,u} \theta(u) > 0$, we wish to find the solution $u \in \mathcal{J}_u \otimes L^2(\Omega^{(N)}, \mathcal{B}^{(N)}, P_{\Xi})$ minimizing $\Theta(u) = \mathbb{E}[\theta(u)]$ under the constraints of realizability III.11. This is equivalent to solving the following minimization problem:

$$T(u(\lambda_0, \dots, \lambda_P)) = -\Theta(u(\lambda_0, \dots, \lambda_P)) + \sum_{\beta=0}^P \mathbb{E}[u(\lambda_0, \dots, \lambda_P) \lambda_\beta \Phi_\beta] - \sum_{\beta=0}^P u_\beta \lambda_\beta, \quad (\text{III.15})$$

where the $\{\lambda_\beta\}_{\beta \in 0, \dots, P}$ are the Lagrange multipliers

Remark III.5

The Θ functional is strictly convex because of the strict convexity of θ and this implies that the solution of the minimization problem is unique.

At the minimum, we show that we satisfy the following relation:

$$\begin{aligned} \lambda(\mathbf{x}, t, \Xi) &= \nabla_u \theta(u(\mathbf{x}, t, \Xi)) \\ &\approx \nabla_u \theta(u^P) = \sum_{\beta=0}^P \lambda_\beta(\mathbf{x}, t) \Phi_\beta(\Xi) = (\Lambda^P)^T \Phi^P = \lambda^P, \end{aligned} \quad (\text{III.16})$$

and consequently (due to the strict convexity):

$$u(\mathbf{x}, t, \Xi) \approx u^P(\mathbf{x}, t, \Xi) = (\nabla_u \theta)^{-1} \lambda^P = (\nabla_u \theta)^{-1} (\Lambda^P)^T \Phi^P, \quad (\text{III.17})$$

The Galerkin system becomes:

$$\begin{aligned} \partial_t U^P(\mathbf{x}, t) + \partial_x F(U^P(\mathbf{x}, t)) &= 0 \\ U^P(\mathbf{x}, t=0) &= U^{P0}(\mathbf{x}), \end{aligned} \quad (\text{III.18})$$

where $U^P = (u_0(\Lambda^P), \dots, u_\beta(\Lambda^P), \dots, u_P(\Lambda^P))^T$ and $F(U^P) = (F_0(U^P), \dots, F_\beta(U^P), \dots, F_P(U^P))^T$, with $F_\beta(U^P) = \mathbb{E}[f((\nabla_u \theta)^{-1} \lambda^P; \cdot) \Phi_\beta]$, $\forall \beta = 0, \dots, P$ and λ^P given by III.16.

Remark III.6

The nonlinear projection approach is a generalization of the classic linear Galerkin-type projection which may be recovered with a choice of $\theta(u) = u^2/2$, i.e. $\nabla_u \theta(u) = u$.

1.4.1 Hyperbolicity of the Galerkin system

We can consider the particular case $\theta \equiv s$, where s denotes the *mathematical* entropy of the system. Following the formalism of [336], we call $v \equiv \lambda$ the *entropic variable* of the system.

Property III.7

By approximating with the gPC basis the entropic variable v rather than the main variable u , we ensure the hyperbolicity of the truncated Galerkin system. In this case, the preservation of the physical invariants of the system is a corollary of the hyperbolicity.

1.4.2 Characteristic speeds and fields

The characteristic *speeds*, i.e. the eigenvalues $\lambda_k^P \in \mathbb{R}^{n \times (P+1)}$ of the Jacobian flux matrix (cf. III.14 for the linear Galerkin expression) are crucial to the propagation of the information into the system but difficult to characterize in a random context [382]. Nevertheless, it is important to get some idea of the eigenspectrum of the problem as numerous solvers and numerical parameters for CFD of compressible flows rely on this information, e.g. ENO/WENO schemes, CFL number for explicit schemes,...

The nature of the characteristic *fields*: i.e. *linearly degenerate fields* (for *contact* wave) or *genuinely nonlinear fields* (for *shock* wave and *rarefaction* wave) is made difficult by the large number of eigenvalues and eigenfunctions. Nevertheless, an extension of the Lax theorem for the Riemann problem states that the similarity solution consists of $n \times (P+1)$ constant states separated by shock waves, contact waves and rarefaction wave. At least, it is possible to bound and sometimes rank the eigenvalues. When the derived Galerkin system is hyperbolic (e.g. for the nonlinear projection), the eigenvalues of the Jacobian matrix of the flux are real. The following properties were proved in [382]:

Property III.8

Extremum eigenvalues corresponding to successive order of Polynomial Chaos truncation are nested, i.e.:

$$\min_{k \in \{1, \dots, n \times (Q+1)\}} \lambda_k^Q \leq \min_{k \in \{1, \dots, n \times (P+1)\}} \lambda_k^P \leq \max_{k \in \{1, \dots, n \times (P+1)\}} \lambda_k^P \leq \max_{k \in \{1, \dots, n \times (Q+1)\}} \lambda_k^Q,$$

for order $Q > P$ and n is the size of the deterministic system.

Property III.9

In the case where $\theta \equiv s$, the eigenvalues $\lambda_k^P \in \mathbb{R}^{n \times (P+1)}$ of the Jacobian flux matrix of the Galerkin system are bounded by the eigenvalues of the Jacobian matrix III.5 of the non discretized stochastic hyperbolic system:

$$-\infty < \inf_{\omega \in \Omega} (\lambda_{\min}(\Xi(\omega))) \leq \lambda_k^P \leq \sup_{\omega \in \Omega} (\lambda_{\max}(\Xi(\omega))) < \infty, \text{ almost surely.}$$

Property III.9 may be seen as a generalization of Theorem 2.1 in [176] to general system of conservation laws. It turns out to be a very useful property to set up the CFL condition by putting an upper bound on the largest eigenvalue of the spectrum.

1.5 Numerical and computational aspects

In this section, we describe more specifically some of the key points of the numerical method (e.g. discretization, robustness,...) and insist on the computational issues arising from the coupling between the stochastic and the deterministic approximations. A Finite Volume method (FV) is chosen for the space discretization and is coupled to the nonlinear Galerkin-type projection of Section 1.4. Nonetheless, some of the considerations in this section may be conveyed to the layout of the linear approach, cf. Section 1.3.

We consider a FV discretization of the deterministic system III.18. The system is integrated thanks to a *high-order 1D Lagrange + Remap FV* scheme with directional splitting. In the following, we highlight the FV scheme in one spatial dimension while the more technical steps are condensed in the Appendix C. For more details, we also refer to [121].

We define a grid along the 1D physical space $x \in \mathcal{D}_x$, with N_x FV cells. We denote the control volume $]t^n, t^{n+1}[\times]x_{i-\frac{1}{2}}, x_{i+\frac{1}{2}}[$, with $\Delta t = t^{n+1} - t^n$ and $\Delta x_i = x_{i+\frac{1}{2}} - x_{i-\frac{1}{2}}$ is the length of the i^{th} -cell with boundaries located at $x_{i-\frac{1}{2}}$ and $x_{i+\frac{1}{2}}$. For shorter notations, the dependency of u^P to λ^P (cf. III.16) is omitted next. We define the stochastic modes (cf. III.18) *mean* value in the i^{th} -cell at time t^n as:

$$U_i^{n,P} = \frac{1}{\Delta x_i} \int_{x_{i-\frac{1}{2}}}^{x_{i+\frac{1}{2}}} U^P(x, t^n) dx, \quad \forall i \in \{1, \dots, N_x\}, \quad (\text{III.19})$$

and the corresponding fluxes:

$$F_{i \pm \frac{1}{2}}(U^P) = (F_{i \pm \frac{1}{2} 0}(U^P), \dots, F_{i \pm \frac{1}{2} \beta}(U^P), \dots, F_{i \pm \frac{1}{2} P}(U^P))^t, \quad \forall i \in \{1, \dots, N_x\}, \quad (\text{III.20})$$

with

$$F_{i \pm \frac{1}{2} \beta}(U^P) = \frac{1}{\Delta t} \int_{t^n}^{t^{n+1}} \mathbb{E} \left[f(u^P(x_{i \pm \frac{1}{2}}, t, \cdot); \cdot) \Phi_\beta \right] dt, \quad (\text{III.21})$$

$$\forall \beta \in \{0, \dots, P\}, \quad \forall i \in \{1, \dots, N_x\},$$

such that, on the control volume, system III.18 becomes equivalent to:

$$U_i^{n+1,P} = U_i^{n,P} - \frac{\Delta t}{\Delta x_i} (F_{i+\frac{1}{2}}(U^P) - F_{i-\frac{1}{2}}(U^P))$$

$$U_i^{0,P} = \frac{1}{\Delta x_i} \int_{x_{i-\frac{1}{2}}}^{x_{i+\frac{1}{2}}} U^{P0}(x) dx. \quad (\text{III.22})$$

This system is exact as long as no approximations are defined to evaluate the flux terms at the cell boundaries.

Remark III.10

Several choices are possible for the discretization of the flux terms $F_{i \pm \frac{1}{2}}(U^P)$ of III.22, among them:

- Roe schemes [382, 384, 480].
- Lagrangian schemes: e.g. high-order dimensionally split Lagrange-remap schemes (cf. Appendix C).

Roe-type schemes

The basic idea of the deterministic Roe scheme is to replace the Jacobian matrix of the nonlinear original problem by a constant Jacobian matrix function of the date state u_L, u_R ¹. The approximated Riemann problem

1. In the formalism of the FV method described previously, we introduce the following notations: we call an interface (I) between two adjacent cells and separating left (L) and right (R) states.

is then solved *exactly*.

Hypothesis III.11

Let us assume that the stochastic hyperbolic system III.1 owns a Roe matrix $\tilde{\mathbb{A}}(u_L, u_R; \Xi) \in \mathbb{R}^{n \times n} \otimes L^2(\Omega^{(N)}, \mathcal{B}^{(N)}, P_\Xi)$ that satisfies the following properties at each interface I :

- \mathbb{R} -diagonalizable, cf. III.40.
- consistency with the exact stochastic Jacobian matrix: $\tilde{\mathbb{A}}(u, u; \Xi) = \nabla_u f(u; \Xi)$, $\forall u \in \mathcal{J}_u \otimes L^2(\Omega^{(N)}, \mathcal{B}^{(N)}, P_\Xi)$.
- conservation across discontinuities:
 $f(u_R; \Xi) - f(u_L; \Xi) = \tilde{\mathbb{A}}(u_L, u_R; \Xi)(u_R - u_L)$, $\forall u_L, u_R \in \mathcal{J}_u \otimes L^2(\Omega^{(N)}, \mathcal{B}^{(N)}, P_\Xi)$.

Moreover, let us assume that there exists a Roe state $\tilde{u}_I \in \mathcal{J}_u \otimes L^2(\Omega^{(N)}, \mathcal{B}^{(N)}, P_\Xi)$, then:

- $\tilde{\mathbb{A}}(u_L, u_R; \Xi) = \nabla_u f(\tilde{u}_I; \Xi)$ is a Roe linearized matrix for the stochastic system.

The approach is very similar to the deterministic case and may be seen as an approximate Riemann solver where a linear approximation is substituted at the interface and at each time step for the fluxes of III.22:

$$F_I(U^P) = \frac{1}{2}(F(U_L^{n,P}) + F(U_R^{n,P})) - \frac{1}{2} \left| \tilde{\mathbb{A}}^P(U_L^{n,P}, U_R^{n,P}) \right| (U_R^{n,P} - U_L^{n,P}). \quad (\text{III.23})$$

Theorem III.12

Under those assumptions, it was shown [382, 479] that there exists a Roe matrix:

$$\tilde{\mathbb{A}}^P(U_L^{*P}, U_R^{*P}) = \mathbb{E} \left[\tilde{\mathbb{A}}(u_L^P, u_R^P; \cdot) \Phi_\alpha \Phi_\beta \right]_{\alpha, \beta=0, \dots, P}, \quad (\text{III.24})$$

$$= \mathbb{E} \left[\nabla_U F(U_I^{*P}) \Phi_\alpha \Phi_\beta \right]_{\alpha, \beta=0, \dots, P} \quad (\text{III.25})$$

(i.e. satisfying similar properties) for the truncated Galerkin system III.12. Then this matrix is a Roe linearized matrix for the Galerkin system if it is \mathbb{R} -diagonalizable.

Remark III.13

The practical layout of this Roe-type solver for systems issued from linear Galerkin projection is straightforward for simple stochastic scalar conservation laws such as the Burgers' equation with positive wave speeds [384].

Remark III.14

For stochastic Burgers' equations treated with the nonlinear Galerkin projection, the Roe solver has to be upwinded which is made easy by the fact that all eigenvalues of III.18 are positive. This result holds for any choice of entropy [384].

In the general case, an important concern is the computation of $|\tilde{\mathbb{A}}^P|$ that is costly as it requires to diagonalize the large matrix with eigenvalues that are not explicitly known. This demands strenuous effort as it has to be done at each interface in the spatial domain and for each time step. At this point there are different options to proceed. Some researchers propose to compute an approximation of $|\tilde{\mathbb{A}}^P|$ by a polynomial transformation applied to $\tilde{\mathbb{A}}^P$ using an approximate spectrum [479]. Others, relying on the determination of the sign of those eigenvalues (in the case of a WENO scheme)², choose to only use mean values of left and right eigenvectors instead of the full projection [262].

Finally, Tryoen et al. propose a Roe-type solver with an adaptation of Dubois & Mehlman [109] entropy corrector (or *entropy fix*), to avoid entropy-violating discontinuous waves (sometimes called *rarefaction shocks*) in the presence of sonic points [480].

High-order dimensionally split Lagrange-remap schemes

In our case, the retained approach allows commuting of the operators and the fluxes read:

$$\begin{aligned} F_{i \pm \frac{1}{2} \beta}(U^P) &= \mathbb{E} \left[\frac{1}{\Delta t} \int_{t^n}^{t^{n+1}} f(u^P(x_{i \pm \frac{1}{2}}, t, \cdot); \cdot) dt \Phi_\beta \right], \\ &= \mathbb{E} \left[f_{i \pm \frac{1}{2}}(u^P) \Phi_\beta \right], \quad \forall \beta \in \{0, \dots, P\}, \quad \forall i \in \{1, \dots, N_x\}. \end{aligned} \quad (\text{III.26})$$

2. Essentially non-oscillatory (ENO) and Weighted ENO (WENO) are finite difference or finite volume schemes. A key idea in WENO schemes is a linear combination of lower order fluxes or reconstruction to obtain a higher order approximation. Both ENO and WENO schemes use nonlinear adaptive procedure to automatically choose the locally smoothest stencil and achieve high order accuracy and non-oscillatory property near discontinuities. Those schemes are based on local characteristic decompositions and flux splitting to avoid spurious oscillatory.

The expectations of the fluxes at the boundaries of the cell are numerically computed thanks to full or sparse numerical cubatures, see Appendix B.

We recall that the nonlinear projection also requires a minimization step (III.15) that allows recovering the stochastic modes of the entropic variable Λ_i^{n+1P} from the stochastic modes of the main variable U_i^{n+1P} at time step t^{n+1} and in each cell, i.e. for $\forall i \in \{1, \dots, N_x\}$. The functional to minimize at each time step and in each cell may be written:

$$T(\Lambda_i^{n+1P}) = \Theta^*(\Lambda_i^{n+1P}) - \left(U_i^{n+1P}\right)^T \Lambda_i^{n+1P}, \quad (\text{III.27})$$

with the expectation of one Legendre transform of the entropy given by:

$$\Theta^*(\Lambda_i^{n+1P}) = -\mathbb{E} \left[\theta(u(\Lambda_i^{n+1P})) \right] + \sum_{\beta=0}^P \mathbb{E} \left[u(\Lambda_i^{n+1P}) \lambda_\beta \Phi_\beta \right]. \quad (\text{III.28})$$

Again, the integrals involved in III.28 are numerically evaluated thanks to full or sparse numerical cubatures, see Appendix B. In fact, λ^P is evaluated at all N_q quadrature points via its gPC expansion III.16 where its coefficients are the unknown. A Newton algorithm with quadratic convergence is used to find the minimum of the discrete version of III.27. The algorithm has recourse to the inversion of the hessian matrix of T . Because T is strictly convex, we have shown that a condition to preserve positivity of the hessian of the matrix is to have $N_q > P$ [382]. When Λ_i^{n+1P} is used as the initial guess, the algorithm converges in 5 to 6 iterations for a threshold of 10^{-13} and about 9 polynomial moments (similar results as in [308]).

In the next section, we apply the nonlinear Galerkin projection approach to stochastic compressible gas dynamics. Inspired by the study of [535], we consider the problem of uncertainty propagation through Euler equations due to initial interface perturbations in a Richtmyer–Meshkov (RM) like problem.

1.6 Derivation of the nonlinear Galerkin projection for 2D stochastic Euler equations

We consider a bidimensional Euler system in cartesian coordinates (initial and boundary conditions are not specified) [474]:

$$\begin{cases} \partial_t \rho + \partial_x \rho u + \partial_y \rho v = 0, \\ \partial_t \rho u + \partial_x (\rho u^2 + p) + \partial_y (\rho u v) = 0, \\ \partial_t \rho v + \partial_x (\rho u v) + \partial_y (\rho v^2 + p) = 0, \\ \partial_t \rho e + \partial_x (\rho u e + p u) + \partial_y (\rho v e + p v) = 0, \end{cases} \quad (\text{III.29})$$

where ρ is the mass density, u and v are the fluid velocity components in cartesian coordinates such that $(x, y) \in \mathcal{D}_x \times \mathcal{D}_y = \mathcal{D} \subset \mathbb{R}^2$, e is the total energy density and p is the pressure of the fluid.

The system is closed by an equation of state. Here, we consider a perfect gas closure for which the pressure has the form $p = (\gamma - 1)\rho\epsilon$ where γ is the adiabatic coefficient and $\epsilon = e - \frac{1}{2}(u^2 + v^2)$ is the specific internal energy.

Remark III.15

The system (III.29) is hyperbolic if $\frac{\partial p}{\partial \rho} > 0$ which implies $\epsilon > 0$ with this choice of equation of state.

The truncated Galerkin Euler system

In our example, the input uncertainty affects the initial condition. We have supposed that the boundary conditions are given and that initial and boundary conditions do not challenge the well-posedness of the system, i.e. the system is hyperbolic for every realizations of the RVs modeling the uncertainties, almost surely.

The uncertainty is modeled by a random vector Ξ of N independent components whose *uniform* distribution functions is referred as P_Ξ .

Following the formalism of equations III.1 we introduce the following notations in order to rewrite the system in a more compact fashion. We denote by $\mathbf{u} = (\rho, \rho u, \rho v, \rho e)^t \in \mathcal{J}_\mathbf{u} \subset \mathbb{R}^4$ with $\mathcal{J}_\mathbf{u} = \{(\rho, \rho u, \rho v, \rho e)^t : \epsilon(\rho, \rho u, \rho v, \rho e) > 0\}$ and we write:

$$\begin{aligned} \partial_t \mathbf{u} + \partial_x f(\mathbf{u}(\mathbf{x}, t, \Xi)) + \partial_y h(\mathbf{u}(\mathbf{x}, t, \Xi)) &= 0, \\ \mathbf{u}(\mathbf{x}, t = 0, \Xi) &= \mathbf{u}^0(\mathbf{x}, \Xi) \end{aligned} \quad (\text{III.30})$$

using the equation of state with the following notations:

$$f(\mathbf{u}) = \begin{pmatrix} \frac{(\rho u)^2}{\rho} + (\gamma - 1) \left(\rho e - \frac{1}{2} \frac{(\rho u)^2 + (\rho v)^2}{\rho} \right) \\ \frac{\rho u \rho v}{\rho} \\ \frac{(\rho u)(\rho e)}{\rho} + (\gamma - 1) \frac{\rho u}{\rho} \left(\rho e - \frac{1}{2} \frac{(\rho u)^2 + (\rho v)^2}{\rho} \right) \end{pmatrix},$$

and

$$h(\mathbf{u}) = \begin{pmatrix} \frac{\rho v \rho v}{\rho} \\ \frac{(\rho v)^2}{\rho} + (\gamma - 1) \left(\rho e - \frac{1}{2} \frac{(\rho u)^2 + (\rho v)^2}{\rho} \right) \\ \frac{(\rho v)(\rho e)}{\rho} + (\gamma - 1) \frac{\rho v}{\rho} \left(\rho e - \frac{1}{2} \frac{(\rho u)^2 + (\rho v)^2}{\rho} \right) \end{pmatrix}.$$

From now on, we will drop the spatial and temporal dependency for conveniency. We denote by $(\Phi_\beta)_{\beta \in \mathbb{N}}$ the multidimensional gPC basis associated to P_Ξ . Then the P -truncated system associated with (III.30) obtained by a Galerkin projection on the gPC basis is given by:

$$\begin{aligned} \partial_t \mathbf{U}^P(\mathbf{x}, t) + \partial_x F(\mathbf{U}^P(\mathbf{x}, t)) + \partial_y H(\mathbf{U}^P(\mathbf{x}, t)) &= 0 \\ \mathbf{U}^P(\mathbf{x}, t = 0) &= \mathbf{U}^{P0}(\mathbf{x}), \end{aligned} \quad (\text{III.31})$$

with

$$\mathbf{u}(\mathbf{x}, t, \Xi) \approx \mathbf{u}^P(\mathbf{x}, t, \Xi) = \sum_{\beta=0}^P \mathbf{u}_\beta(\mathbf{x}, t) \Phi_\beta(\Xi) = \mathbf{U}^P \Phi^P, \quad (\text{III.32})$$

where $\mathbf{U}^P = (\mathbf{u}_0, \dots, \mathbf{u}_\beta, \dots, \mathbf{u}_P)^t \in \mathbb{R}^{(P+1) \times n}$, and

$$\mathbf{u}_\beta(\mathbf{x}, t) = \mathbb{E}[\mathbf{u}(\mathbf{x}, t, \Xi) \Phi_\beta(\Xi)], \quad \text{for all } \beta = 0, \dots, P. \quad (\text{III.33})$$

We choose the mathematical entropy $\theta(\mathbf{u}) = s(\mathbf{u})$ to close the stochastic system. The couple entropy-entropy flux (s, g) may be expressed. We have:

$$s(\mathbf{u}) = -\rho \ln \left(\rho^{-\gamma} \left(\rho e - \frac{(\rho u)^2 + (\rho v)^2}{2\rho} \right) \right) \quad (\text{III.34})$$

with its entropy flux:

$$g(\mathbf{u}) = \begin{pmatrix} \frac{\rho u}{\rho} s(\rho, \rho u, \rho v, \rho e) \\ \frac{\rho v}{\rho} s(\rho, \rho u, \rho v, \rho e) \end{pmatrix}. \quad (\text{III.35})$$

Remark III.16

Note that in our case of Euler equations, the mathematical entropy of the Euler system is opposite to the physical entropy. Nevertheless, there exists several strictly convex mathematical entropies for this system, see [436, 382]

We call $\nabla_{\mathbf{u}} s(\mathbf{u}) = \lambda = \mathbf{v}$ the *entropic variable*. We recall that developing that variable on the gPC basis symmetrizes the Galerkin system and ensures its hyperbolicity. The entropic variable $\mathbf{v} = (v_1, v_2, v_3, v_4)^t$ associated with s , expressed as a function of the main variable \mathbf{u} is given by

$$\mathbf{v}(\mathbf{u}) = \begin{pmatrix} -\ln \left(\frac{2(\rho e)\rho - (\rho u)^2 - (\rho v)^2}{2\rho^{\gamma+1}} \right) + \gamma - \frac{(\rho u)^2 + (\rho v)^2}{2\rho(\rho e) - (\rho u)^2 - (\rho v)^2} \\ \frac{2\rho(\rho u)}{2\rho(\rho e) - (\rho u)^2 - (\rho v)^2} \\ \frac{2\rho(\rho v)}{2\rho(\rho e) - (\rho u)^2 - (\rho v)^2} \\ -\frac{2\rho^2}{2\rho(\rho e) - (\rho u)^2 - (\rho v)^2} \end{pmatrix}, \quad (\text{III.36})$$

and the bijection $\mathbf{v} \mapsto \mathbf{u}(\mathbf{v})$ gives:

$$\mathbf{u}(\mathbf{v}) = \begin{pmatrix} \exp \frac{2v_1 v_4 - 2v_4 \ln(-v_4) - 2v_4 \gamma - v_2^2 - v_3^2}{2v_4(\gamma-1)} \\ -\frac{v_2}{v_4} \exp \frac{2v_1 v_4 - 2v_4 \ln(-v_4) - 2v_4 \gamma - v_2^2 - v_3^2}{2v_4(\gamma-1)} \\ -\frac{v_3}{v_4} \exp \frac{2v_1 v_4 - 2v_4 \ln(-v_4) - 2v_4 \gamma - v_2^2 - v_3^2}{2v_4(\gamma-1)} \\ \frac{v_2^2 + v_3^2 - 2v_4}{2v_4^2} \exp \frac{2v_1 v_4 - 2v_4 \ln(-v_4) - 2v_4 \gamma - v_2^2 - v_3^2}{2v_4(\gamma-1)} \end{pmatrix}. \quad (\text{III.37})$$

We notice that the first component of \mathbf{u} in (III.37) (i.e. ρ) is positive by construction. This still holds when \mathbf{v} is developed on a gPC basis.

After that, the different numerical steps described in the previous section may be straightforwardly deployed in order to solve the problem. An application of this numerical scheme to compressible gas dynamics with uncertain initial conditions is presented in Section 1.7.3.

1.7 Applications

After a short review of the instructive case of the random linear advection equation, we present results for nonlinear hyperbolic systems of conservation laws: one-dimensional inviscid Burgers' equation and two-dimensional Euler systems.

1.7.1 Linear advection equation

The linear advection equation in a random media or with a random transport velocity is an instructive prototype problem to propagation phenomena in uncertain context. While exact [426], theoretical [414] or MC methods [129] have been extensively used for this type of equations, there exist recent studies that rely on the use of stochastic spectral methods instead [208, 176, 214, 460].

Gottlieb et al. [176] consider a simple scalar equation in one dimension with random advection velocity represented by a RV Ξ of known density encompassing the zero value:

$$\begin{aligned} \partial_t u(x, t, \Xi) + c(\Xi) \partial_x u(x, t, \Xi) &= 0 \\ u(x, t = 0, \Xi) &= u^0(x, \Xi), \end{aligned} \quad (\text{III.38})$$

where the domain has been carefully mapped into $x \in (-1, 1)$ and $t \geq 0$.

Remark III.17

Non-periodic boundary conditions depend on the sign of the RV $c(\Xi)$ and a well-posed problem should be:

$$\begin{aligned} u(1, t, \Xi) &= u_R(t, \Xi), \quad \text{if } c(\Xi) > 0, \\ u(-1, t, \Xi) &= u_L(t, \Xi), \quad \text{if } c(\Xi) < 0. \end{aligned}$$

Standard Galerkin-type stochastic projection transforms the problem into a deterministic system, such as the one of III.13, where $A^P = \mathbb{E}[c \Phi_\alpha \Phi_\beta]_{\alpha, \beta=0, \dots, P} \in \mathbb{R}^{(P+1) \times (P+1)}$ is symmetric hyperbolic which is consistent with the fact that the original equation is hyperbolic for each realization of the random transport equation. However if $c(\Xi)$ changes sign for some realizations of Ξ , then the system has both positive and negative eigenvalues for sufficiently large P .

Consistent boundary conditions

We can diagonalize the system by means of the following decomposition:

$$R^{-1} A^P R = D^P, \quad (\text{III.39})$$

with diagonal matrix of eigenvalues $D^P = \text{diag}(\lambda_0, \dots, \lambda_{k_+}, \lambda_{k_-}, \dots, \lambda_P)$ with positive $\{\lambda_0, \dots, \lambda_{k_+}\}$ and negative $\{\lambda_{k_-}, \dots, \lambda_P\}$ eigenvalues and we obtain the new *decoupled* system:

$$\begin{aligned} \partial_t Q^P(x, t) + D^P \partial_x Q^P(x, t) &= 0 \quad \text{with} \quad Q^P(x, t) = R^{-1} U^P(x, t) \\ Q^P(x, t = 0) &= Q^{P0}(x). \end{aligned} \quad (\text{III.40})$$

The boundary conditions to impose on the stochastic modes of the characteristic variables are determined by the sign of the eigenvalues:

$$\begin{aligned} q_j(x = 1, t) &= \sum_{i=0}^P r_{i,j} u_i(x = 1, t) = \sum_{i=0}^P r_{i,j} \mathbb{E}[u_R(t, \Xi) \Phi_i] \quad \text{for } j = 0, \dots, k_+, \\ q_j(x = -1, t) &= \sum_{i=0}^P r_{i,j} u_i(x = -1, t) = \sum_{i=0}^P r_{i,j} \mathbb{E}[u_L(t, \Xi) \Phi_i] \quad \text{for } j = k_-, \dots, P. \end{aligned} \quad (\text{III.41})$$

It leads to specifying the following conditions on the original system:

$$U^P(x = 1, t) = RQ^P(x = 1, t) \quad \text{and} \quad U^P(x = -1, t) = RQ^P(x = -1, t). \quad (\text{III.42})$$

Convergence analysis

In the case of a *beta* (respectively *uniform*) distribution for $c(\Xi)$ combined with a Jacobi (respectively Legendre) Polynomial Chaos basis, they show that under some assumptions of fast asymptotic convergence of the solution gPC expansion coefficients, i.e. $\|u_j(x, t)\|_1^2 \leq \kappa/j^{2m}$, with $j \gg 1$ and constants $\kappa, m > 0$, then the *mean-square* error exhibits a *linear growth* in time:

$$\mathbb{E}[\|u - u^P\|_2^2] \leq \frac{\kappa}{P^{m-1}} t, \quad (\text{III.43})$$

with u^P defined in III.10 and $\|\cdot\|_2$ denotes the standard L^2 norm. This degeneration of the accuracy of the gPC approximation is similar to the problem encountered in the long-term integration of some random oscillatory flows, see for instance [495].

Remark III.18

This linear growth of the error in time is independent of the boundary conditions. Tang & Zhou [460] perform some convergence analysis for stochastic collocation methods for the same system.

1.7.2 Inviscid Burgers' equation

The study of inviscid Burgers' equation is a must-have when approaching stochastic nonlinear hyperbolic equations. Several authors have applied Polynomial Chaos based numerical approximations in order to solve this class of problems [197, 528, 72, 29, 384, 372, 479, 373]. Despite being of simple form, this equation sheds some light onto some of the recurrent problems that one might encounter. For instance, in [72], the authors study the effect of random initial conditions on the structure of the shocked steady-state isentropic flow in a dual-throat nozzle. In particular they focus on the uncertainty quantification of the shock position for different stochastic initial conditions. They conclude that:

Quote III.19 ([72])

"... The largest absolute eigenvalue of the flux-Jacobian matrix of the system increases quickly with respect to the number of the polynomial chaos terms used in the expansion. This might cause large dissipation for some numerical schemes. The increasing size of the system ... could also be problematic if one wants to solve the system with a high order numerical scheme using characteristic decomposition, e.g., high order ENO or WENO methods."

Burgers' equation in 1D random dimension

One of the simplest non linear stochastic conservation laws is the inviscid Burgers' equation in 1D for the physical variable ($n = 1$) and 1D for the uncertain variable ($N = 1$).

$$\partial_t u(x, t, \xi) + \partial_x \frac{u^2(x, t, \xi)}{2} = 0. \quad (\text{III.44})$$

This equation has been studied extensively, see for example [27] in the context of turbulent flows. One important property of (III.44) is that except for very special cases, discontinuous solutions (i.e. shocks) will eventually develop even for smooth initial conditions. In the following, we denote by t^* the time of formation of the last shock.

Discontinuous solutions (ie shocks) propagating in the x -space will generate discontinuities in the random space leading to convergence problem. In the following, we consider this equation with parametric uncertainties in the initial condition. The system has an infinite number of entropy-entropy flux pairs (see [175]). We compare

three different ones:

$$\begin{aligned}
 s_0(u) &= \frac{u^2}{2} & |v = \nabla_u s_0(u) = u, \\
 s_1(u) &= -\ln(u - u_-) & |v = \nabla_u s_1(u) = -\frac{1}{u - u_-}, \\
 s_2(u) &= -\ln(u - u_-) - \ln(u_+ - u) & |v = \nabla_u s_2(u) = -\frac{1}{u - u_-} + \frac{1}{u_+ - u}.
 \end{aligned} \tag{III.45}$$

For the first entropy s_0 , $u = v$ and the original system is recovered. The two other entropies depend on parameters, u_- and u_+ which will be defined afterward. There exists a one-to-one transformation to obtain u from v :

$$\begin{aligned}
 u(v) &= v & \text{with entropy } s_0, \\
 u(v) &= \frac{-1 + vu_-}{v} & \text{with entropy } s_1, \\
 u(v) &= -\frac{1}{v} + \frac{u_- + u_+}{2} + \frac{\sqrt{(u_- - u_+)^2 v^2 + 4}}{2v} & \text{with entropy } s_2.
 \end{aligned} \tag{III.46}$$

Remark III.20

Burgers' equation being a scalar conservation law, there exists a maximum principle for the entropic solution (see [437] (II p. 2)). Consequently, once the initial condition is given, it is possible to choose the parameters u_- and u_+ according to the domain invariants.

We test two different initial conditions: the first one is piecewise linear (IC_1) and the second one is its smoother counterpart (IC_2), see figure III.1.

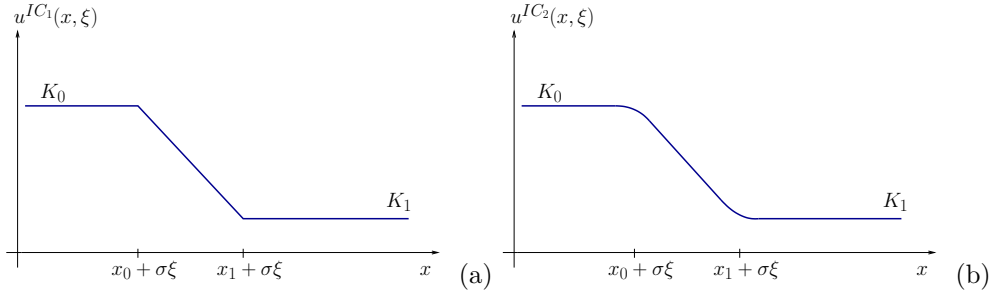


Figure III.1 – Initializations for test-cases IC_1 (a) and IC_2 (b).

In both cases, after t^* , the solutions are discontinuous with a step-function-like behaviour and the discontinuity velocity is $D = \frac{u_R + u_L}{2}$ where u_R and u_L are the right and left states of u (the velocity is obtained thanks to the Rankine-Hugoniot relations). Besides, the theoretical value of $t^*(\xi)$ is known

$$t^*(\xi) = -\frac{1}{\inf_{x \in \mathcal{D}} \left(\frac{du}{dx}(x, 0, \xi) \right)}. \tag{III.47}$$

For both initial conditions IC_1 and IC_2 , $u(x, 0, \xi)$ is a translation of $u(x, 0, 0)$ so that the discontinuity velocity D and t^* do not depend on the random variable ξ . According to (III.47),

$$\text{for } IC_1: t^* = -\frac{x_1 - x_0}{K_1 - K_0}, \text{ and for } IC_2: t^* = -\frac{1}{-\frac{b^2}{3a} + c},$$

where the constant coefficients a, b, c are given in [384]. In the following, for the sake of simplicity, we choose ξ to parametrize a *uniform* random variable of zero mean on $[-0.2, 0.2]$ for both 1D random initializations: we actually use $\sigma\xi$ in the following with $\sigma = 0.2$ and $\xi \in [-1, 1]$. The same choice is made for the 2D random initializations as (ξ_0, ξ_1) will be i.i.d. uniform laws on $[-1, 1]$ and we will take $\sigma_0 = 0.1$ and $\sigma_1 = 0.2$. The polynomial basis is the orthonormal Legendre basis for the 1D case and a tensorized Legendre basis for the 2D one, see [459].

IC_1 test-case

This test-case has a continuous initial condition that consists of three different states, translated by $\sigma\xi$ on the x -axis: $u(x, 0, \xi) = u^0(x + \sigma\xi)$. Figure III.2 (b) shows the initial conditions for several realizations of ξ . For a specific realization, see figure III.2 (a), as t increases, the left state moves toward increasing x and the intermediate slope is steepening until the formation of a discontinuity at $t^* = -\frac{x_1 - x_0}{K_1 - K_0} = 1/11$ and $x^* = x_1 = 1.5$. On figure III.2 (c) we show the time evolution of the mean and standard deviation until

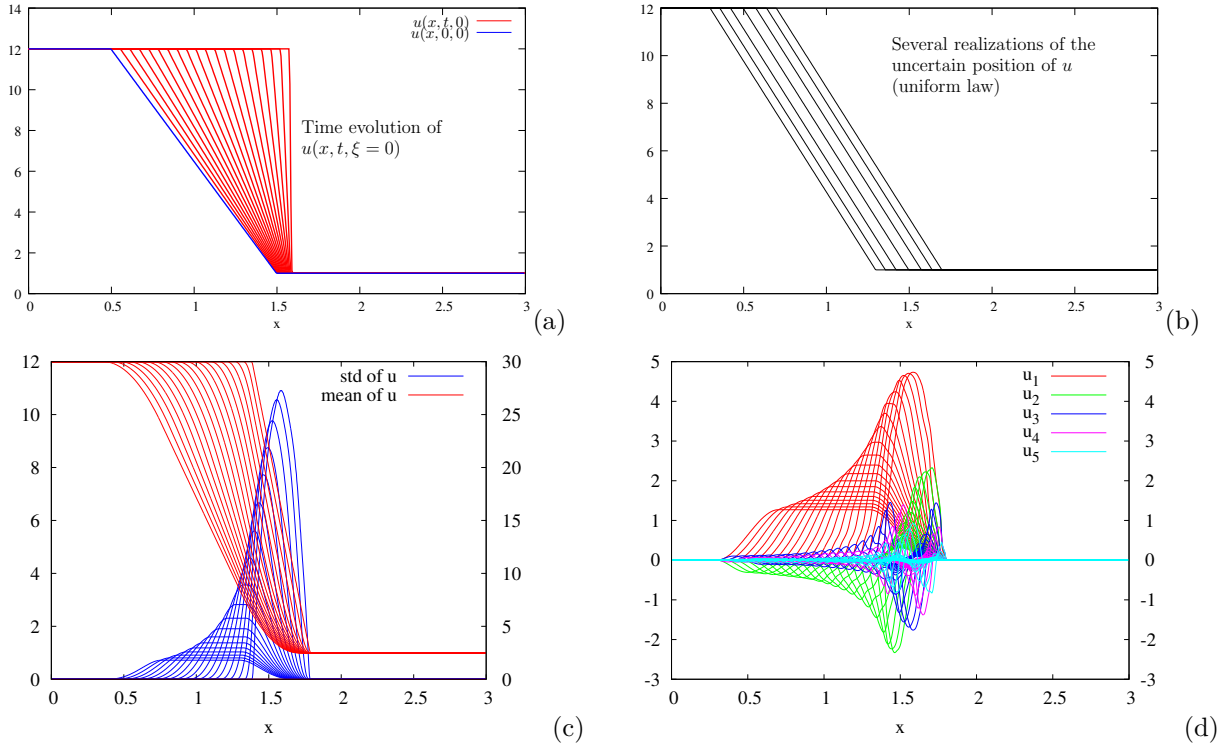


Figure III.2 – (a): Typical time evolution of the solution spatial distribution. (b): example of several realizations of the uncertain initial condition. (c): time evolution of the exact mean and standard deviation solutions. (d): time evolution of the polynomial coefficients u_1, \dots, u_5 , until $t = T_f = 0.0909 \approx t^*$; remark: left axis refers to the mean and the right axis to the standard deviation, respectively.

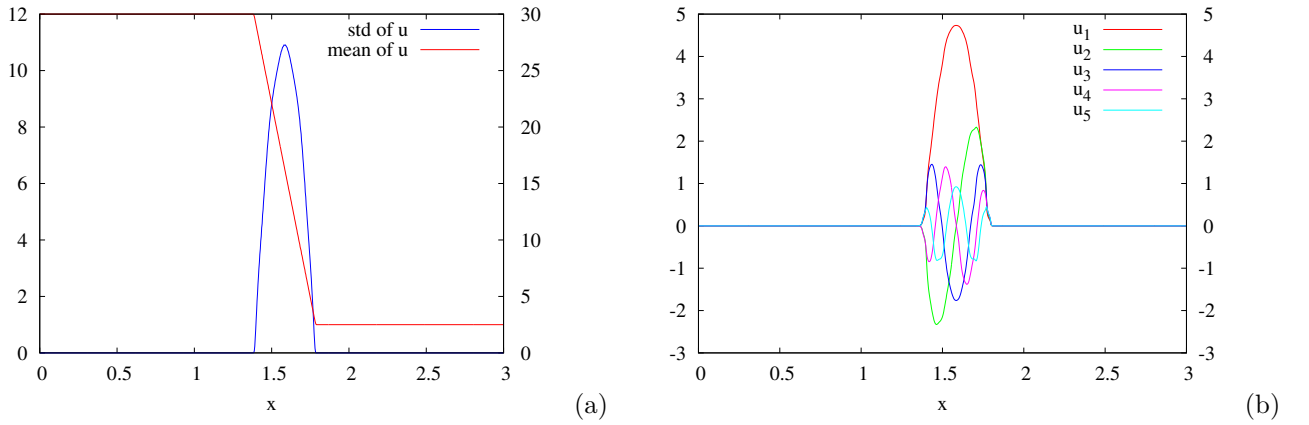


Figure III.3 – (a): mean and standard deviation at $t \approx t^*$. (b): polynomial coefficients u_1, \dots, u_5 at $t \approx t^*$.

$t = T_f = 0.0909 \approx t^*$. On figure III.2 (d), we show the polynomial moments of order 1 to 5 whose integrals have been calculated by numerical integration of the analytical solution.

Figure III.3 shows the same quantities at time $t = T_f = 0.0909 \approx t^*$. After t^* , all quantities and related statistics are simply advected to the right at the deterministic $\frac{u_R + u_L}{2}$ velocity.

Figure III.4 (a) shows the analytical solution at $x^* = 1.5$ for different times; at $t = t^*$ a discontinuity occurs in the random space. Figure III.4 (b) shows the analytical solution at $t = 0$ and $t = t^*$ and the sG-gPC₅ solution at the same times: initially, the Gibbs phenomenon is subtle but when $t = t^*$, the oscillations on each part of the discontinuity are aggravated and for some values of ξ , u falls far below the zero-level. In this case, this has no physical implication on the stability of the numerical approximation. However it can become a hassle for the stochastic Euler equations for example, for which a negative internal energy questions the hyperbolicity of the system or a negative density would not be physical.

Let us now consider the results from the IPMM and compare them to the results from the sG-gPC. Figure III.5 shows the results for $P = 5$ at $x^* = 1.5$ and $t = t^*$ for the entropies s_0, s_1 and s_2 given in (III.45). The entropy s_0 is such that the entropic variable is equal to the classical variable and consequently $\text{IPMM}_P - s_0$ is

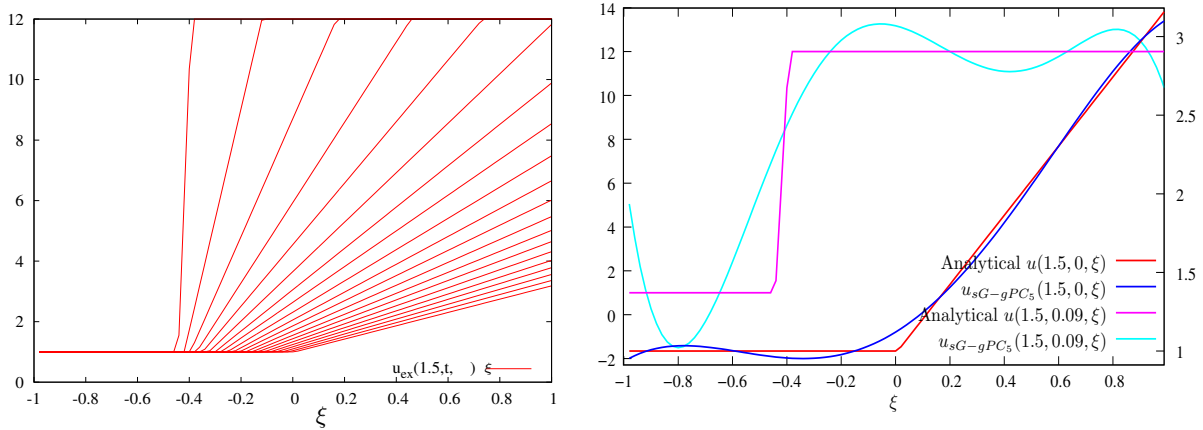


Figure III.4 – Left: time evolution of the analytical solution at $x^* = 1.5$ vs. the random parameter ξ . Right: comparison between the analytical solution and the sG-gPC₅ solution at $t = 0$ and $t \approx t^*$ for $x^* = 1.5$ (the left axis refers to $t \approx t^*$ and the right one to $t = 0$).

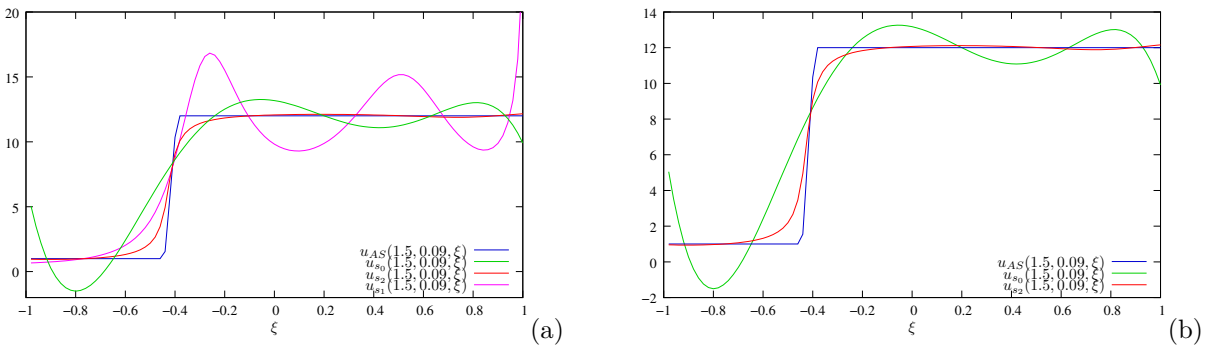


Figure III.5 – (a): analytical solution, IPMM₅ – s_0 , IPMM₅ – $s_1 - 0.5$ and IPMM₅ – $s_2 - 0.5 - 12.5$ at $x^* = 1.5$ and $T_f = 0.09 \approx t^*$. (b): Comparison between the analytical solution, sG-gPC₅ solution and IPMM₅ – $s_2 - 0.5 - 12.5$. Both pictures show solutions at $t = T_f = 0.0909 \approx t^*$ and $x^* = 1.5$ with respect to ξ . The number of grid cells is 100.

equivalent to the sG-gPC_P. Let us consider the entropy s_1 (III.46): the definition implies that u is constrained to $]u_-, +\infty[$ ³. On figure III.5, the oscillations of the s_1 -curve are controlled near u_- but are not controlled in the upper part of the domain. For the entropy s_2 , the definition domain of u is $]u_-, u_+[$ so that the oscillations are controlled on both sides of the random domain. Some oscillations still exist but they are forced to remain within the definition domain by construction, see figure III.5 (right).

Figure III.6 shows how the expansion order P affects the solution with respect to ξ . We notice that even for low polynomial approximation, the IPMM method constrains the oscillations to the domain $]u_-, u_+[$. Moreover, the approximation gets closer to the exact solution as the polynomial approximation order is increased. We recall that Burgers' equation satisfying a maximum principle, the choice of u_- and u_+ is done in function of the initial condition (see remark III.20): in our examples, we had to take $u_- < 1$ and $u_+ > 12$ as $\forall \xi \in [-1, 1], 1 \leq u(x, 0, \xi) \leq 12$.

In order to examine the results more quantitatively, we consider the IC_2 test-case in the next section to perform some convergence tests with respect to the polynomial order P for several values of the parameters u_- and u_+ . We will also compare the CPU times for both methods.

IC_2 test-case

The IC_2 initial condition is similar to the IC_1 but it bears a polynomial shape that insures continuity of the slope and the curvature, instead of an affine section between $x_0 + \sigma\xi$ and $x_1 + \sigma\xi$. This implies that the P -convergence is reached at $t = 0$ for low polynomial developments. However, the dynamics will become more challenging to capture as t tends to t^* . Indeed, despite the smooth nature of the solution and its derivatives for a finite time, this problem is still a numerically hard test-case as it exhibits very steep dependencies with respect to ξ at the space location $x = 1.4$ and at time $t = 0.06$.

We compare the performances of both method on this test case. We consider the relative error in the mean and the standard deviation taken over the whole physical space and the relative errors in the $L^1(\Omega)$ and $L^2(\Omega)$ -norms at $x = 1.4, t = 0.06$. Their expressions are for the sG-gPC and the IPMM are respectively:

3. $]a, b[$ denotes the open interval whereas (a, b) denotes the couple.

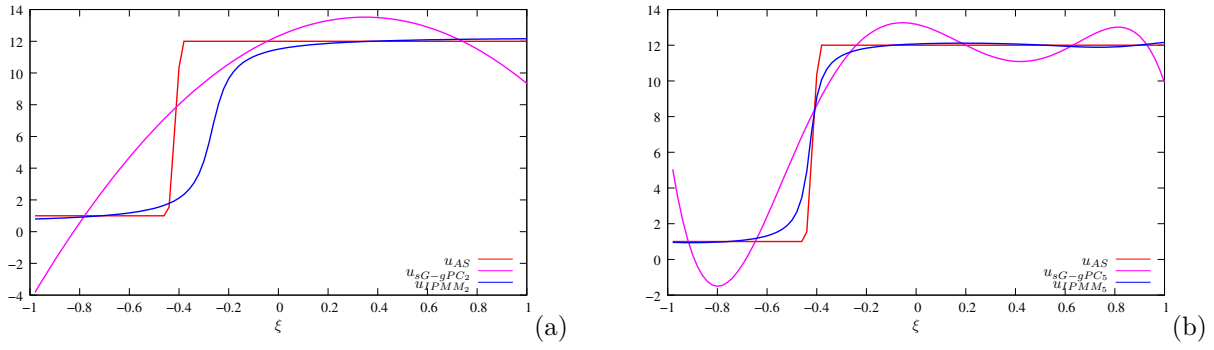


Figure III.6 – Comparison between analytical solution, sG-gPC_P and IPMM_P – s_2 – 0.5 – 12.5 for polynomial expansions $P = 2$ (a) and $P = 5$ (b) showing $u(x^*, t^*, \xi)$ for IC_1 with $x^* = 1.5$ and $t^* = 0.0909$.

$$e_{sG-gPC}^{L^j}(x, t) = \frac{\int |u_{ex}(x, t, \xi) - \sum_{i=0}^P u_i(x, t) \phi_i(\xi)|^j d_w \xi}{\int |u_{ex}(x, t, \xi)|^j d_w \xi}, j = 1, 2$$

$$e_{IPMM}^{L^j}(x, t) = \frac{\int |u_{ex}(x, t, \xi) - u(\sum_{i=0}^P v_i(x, t) \phi_i(\xi))|^j d_w \xi}{\int |u_{ex}(x, t, \xi)|^j d_w \xi}, j = 1, 2.$$

Figure III.7 shows that the IPMM_P errors for the mean and the standard deviation in the $L^2(\Omega)$ – and the $L^1(\Omega)$ –norm are always lower than the sG-gPC_P errors for all spatial discretizations. The figure also shows that IPMM presents a spectral convergence with respect to P for early polynomial orders: for 500 cells, the spectral convergence occurs up to $P = 4$, for 1000 cells up to $P = 5$ and for 2000 cells up to $P = 7$.

It shows that refining the spatial domain ensures spectral convergence up to higher polynomial orders. Besides, for higher polynomial orders, the errors have the same asymptotic behaviours: the limits depend only on the spatial discretizations and are the same for sG-gPC and IPMM. IPMM shows a faster convergence to this limit. Figure III.7 (bottom-left) compares the convergence tests for sG-gPC_P and IPMM_P – s_2 for several values of the pair (u_-, u_+) : the closer is the pair to the analytical solution’s extremal values, the more accurate is the solution. In practice, we have noticed that if u_- and u_+ are too close to the extremal values of the analytical solution, the problem of the minimization of the entropy is ill-posed. In practice, the remedy is to increase the polynomial order.

Figure III.7 (bottom right) compares the logarithm of the computational times for both methods (sG-gPC vs. IPMM – s_2 – 0.5 – 12.5) for the precedent discretizations. IPMM is more time consuming than sG-gPC. Indeed, it needs a minimization operation in addition to the classical steps. Nevertheless, the growth of the computational cost with respect to the polynomial order P is the same for both methods.

Table III.1 compares (for a given accuracy on the mean) the polynomial order, the accuracy on the standard deviation, the CPU time and the error in $L^1(\Omega)$ and $L^2(\Omega)$ –norm of both methods. Besides, for a given accuracy, IPMM needs a lower truncation order which is directly linked with the memory requirements: this is encouraging for higher stochastic dimension problems for which the number of polynomial moments grows exponentially fast.

	mean	std	CPU time	$L^2(\Omega)$ –norm	$L^1(\Omega)$ –norm	P
IPMM	3.1205×10^{-7}	2.541×10^{-5}	2min.15s.	5.3407×10^{-4}	1.06077×10^{-2}	7
sG-gPC	3.1128×10^{-7}	1.936×10^{-4}	7min.18s.	9.4370×10^{-4}	1.75344×10^{-2}	27
sG-gPC/IPMM	$0.9975 \approx 1$	7.62	3.5	1.76	1.652	3.5

Table III.1 – Computational speedups and accuracy of the IPMM compared to the sG-gPC approach for the stochastic Burgers’ equation. A 2000 grid cells spatial discretization is used and the level of stochastic approximation retained is chosen based on the mean solution accuracy level.

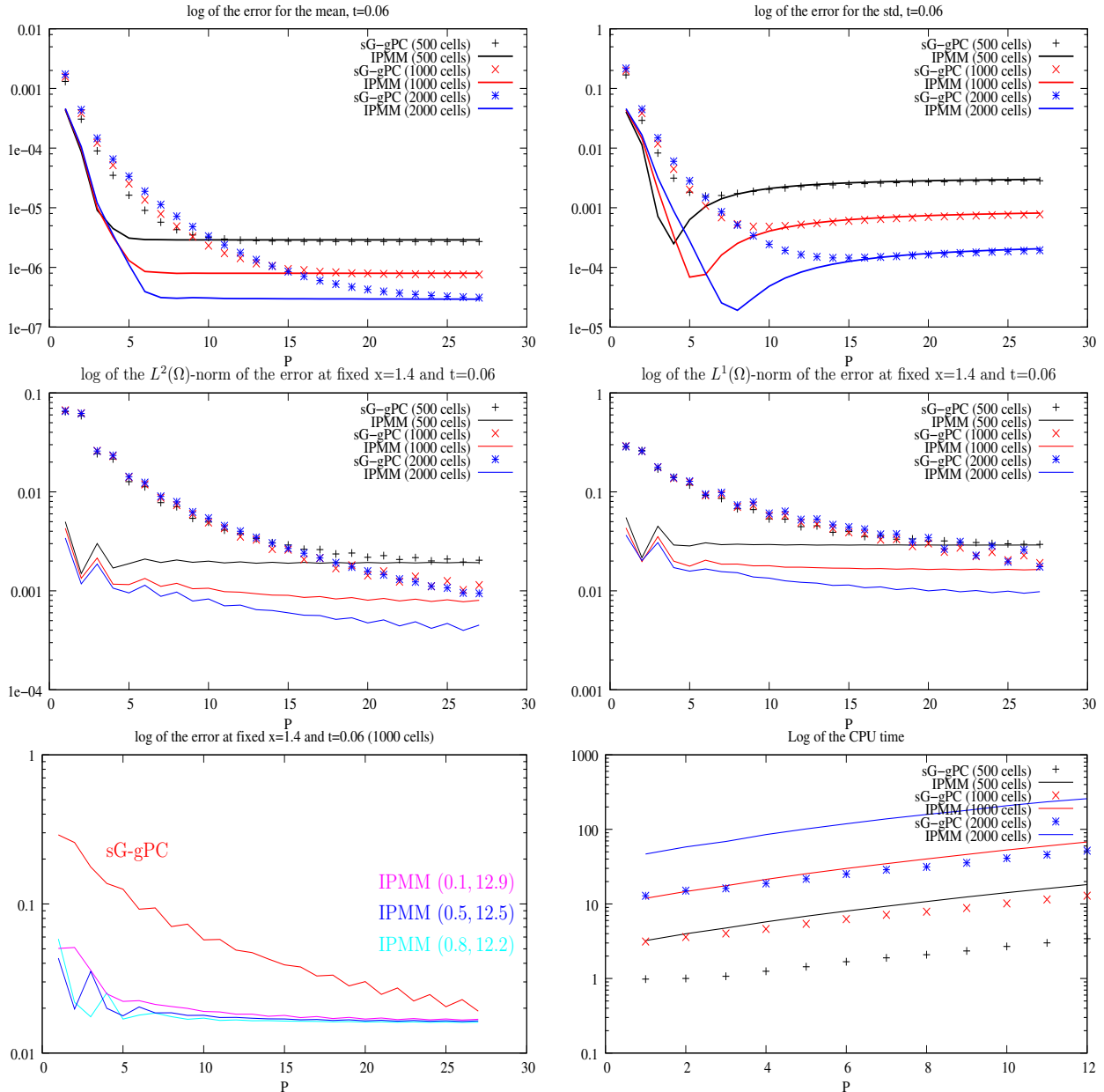


Figure III.7 – Convergence tests and corresponding CPU times for $sG-gPC_P$ and $IPMM_P$ for the resolution of the stochastic Burgers' equation with random initial condition IC_2 . Different spatial discretizations (500, 1000 and 2000 cells) are tested. Top: convergence tests at $t = 0.06$ for the mean (left) and the standard deviation (right) taken over the whole x -space. Middle: convergence tests at $t = 0.06$ and $x^* = 1.4$, $L^2(\Omega)$ -norm of the error (left) and $L^1(\Omega)$ -norm of the error (right). Bottom left: comparison between $sG-gPC_p$, $IPMM_p - s_2 - 0.1 - 12.9$, $IPMM_p - s_2 - 0.5 - 12.5$ and $IPMM_p - s_2 - 0.8 - 12.2$. Bottom right: CPU times vs. polynomial order P .

Burgers' equation in 2D random dimension

We consider a 2D initial condition illustrative of multiple shock flows encountered in compressible fluid mechanics. This scenario is encountered in the context of **Inertial Confinement Fusion** (ICF) flows where one wishes to maximize the compression rate of a fluid so that it reaches required temperature and pressure for ignition at one specific location. Therefore, a succession of multiple small shocks is preferable to be close to the isentropic limit (otherwise, in the case of a perfect gas, the maximum compression is limited to $\frac{\gamma+1}{\gamma-1}$). The IC_3 test-case tackles the issue of a succession of two shocks with uncertain left states, see figure III.8 (left). As t increases, the first shock reaches the second one to form a unique shock at time $t^* = 0.055$, see figure III.8 (right) for the time evolution of the solution for one realization of the random variables. This capture always happens whatever the realizations of the uncertain parameters are, as $\overline{K_0} + \sigma_0 \xi_0 > \overline{K_1} + \sigma_1 \xi_1, \forall (\xi_0, \xi_1) \in [-1, 1] \times [-1, 1]$. In the space of the uncertain parameters, the solution presents two or three different affine states depending on the position and time of interest, cf. figures III.9, III.10.

Remark III.21

|

The test case can be made stiffer by changing the values of σ_0 and σ_1 to increase the slope $\frac{\sigma_0}{\sigma_1}$ of the oblique shock in the (ξ_0, ξ_1) -space, see figure III.9.

The oblique shock, the fastest one, reaches the second one and overtakes it at time $t^* = 0.055$, see figure III.10 (top right picture).

We now compare sG-gPC and IPMM solutions in the random space. In the following, the solution is computed with 6000 cells (for both sG-gPC and IPMM), $CFL = 0.5$ and the polynomial order is 4–4; besides, for the IPMM, the entropy is s_2 and the pair (u_-, u_+) is $(0, 12.5)$. IPMM also involves the computation of 25×25 matrix in the minimization algorithm and a full 2D quadrature points grids (tensorised level 3 in the 1D Clenshaw-Curtis rule). Note that in higher stochastic dimension, the calculation could be optimized by using sparse grids or adaptative sparse grids for the numerical integration, see B.

Figure III.9 shows the analytical solutions (top pictures), the sG-gPC solutions (middle pictures) and the IPMM solutions (bottom pictures) at time $t = 0.0538$ and position $x = 0.785$ (left column) and at time $t = 0.054$ and position $x = 0.785$ (right column). We notice that the sG-gPC solution exhibits important oscillations whereas the solution from IPMM is more stable. Besides, the sG-gPC solution does not capture the intermediate state (state $u = 6$ for the analytical solution) whereas the state is clearly identifiable for the IPMM solution at the bottom left of figure III.9. The intermediate state is captured but some oscillations are generated in its vicinity. This is because IPMM controls better the oscillations at the bounds of the domain of u but less within the domain. Moreover, the fluctuating scales are not the same for both methods: the sG-gPC solution is going far below the 0-bound and the 12.5-bound as one can see on figures III.9 and III.10.

The results at time $t = 0.0545$ are given for $x = 0.791$ on figure III.10 (left column). At this time and position, the intermediate state is even harder to capture. The sG-gPC solution fails whereas the IPMM captures it. Besides, as the solution starts having steeper dependencies with respect to the uncertain parameters, the amplitude of the oscillations for sG-gPC are more important than on the previous figures. The phenomenon is even aggravated on figure III.10 (right column) for the final time for which the analytical solution consists in one step and oblique discontinuity with respect to the uncertain parameters.

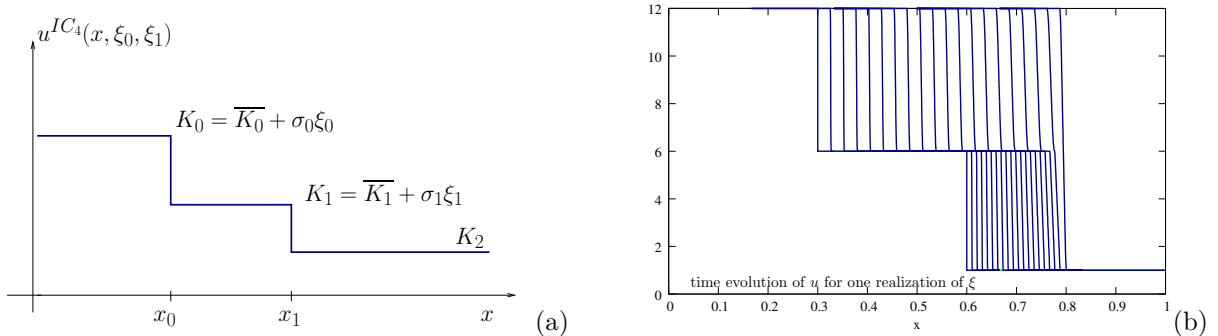


Figure III.8 – Initializations for test-case IC_3 (a) and time evolution of the solution for one realization of the random variables (b). We refer to [384] for details about the initial conditions and their respective analytical expressions.

Several tracks have been investigated in order to control the oscillations within the bounds defined by the entropy. We considered, for example, the possibility of defining several entropies depending on the space location of the discontinuities, in agreement with a global entropy over the whole domain. Discussion...

1.7.3 Compressible gas dynamics with uncertain initial conditions

Several test cases have been tackled with the numerical approach previously described: the one-dimensional version of a simple Riemann problem called *shock-tube problem* with random initial condition in the location of the interface is treated in [384]. The two-dimensional version of the shock-tube problem with uncertainty in the initial condition of the heavy fluid density and velocity is treated in [382].

In this section, we address the more difficult problem of the characterization of randomly perturbed interfaces between compressible fluids of different densities described by Euler equations. Our particular application leads to a fluid **Richtmyer-Meshkov Instability (RMI)** which is interesting from an uncertainty quantification/stochastic point of view (see [535, 253]) to test the robustness of the proposed method. RMI is generated when a shock wave refracts through the interface between two materials of different densities. Initial perturbations present on the interface grow in size and cause the materials to mix. RMI plays an important role in ICF where the geometry is often spherical or axisymmetric. We first describe the statistics of the perturbed interface position before propagating the uncertainty through the system described by Euler equations.

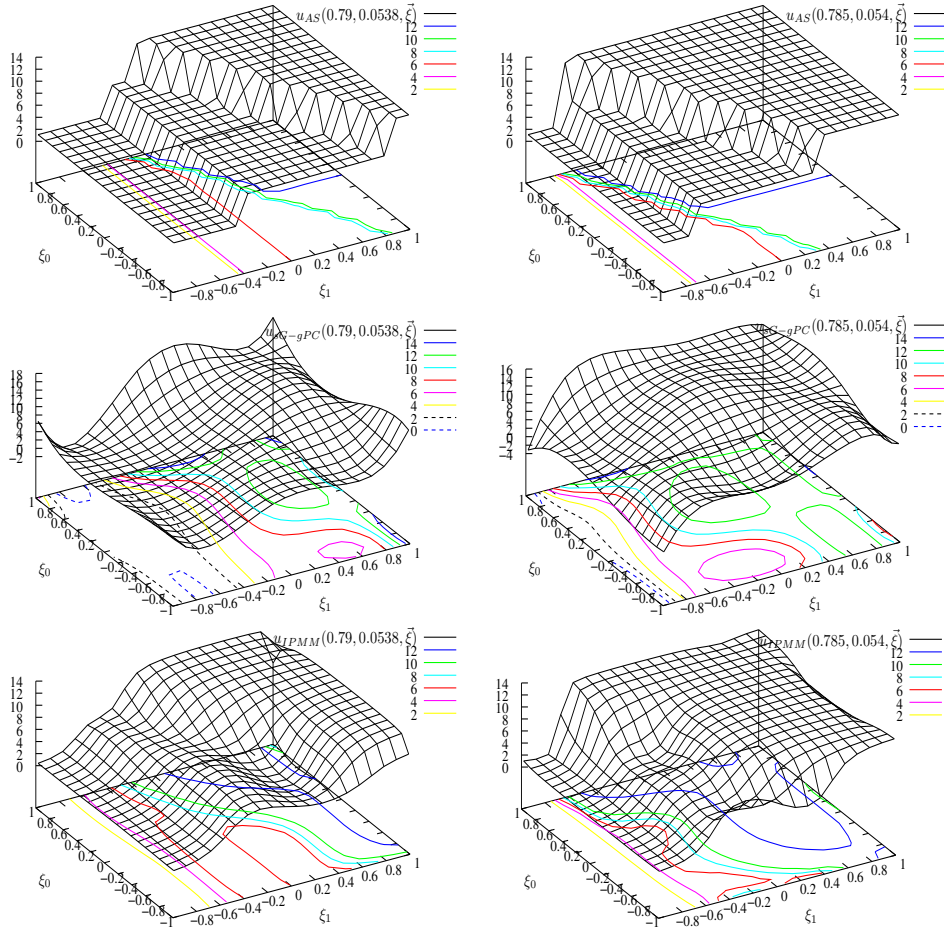


Figure III.9 – Burgers' response surfaces at $t = 0.0538$ and $x = 0.79$ (left column) and at $t = 0.054$ and $x = 0.785$ (right column). Analytical solution (top), sG-gPC (middle), IPMM (bottom). The IPMM solution is more accurate than the sG-gPC solution. On the sG-gPC figure, oscillations are not controlled, the solution goes above the upper state and beneath the lower one. The discontinuities are well located for the IPMM solution, this is characteristic of conservative schemes.

Randomly perturbed interface position

For this kind of applications, it is hard to have a complete knowledge on the shape of the material interface frontier at the beginning of the experiment. That is why we model the material interface location by a spatial SP: $(F_\theta)_{\theta \in [0, \frac{\pi}{2}]}$ of mean μ , variance σ^2 with the following covariance kernel, cf. Eq. (I.17):

$$K(\theta_1, \theta_2) = e^{-\frac{L}{c} |\theta_1 - \theta_2|}, \quad (\text{III.48})$$

where $L = \frac{\pi}{2}$ is the length of the simulation domain. We recall that r, θ are polar coordinates. Consequently, $r(x, y) = \sqrt{x^2 + y^2}$ and $\theta(x, y) = \arctan \frac{y}{x}$ (with $x, y \geq 0$). The correlation length is defined by $L_c = \frac{L}{c}$. The covariance kernel (III.48) is homogeneous, $K(\theta_1, \theta_2) = \tilde{K}(\theta_1 - \theta_2)$ and the correlation drop between two points directly relates to the value of L_c .

We use the Karhunen-Loève representation described in Section 2.1 to discretize the stochastic field. The KL expansion of $(F_\theta)_{\theta \in [0, \frac{\pi}{2}]}$ is given by:

$$F_\theta = \mu + \sigma \sum_{n=1}^{\infty} \sqrt{\lambda_n} g_n(\theta) \Xi_n, \quad (\text{III.49})$$

where

- the eigenvalues listed in decreasing order including: $i \in \{1, 2\}$

$$\lambda_n^i = \frac{2L_c}{(w_n^i)^2 + L_c^2}, \quad (\text{III.50})$$

with

$$\begin{cases} (w_n^1)_{n \in \mathbb{N}} \text{ are solutions of } L_c - w \tan\left(\frac{\pi}{4} w\right) = 0, \\ (w_n^2)_{n \in \mathbb{N}} \text{ are solutions of } w + L_c \tan\left(\frac{\pi}{4} w\right) = 0. \end{cases}$$

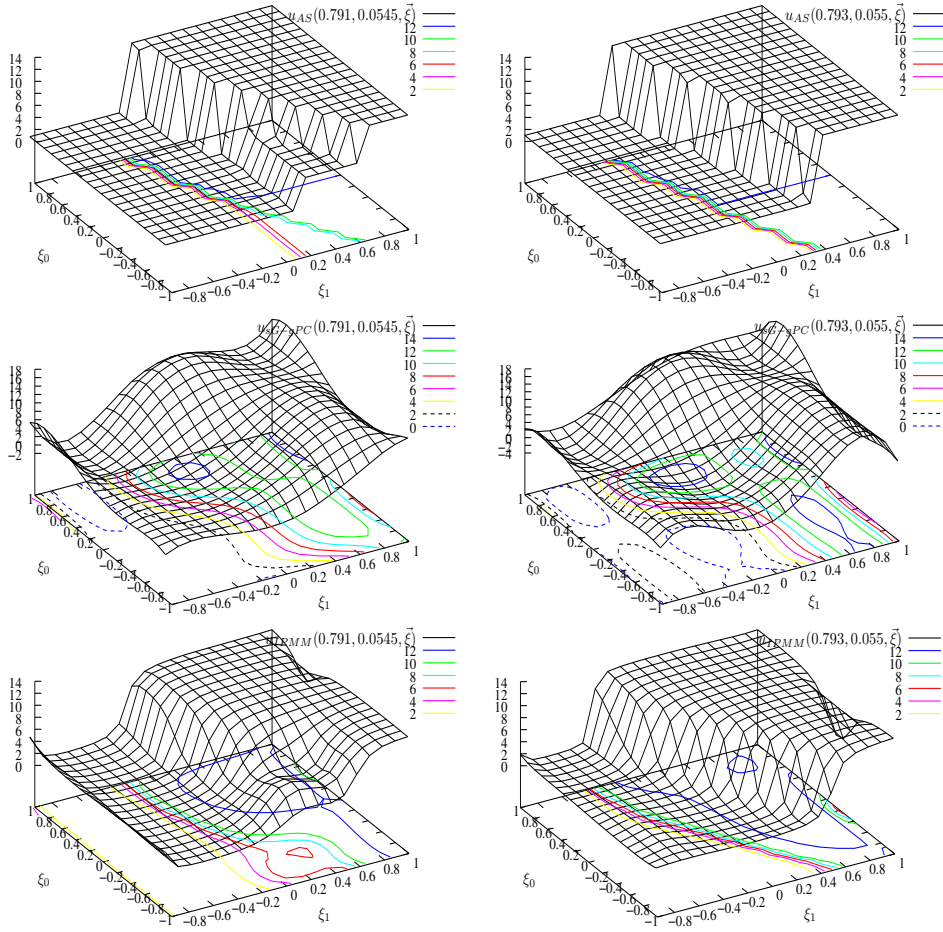


Figure III.10 – Burgers' response surfaces at $t = 0.0545$ and $x = 0.791$ (left column) and at $t = 0.055$ and $x = 0.793$ (right column). Analytical solution (top), sG-gPC (middle), IPMM (bottom). The IPMM solution is more accurate than the sG-gPC solution. For the IPMM solution, the discontinuities are well located and the solution captures the intermediate state (bottom left picture).

- the basis functions are reorganized according to the order of the eigenvalues so that $g_n \in \{g_n^1, g_n^2\}$ given by

$$g_n^1(\theta) = \frac{f_n^1(\theta)}{d(\theta)}, \quad \text{and} \quad g_n^2(\theta) = \frac{f_n^2(\theta)}{d(\theta)},$$

where

$$\left\{ \begin{array}{l} f_n^1(\theta) = \frac{\cos\left(w_n^1\left(\theta - \frac{\pi}{4}\right)\right)}{\sqrt{\frac{\pi}{4} + \frac{\sin(w_n^1\pi)}{4w_n^1}}}, \\ f_n^2(\theta) = \frac{\sin\left(w_n^2\left(\theta - \frac{\pi}{4}\right)\right)}{\sqrt{\frac{\pi}{4} - \frac{\sin(w_n^2\pi)}{4w_n^2}}}, \\ d(\theta) = \sqrt{\sum_{n=1}^{\infty} \lambda_n (f_n(\theta))^2 \text{var}(\Xi_n)}. \end{array} \right. \quad (\text{III.51})$$

The normalization factor $d(\theta)$ ensures a constant σ , $\forall \theta \in [0, \frac{\pi}{2}]$ if the KL development is converged.

- the definition of the uncorrelated RVs $(\Xi_n^i)_{i \in \{1,2\}, n \in \mathbb{N}}$ completes the characterization of the SP. Note that the construction of such basis $(\Xi_n^i)_{i \in \{1,2\}, n \in \mathbb{N}}$ for a given SP is not straightforward and remains an active research area, see [458] for example and references of section 2.1. Similarly to [533], we assume in the following that *uniform* iid RVs allow the characterization of the random input with satisfactory accuracy.

In practice, only a finite number Q of modes are retained in (III.49).

We consider the stochastic problem in axisymmetric geometry with perturbed interface position between a light and a heavy fluid as in [535]. The initial conditions are given by:

$$\begin{cases} \rho(x, y, 0, \Xi(\omega)) &= \begin{cases} 1 & \text{if } r \leq F_\beta^Q(\omega), \\ 0.125 & \text{otherwise,} \end{cases} \\ \rho u(x, y, 0, \Xi(\omega)) &= 0, \\ \rho v(x, y, 0, \Xi(\omega)) &= 0, \\ \rho e(x, y, 0, \Xi(\omega)) &= \begin{cases} 2.5 & \text{if } r \leq F_\beta^Q(\omega), \\ 0.25 & \text{otherwise,} \end{cases} \end{cases} \quad (\text{III.52})$$

and are illustrated in figure III.11 (left). At $t = 0$, the fluids are at rest and $\gamma = 1.4$: it corresponds to a stochastic Riemann Problem. For $t > 0.37$, see figure III.11 (right), an ‘‘uncertain shock’’ reflects at the center of the domain and hits the perturbed interface, affecting strongly the topology of the frontier shape.

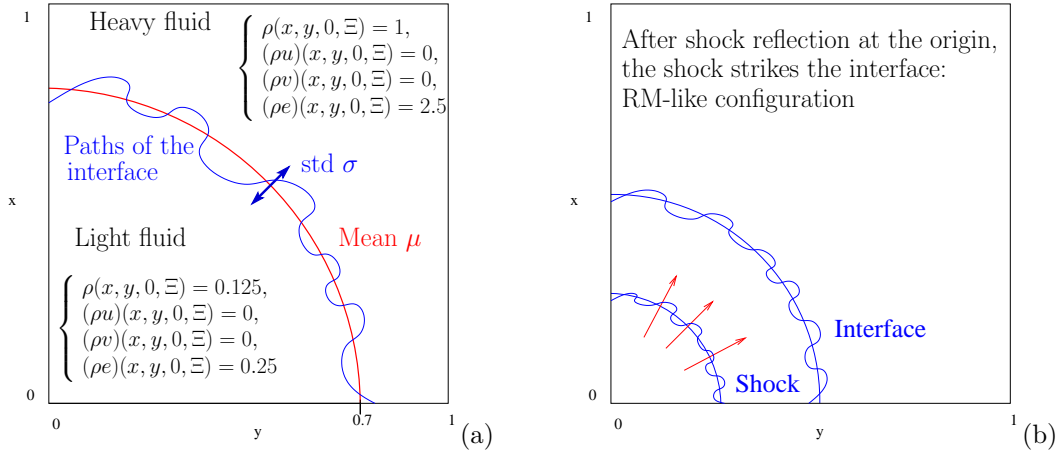


Figure III.11 – Schematics of the stochastic RMI dynamics (flow scales are not respected). (a): random initial conditions of the stochastic Riemann problem with perturbed interface. Then an inward shock goes through the interface and (b): after a certain time ($t > 0.37$) it reflects at the origin and bounces back to hit the interface leading to a RMI type of flow.

Initialization Procedure

An important aspect of the stochastic simulation involves the correct initialization of the computation. The initial conditions being described by the random vector Ξ modeling the uncertainty, accurate gPC modes must be fed for the quantities $\rho, \rho u, \rho v$ and ρe .

In the following, we detail the initialization procedure for some arbitrary random mode $(\rho\psi)_k$ where $\psi \in \{1, u, v, e\}$. We denote by $(\rho\psi)_{k,i,j}^0$ the (spatial) mean of the moment $(\rho\psi)_k$ on the cell i, j of volume $\Delta x_i \times \Delta y_j$ at time $t = 0$. With the FV formulation, we have

$$(\rho\psi)_{k,i,j}^0 = \frac{1}{\Delta x_i \Delta y_j} \int_{i-\frac{1}{2}}^{i+\frac{1}{2}} \int_{j-\frac{1}{2}}^{j+\frac{1}{2}} (\rho\psi)_k(x, y, 0) dx dy, \quad (\text{III.53})$$

with

$$(\rho\psi)_k(x, y, t) = \mathbb{E}[(\rho\psi)(x, y, t, \Xi) \Phi_k(\Xi)]. \quad (\text{III.54})$$

By commuting the FV formulation and Galerkin projection on the polynomial basis, we obtain

$$(\rho\psi)_{k,i,j}^0 = \mathbb{E}\left[\frac{1}{\Delta x_i \Delta y_j} \int_{i-\frac{1}{2}}^{i+\frac{1}{2}} \int_{j-\frac{1}{2}}^{j+\frac{1}{2}} (\rho\psi)(x, y, 0, \Xi) dx dy \Phi_k(\Xi)\right], \quad (\text{III.55})$$

which we compact in:

$$(\rho\psi)_{k,i,j}^0 = \mathbb{E}\left[\overline{(\rho\psi)_{i,j}^0(\Xi)} \Phi_k(\Xi)\right]. \quad (\text{III.56})$$

In practice, the expectation is evaluated thanks to high-order numerical quadratures.

Numerical results

In the following sections, we present the results for random interfaces characterized by different levels of correlation L_c and for a fixed std ($\sigma = 0.08$). The goal is quantify the effect of the change in the correlation length on the flow statistical response. For each computation, the mean of the SP is $\mu = 0.7$ and the length of the domain is $L = \frac{\pi}{2} \approx 1.5708$ corresponding to a quarter of a circle. Simulations are performed with 200×200 cells. The scheme used is presented in appendix B. The boundary conditions are of “non-reflective” kind on the upper and right boundaries and are of “wall” kind on the lower and left boundaries. The number of quadrature points required in the computations is chosen to ensure the strict convexity of the functional \tilde{T} to minimize. For the chosen stochastic dimensions ($Q = 2, 3, 4, 5$), Legendre quadrature (full tensorization) is chosen to integrate exactly polynomials of order $2N+1$ with N points. For higher dimensions, Smolyak-Legendre points (cf. Section 2.2.2) are used.

The reference simulation is obtained for $L_c = \infty$. Indeed, this case corresponds to the limit F_β being a RV rather than a RP: $F_\beta^{Q=1} = 0.7 + 0.08 \Xi$ where Ξ is uniformly distributed. We set the truncation order to $P = 20$. The results are displayed in figures III.12 and III.13 and show the same quantities at the same times (figure III.13 is only a cut along the first bisector of the plots of figure III.12). In the following, our analysis will focus on mass density visualizations as it is the most interesting quantity. Indeed pressure and velocity fields remain continuous across the interface.

For one path of the interface, as time increases, a shock (1st wave) propagates in the light fluid toward the origin and a rarefaction fan (2nd wave) propagates in the heavy fluid. Both fluids are still separated by a contact discontinuity (3rd wave). The three waves are affected by the uncertainty originally present in the interface. Figure III.12–III.13 shows the moments of the mass density at times $t = 0.185$ and $t = 0.222$ for which the three waves are easily identifiable, especially in the right columns of figures III.12–III.13: the waves are separated by areas of low variance. This is interpreted as a stochastic Sod shock tube. Between time $t = 0.222$ and time $t = 0.74$, the uncertain shock hits the boundaries at the origin and reflects to go back and pass through the interface. This configuration is typical of a RMI problem.

Note that during that time, the rarefaction fan exists the domain through the “non-reflective” boundary conditions. At time $t = 0.74$, figures III.12–III.13 (bottom), the shock (cf. outermost crown in the vicinity of $r = 0.5$) has gone through the interface (innermost crown in the vicinity of $r = 0.3$). At this stage, mass density variability is very strong though confined into small regions of space.

An important concern is the impact of a correlation length shortening (at constant fluctuation amplitude σ) on the flow statistics. In the following, we test three shorter correlation lengths: $L_c = (3.14, 1.74, 0.31)$ and make sure that the chosen stochastic discretization is as accurate as possible in representing both random input and outputs. A careful analysis of the KL representation spectrum (via convergence analysis of the eigenvalues) prescribes the dimensionality of the stochastic approximation basis to use. We conclude that we should use $Q = 3$, $Q = 5$ and $Q = 10$ for $L_c = (3.14, 1.74, 0.31)$, respectively. Unfortunately, due to memory requirements, we are only able to use up to $Q = 5$ for the last case.

Some of the results are summarized in figures III.14 that show spatial distributions of the fluid mass density *variance* at different instant of times and for different correlation lengths. We notice that as the typical wavelength of the initial interface perturbation decreases, areas where the mass density is likely to be variable are not exactly at the same positions. For instance, at early times, the shape of the uncertain region associated with the rarefaction fan is different. Indeed, due to the random wave speeds combined to the chaotic nature of the flow, the different waves behave differently and become harder to distinguish. For instance, we point to the “overlap” region of strong variability around $r = 0.45$ in figure III.14-(b) at $t = 0.185$. At late times, strongest variability are obtained in the vicinity of the shock waves. In these regions, stronger, but less organized density variabilities are obtained for shorter correlation lengths. Moreover, smaller irregularities of the initial interface induce smaller flow scales fluctuations, once the reflected shock wave has passed through the material interface, cf. realizations of the interface frontier in figures III.14-(d-e-f). This induces a spreading or “mixing” of the interface frontier over a larger portion of space, justifying the decrease in the variance of the fluid density.

Remark III.22

It is not clear at the time if the loss of axisymmetry in the case of $L_c = 0.31$, cf. figures III.14-(c-f), is fully related to the physical sensitivity of the system or due to numerical truncation error. Indeed, we recall that the stochastic dimensionality (i.e. $Q = 10$) imposed by the correlation length was too large to be handled with our numerical approach.

The physical interpretation on the mixing zone may be refined if one looks at the mass density pdf in the vicinity of the material interface. Figure III.15 shows the pdfs of the mass density at $t = 0.74$, and the same space locations, $x = y = 0.3525$ for all cases. For the reference solution (figure III.15-(a)), $\rho(x, y, t, \Xi)$ behaves like a mixed discrete/continuous RV: indeed, the pdf shows one Dirac mass near $\rho \approx 0.85$ and has a continuous

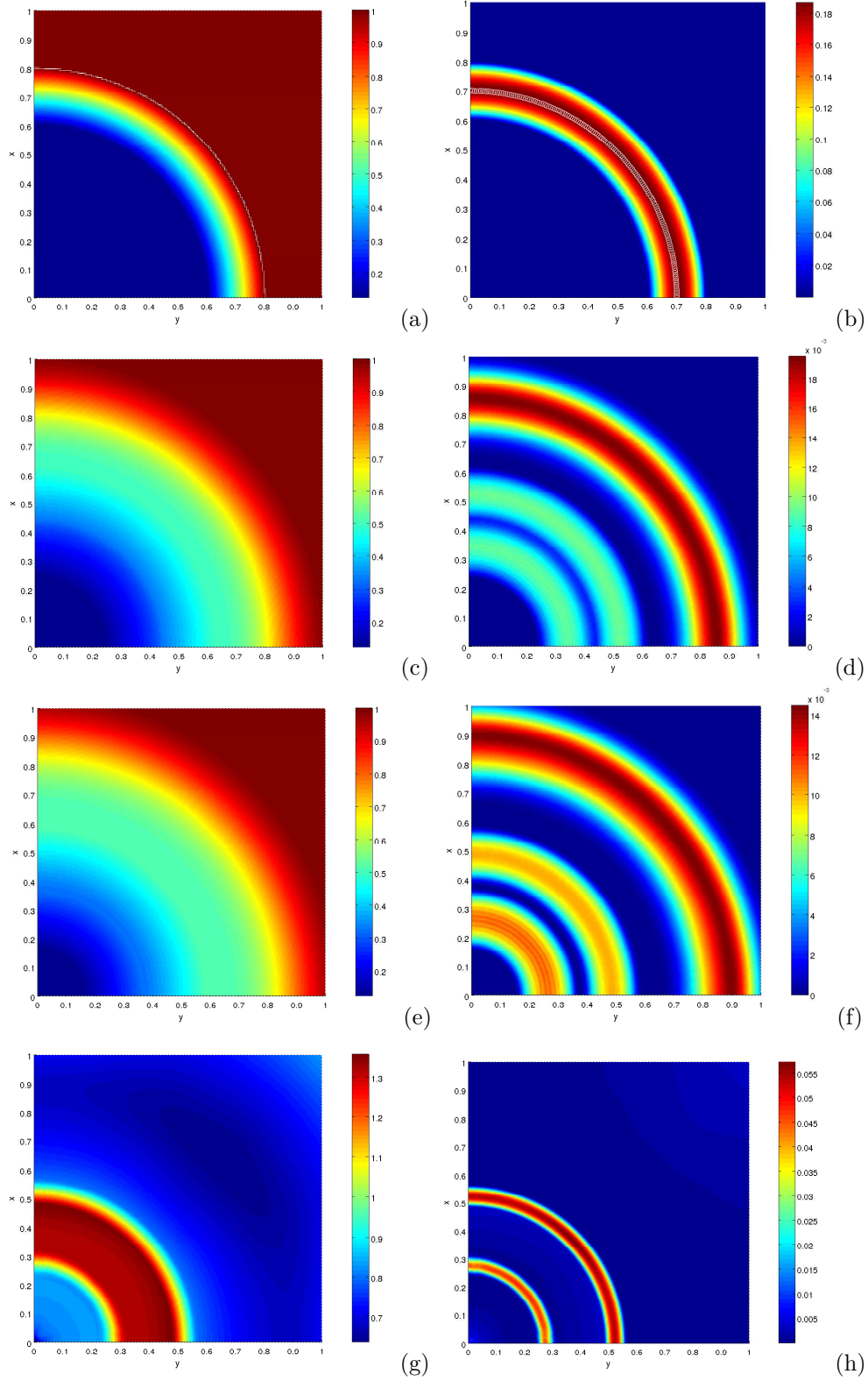


Figure III.12 – Spatial distributions of ρ mean (left) and variance (right) at different times of the simulation, with uncertain initial interface position $F_{\theta}^{Q=1}$ corresponding to $\mu = 0.7$, $\sigma = 0.08$ & $L_c = \infty$; (a-b): $t = 0$, (c-d): $t = 0.185$, (e-f): $t = 0.222$, (g-h): $t = 0.74$.

behavior for $1.25 \leq \rho \leq 1.45$. This is expected as the region of strong uncertainty are very confined. For shorter correlation lengths, the support of the pdfs widens and the distributions tend to be more uniform and not as peaked. Even if it is hard to study only one location in the domain (though at the same computational time), as this point might not be located in the vicinity of similar flow physics due to the difference in propagation and refraction time, one trend emerges: less correlated (i.e. noisier) initial material interfaces induce a wider

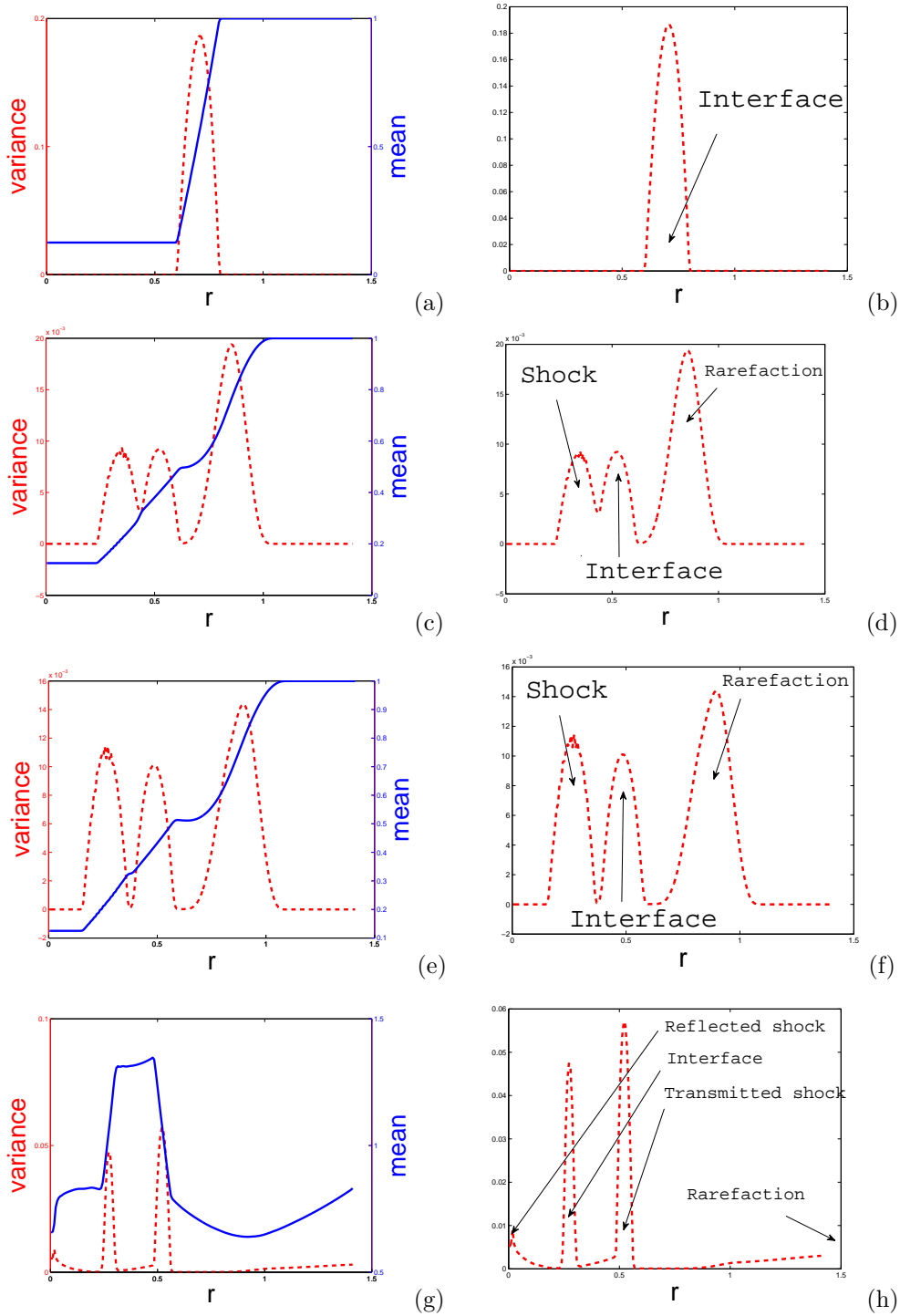


Figure III.13 – Radial distributions (left) and interpretations (right) of ρ moments at different times (it corresponds to a cut along $\beta = \frac{\pi}{4}$ of the plots of figure III.12; (a-b): $t = 0$, (c-d): $t = 0.185$, (e-f): $t = 0.222$, (g-h): $t = 0.74$).

and smoother spectrum of probable flow scales and mass densities in the vicinity of that interface later on.

1.8 Closing remarks

The nonlinear Galerkin-type projection method introduced in this section seems a promising approach for stochastic nonlinear hyperbolic problems but some key aspects may impair its flexibility and require some discussion.

The choice of the entropy pair requires quite specific *a priori* knowledge about the solution bounds for the method to have any appreciable advantage. While this seems a potential drawback of the method, it is not a

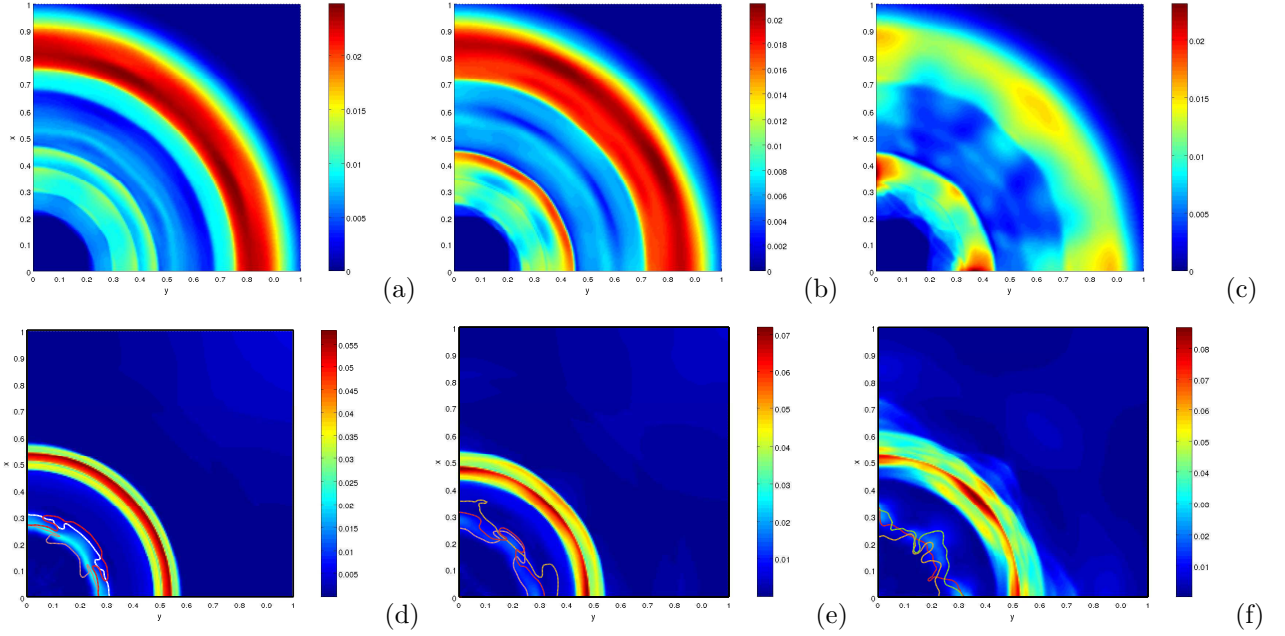


Figure III.14 – Influence of the correlation length L_c of the initial random interface on the mass density variance at early $t = 0.185$ (top) and late $t = 0.74$ (bottom) times; (a-d): $L_c = 3.14$, (b-e): $L_c = 1.74$, (c-f): $L_c = 0.31$. Several realizations of the interface frontier are added on top of the bottom contour plots.

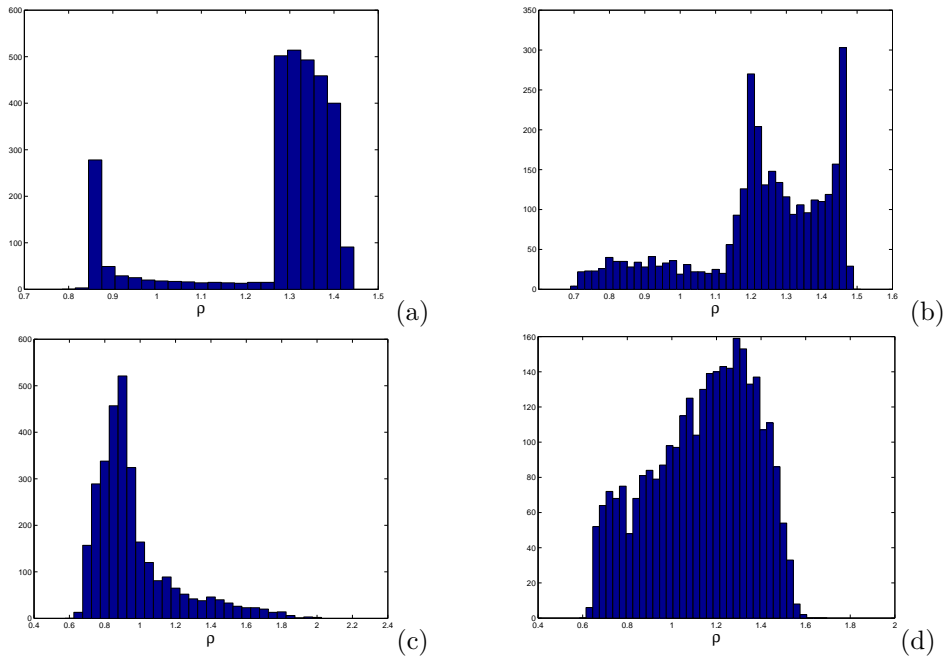


Figure III.15 – Mass density pdf in the probable vicinity of the material interface (here empirically chosen at $x = y = 0.3525$) at time $t = 0.74$; (a): $L_c = \infty$, (b): $L_c = 3.14$, (c): $L_c = 1.74$, (d): $L_c = 0.31$.

problem for scalar systems of conservation laws thanks to the maximum principle for the entropic solution. In this case, it becomes easy to carefully tune the parameters u_- and u_+ involved in the entropy expression. This is not as straightforward for other (non-scalar) system of conservation laws such as compressible gas dynamics (cf. Euler system in Section 1.6). In this case a possible choice for the entropy is the mathematical entropy which is the opposite of the physical entropy, cf. Eqs (III.34-III.35).

There exists in fact different choices of entropy for Euler systems. Indeed, if $h : x \rightarrow h(x)$ is such that $h'(x) \leq 0$ and $\gamma h''(x) + h'(x) \geq 0$, then $\tilde{s}(\rho, \rho u, \rho e) = -\rho h(s(\rho, \rho u, \rho e))$ is also an entropy for the system, see [437]. We have not tested other entropies because our choice implicitly imposed physically meaningful bounds to the solution, precluding for instance negative oscillations of the mass density and the internal energy [384].

Several tracks have also been investigated in order to control the oscillations *within* the bounds defined by the entropy: e.g. the possibility to define several entropies depending on the space location of the discontinuities, in agreement with a global entropy over the whole domain (the different local entropies enabling to control the oscillations within the range defined by the global entropy and not only at the bounds of the domain).

Another key point in the application of this method is the computational cost associated to the minimization step required in each cell and for every time step. This numerical overhead is $> 50\%$ of the total cost. Aside from relying on more elaborate and efficient minimization algorithms, one possible tradeoff is to apply the technique only whenever the non-smoothness of the solution needs it but otherwise solve the problem with the traditional gPC approach. This adaptive “hybrid” spectral approach was investigated and further extended to a coupling with Monte-Carlo sampling techniques in [385].

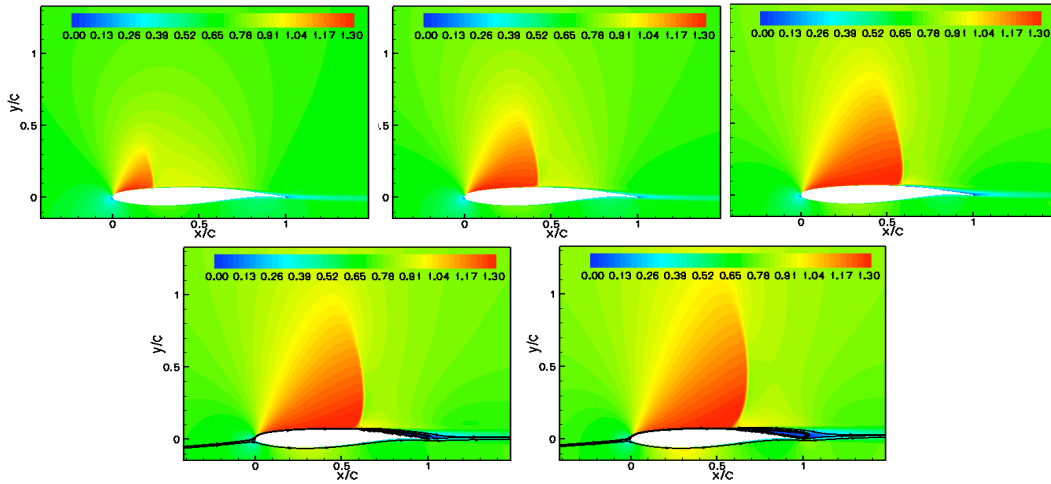


Figure III.16 – Mach number isocontour fields around an OAT15A airfoil (at constant angle of attack) for 5 different (increasing) inflow Mach number M_∞ operating conditions. Any uncertainty on the value of M_∞ has obviously a strong influence on the supersonic region width and the terminal shock position.

2 Stochastic investigation of uncertain transonic aerodynamics

The development of design methodologies, with respect to minimum sensitivity to inherent fluctuations of the operating conditions or to manufacturing process, is of crucial importance in aeronautics and aerospace engineering. Nonlinear aerodynamic or aeroelastic systems subject to random parameters can result in poor off-design performances or may exhibit losses of dynamic stability. UQ plays an important role in reliability assessment. Such analysis can be viewed as the determination of error bars to be assigned to the numerical solution algorithms and its application is of great importance in reliability assessment.

Probabilistic collocation methodologies are promising candidates to get more insights in physical mechanisms of flutter and Limit Cycle Oscillations (LCO) for example [374, 32] with affordable computational cost [513, 516, 312]. These studies are generally based on the use of *ad hoc* inviscid linear aerodynamics while the stochastic response of the system is governed by the uncertainties associated to the nonlinear structural stiffness coefficients [330, 312].

Another challenging and complementary task is the development of numerical method for stochastic fluid structure interaction problems based on CFD tools. The prediction of a transonic flow around a 2D clean wing in the presence of external flow related uncertainties is of great interest for aerospace engineering related studies. Here, the aim is to characterize the effect of variabilities in the operating conditions when the aerodynamic operator is strongly affected by nonlinearities due to transonic effects [270] or dynamic stall effects [517]. For the sake of convenience, the influence of the aeromechanical coupling is often neglected in this case. Instead, the emphasis is put on the features of the Reynolds-averaged mean flow, which are the useful and meaningful data used for aerodynamic analysis and shape optimization. For such an analysis, global or oversimplified surrogate models are no longer relevant, and high fidelity Navier–Stokes simulations must be carried out, since engineers are interested in getting a detailed prediction of the flow structure for shape optimization purposes.

Figure III.16 from [443] is a good example of the sensitivity of a compressible (here transonic) flow to operating conditions. It shows the Mach number isocontour fields for five different inflow Mach numbers M_∞ ranging from $0.73(1 - 8\%)$ to $0.73(1 + 8\%)$ with an increment of 4% and a common incidence of $\alpha = 2.5$ degrees. In all cases a supersonic area (in red) is present on the leeward side. This supersonic region ends with a shock downwards. As the Mach number increases, the supersonic region widens with the terminal shock moving downwards to a limit value. Once this limit value has been reached (for $M_\infty \approx 0.73$), a separated area (in blue) appears along the foil to the right of the shock and expands as the inflow Mach number increases. By opposition, the windward side evolves very little and does not exhibit any nonlinear features.

In the following, stochastic investigations on transonic flows around a NACA0012 and a OAT15A airfoils are proposed for the propagation of multiple aerodynamic uncertainties through transonic flows with possibly separated shear-layers. The uncertain parameters under consideration are the free-stream Mach number and the angle of attack. The variability of these parameters can be attributed to inherent randomness due to free-stream turbulence and/or aeroelastic deformations of the structure. First, we intend to demonstrate the efficiency and robustness, as well as to point to the limitations, of the non-intrusive stochastic projection approach with flows presenting shock-waves and separation regions. Second, we intend to highlight the potential importance of considering multiple uncertainties concomitantly, with possibly different random distributions, on the stochastic

response of the system. Finally, differences between the symmetric (i.e. NACA0012) and non-symmetric (i.e. OAT15A) airfoils stochastic responses are examined. Stochastic results are analysed in details by means of various post-processings of the stochastic aerodynamic field, including error bars, probabilistic density function and sensitivity analysis.

For each case, a deterministic compressible solver is coupled to a non-intrusive stochastic spectral projection method to propagate the aerodynamic uncertainties. The stochastic model is solved in a generalized Polynomial Chaos framework.

Due to the choice of uniform and/or truncated Gaussian distributions for the inputs and without any *a priori* knowledge of the outputs pdf solution, appropriate basis from a mathematical point of view are the Legendre polynomials (*uniform*) [523], the Jacobi polynomials (beta) [527], or the Legendre-Jacobi mixed polynomial basis.

2.1 Stochastic transonic flows past a NACA0012 airfoil

In this section, the non-intrusive stochastic projection formulation is applied to the propagation of several aerodynamic uncertainties through a transonic steady flow around a NACA0012 airfoil. The deterministic CFD solver is described in the next section and the stochastic model and analysis are presented in section 2.1.2. Different bounded distributions for the parameters such as *uniform* distributions and some extension to non-*uniform* distributions are investigated.

2.1.1 Deterministic flow computations

The deterministic steady-state flow solutions are computed using a Favre-Reynolds-averaged Navier-Stokes solver and a near-wall wall-normal-free Reynolds-Stress model[152, 151]. The governing equations are discretized using a $O(\Delta x^3)$ finite volume upwind-biased MUSCL scheme and the time integration is based on an implicit dual-time-stepping procedure with alternating direction implicit subiterations [66]. This solver has been validated for various steady and unsteady flow configurations [152, 66, 67]. All computations performed in this work were obtained using the following CFL numbers: $CFL = 100$ for the time step and $CFL^* = 10$ for the dual pseudo time step. The number of sub-iterations is chosen dynamically. A complete description of the pseudo-time implicit dual-time-stepping algorithm can be found [66].

The computational mesh is based on a structured O-grid with 301 grid points around the airfoil and 151 points in the radial direction [67]. The chord is $c = 0.1$ m and the far-field boundary is placed at $d = 20c$ from the airfoil. The minimum non-dimensional grid spacing at the wall is $y_w^+ < 0.3$. A geometric progression ratio of $r_j = 1.35$ is used to stretch the computational grid in the radial direction. The geometric progression ratio used near the leading edge and the trailing edge are $r_{i_{LE}} = 1.16$ and $r_{i_{TE}} = 1.3$, respectively. At the far-field, the total temperature is taken to be $T_{t_\infty} = 280$ K and the total pressure to $p_{t_\infty} = 382197.9$ Pa. The turbulence-intensity T_{u_∞} and the turbulence-length-scale ℓ_{T_∞} are respectively set to $T_{u_\infty} = 0.8\%$ and $\ell_{T_\infty} = 0.1$ m.

2.1.2 Combined free-stream Mach number and angle of attack uncertainties

Here, the stochastic flow model is based on the uncertainty propagation of two random disturbances associated to the angle of attack α and the free-stream Mach number M_∞ . These two parameters were selected because they are classically used in the context of robust design of airfoils. It is obvious that from the point of view of aeroelastic investigations, the choice of these uncorrelated variables results in a crude model since no aeromechanical coupling is assumed.

A critical point which arises when dealing with UQ is how to model the uncertain parameters. We prefer to first consider *uniform* distributions for both parameters. This choice means that we do not favor any particular parametric value within the domain of interest. Moreover, this choice is the maximum entropy distribution for any continuous random variable on an interval of compact support. In other words, an assumption of any other prior distribution satisfying the constraints will have a smaller entropy, thus containing more information and less uncertainty than the uniform distribution [209].

Hence, considering $\Theta = [\Theta_1(\omega), \Theta_2(\omega)]^T$ where Θ_1 and Θ_2 are associated to α and M_∞ respectively, any aerodynamic variable $q(\mathbf{x}, \Theta_1, \Theta_2)$ is then approximated, thanks to the gPC representation, by the following expansion

$$q(\mathbf{x}, \Theta_1, \Theta_2) = \sum_{j=0}^{Q-1} \hat{q}_j(\mathbf{x}) \phi_j(\Theta_1, \Theta_2), \quad (\text{III.57})$$

Table III.2 – Characteristics of the studied stochastic flow regimes based on uncertain angle of attack and free-stream Mach number

case	μ_α (deg)	σ_α (deg)	Θ_1	μ_{M_∞}	σ_{M_∞}	Θ_2	dominant flow regime
<i>A</i>	3	1	<i>uniform</i>	0.55	0.05	<i>uniform</i>	high subsonic
<i>B</i>	3	1	<i>uniform</i>	0.65	0.05	<i>uniform</i>	transonic
<i>C</i>	5	1	<i>uniform</i>	0.55	0.05	<i>uniform</i>	transonic
<i>D</i>	5	1	<i>uniform</i>	0.65	0.05	<i>uniform</i>	transonic with separation

and the random inputs are defined with their mean values μ and standard deviations σ

$$\begin{aligned}\alpha &= \mu_\alpha + \sigma_\alpha \Theta_1 \\ M_\infty &= \mu_{M_\infty} + \sigma_{M_\infty} \Theta_2\end{aligned}\quad (\text{III.58})$$

We pick $\sigma_\alpha = 1$ deg and $\sigma_{M_\infty} = 0.05$. The range of α is representative of typical amplitudes of static deformations observed on flexible wings with a NACA0012 section at similar operating points [342, 363]. The variation interval of the free-stream Mach number ($M_\infty = \mu_{M_\infty} \pm 0.05$) is relevant to typical operating ranges used for the study of robust shape optimization problems [112, 364]. In the present study, a parametric stochastic analysis was conducted using different mean values of the uncertain parameters α and M_∞ . These conditions are reported in Table III.2. As a consequence, the global parametric range covered by the 4 stochastic flow regimes corresponds to $2 \text{ deg} \leq \alpha \leq 6 \text{ deg}$ and $0.5 \leq M_\infty \leq 0.7$. The corresponding Re range is $4.1 \times 10^6 \leq Re \leq 5.2 \times 10^6$. Note that the present operating range excludes the buffet boundary of the NACA0012 airfoil identified experimentally by Bartels [23] for the same range of Reynolds numbers.

The first configuration, namely *case A*, corresponds to highly subsonic flow conditions at low incidence ($\mu_\alpha = 3$ deg, $\mu_{M_\infty} = 0.55$). The next two stochastic operating ranges (*case B* and *case C*) are likely to include shock wave effects at moderate angle of attack (*case B*: $\mu_\alpha = 5$ deg, $\mu_{M_\infty} = 0.55$) or at higher Mach number (*case C*: $\mu_\alpha = 3$ deg, $\mu_{M_\infty} = 0.65$). Finally, *case D* ($\mu_\alpha = 5$ deg, $\mu_{M_\infty} = 0.65$), is likely to include flow realizations with a separated shear layer on the suction side of the airfoil in addition to shock waves. Each stochastic computation was performed using $n_q = 8$ Gauss-Legendre quadrature points per random dimension. The corresponding stochastic $n_q \times n_q$ grids of the uncertain parameter space (α, M_∞) are shown in Figure III.17. The results in the next sections were obtained using a 7th order gPC expansion (i.e. $P = 7$).

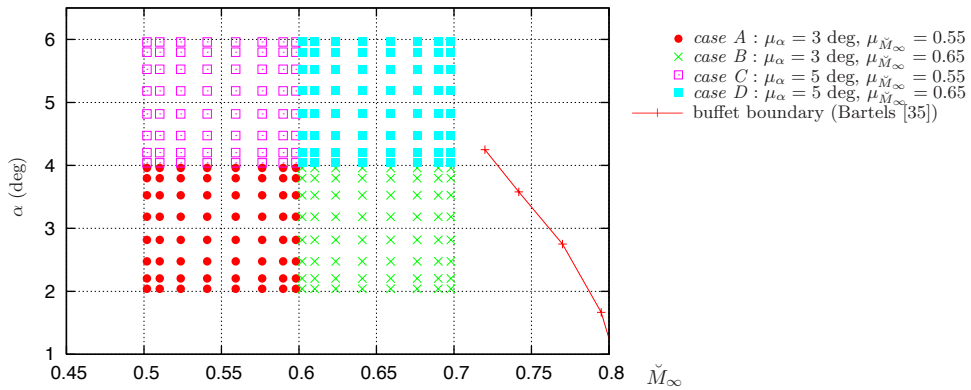


Figure III.17 – Gridding of the aerodynamic (α, M_∞) parameter space corresponding to the four stochastic flows described in Table III.2 and buffet boundary of the NACA0012 airfoil [23]. The computational grid totals up to 4×64 RSM-RANS simulations.

Analysis of the stochastic flows for *uniform* distributions

The first two statistical moments of the lift and drag forces are summarized in Table III.3 for the flow regimes depicted in Table III.2. Here, the mean and the coefficient of variation ($c_v = \sigma/\mu$) of the lift-to-drag ratio L/D are chosen as representative indicators of the global aerodynamic performance of the airfoil. We notice that the stochastic conditions of highest efficiency (*case C*, $\alpha = 3$ deg, $M_\infty = 0.55$) correspond to the lowest sensitivity level of L/D due to the input uncertainties, cf. Table III.3. As expected, *case D* ($\alpha = 5$ deg, $M_\infty = 0.65$)

Table III.3 – Statistical moments (mean and standard deviation) of the lift and drag forces and (mean and coefficient of variation: $c_v = \sigma/\mu$) of lift-to-drag ratio C_l/C_d obtained for the four stochastic flows described in table III.2

case	μ_L (N)	σ_L (N)	μ_D (N)	σ_D (N)	μ_{C_l/C_d}	$c_{v,C_l/C_d}$ (%)
A	2651	592	70	7	37.6	15.6
B	3847	825	106	30	36.9	14.2
C	4397	678	88	18	50.5	6.8
D	5989	628	229	102	30.3	32.9

exhibits the minimum value of $\mu_{L/D}$ but in conjunction with the highest variability level, therefore making it the most challenging case.

Figure III.18 shows the mean and the standard deviation of the Mach number obtained for *case D*. The mean Mach number field is illustrated in Figure III.18(a). We notice that shock discontinuities are smoothed out due to the uncertainty. It then becomes impossible to distinguish the discontinuities associated to the shock waves, resulting in substantial modifications of the mean value of the solution.

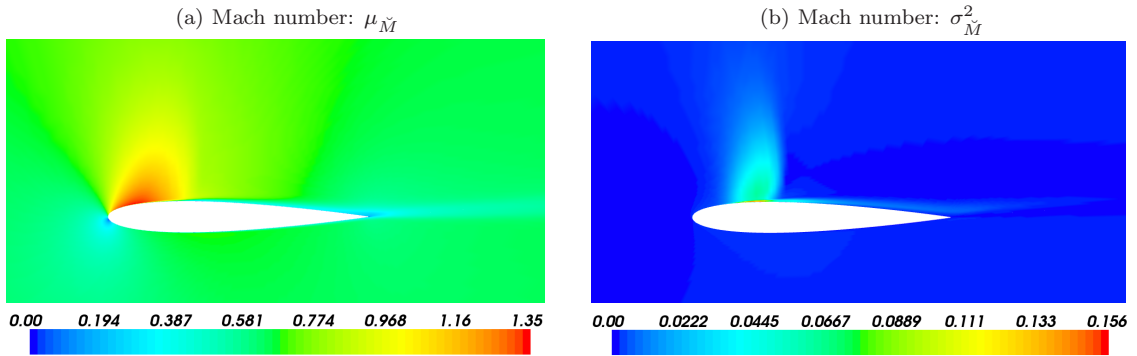


Figure III.18 – Mean and variance of the Mach number field, around a NACA0012 airfoil (*case D*: $\mu_\alpha = 5$ deg, $\mu_{M_\infty} = 0.65$).

The sensitivity of the shock response to the input uncertainty is seen in the variance of the Mach number σ_M^2 , as shown in Figure III.18(b), where important variations are observed on the upper side of the airfoil for $1/6 \leq x/c \leq 1/4$. The maximum of σ_M^2 is located near the airfoil surface around the first quarter of the chord. This uncertain region reflects the aerodynamic non-linearities associated to the interaction between the shock wave and the turbulent boundary layer. However, the edge of the turbulent boundary layer is sensitive to the input random parameters but no variations are observed neither on the pressure side nor in the wake of the airfoil. The prediction of the stochastic response of the turbulent field is straightforward, see Figure III.19 where the regions of sensitivity of the turbulent field strongly differs between the normal Reynolds-stress component $\widetilde{u''u''}$ and $\widetilde{v''v''}$.

Next, the stochastic results were analyzed by means of the uncertainty bars of the isentropic Mach number M_{is} distribution along the airfoil surface:

$$M_{is}(p, p_{t_\infty}) = \sqrt{\frac{2}{\gamma - 1} \left[\left(\frac{p_{t_\infty}}{p} \right)^{\frac{\gamma-1}{\gamma}} - 1 \right]}, \quad (\text{III.59})$$

where p denotes the static pressure. Figure III.20 displays, for each stochastic flow regime, the M_{is} confidence intervals. Both std-based confidence intervals and full confidence intervals are included. Full confidence intervals coincide with the supports of the response pdfs. For sake of clarity, only the distributions along the upper airfoil surface are presented.

One may notice from the results of *case A* that the maximum M_{is} mean value on the airfoil is $\mu_M = 0.9$, and all flow realizations within the interval $\mu_M \pm \sigma_M$ correspond to subsonic conditions. However, this is not the case for the full confidence interval, which includes transonic flow realizations (e.g. shocks up to $M_{is} = 1.19$). As already observed by Loeven et al. [270], the flow region characterized by an important level of variation is

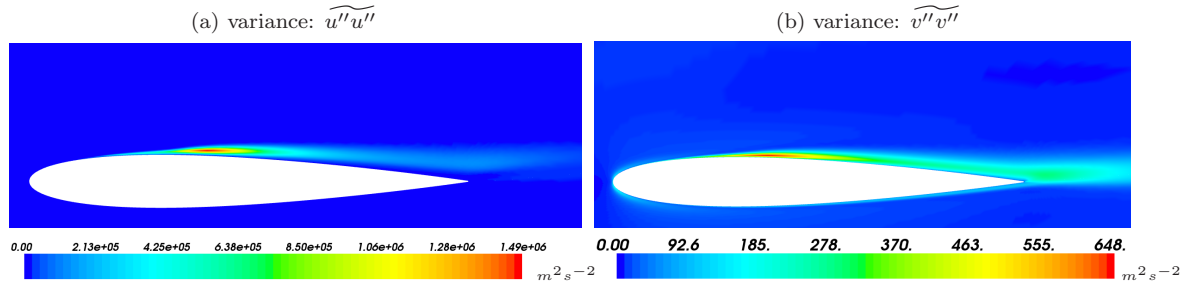


Figure III.19 – Variance of the Reynolds-Stress components, around a NACA0012 airfoil (*case D*: $\mu_\alpha = 5$ deg, $\mu_{M_\infty} = 0.65$)

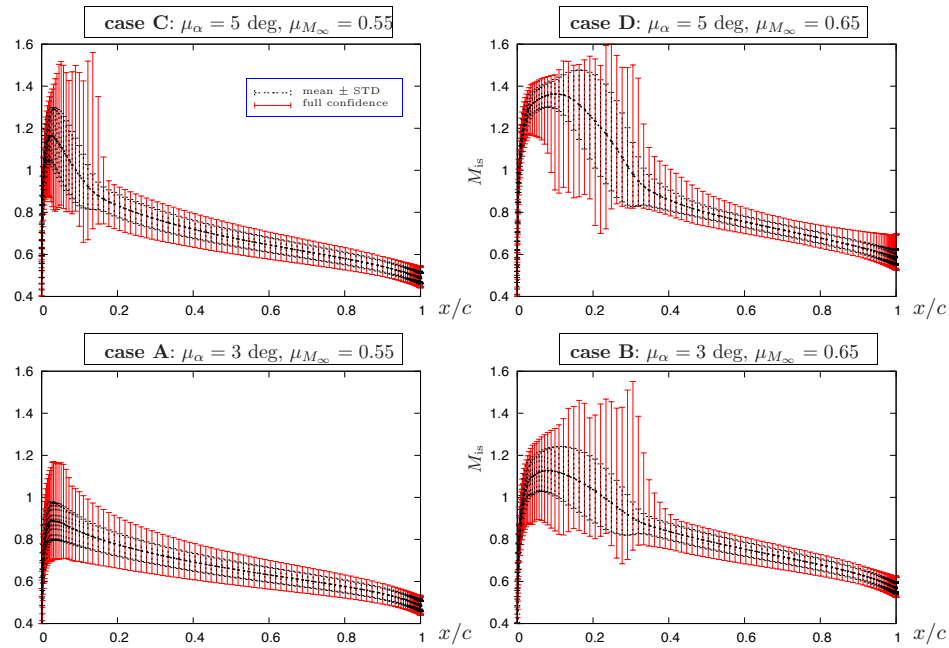


Figure III.20 – Steady-state isentropic Mach number M_{is} confidence intervals along the upper NACA0012 airfoil surface. Both std-based and full confidence intervals are represented together with the mean distributions.

located on the upper surface of the airfoil near the leading edge. The position giving the highest flow sensitivity level coincides with the position of the maximum value of $\mu_{M_{is}}$ ($x/c = 0.02$). Further, the amplitude of the error bar decreases smoothly down to the trailing edge. For the same Mach number range, but increasing the angle of attack up to $\alpha = 5$ deg, results in much larger variations of the stochastic flow-field, as shown in Figure III.20 (*case C*). The statistical response of the isentropic Mach number on the airfoil surface is now clearly separated into two distinct regions: 1) The flow in the region where $x/c < 0.2$ is characterized by an important sensitivity to the uncertain conditions. These large variations can be attributed to the non-linear effects of the shock-wave. In this case, the position of the maximum $\mu_{M_{is}}$ located at $x/c = 0.03$ does not coincide with the maximum $\sigma_{M_{is}}^2$. 2) For $x/c > 0.2$, the influence of the shock wave vanishes and the error bar amplitudes become comparable to those obtained for the subsonic configuration.

A quite different distribution is observed on the results of *case B*. The region affected by high variabilities extends up to $x/c < 0.4$ which is approximately twice further than those obtained for *case C* ($\alpha = 5$ deg, $M_\infty = 0.55$). Finally, the region of sensitivity computed for *case D* ($\alpha = 5$ deg, $M_\infty = 0.65$; Figure III.20d) is relatively similar to those obtained with $\mu_\alpha = 5$ deg (*case C*). A possible explanation is that, when the flow is dominated by a separated shear layer, the stochastic motion of the shock wave in the direction toward the trailing edge is restrained by the separation bubble whose position of the separating point is practically independent of the angle of attack.

Next, richer statistical information is obtained by considering the pdf of the solution which was computed using a population of 10,000 samples.

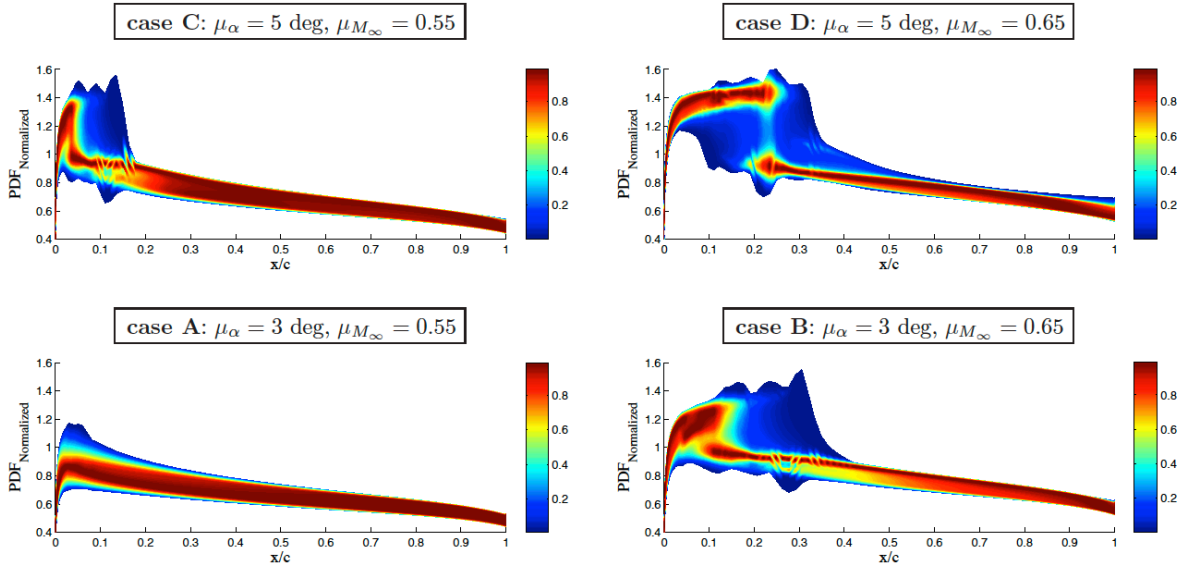


Figure III.21 – Steady-state isentropic Mach number M_{is} pdf contours along the upper NACA0012 airfoil surface.

The pdf contours are normalized at each streamwise location such that the maximum probability density is always unity⁴.

Keeping in mind that the aerodynamic uncertainties on α and M_∞ were modeled using *uniform* random distributions, it is interesting to note that the pdf of the stochastic solution are not uniform in some regions. This is the signature of the system nonlinearity. Considering by instance the results of *case A* ($\alpha = 3$ deg, $M_\infty = 0.55$), we remark that *uniform* pdf of the flow response are only observed for $x/c > 0.5$ but not for the upward region which presents large variations of the stochastic solution.

At transonic conditions (Figure III.21, *case B* and *case C*), the pdf of M_{is} can lead to very complex distributions in the regions characterized by non-linear effects. More surprisingly, it can be clearly observed on the results of *case D* ($\alpha = 5$ deg, $M_\infty = 0.65$), that the pdf of M_{is} is *bi-modal* (double peaks) around the position $x/c = 2.2$. The existence of a such bifurcation is probably due to the combined effects of the shock wave and the separated shear layer. Contour plots for *cases B* and *C* hint for a somewhat similar “jump” in the solution with a most probable value quickly switching from a larger to a lower value. This phenomenon takes place around $x/c \approx 0.12$ for *case B* and $x/c \approx 0.05$ for *case C*. Note also, that the distribution of the pdf near the trailing-edge of *case D* is slightly modified compared to the previous cases. It must be noted that the streaks observed for *case B* around $x/c \approx 0.3$ and for *case C* around $x/c \approx 0.1$ are strongly accentuated due to the rendering of the contour plots on irregularly spaced grids.

Figure III.22 shows the confidence intervals and statistics of the skin friction coefficient (C_f) along the upper airfoil surface.

We observe that the distribution of C_f computed for the subsonic configuration (*case A*: $\alpha = 3$ deg, $M_\infty = 0.55$) is quite insensitive to the input uncertainty. Nonetheless, at higher free-stream Mach number (Figure III.22b) or angle of attack (Figure III.22c), the confidence interval in the predictions of C_f presents larger variations, particularly along the windward part of the airfoil. These regions of high sensitivity are similar to those observed on the stochastic distributions of M_{is} (Figure III.20). Again, the results of *case D* ($\alpha = 5$ deg, $M_\infty = 0.65$) exhibit the largest variations to the stochastic flow.

Finally, it is interesting to analyse how the stochastic distributions of C_p and C_f vary together on the upper surface of the airfoil. Figure III.23 presents the results of the covariance $R_{C_p C_f}$ for *case D*. The region where the stochastic distributions of C_p and C_f are highly correlated ranges mainly from the leading edge up to the mid-chord of the airfoil ($0 \leq x/c \leq 0.5$). One can also observe that both negative and positive values of $R_{C_p C_f}$ are obtained. Therefore, the skin friction at a particular location x_1/c and the pressure coefficient at x_2/c can vary together or in an opposite manner. For instance, it appears that the stochastic values of C_p and C_f

4. This is done because we are more interested by the distribution of the strongest gradients and most probable solutions than by the pdf amplitudes.

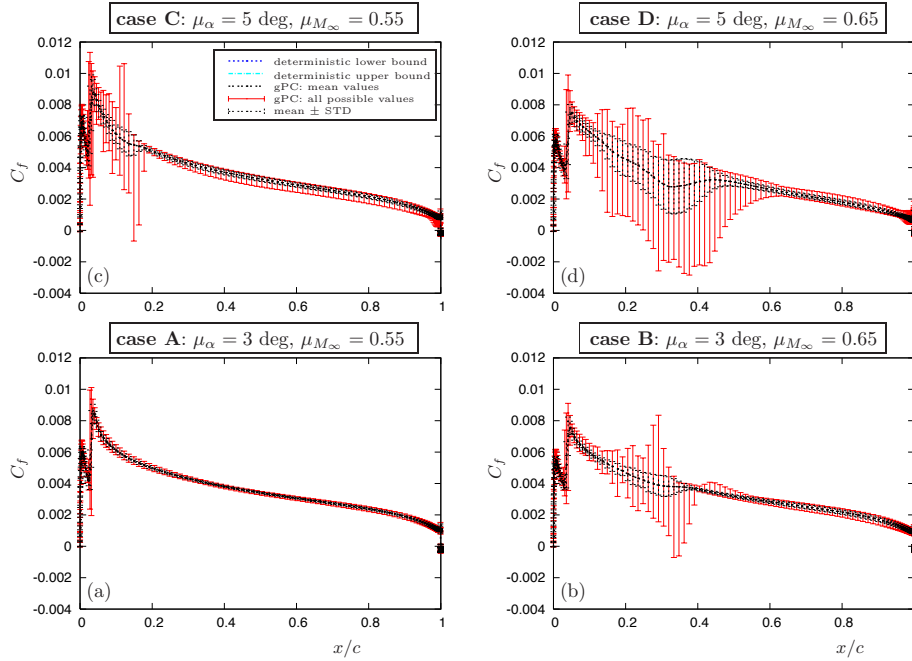


Figure III.22 – Steady-state skin friction C_f statistical distributions along the upper NACA0012 airfoil surface. Both std-based and full confidence intervals are represented together with the mean distributions.

between the leading edge ($0.04 \leq x/c \leq 0.06$) and the region defined by $0.2 \leq x/c \leq 0.4$ are correlated in the same way. Consequently, when one of these two variables is above its expected value, then the second variable will be above its expected value too. A similar behavior is observed for the region defined by $0.2 \leq x/c \leq 0.4$. However, this region is bounded by two additional regions with negative $R_{C_p C_f}$. This means that when one of these variables is above its expected value the other variable tends to be below its expected value.

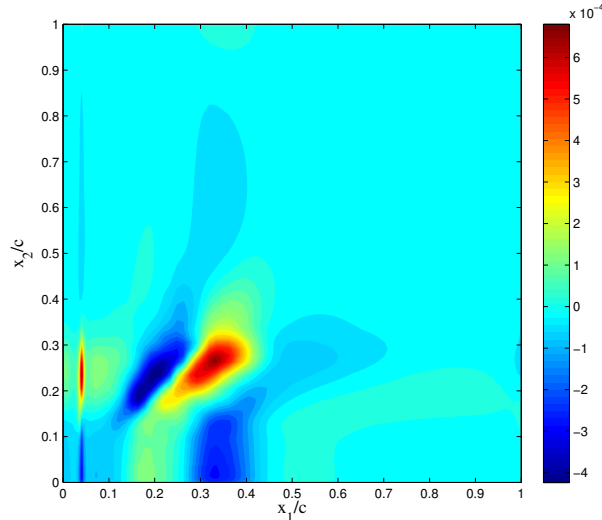


Figure III.23 – Cartography of the covariance between C_p & C_f along the upper NACA0012 airfoil surface (*case D*).

Remark III.23

Uniform distributions of uncertain angle of attack and free-stream Mach number lead to non-uniform distributions of the aerodynamic coefficients C_p and C_f on the airfoil when the nonlinearities associated to the compressible flow features are reported into the uncertain probabilistic space. In this case, the coupling between these uncertainties becomes non-negligible (especially for case D, $\alpha = 5$ deg, $M_\infty = 0.65$). Cross-

correlation between C_p and C_f shows that it is possible to identify particular regions on the airfoil surface for which these coefficients are more likely to vary together or oppositely.

Extension to non-uniform mixed distributions

The gPC representation has the capability of representing random functional processes whose underlying random variables have different distributions. Spectral convergence of the gPC representation based on *mixed* basis was demonstrated for simple stochastic ODEs [232]. In the following, test cases with *mixed* random distributions are considered. We choose to keep a uniform distribution for α and to assign a *truncated* Gaussian distribution f_{tG} to M_∞ . The latter distribution resembles a Gaussian distribution but bears truncated tails. While Gaussian distributions seem a natural choice when the nature of the actual random inputs is unclear, *truncated* Gaussian distributions are convenient to insure that negative values of the M_∞ have zero probability of occurrence, i.e. the problem is not ill-posed.

Starting from the *case D* ($\mu_\alpha = 5$ deg, $\mu_{M_\infty} = 0.65$), we have performed $n_q^2 = 8 \times 8$ additional stochastic computations to highlight the effect of the truncated Gaussian distribution f_{tG} ($\mu_{M_\infty} = 0.65, \sigma_{M_\infty} = 0.05, a = \min_{M_\infty} \approx 0.5, b = \max_{M_\infty} \approx 0.8$) for M_{is} . For the comparison to be fair, mean and std of the random parameter are taken the same as previously, while the bounds of the distribution (a, b) are accurately adjusted to match the imposed moments and shape of the distribution. Following the method proposed by Xiu & Karniadakis [527], we approximate the f_{tG} distribution by a p^{th} -order gPC expansion of Jacobi-type polynomials $P_p^{\alpha, \beta}$ of a $beta(\alpha, \beta)$ distributed random variable. Based on our choice of quadrature, we have found that ($\alpha = 8, \beta = 8$) matches the f_{tG} distribution best. For a $p = 7^{\text{th}}$ -order gPC Jacobi expansion, we have no error in the mean of the distribution and an absolute error in variance of the order of 10^{-7} . The optimal nodes and corresponding weights associated with the $beta(\alpha = 8, \beta = 8)$ distribution are computed thanks to a Gauss-Jacobi quadrature rule. The hybrid gPC polynomial basis is constructed by tensor products of Legendre and Jacobi polynomials, following the same guidelines as the classical approach.

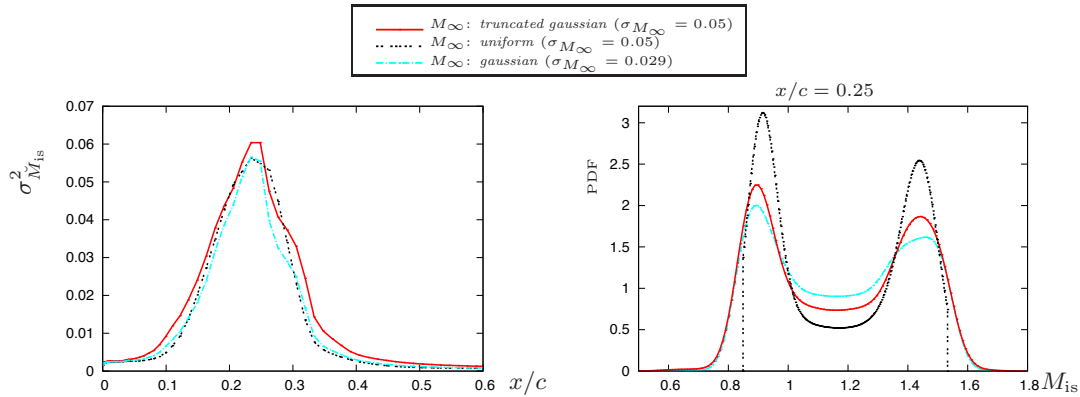


Figure III.24 – Comparison of the effect of *uniform*, Gaussian and *truncated* Gaussian random distributions of M_∞ with $\mu_{M_\infty} = 0.65$ onto $\sigma_{M_{is}}^2$ along the upper surface of the airfoil (left) and corresponding pdf computed at $x/c=0.25$ (right). The angle of attack is modelled using a *uniform* distribution identical to the one defined in *case D*.

The results are analyzed by means of the variance of M_{is} along the upper surface of the airfoil (Figure III.24). We also consider a fully Gaussian representation of M_∞ for the sake of comparison. Figure III.24 (left) compares the distribution of variance of M_{is} along the extrados for the three different measures. We notice that the injection of truncated Gaussian uncertainty into M_∞ provides similar results than the previous ones with a somewhat slightly larger variance in most of the region of interest. The location of the maximum peak remains unchanged for all cases.

The inspection of the M_{is} pdf profiles at one specific location along the chord ($x/c = 0.25$) shows that the bipolar trend of the solution probability distribution at this location subsists despite the input gaussianity (Figure 9-right). We notice that intermediate values of the response, around $M_{is} \approx 1.2$, have more chance to appear than in the *uniform* case. These values will in fact become more dominant as the standard deviation of the Gaussian-like M_∞ will be reduced.

2.2 Stochastic transonic flows past a supercritical OAT15A airfoil

A similar analysis is carried out for a different airfoil profile that we wish non-symmetric. Our goal is to quantify the effect of a more pronounced camber on the sensitivity of the flow to the operating conditions. The bi-dimensional airfoil retained to perform the current study is the supercritical OAT15A profile with a chord $c = 0.23$ m. The freestream conditions are the same as those previously used for wind tunnels experiments [203] as well as numerous numerical simulations with $P_i = 1$ bar and $T_i = 300$ K. The Mach number M_∞ and the angle of attack α are respectively equal to 0.73 and 2.5 degrees. The Reynolds number Re based on c is equal to 3×10^6 . In the following, the deterministic simulation with $(M_\infty, \alpha) = (0.73, 2.5)$ will be referred to as the reference simulation. A realistic range of variation for the uncertain parameters will be chosen as to make sure that buffeting does not occur within the parametric region.

Since the emphasis is put on the Reynolds-Averaged flow features, Reynolds-Averaged Navier-Stokes (RANS) are retained as the relevant mathematical model in this work. The compressible RANS equations are solved using the *ElsA* aerodynamic solver developed at ONERA for the past ten years, [58]. A Jameson spatial scheme is used along with the one-equation Spalart-Allmaras model. The 2D mesh is composed of two blocks of size 385×161 cells (C block surrounding the airfoil) and 129×369 cells in the wake, leading to 110 000 cells and has been extended to 80 chords in all directions. The mesh and the accuracy of the CFD tool has been carefully checked in past studies, [100]. The capability of the turbulence model, the numerical scheme and computational grid to accurately predict the RANS steady solution has been assessed. Moreover, we have checked that the stochastic predictions are not too sensitive to our RANS parameters as long as we use a sufficiently resolved spatial discretization.

2.2.1 Deterministic flow computations

Again, we consider the case of a 2D foil in a randomly perturbed flow in transonic regime. We suppose that the stochastic perturbation affects the magnitude and direction of the incoming inflow velocity. We treat the uncertain input parameters to our simulations as iid *uniform* random variables. The non-linearity of the system then transforms these uncorrelated random variables to spatial random processes. The range of variation of the uncertain parameters is chosen as to avoid the buffeting region for which the RANS solver would not be accurate. The uncertain parameters retained for the current study are M_∞ and α . The Mach number M_∞ has a 0.73 mean value and a $\pm 5\%$ variability and the angle of attack α has a 2.5 degrees mean value and a $\pm 20\%$ variability.

Due to the choice of uniform distributions for the inputs and without any *a priori* knowledge of the outputs pdf solution, an appropriate basis from a mathematical point of view is the Legendre polynomial basis [523]. This latter one will be used in the following as our expansion basis. Additional studies were also completed for mono-dimensional cases (i.e. the uncertainties on M_∞ and α have been studied separately) and will be used for comparison in the sensitivity analysis in the last section.

2.2.2 Stochastic response

Fig. (III.25) present the mean and standard deviation distribution of wall data along the airfoil for the stochastic bidimensional case as well as their associated pdfs distributions and pdfs profiles for five locations on the leeward side. Reference cases are also included.

For $0.35 < x/c < 0.65$, we notice that K_p stochastic solutions greatly depart from the reference solution. We also notice that the uncertain mean solution differs from the deterministic one. The main discrepancy consists in a less pronounced compression region surrounding the mean shock position. This result is consistent with the fact that the shock location is not fixed for different low Mach number realizations. Indeed, the shock moves upstream as the Mach number value decreases from the averaged value of 0.73 to its lower bound. No clear influence of the parametric uncertainty can be observed for $x/c > 0.65$ as well as for $x/c < 0.35$ which is the most upstream shock position for the uncertainty range investigated here. These observations have to be related to the behavior of the standard deviations. For $0 < x/c < 0.35$, σ_{K_p} results from a linear response of the flow to the uncertainty as the shock-wave never penetrates this area whatever M_∞ values in our range. Downstream this location, higher magnitudes of the standard deviation are observed. It appears that the strong spatial non linearities introduced by the shocks translate to the random domain. The dependency of the shock location to M_∞ accounts for the high sensitivity of the flow in this wide region. Further downstream, σ_{K_p} becomes very weak except for $x/c > 0.9$ where trailing-edge effects can be observed.

The analysis of Mach fields indicates that the shock position has the tendency to shift downstream when M_∞ is raised to 0.73. For higher M_∞ values, its position remains fixed and only the boundary-layer state behind the shock is altered, leading to separation. Such evolution can be clearly evidenced when looking at the Mach contours of the mono-dimensional cases. It shows why the skin-friction coefficient is much more sensitive to the uncertainty than the pressure coefficient in the second half of the profile [443]. This trend is similar for the

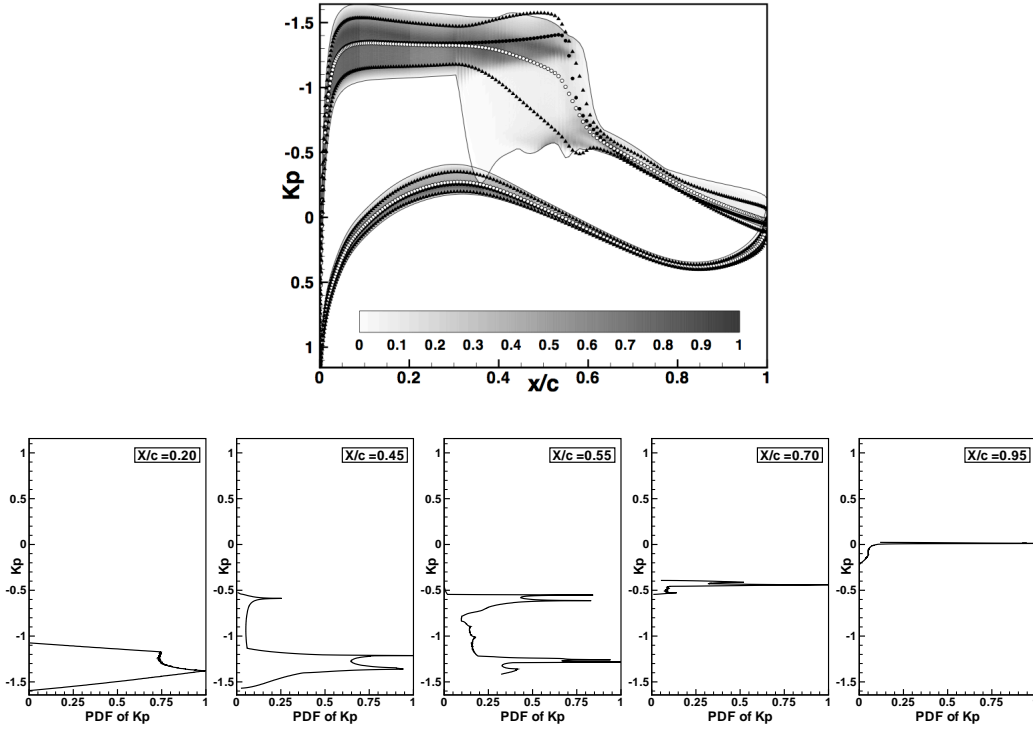


Figure III.25 – K_p pdf contours along the OAT15A airfoil surface and the corresponding local pdf profiles at five chord locations (\circ : stochastic mean - \blacktriangle : stochastic mean \pm standard deviation - \bullet : reference deterministic case - $---$: pdfs minimum and maximum values).

standard deviation distributions where high magnitudes of σ_{C_f} can be observed both upstream and downstream of the reference shock position.

Additional knowledge can be brought with the use of the pdfs. For the wall pressure, the pdfs distribution are almost centered around the most probable value which also corresponds to the mean stochastic K_p value for $x/c < 0.35$. This is no more the case in the area where the flow response is non-linear. The pdfs exhibit a wider range of K_p values with two dominant peaks. As a consequence, in this region, the mean stochastic K_p differs from the most probable K_p magnitude. For $x/c > 0.65$, the shock-wave is always located upstream independently of M_∞ in the uncertainty bounds considered and a narrow peak is observed on the pdfs. The K_p values are almost insensitive to the uncertainty as previously observed on both the mean stochastic K_p values and σ_{K_p} .

Previous results are consistent with the results shown in figure III.26 which depicts the spatial distribution of the Mach number coefficient of variation c_v , cf. 1.79. Two distinct areas with high c_v magnitudes can be isolated. The first one, for $0.35 < x/c < 0.65$, corresponds to the region where non-linear variations of the pressure coefficient were underlined (figure III.25) due to the variable shock position. In this region, dispersion as high as 30% can be observed. The second area of high variability is located in the boundary layer behind the reference shock position. On the lower figure, a coefficient superior to one can be observed very locally whereas all the boundary layer area exhibits c_v values superior to 0.5. These high dispersion values agree well with the observations previously drawn dealing with the boundary layer separation downstream the shock when $M_\infty > 0.73$.

2.2.3 Coupling process

A sensitivity analysis can be performed by using the Sobol' decomposition adapted to the gPC framework, cf. Section 4. Next, we compute total and partial variances, according to the following notations: $\sigma_{\text{Total}}^2 = \sigma_M^2 + \sigma_\alpha^2 + \sigma_{M-\alpha}^2$, where σ_{Total} is the total std whereas σ_M and σ_α are the partial std respectively due to the Mach number and the angle of attack uncertainties. The $\sigma_{M-\alpha}$ term is the standard deviation resulting from the coupling process between the 2 stochastic parameters.

Figure III.27 presents the distribution of the partial standard deviations as well as the reference standard deviations from the mono-dimensional cases which have been denoted $\sigma_M(\text{Ref.})$ and $\sigma_\alpha(\text{Ref.})$, respectively. Both figures prove that σ_{Total} and σ_M exhibit the same shape and almost the same amplitudes. Therefore σ_M dominates the whole standard deviation, and the compressibility effect are the most influential. The physical

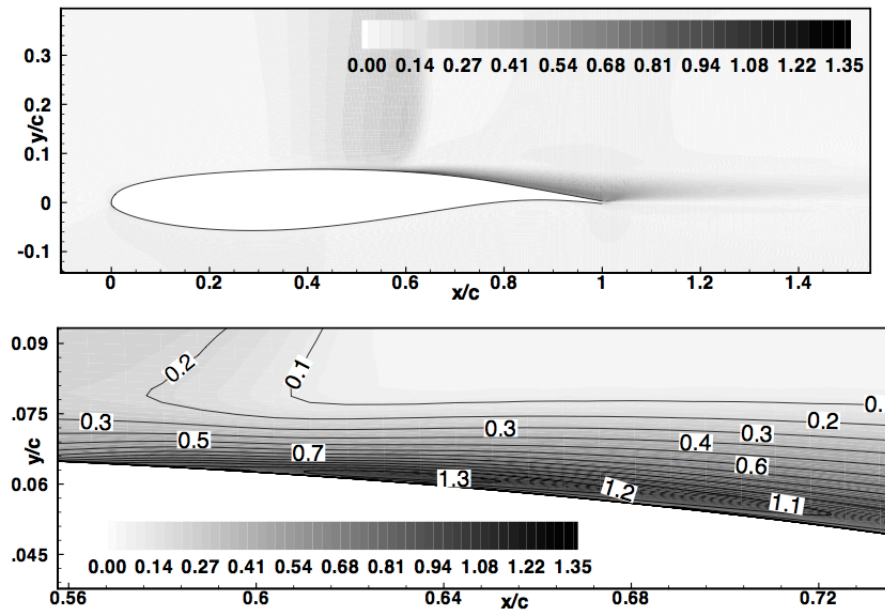


Figure III.26 – Spatial distribution of the Mach number coefficient of variation c_v (top : whole airfoil, bottom : detailed view).

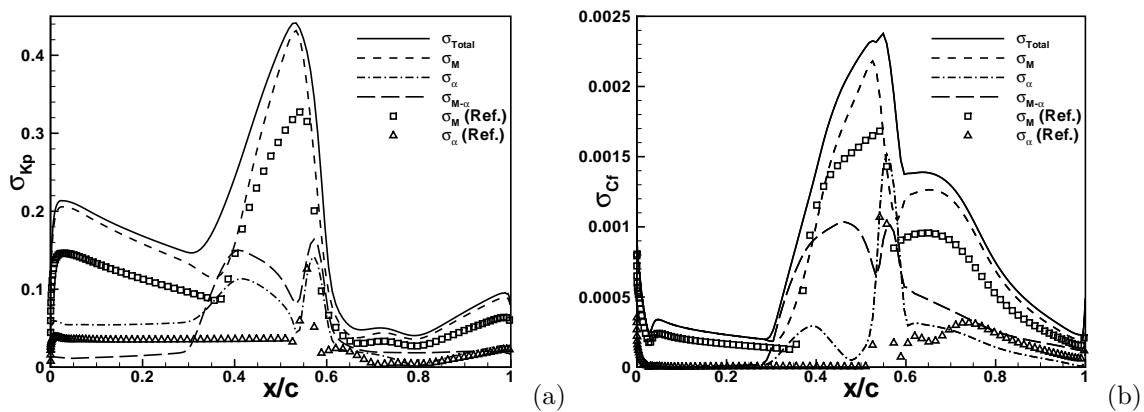


Figure III.27 – Sensitivity analysis expressed as Sobol' coefficients of K_p (a) and C_f (b), along the OAT15A airfoil - Standard deviations extracted from monodimensional simulations have been added (winward side only).

rationale for is that variations in the Mach number induces a change of both the shock location and the shock strength on the suction side, these two effects having a deep impact on the boundary layer state downstream the shock. But there is also a significant coupling between compressibility effects and incidence effects resulting in a coupling term $\sigma_{M-\alpha}$ with magnitude larger than σ_α in the interaction region ($0.3 < x/c < 0.65$). Moreover, when both the mono- and bi-dimensional cases are compared, discrepancies appear both in magnitude and shape of the standard deviation. A 20% increase of the pick value is observed in the 2-parameter case compared to the mono-dimensional one for both the pressure and the skin friction coefficients. One can also observe the absence of the bump in the standard deviation distributions $\sigma_M(Ref.)$ and $\sigma_\alpha(Ref.)$ due to the coupling process in the bi-dimensional case. This coupling process is much more evident on $\sigma_{M-\alpha}$ related to the skin-friction coefficient where the coupling term reaches a 40% value of the whole standard deviation in the interaction region.

Moreover, spatial distinction can be made due to the different non-linearities involved in the flow. Pressure discontinuities (shocks) require the use of high-order polynomial expansions due to the stochastic parameters on the steep dependency of the shock position. On the contrary, the existence of non-linearities through the appearance of separation behind the mean shock position does not require high-order terms. Discrepancies appear between the most probable pressure and skin friction distributions and the deterministic case in the interaction region where the shock moves dependently of the stochastic parameters which demonstrate the influence of the uncertainties on the response of the flow.

2.3 Error analysis

In this section we investigate the accuracy of the stochastic approximation and its interplay with the numerical error introduced by the spatial discretization for the two cases previously assessed, i.e. transonic flows around NACA0012 and OAT15A airfoils.

2.3.1 Preliminary study

First, we conduct a one dimensional study on the accuracy on a simplified model drawn from the configuration of *case D* (NACA0012) where we keep the angle of attack as deterministic ($\alpha = 5$ deg). The free-stream Mach number is modeled as a *uniform* random variable characterized by $\mu_{M_\infty} = 0.65$ and $\sigma_{M_\infty} = 0.05$. This one random parameter study is relevant as it is more stringent on the numerical representation than a two random parameters study. Indeed, uncertainty in the angle of attack introduces additional smoothing to the solution statistics due to data scattering. We also compare those results with the OAT15A configuration with two uncertainties from the previous section.

Stochastic results computed using Gauss-Legendre (GL) quadrature with $n_q = 8$ points are compared with those obtained with a Gauss-Kronrod (GK) quadrature rule [245]. The GK rule only requires the computation of $n_q + 1$ additional points compared to the GL grid, i.e. 9 new runs in the present case.

Figures III.28 presents a comparison between these two approaches on the computation of the mean of $\mu_{M_{is}}$ and μ_{C_f} over the airfoil extrados. The accuracy of the mean solution only depends on the aliasing error via n_q and the spatial discretization error. In addition, the figures display the different realizations (corresponding to the GL and GK points) as well as the spatial grid. When the mean solution is computed from the 8 GL points or the (8 + 9) GK points, the profiles are very similar and smooth. However, when one only uses $n_q = 3$ points, the results are disastrous, with strong oscillations (stair-like profile) due to aliasing.

The conclusion is identical for the case of the OAT15A profile (with two uncertainties), cf. figure III.29. It shows that a sufficient number of samples (higher than for the NACA0012 case) is necessary to obtain smooth distributions. As we will see this increase is due to a finer spatial grid.

Next, we investigate the coupling between aliasing and truncation errors by considering higher moments. Figures III.30 present results for $\sigma_{C_p}^2$ and $\sigma_{C_f}^2$. In this case the accuracy depends on both the aliasing error via n_q , the truncation error via P , and the spatial discretization error. Assuming that the latter is of comparable magnitude as the other two, we investigate the effect of n_q and P .

Figure III.30-(right) shows $\sigma_{C_p}^2$ for different combinations of quadratures and truncations. When the integration is sufficiently resolved, as in the case of the GK quadrature with 17 points, the results are very smooth and $P = 7^{th}$ or $P = 12^{th}$ order approximations provide very similar profiles for the variance. Therefore, the increase of the quadrature accuracy (GL \rightarrow GK) notably improves the solution locally by suppressing the spurious oscillations observed on the results of the 7^{th} order gPC expansion (i.e. $n_q = 8$).

Figure III.30-(left) displays the relative error in variance (based on the best estimate – i.e. $P = 12$), as no other reference solution is available. Open symbols represent our computations and the decay rates are linearly fitted in a semi-logarithmic scale (solid lines: $\sigma_{C_p}^2$; dashed lines: $\sigma_{C_f}^2$). We notice that we get close to spectral convergence up to high order for both coefficients. The convergence rate is similar for both quantities at the different locations, except for the skin friction at $x/c = 0.2$ where the solution converges somewhat slower.

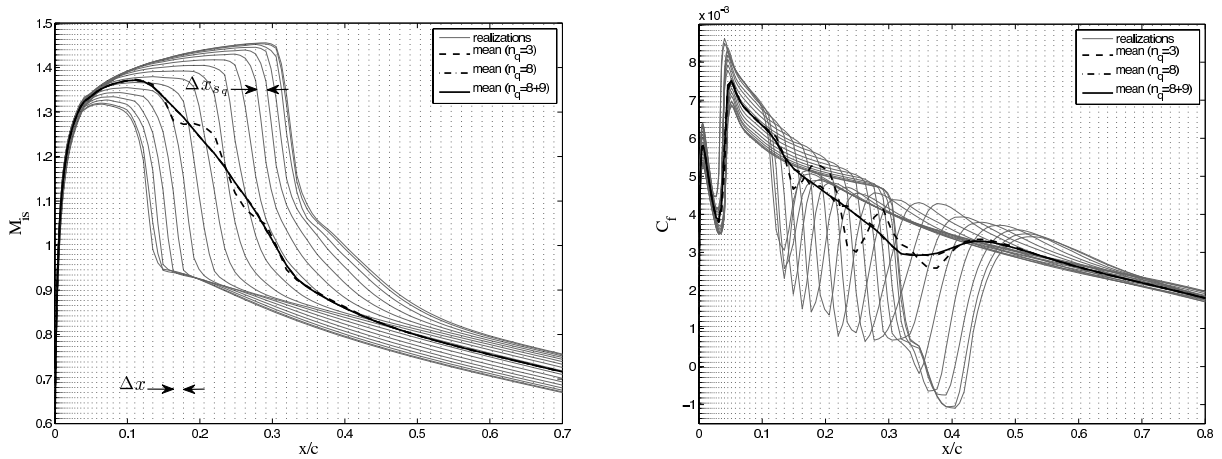


Figure III.28 – Effect of aliasing error: realizations and corresponding mean profiles of $\mu_{M_{is}}$ (left) and C_f (right) for different quadrature levels (Gauss-Legendre vs. Gauss-Kronrod) (*case D**: $\alpha = 5$ deg; $\mu_{M_\infty} = 0.65$, $\sigma_{M_\infty} = 0.05$).

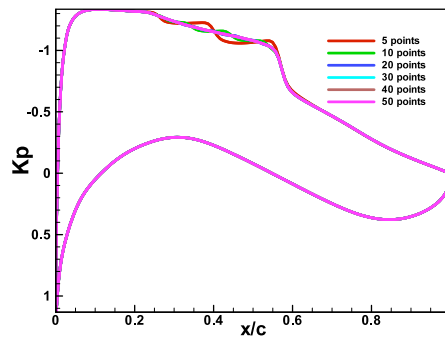


Figure III.29 – Influence of the number of samples on the mean value distribution of K_p along the chord.

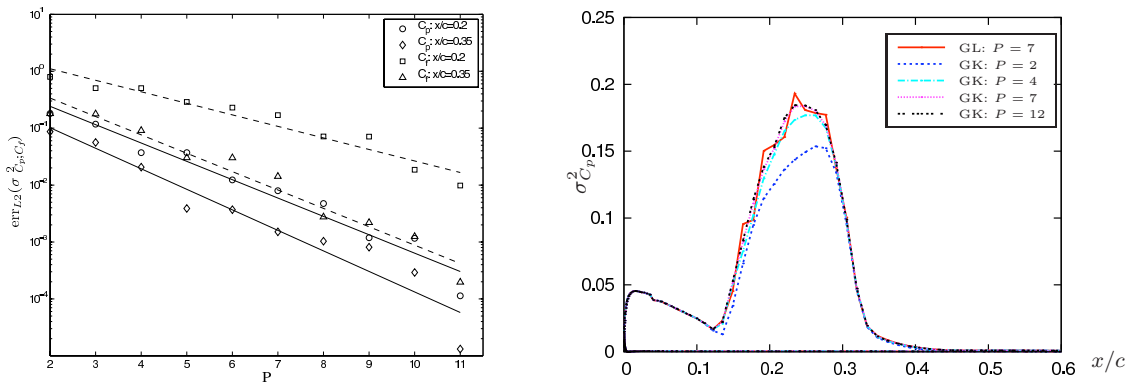


Figure III.30 – Effect of truncation error: C_p variance distribution along the NACA0012 extrados for different choices of gPC truncation (right) and convergence rates of the solution variance (left) vs. the polynomial order P . (*case D**: $\alpha = 5$ deg; $\mu_{M_\infty} = 0.65$, $\sigma_{M_\infty} = 0.05$).

The conclusions are identical for the case of the OAT15A profile (with two uncertainties) in figure III.31.

As expected, the level of accuracy of the stochastic representation depends on the type of statistics and the choice of the physical quantity under consideration as well as the spatial location where this quantity is monitored. Moreover, the comparison between the two types of profiles seems to point to a coupling between deterministic and stochastic errors which interplay through the two levels of discretization.

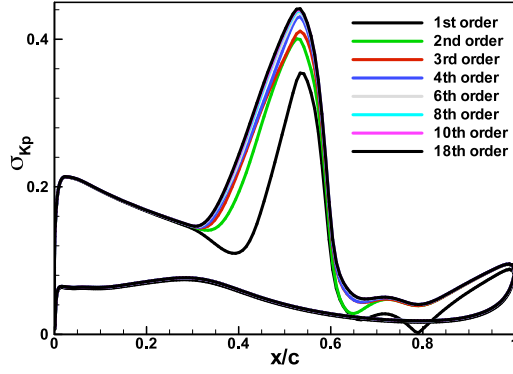


Figure III.31 – K_p *std* distributions along the OAT15A extrado for different choices of polynomial truncation.

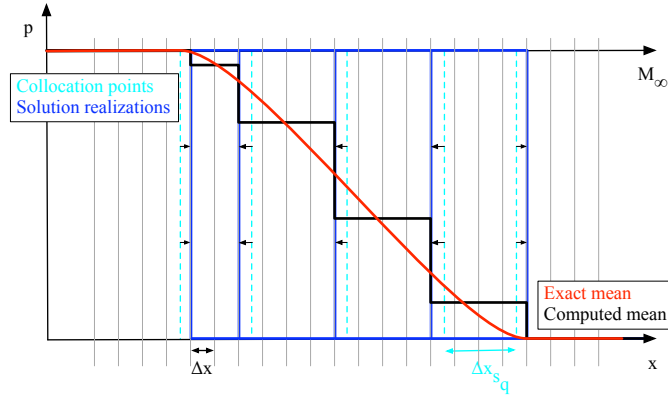


Figure III.32 – Schematic illustrating the dependence between physical (Δx) and stochastic (Δx_{sq}) discretizations. When $\Delta x_{sq} \gg \Delta x$, i.e. the parametric (here M_∞) collocation points distribution (dotted cyan curves) is such that the corresponding discontinuous realizations are far apart (blue curves), the distribution of the gPC solution moments may exhibit some irregular and unphysical patterns (black curve). These irregularities are smoothed out (red curve) if $\Delta x_{sq} \approx \Delta x$.

2.3.2 Spatial and stochastic grid requirements

Some results from the literature suggest that global gPC approximation based on spectral projection is not appropriate in the case of discontinuous or sharp solutions. In this case, the continuous approximated solution may exhibit some oscillations inducing irregular and unphysical patterns in the spatial distribution of the solution moments or pdf, e.g. stair-like profile for the mean solution [270]. The location of these irregularities coincide with the collocation points and is more noticeable for local physical quantity (such as C_f), more sensitive to discretization errors.

In the following paragraph, we refer to the simplified diagram of Figure III.32 for visual assistance. Given a fixed spatial discretization grid of typical resolution size Δx along the chord, the accuracy of the gPC approximation depends on the choice of P and n_q . Let us call $p_{s_q} \equiv p(x_{s_q}, Z_q)$ the value of the discontinuous solution at the location of the shock x_{s_q} obtained for the quadrature point Z_q (cf. Figure III.28-(left)). When the number n_q of collocation points is not sufficient, it may happen that $\Delta x_{s_q} \gg \Delta x$ and the problem described hereinbefore appears [384]. However, several of our studies have shown that the profiles recover regularity when we increase n_q as $\Delta x_{s_q} \rightarrow \Delta x$. This is the case in Figures III.28 for sufficiently high n_q . In the case where $\Delta x_{s_q} \ll \Delta x$, one faces aliasing error as the shocks are not assigned to the correct cell in physical space. For some higher moments or pdf contours, some oscillations may remain along the distribution (cf. Figure III.30-(right) for $n_q = 8$ and $P = 7$), but the right profile magnitude is generally captured for a good (n_q, P) choice.

It is in general difficult to predict the appropriate n_q as the average Δx_{s_q} is not known a priori. This latter depends on the distribution of the chosen quadrature rule as well as the sensitivity of the response to the parametric uncertainty. This sensitivity relates to the span length of the geometric envelop in which all probable discontinuous events may take place. Non-linearity of the model, monotonicity of the response and airfoil geometry will affect differently this range.

Table III.4 – Relative error of the lift and drag variance versus the polynomial order P for the four stochastic flow regimes (*case A*: $\alpha = 3$ deg, $M_\infty = 0.55$, *case B*: $\alpha = 3$ deg, $M_\infty = 0.65$, *case C*: $\alpha = 5$ deg, $M_\infty = 0.55$, *case D*: $\alpha = 5$ deg, $M_\infty = 0.65$)

P	$\text{err}_{L_2}(\sigma_L^2)$				$\text{err}_{L_2}(\sigma_D^2)$			
	<i>A</i>	<i>B</i>	<i>C</i>	<i>D</i>	<i>A</i>	<i>B</i>	<i>C</i>	<i>D</i>
2	2.021E-5	2.383E-4	3.156E-3	5.168E-3	1.981E-4	3.796E-2	1.537E-4	8.554E-4
3	7.776E-7	1.963E-5	2.249E-5	5.058E-4	2.977E-5	1.040E-3	9.318E-4	2.267E-4
4	5.016E-7	1.690E-5	1.248E-5	7.946E-5	1.940E-5	4.663E-4	1.978E-4	5.013E-6
5	3.455E-7	1.358E-5	1.987E-6	4.551E-5	1.588E-5	5.966E-5	3.973E-5	3.289E-6
6	1.995E-7	5.042E-6	1.235E-6	2.592E-5	1.137E-5	8.405E-6	2.434E-5	1.112E-6

In conclusion, there exists a strong coupling between the discretization in physical space and the stochastic grid in random space. As a result, refinement of the grid in one of the two spaces *must* happen together within the other one.

2.3.3 Convergence analysis

This first part presents a detailed convergence study for the four stochastic transonic flow regimes around the NACA0012 airfoil, based on *uniform* random distributions of the uncertain angle of attack and free-stream Mach number (*c.f.* section III.2.1.2). Based on our previous analysis, and considering our level of confidence in the accuracy of the spatial discretization provided by the choice of our computational grid [67], we design a stochastic grid that matches in most situations the requirement described in the previous section. This choice also reflects the computational bottleneck induced by the numerical cost related to the uncertainty propagation. In this study, the number of quadrature points is fixed to $n_q = 8$ along each direction and is an appropriate trade-off between accuracy and computational burden.

First, the convergence properties of the global aerodynamic coefficient are presented. The relative errors of the lift and drag variances versus various polynomial order P are reported in Table III.4 for each stochastic flow regime investigated in section III.2.1.2. Because we do not have an exact reference solution to compare with, the error is monitored as the normalized L_2 norm of the difference of a given flow quantity between the stochastic solution of interest and that of the most resolved computation (obtained using $P = 7$) that we pick as our reference solution. Typically, we have seen that an increase from $P = 2$ to $P = 6$ permits to reduce substantially the truncation error of the gPC expansion.

Next, the effect of the polynomial order P on the accuracy of the gPC formulation was investigated for the most difficult case, *i.e.* *case D*.

Figure III.33 shows the influence of the number of quadrature points n_q on the mean solution of the isentropic Mach number.

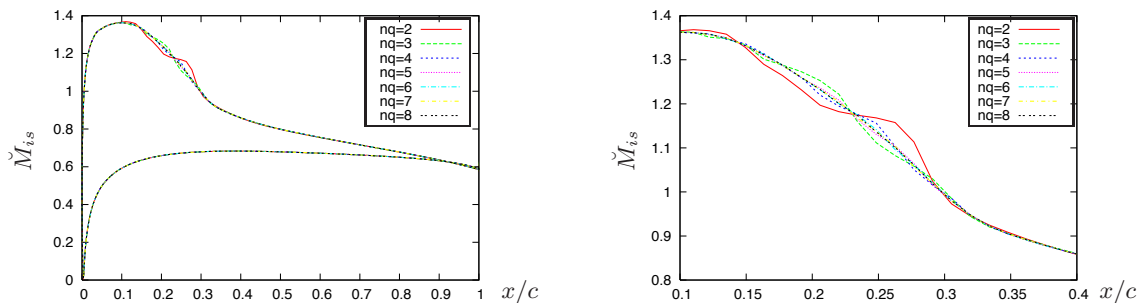


Figure III.33 – Effect of the number of collocation points n_q on the distribution of the mean value of M_{is} for *case D*: $\mu_\alpha = 5$ deg, $\mu_{M_\infty} = 0.65$

While a relatively small number of quadrature points ($2 \leq n_q \leq 4$) is sufficient to capture correctly the zero order moment of the solution, it is not sufficient for the $0.1 < x/c < 0.3$ region (Figure III.33b). As explained

previously, this is due to the fact that this region is strongly affected by the aerodynamic non-linearities related to shock waves and that the stochastic quadrature grid is not refined enough compared to the spatial resolution. It is then necessary to increase the number of collocation points per random dimension up to $n_q = 6$ to obtain converged and smooth values of the mean distribution of M_{is} .

Next, the convergence analysis of the variance distribution of the pressure coefficient C_p and the skin friction coefficient C_f along the upper surface of the airfoil is presented. Figure III.34(a), which shows the distribution of $\sigma_{C_p}^2$, reveals that the peak of flow variability at $x/c = 0.28$ is adequately captured for $P \geq 5$.

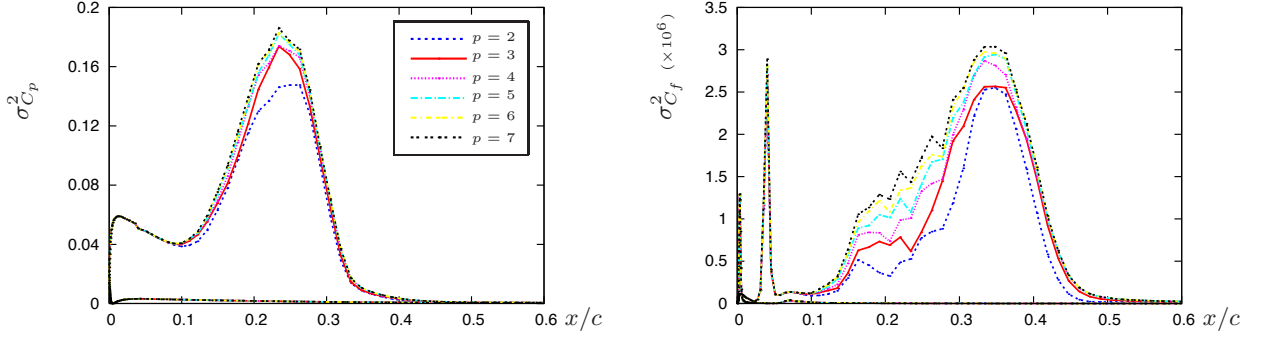


Figure III.34 – Influence of the polynomial order P on the pressure coefficient C_p and the skin-friction C_f variances along the airfoil surfaces (*case D*).

However, we can clearly see on Figure III.34(b) that a fully converged representation of the $\sigma_{C_f}^2$ distribution is more problematic to achieve. It is then necessary to increase the polynomial order up to $P = 7$ to get an almost converged prediction of the variance of the skin-friction coefficients. Notice that, similarly to the case discussed in Figure III.30-(right), the use of a 7th order gPC expansion does not fully remove all non-physical oscillations for $0.15 \leq x/c \leq 0.3$ (Figure III.34(b)). Indeed the skin friction is a very sensitive quantity to numerical noise.

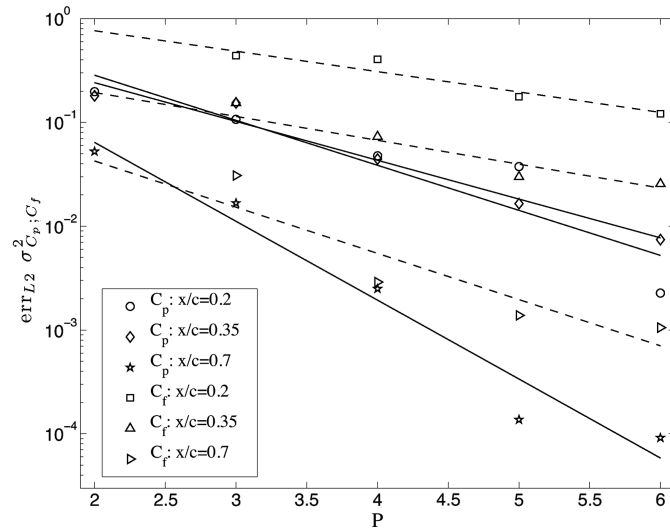


Figure III.35 – Convergence rate of the pressure coefficient C_p and the skin-friction C_f variances with respect to P (*case D*).

Figure III.35 shows the convergence error of $\sigma_{C_p}^2$ and $\sigma_{C_f}^2$ for $x/c = 0.2$, $x/c = 0.35$ and $x/c = 0.7$. Open symbols represent the computations and the decay rates are linearly fitted in a semi-logarithmic scale (solid lines: $\sigma_{C_p}^2$; dashed lines: $\sigma_{C_f}^2$). It is confirmed that the convergence rates obtained for $\sigma_{C_p}^2$ are better than those computed for $\sigma_{C_f}^2$. Moreover, we observe that the sensitivity level of the stochastic flow-field (as seen for instance at $x/c = 0.2$ in Figure III.34b) results in some deterioration of the convergence rate. Convergence rates are best where the solution is regular (e.g. $x/c = 0.7$).

2.4 Concluding remarks

In these studies a stochastic spectral projection solver, based on gPC expansions, was applied to the uncertainty quantification of stochastic compressible flows around a NACA0012 and OAT15A airfoils due to random free-stream Mach number and angle of attack. Simple stochastic models were considered in which the free-stream Mach number and the angle of attack are represented by independent random variables with bounded supports. Since the stochastic solution is directly projected onto each member of the orthogonal basis chosen to span the random space, this method has the advantage of being non-intrusive. Therefore, the stochastic solver was easily coupled with a RANS deterministic codes to extract statistical informations of both the mean-flow and the anisotropic turbulent field.

A careful error analysis of the global representation, based on the number of solution samples and the polynomial order at use, has allowed a better understanding of the coupling between aliasing error, finite-term projection error and the numerical error related to the intrinsic numerical approximation of the deterministic solver. Monitoring of pressure and skin friction coefficients moments along the surface of the airfoil have shown fast convergence rates for global aerodynamic quantities (e.g. lift and drag coefficients) and local quantities such as the isentropic Mach number and the pressure coefficient. Nonetheless, the accuracy of the approximation remains acceptable for derived quantities, more sensitive to numerical noise, such as the skin friction.

It must be noted that, for the parametric stochastic ranges of interest, this methodology did not suffer from any lack of robustness despite strong non-linearities (due to the shock waves) and a recirculation zone present in the stochastic solution.

As far as the physical aspects are concerned, this study was focussed on the potential importance of dealing with combined angle of attack and free-stream Mach number uncertainties. Their consequences on the resulting stochastic flow were demonstrated using a detailed sensitivity analysis conducted with the computation of the Sobol's coefficients. This analysis confirmed that the uncertainty present in the free-stream Mach number is the driving mechanism in the resulting probability density function of the stochastic aerodynamic field. Nonetheless, once the mean-position of the shock wave is constrained by the existence of the separated shear layer, the probability density function of the solution may exhibit a bifurcation corresponding to a jump in the solution with a most probable value quickly switching from a larger to a lower value.

The impact of non-uniform mixed distributions on the stochastic flow was also investigated. A truncated Gaussian distribution for the free-stream Mach number was considered and the results were qualitatively similar to the results obtained for *uniform* distributions, with the predominance of the free-stream Mach number uncertainty onto the solution variability.

The global error of the stochastic projection gPC representation can be seen as a superposition of an aliasing error (coming from the interpolation related to the numerical quadrature), a finite-term projection error (due to the truncated gPC representation) and a numerical error due to the intrinsic numerical approximation of the deterministic solver. In this context, classical assessment of numerical accuracy of the method through convergence analysis becomes intricate. When studying stochastic approximations, it is common sense to wish the numerical errors associated with the deterministic solver to be independent and of smaller magnitude than the other errors. In the following, we will try to show, first with an example followed by some explanations that it is better to handle sources of errors of *comparable magnitude*. Then we will carry out a complete convergence study for the four stochastic flow regimes investigated in the paper.

Chapter IV

Ongoing research interests

This chapter summarizes some of my current research interests. Some less active or fruitful topics are very briefly introduced last.

Sommaire

1	Quantification of errors in turbulence modeling	127
1.1	Sensitivity of Large-Eddy Simulation to subgrid-scale-model	128
1.2	A stochastic view of self-similar isotropic turbulence decay	131
2	Subsonic and supersonic nonlinear stochastic aeroelastic flutter	133

1 Quantification of errors in turbulence modeling with emphasis on homogeneous isotropic turbulence

This topic is dedicated to some aspects of the quantification of errors in turbulence modeling with emphasis on (decaying) Homogeneous Isotropic Turbulence (HIT). In particular we are interested in the sensitivity of the relationship between Smagorinsky subgrid-scale-model and turbulent energy spectrum to uncertainties. We also look into the influence of initial energy spectrum variability onto the decay power-law exponents of the turbulent physical quantities. Both analytical and computational approaches, including Large-Eddy Simulation (LES) and Eddy Damped Quasi-Normal Markovian (EDQNM) based simulation, are followed. The stochastic methodology relies onto global gPC approximation obtained via spectral projection, cf. Section 3.2. The basis of approximation is chosen based on input parameters probability distribution and the numerical projection is carried out thanks to standard Gauss-type quadrature. This work has been communicated in the following publications [281, 316, 315].

Homogeneous turbulence dynamics represents the true core of turbulent dynamics, see the following influential works and general-purpose textbooks written on the subject by Batchelor(6), Tennekes & Lumley(129), Pope(107), Bailly & Comte- Bellot(4), Davidson(25) and Sagaut & Cambon(117). Homogeneous isotropic turbulence (HIT) is the simplest turbulence problem that may be analyzed as no interaction with a structuring effect (mean flow, body force, shock wave, wall, etc.) may occur. We refer the reader to [314] for complementary details.

Considering Navier-Stokes equations, the primary approximations for unsteady simulations of turbulent flows are *direct* numerical simulations (DNS), *averaged* simulations (e.g. RANS or URANS) and *filtered* simulations (e.g. LES). While the principal operation in LES relies onto *low-pass* filtering, the *effective* filter recovered in practical LES computations is actually determined by different sources: *grid* filter, *theoretical* filter, *numerical* filter and *subgrid model* filter. Most of the work presented in literature deals with the theoretical filter, while very little is known at the present time about the numerical filter and subgrid model filter.

In order to obtain a tractable set of governing equations from the filtered equations, it is necessary to close the problem (i.e., the subgrid tensor must be expressed as a function of the variables of the filtered problem). The effectiveness of the subgrid model may be estimated by its capacity to comply with physical constraints as well as by its numerical performances [421]. The most popular subgrid model is certainly the Smagorinsky model, which is also the oldest one [444]. It is obtained by performing a simple dimensional analysis. Assuming that the cutoff length scale is representative of the subgrid modes and that the local equilibrium hypothesis is satisfied – that is, the production rate of kinetic energy is equal to the transfer rate across the cutoff, which is

equal to the dissipation rate by the viscous effect, resulting in an automatic adaptation of subgrid scales to the resolved ones, one obtains for the eddy viscosity:

$$\nu_t = (C_S \Delta)^2 |\bar{S}|, \quad \text{with } |\bar{S}| = (2 \bar{S}_{ij} \bar{S}_{ij})^{1/2}. \quad (\text{IV.1})$$

But the constant of the model C_S remains to be evaluated. A theoretical value of the constant can be derived under the assumptions that the spectrum is a Kolmogorov spectrum. In fact that value is not a universal one and depends *a priori* on the energy spectrum.

1.1 Sensitivity of Large-Eddy Simulation to subgrid-scale-model

Large-Eddy simulations (LES) [409, 421], are based on a scale separation by reducing the complexity of the Navier-Stokes equations by means of a low-pass filter. The larger scales are directly simulated while the smallest scales are parametrized by a statistical model referred to as *subgrid-scale model* which accounts for the subgrid-scale stresses [421]. Regrettably, as reviewed by [210], one can estimate, based on conditional averages, that the statistical error between the “best” model based on resolved properties and the effective subgrid-scale stresses is at the best in the order of 80%. Indeed, subgrid-scale models do not always yield their theoretically expected solution, and there often exists a significant discrepancy between *a priori* tests and *a posteriori* results.

This not only illustrates the difficulty related to the formulation of subgrid-scale closures, but also outlines the limitations of the LES approach to predicting turbulence, indicating that instantaneous LES solutions will quickly diverge from the exact filtered solution.

Remark IV.1

It is however one of the most central assumptions in LES that statistically averaged properties, such as mean profiles, the average turbulent kinetic energy distribution, etc., can be predicted well when a suitable subgrid closure is used [317].

In practice, simplifications and assumptions related to the shape of the LES filter, the type of turbulence at the filter cut-off, the numerical implementation of the modeled LES equations, etc., in combination with the nonlinear nature of the Navier–Stokes equations introduce numerous errors in the simulation [167, 156, 322]. All these source of errors lead to a certain level of *uncertainty* in the subgrid-scale models, most notoriously when they bear an adaptable model parameter, such as, e.g. the well-known *Smagorinsky* model [444].

There have been several attempts to apply a PC-based approach to turbulence. In fact, this approach was suggested in the early works of Wiener in 1939, but the idea lay dormant for twenty years. During the 1960’s, several proposals have suggested developing a theory of turbulence involving a truncated Wiener–Hermite expansion of the velocity field [310, 360, 309, 90, 61, 77]. Unfortunately, all these works failed in the sense that the *finite* Hermite polynomial approximation yielded non-physical kinetic energy spectra. The main reason was that, due to the non local and nonlinear character of turbulence, a truncated polynomial expansion was not able to account for *long-term dynamics* of the kinetic energy transfers among modes and their correlations. This drawback is associated with a well-known difficulty in the UQ of uncertain dynamical systems over long times. In this case, the parametric uncertainty directly affects the system phase velocity which translates in a broadening spectral content of the solution with time, precluding accurate approximations using usual discretization techniques based on fixed-order stochastic polynomial bases. That is why the direct decomposition of the instantaneous turbulent field onto a PC approach can not presently be considered as an efficient way to address the issue of the sensitivity of a simulated turbulent flow. Instead, the statistical moments of the simulated turbulence field (or related quantities such as the kinetic energy spectrum) may be successfully approximated as functions of the uncertain parameters [281, 316].

Here, we address the sensitivity of LES to parametric uncertainty in the subgrid-scale model. More specifically, we investigate the sensitivity of the LES statistical moments of decaying HIT to the uncertainty in the Smagorinsky model free parameter C_s (i.e. the Smagorinsky constant). In all simulations a second-order cell-centred finite-volume method is employed to discretize the closed LES equations. This is combined with a four-stage, second-order accurate Runge–Kutta time integration. LES of decaying homogeneous isotropic turbulence are carried out at a number of resolutions and different values for the model parameter C_s , and a Taylor scale-based Reynolds number $Re_\lambda = 100$. The initial fields for the LES are generated by filtering the initial DNS fields taken from [322] with a sharp cut-off filter, with cut-off related to the grid cut-off wavenumber. During the simulations, no additional explicit filtering is performed and for the implementation of the Smagorinsky model, we further take $\Delta = h$. The analysis is carried out for different grid resolutions and C_s distributions. Numerical predictions are also compared against DNS evidence.

Results demonstrate that the LES solution is very sensitive to C_s , cf. the temporal energy decay in Figure IV.1(a). For low to moderate values of C_s ($0 \leq C_s \lesssim 0.2$), it was observed that all spectra share a common

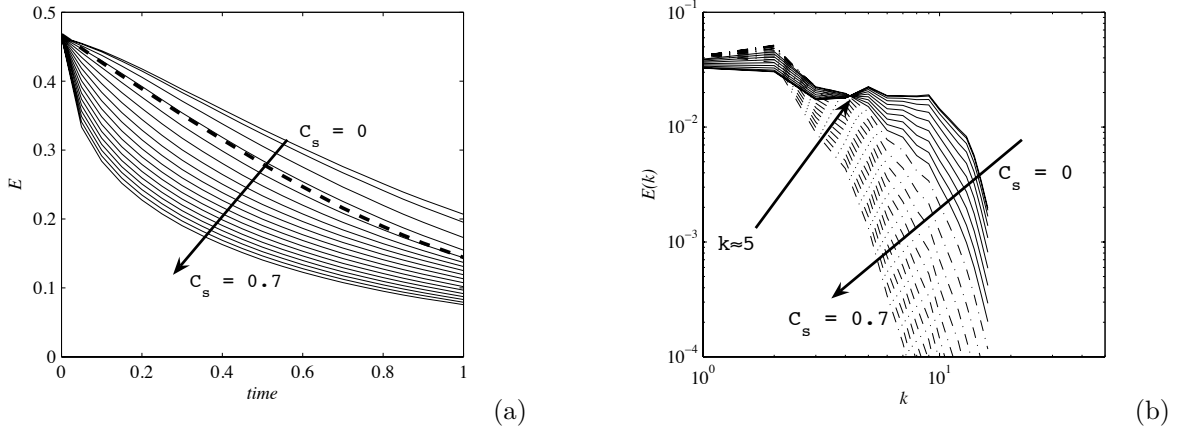


Figure IV.1 – (a): Temporal energy decay of 32^3 LES with Smagorinsky constants ranging between 0 and 0.7. (—): LES results; (---): filtered DNS results. (b): Energy spectra at $t = 0.8$ of 32^3 LES with Smagorinsky constants ranging between 0 and 0.7. (—): low to medium C_s range ($0 \leq C_s \lesssim 0.2$); (---): medium to high C_s range ($0.2 \lesssim C_s \leq 0.7$).

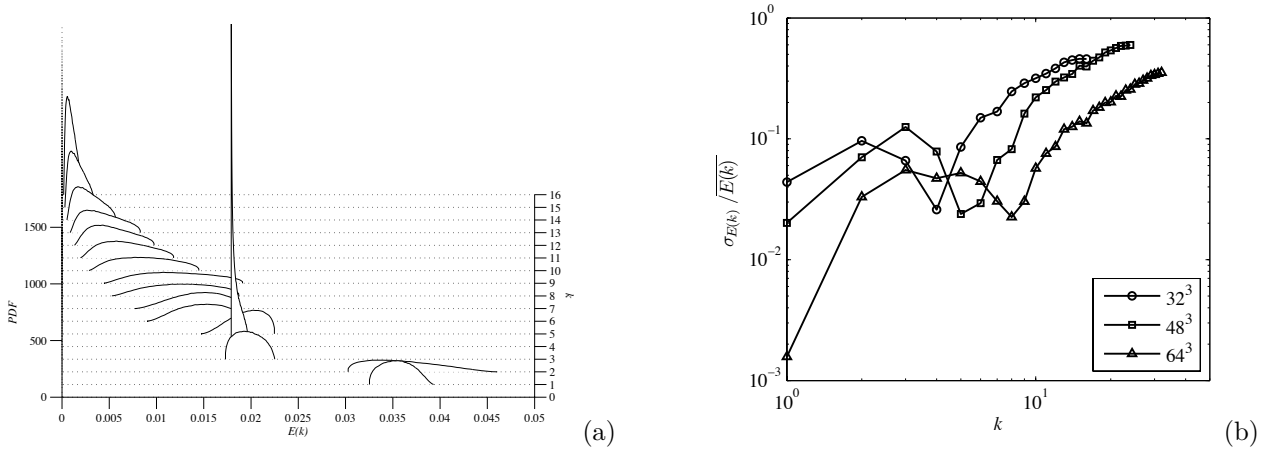


Figure IV.2 – (a): Turbulent kinetic energy pdf results for 32^3 grid cells. (b): Coefficient of variation $c_v = \sigma_{E_k} / \sqrt{E_k}$ of the turbulent kinetic energy.

point named C_s^+ (at $k \approx 5$, $k \approx 6$, and $k \approx 9$ for 32^3 , 48^3 and 64^3 respectively), in which the energy seems independent of C_s [281], cf. Figure IV.1(b) for 32^3 . The tail of the spectrum is adapted drastically. Due to the low simulation resolution, the variation of C_s also reflects on the large scales. However, their dependence on C_s is weaker. The transition to small-scale behaviour is sharply marked by the above-discussed point. To the right of this point, we observe a monotonous decrease of $E(k)$ (while to the left, $E(k)$ does not change monotonously with C_s). An interesting result is that this critical value is very close to the usual heuristic values found for C_s in the literature. This may lead to the definition of an *a priori* criterion for the choice of the optimal C_s , and is an interesting subject for further research.

Results show that the different turbulent scales of the LES solution respond differently to the variability in C_s . In particular, the study of the relative turbulent kinetic energy distributions for different C_s distributions indicates that small scales are mainly affected and adapt to the changes in the subgrid model parametric uncertainty. The smallest resolved scales exhibit the largest relative variation to a change in C_s , cf. figures IV.2. This is in agreement with the general idea that the turbulent motion at small scales is more “random” than the large-scale motion. This view yielded the proposition of the local-chaos hypothesis [304]. The observed behaviour of the skewness of the pdf of the smallest resolved scales is coherent with the dynamical picture that a preferentially underestimated value of C_s will yield a preferential overestimation of the kinetic energy borne by these scales, related to an energy pile-up. The change in the sign of the skewness of the pdf between very large and small scales can also be interpreted. An overestimation of the smallest-scale kinetic energy may result in a too high kinetic-energy transfer rate from large to small scales due to triadic interactions, i.e. an accelerated forward energy cascade process, leading to an underestimation of the large-scale energy. On the contrary, an underestimation of the smallest-scale kinetic energy can yield a too small energy-transfer rate and the so-called “bottleneck effect”, i.e. an overestimation of the large-scale kinetic energy.

1.1.1 Influence of energy spectrum shape uncertainty over optimum Smagorinsky model constant

In the previous study, the proposed analysis quantified the effects of different C_s values over the resolved large scales of LES simulations of decaying HIT. However, no information about the constant C_s itself could be recovered since it was *a priori* modeled as a random variable over different types of distributions and supports. In the present approach we propose to take this analysis to a complementary point of view, directly analyzing the effects of uncertainties in the energy spectrum formulation over the *optimum* Smagorinsky model constant predicted from the *exact* relation governing the dissipation rate of the flow [321]. The goal is also to carry out this analysis for a wider range of Reynolds number from moderate to high Reynolds numbers.

Meyers & Sagaut reformulate the Smagorinsky parameter as:

$$C_S = \frac{C_{S,\infty}}{\gamma} \Phi^{-3/4} \sqrt{1 - \left(\frac{\gamma L}{C_{S,\infty} \Delta} \right)^{4/3} \frac{1}{Re_L} \Phi} \quad (IV.2)$$

where Φ , γ are integral quantities dependent over the resolved part of the energy spectrum, defined as:

$$\gamma = \frac{\left(\frac{4}{3} \int_0^{+\infty} k^{1/3} G^2(k) dk \right)^{3/4}}{\pi / \Delta} \quad (IV.3)$$

$$\Phi = \frac{4}{3} \frac{\int_0^{+\infty} x^{1/3} G^2(x/L) f_L(x) f_\eta(x Re_L^{-3/4}) dx}{(\gamma \pi L / \Delta)^{4/3}} \quad (IV.4)$$

were $x = kL$, with L the characteristic length of the flow, Δ the filter width, $C_{S,\infty}$ the Lilly-Smagorinsky parameters, f_L and f_η are the functions shaping the energy spectrum close to the large scales and the small scales respectively, and G is the LES filter kernel.

The considered energy spectrum will not be computed by a numerical simulation but directly evaluated from two different theoretical functional forms, namely the functional form proposed by Pope [391] and the more complex one proposed by Meyers & Meneveau [323] including bottleneck and intermittency effects.

Remark IV.2

We consider the influence of uncertainties in the shape of the energy spectrum over the optimum Smagorinsky model constant [321]. The free parameters controlling the energy spectrum functional form at different (large & small) scales are modeled as random variables over bounded supports: two models of the energy spectrum are investigated, namely the functional form proposed by Pope [391] and by Meyers & Meneveau [323]. The analysis is performed for two different LES filter shape (i.e. sharp cutoff and Gaussian filter).

For instance, here is the recent energy spectrum model proposed by Meyers & Meneveau [323]:

$$E(k) = C_K \varepsilon^{2/3} k^{-5/3} (kL)^{-\beta} f_L(kL) f_\eta(k\eta) \quad (IV.5)$$

where $\beta = \mu/9$ is the intermittency correction in the inertial range of the spectrum, C_K is the Kolmogorov constant, $L = E_t^{3/2}/\varepsilon$ is the integral length scale, η is the Kolmogorov length scale and ε is the rate of energy dissipation. The functions f_L and f_η are expressed as:

$$f_L(kL) = \left(\frac{kL}{[(kL)^p + \alpha_5]^{1/p}} \right)^{5/3+\beta+\sigma}, \quad f_\eta(k\eta) = e^{-\alpha_1 k\eta} B(k\eta). \quad (IV.6)$$

The *bottleneck* correction $B(k\eta)$ is

$$B(k\eta) = 1 + \frac{\alpha_2 (k\eta/\alpha_4)^{\alpha_3}}{1 + (k\eta/\alpha_4)^{\alpha_3}} \quad (IV.7)$$

The parameter σ is related to the slope of the energy spectrum at very large scales, while p drives the position and the smoothness of the energy peak. Parameters $\alpha_1 - \alpha_4$ govern the shape of the spectrum at high wave numbers while α_5 controls it at low wavenumbers. The α_i , $i = 1, 5$ parameters are obtained by solving a system of five equations, which are related to the recovery of target values for the turbulent kinetic energy, the turbulent dissipation (or equivalently the enstrophy), the palinstrophy (or equivalently the longitudinal velocity derivative skewness) and constraints derived considering some possibly universal feature of the dissipation spectrum.

High Reynolds numbers sensitivity analysis

The study at high Reynolds numbers, $Re_\lambda = 10^4, 10^5$, consider uncertainties in the *large* scales via the tridimensional parametric space $[\sigma, \mu, C_k]$ (taken as iid *uniform* RV) together with the Pope's energy spectrum form. Results show that:

1. The obtained optimum C_S pdf are close to *uniformly* distributed when the LES cut is applied in the inertial region. In this region the pdf bounds are quite insensitive to the change in the filter cut position. Interestingly, the stochastic mean value of the model constant preserves all the characteristic of the algebraic theoretical behavior (i.e. the Smagorinsky - Lilly model constant value is recovered) at $L/\Delta \gg 1$.
2. If the LES cut is moved toward the dissipation region, probable values of C_S are lower with more “peaked” pdf and smaller variance.
3. It is found that the the model constant is sensitive to μ variations if the LES cut is operated close to the dissipation region of the spectrum, while the effect of the Kolmogorov constant C_k is dominant if the cut is applied in the inertial range.
4. However, the model constant prediction showed no sensitivity to σ parameter variations: this highlights that the shape of the energy spectrum at the large scales.

Moreover, it was shown that the choice of a suitable C_S is not significantly sensitive to the filter used.

Point 4. is interesting because large scales are considered a characterizing feature of the flow type and the literature reports variable C_S values for practical applications. Our results suggest that large scales knowledge may actually not be a crucial information to determine the right level of dissipation to introduce in the numerical simulation. The different C_S values reported in literature for practical applications may be due to different reasons:

- The Reynolds number considered is not sufficiently high to satisfy the scale separation hypothesis. It will be shown in the next section that at moderate Reynolds number a significant overlap of the optimum model constant is recovered as a function of the parameters $[Re_\lambda, \Delta]$.
- The application of non spectral methods to practical numerical simulations of flows may lead to controversial results because the energy spectrum is local in space and time, while the grid filter is usually global.
- The numerical error, which modifies principally the smallest resolved scales, introduces a high degree of uncertainty in the prediction of the optimum model constant.

These considerations point out how different optimum values of the model constant may be recovered because the whole simulation process presents different characteristics and not necessarily because different flows are analyzed.

Moderate Reynolds numbers sensitivity analysis

The study at moderate Reynolds numbers, $250 \leq Re_\lambda \leq 1200$, consider uncertainties in both the large and small scales.

The introduction of uncertainties in the large scales show that the predicted model constant is almost not sensitive to the shape of the energy spectrum for low k values. This result is not in agreement with most of the works reported in literature, which generally point out a sensitivity of the model constant to the kind of flow simulated. In our opinion, this result could be assigned to the numerical setup of the problem and not to the flow characteristics. In fact, the model constant shows an almost deterministic behavior if the cut is operated in the inertial region, but it exhibits a strong sensitivity if the filter width Δ is comparable in magnitude to the Kolmogorov scale η .

Small scales uncertainties are introduced via the bottleneck correction term in the Meyers & Meneveau model only, as preliminary analysis showed that the spectrum functional form proposed by Pope is not significantly sensitive to uncertainties propagated at the small scales. Results show that the sensitivity of the model constant prediction to uncertainty in the bottleneck correction term is much stronger. This means that a great care has to be payed to the choice of the model constant, if the LES cut is not performed in the inertial range, since a wide range of possible values of the constant may introduce the right level of dissipation.

1.2 A stochastic view of self-similar isotropic turbulence decay

The decay of isotropic turbulence is one of the oldest topic considered in the field of turbulence theory, which started with the seminal studies of [467]. Comprehensive reviews are presented by [27], [185], [93] and [419]. One of the most famous related issue deals with the existence and uniqueness of self-similar regimes, in which global turbulent quantities, such as turbulence kinetic energy q , behave like

$$q(x) = A(x/M_u - x_0/M_u)^n \quad \text{or} \quad q(t) = A'(t - t_0)^n \quad (\text{IV.8})$$

where x, x_0, M_u, A, A' and n are the distance downstream the grid, the virtual origin of isotropic turbulence, the mesh size of the grid used to trigger turbulence, two parameters and the *decay exponent*, respectively.

Remark IV.3

|

The value of the decay exponent value n of Eq. (IV.8) (or equivalent power law exponent for other global physical quantities) is not unique but mainly governed by initial conditions [238, 28, 417]. More specifically, the shape of the spectrum at very large scales is observed to be of primary importance.

In fact several spectrum shapes at very large scale are known to be physically realizable in isotropic turbulence. This point has been discussed by many authors, since it is related to the famous controversy dealing with existence of invariants in high-Reynolds decaying turbulence. [417] showed that the invariance of the Birkhoff-Saffman invariant $L = \int \langle \mathbf{u} \cdot \mathbf{u}' \rangle d\mathbf{r}$ during turbulence decay is related to linear momentum conservation. The associated kinetic energy spectrum behaves like $E(k \rightarrow 0) = Lk^2/4\pi^2$ and theoretical analysis shows that the turbulent kinetic energy decays as $q(t) \sim t^{-6/5}$. If $L = 0$ the resulting condition is referred to as Batchelor turbulence: the corresponding large scales behaves like $E(k \rightarrow 0) = Ik^4/24\pi^2$, where $I = \int \mathbf{r}^2 \langle \mathbf{u} \cdot \mathbf{u}' \rangle d\mathbf{r}$ is the Loitsyansky's integral. In this case, the turbulent kinetic energy scales as $q(t) \sim t^{-10/7}$.

The Reynolds number is also known to be a key parameter: low-Reynolds number flows do not exhibit the same power-law exponent as high-Reynolds number flows (see e.g. [55]).

Prediction of power-law exponent starting from a simplified kinetic energy spectrum shape was introduced by [84] and then revised by [417, 418]. Following these works, the spectrum is divided into two power-law ranges joining at a peak located at k_L : one for the very large scales, $E(k \leq k_L) = Ak^\sigma$, $\sigma \in [1, 4]$, and a Kolmogorov-type inertial range at smaller scales $E(k \geq k_L) = C_K \varepsilon^{2/3} k^{-5/3}$, where σ , C_K and ε denote the spectrum slope at large scales, the Kolmogorov constant and the turbulent dissipation rate, respectively. While Saffman ($\sigma = 2$) and Batchelor ($\sigma = 4$) turbulences have been extensively analysed, other possibilities have also been considered, e.g. $\sigma = 1$ and $\sigma = 3$ in [80], [356]. Predictions dealing with power-law exponents of some usual physical quantities in the high-Reynolds number case are presented in the first column of Table IV.1.

This analysis was then developed to investigate the sensitivity of the power-law exponent to additional features of the initial condition. An important conclusion is that saturation induced by boundary condition yields a dramatic change in the power-law exponent, making it very difficult to distinguish between saturated high-Reynolds regime and free low-Reynolds evolution. Truncation of energy spectrum at very large scales also corrupts the computation of integral quantities, such as integral length scale [503].

An important point is that experimental validation of theoretical predicted behavior is elusive for many reasons:

1. it is almost impossible to enforce the spectrum shape at very large scales in laboratory experiments
2. the large-scale spectrum shape is often not directly measured but deduced from the measured decay law and theoretical relations which bridge between them
3. identification of free parameters in Eq. (IV.8), namely A (or A'), x_0 and n , leads to the definition of a non-robust optimization problem, which introduces a significant uncertainty in the estimates [332, 241]
4. spurious saturation effects may occur in numerical simulations due to the use of periodic boundary conditions, and that very large computational domains must be used in order to preclude such problem, [201] which is not the case in most published papers

Another important issue is the possible existence of a universal decay regime, in which kinetic energy should decay as t^{-1} . Such a regime is predicted by some theoretical models like [150], but it has not been observed up to now and seems at least partially contradictory with a strong dependency upon initial conditions.

The results confirm that the slope of the spectrum at large scales at initial time is the leading parameter that governs the decay regime. A $q \sim t^{-1}$ decay can be observed at finite time and finite Reynolds number for $\sigma \simeq 1$, a small variability with other large-scale parameters being observed. In that regime, turbulence decays at almost constant Re_λ . The occurrence of this regime shows that $n = -1$ is not tied to the existence of a universal asymptotic regime, and that experimental evidence of the existence of such a universal regime may be very difficult to obtain, unless σ is accurately and independently measured.

The dependency upon σ is observed to remain, even at Reynolds numbers considered in the present study ($Re_\lambda > 400$), which are higher than those considered in almost all existing published results. The variability observed for Batchelor and Saffman turbulence with respect to details of spectrum shape is relatively small, leading to an almost univoque identification of σ from n , inverting relations retrieved from the CBC theory, at least at high Reynolds number and restricting the analysis to integer values for σ . Present results show no evidence of the existence of a universal regime with $q \sim t^{-1}$ at high but *finite* Reynolds number, even looking at long-time evolution.

Another point is that, even though isotropy is perfectly satisfied and finite size effects are absent (the ratio integral lengthscale / lowest resolved scale is greater than 250), the decay exponent is governed by σ . Therefore, convergence toward a single value reported in some experimental works when isotropy is refined (e.g. [246]) might be the signature of the large-scale spectrum produced by a given experimental set-up rather than a true universal value.

Quantity	CBC formula	$\sigma = 1$	$\sigma = 2$	$\sigma = 3$	$\sigma = 4$
q	$-2 \frac{\sigma + 1}{\sigma + 3}$	-1.005 (<1%)	-1.213 (1.2%)	-1.342 (<1%)	-1.4014 (2%)
L	$\frac{\sigma + 3}{3\sigma + 5}$	0.457 (8%)	0.402 (<1%)	0.336 (1.8%)	0.307 (7.8%)
η	$\frac{4(\sigma + 3)}{3\sigma + 5}$	0.502 (1%)	0.556 (1.2%)	0.588 (<1%)	0.603 (<1%)
λ	$\frac{1}{2}$	0.501 (<1%)	0.505 (1%)	0.505 (1%)	0.505 (1%)
ε	$\frac{-3\sigma - 5}{\sigma + 3}$	-2.009 (<1%)	-2.226 (1.2%)	-2.352 (<1%)	-2.412 (<1%)
Re_λ	$\frac{2(\sigma + 3)}{1 - \sigma}$	-0.0006	-0.1006 (<1%)	-0.166 (<1%)	-0.195 (8.9%)
Re_L	$\frac{1 - \sigma}{\sigma + 3}$	-0.044	-0.204 (2.3%)	-0.335 (<1%)	-0.393 (8.3%)

Table IV.1 – Power-law exponents in high-Reynolds isotropic turbulence decay. Comte–Bellot–Corrsin (CBC) formula denotes expressions obtained via dimensional analysis. Other columns display values computed using classical deterministic EDQNM simulations, using a two-range CBC spectrum at initial time and $(Re_\lambda(t = 0) = 10^4)$. Relative error vs. theoretical predictions are reported between parentheses. q : turbulent kinetic energy; L : integral lengthscale; η : Kolmogorov lengthscale; λ : Taylor micro-scale; ε : turbulent dissipation rate; $Re_\lambda = \sqrt{2q/3}\lambda/\nu$; $Re_L = \sqrt{2q/3}L/\nu$.

2 Subsonic and supersonic nonlinear stochastic aeroelastic flutter

This topic is dedicated to the development and integration of adaptive stochastic spectral projection methods for the uncertainty quantification in limit-cycle oscillations of elastically mounted 2-D lifting surfaces in subsonic or supersonic flow fields. The physical nonlinearities of the system promote sharp and sudden flutter onset for small change of the reduced velocity. In a stochastic context, this behavior translates to steep solution gradients developing in the parametric space. A remedy is to expand the stochastic response of the airfoil on a piecewise generalized Polynomial Chaos basis, cf. Section 2.3.2. Accurate approximation and affordable computational costs are obtained taking advantage of sensitivity-based adaptivity for various types of stochastic responses depending on the selected values of the flow speed on the bifurcation map. This work has been communicated in the following publications [312, 251, 70, 71].

Certification of aeroelastic stability is of primary importance in the design of high-speed aeronautical vehicles. The presence of inherent structural and aerodynamic nonlinearities in military aircraft with store configurations may dramatically affect aircraft maneuverability and thus reduces the flight envelope. In particular, important vibrations of nonlinear aeroelastic configurations can be observed in the vicinity of the flutter boundary [252]. These limit cycle oscillations (LCO), which result from the bifurcation from a stationary state to an oscillatory response of the dynamical system, are very sensitive to inherent small variations in the mechanical properties of the structure or in flight conditions [259]. Therefore, reliability-based design approaches have received particular attention for quantitative risk analysis in nonlinear aeroelasticity by means of UQ [375]. To this end, a stochastic framework is considered where the uncertain parameters are modeled as input RV with bounded distributions. Uncertainties are then propagated to LCO using suitable probabilistic approaches for nonlinear systems.

Recently, stochastic approximation methods have been proposed in the field for efficient propagation of parametric uncertainties: among others, the probabilistic collocation method [492, 328, 31, 330, 32, 194], unsteady adaptive stochastic finite elements (FE) [516, 513, 512, 515, 514] and stochastic spectral projections [53, 313, 105]. Pioneering attempts devoted to the computation of stochastic LCO using a spectral approach can be found in [329, 376, 330, 328, 331, 31]. LCO pdf were initially obtained in an *intrusive* manner using PC expansion or Fourier-Chaos expansion of the stochastic solution [329, 376, 330]. Stochastic LCO due to bounded random variables with λ -pdf were computed by Wu et al. [520] using Gegenbauer polynomials. Non-intrusive approaches were also investigated by means of time-domain stochastic projections with multivariate B-spline samples [331] or Wiener-Haar expansions [32].

In a recent series of papers, Witteveen et al. [516, 513, 512, 515, 514] developed efficient unsteady stochastic FE methods for the study of period-1 or higher period stochastic bifurcations of a nonlinear airfoil model. Long-term stochastic effects of random parameters are resolved using a time-independent parametrization of the periodic response of the deterministic samples [513]. On the other hand, long transients of the stochastic solution can be captured using probabilistic collocation method based on interpolation with constant phase [512]. Total variation diminishing (TVD) properties in probability space of the unsteady adaptive stochastic FE method are assessed in [515].

As seen in Section 2.3.2, Wan & Karniadakis [494] proposed a decomposition of the random space based on piecewise gPC expansions of the stochastic solution for problems with strong discontinuities in random space. This approach was successfully employed for uncertainty quantification of flat plate aeroelasticity under uncertain Reynolds number [53]. In practice, the need of this method for extensive computational resources is limited by the use of an adaptive formulation [494, 496, 313].

The aim of this study is to compute the stochastic nonlinear response of a supersonic lifting surface in the presence of supercritical bifurcations. Both structural and aerodynamic nonlinearities are taken into account in the aeroelastic model. The stochastic behavior of the airfoil due to several uncertain structural parameters with bounded distributions is expanded on a piecewise gPC basis. Adaptive refinement algorithms are employed to capture fronts and discontinuities in the response surfaces when strong nonlinearities are present in the physical space. The two-degree-of-freedom motion is described by means of the plunge displacement h of the elastic axis (positive up) and the pitch angle α (positive nose up). The torsional restoring stiffness is controlled by a nonlinear spring, and a linear spring is employed for the vertical motion. Additional parameters, which are represented in Fig. IV.3, are the half-chord length b , the dimensionless static unbalance x_α about the elastic axis and the free-stream velocity U_∞ . The aeroelastic motion of a two-degree-of-freedom pitch-and-plunge

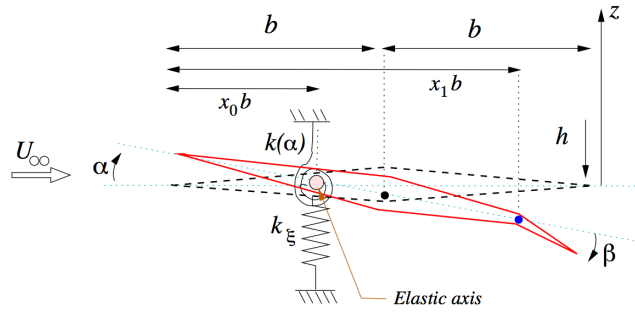


Figure IV.3 – Two-degree-of-freedom pitch-and-plunge supersonic lifting surface model

supersonic lifting surface model are governed by the following coupled bending-torsion equations [259]

$$\xi'' + x_\alpha \alpha'' + 2\zeta_h \frac{\bar{\omega}}{V} \xi' + \left(\frac{\bar{\omega}}{V}\right)^2 \xi = l_a(\tau) \quad (\text{IV.9})$$

$$\frac{x_\alpha}{r_\alpha^2} \xi'' + \alpha'' + 2\frac{\zeta_\alpha}{V} \alpha' + \left(\frac{1}{V}\right)^2 k(\alpha) = -m_a(\tau) \quad (\text{IV.10})$$

Herein, $\xi = h/b$ is the dimensionless displacement of the elastic axis with half-chord b , r_α is the radius of gyration about the elastic axis x_{EA} , μ represents the mass ratio, damping coefficients in pitch and plunge are ζ_α and ζ_ξ respectively, $\bar{\omega} = \omega_h/\omega_\alpha$ is the frequency ratio computed from the uncoupled plunging ω_h and ω_α frequencies of the undamped motion, $V = U_\infty/b\omega_\alpha$ denotes the nondimensional airspeed parameter, $k(\alpha)$ is the pitching restoring force which is a nonlinear function of the pitch angle α and the primes refer to differentiation with respect to the nondimensional time $\tau = U_\infty t/b$.

The aerodynamic operator contribution is through non-dimensional lift $l_a(\tau)$ and pitching $m_a(\tau)$ moments. We use an unsteady nonlinear aerodynamic model based on piston theory in the third approximation [259] and accounting for flap deflection β [395]. The pitching restoring forces $k(\alpha)$ are modeled by means of a 3rd order polynomial expression $k(\alpha) = \alpha + B\alpha^3$, where the coefficient B , which is representative of the level of nonlinearity of the dynamic system. Soft structural nonlinearities corresponds to negative values of B while positive values of B account for hardening springs.

The governing equations of motion (Eqs. IV.9-IV.10) can be converted into a state-space matrix form:

$$\dot{\mathbf{x}} = \mathbf{A}\mathbf{x} + (\mathbf{p}_s + \mathbf{p}_a)\alpha^3 + \mathbf{f} \quad (\text{IV.11})$$

where $\mathbf{x} = [\xi \ \alpha \ \xi' \ \alpha']^T \in \mathbb{R}^4$ defines the state vector of the system, $\mathbf{A} \in \mathbb{R}^{4 \times 4}$ is the linear system matrix, $\mathbf{p}_s \in \mathbb{R}^4$ and $\mathbf{p}_a \in \mathbb{R}^4$ correspond to the non-linear contributions of the structural and aerodynamic nonlinearities respectively and $\mathbf{f} \in \mathbb{R}^4$ accounts for aerodynamic effects of the flap [395]. The coefficients, which are functions of system parameters are detailed in [71]. In this work, Eq. (IV.11) is solved using an explicit fourth-order Runge-kutta time-integration scheme which was widely used in the context of incompressible flows [266, 313]. Figure IV.4 shows a successful example of successive steps in the refinement procedure of the stochastic approximation. We notice that the pitch amplitude α_{LCO} response surface correctly captures the oblique steep front separating the stable state from the LCO branch at Mach number $M = 2.1$. Here there are two uncertain parameters, structural damping coefficients, with bounded independent distributions and the

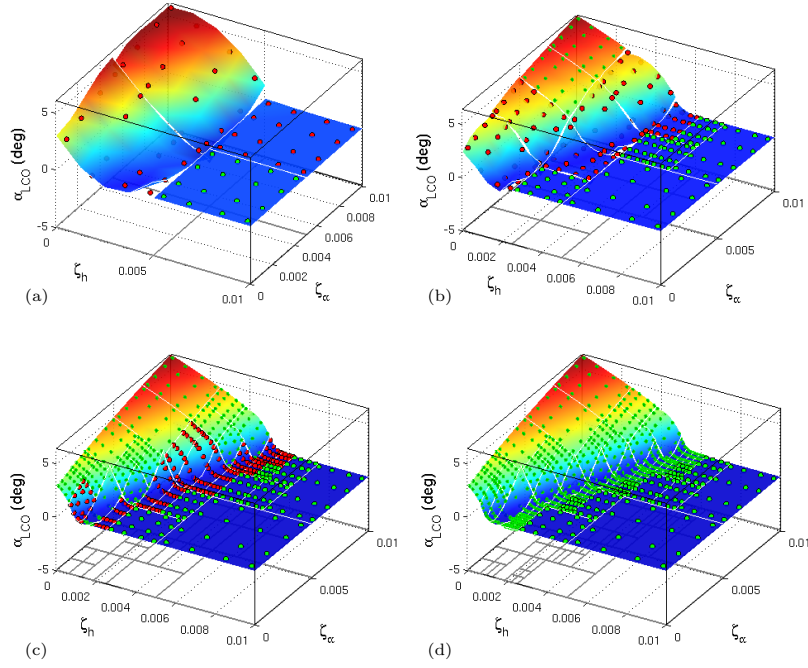


Figure IV.4 – Illustration of the piecewise gPC parametric grid-refinement process for the α_{LCO} response surface at $M = 2.1$. The combined uncertainties is in the structural damping coefficients ζ_h and ζ_α . (a) Level 2, $N = 4$; (b) Level 4, $N = 14$; (c) Level 6, $N = 35$; (d) Level 8, $N = 55$ elements.

polynomial order of approximation in each element is moderate, $P = 3$.

The adaptive method also works very well in 3 or 4 random dimensions. Figure IV.5 shows some results for a case with combined elastic axis location, torsional stiffness and flap angle uncertainties, cf. Table III.3. Again the adaptive refinement automatically captures the nonlinear flutter frontier. A sensitivity analysis based on Sobol' coefficients coupled to a multi-dimensional pdf analysis, cf. Figure IV.6, allowed to quantify the preponderance of each random parameter on the response for a wide Mach number range.

Dimension N_d	Parameter	Mean value	Range	Distribution
1	x_0	0.5	[0.475, 0.525]	<i>uniform</i>
2	B	12.5	[5, 20]	<i>uniform</i>
3	β	-1.5	[-3, 0]	<i>uniform</i>

Accuracy of the proposed method is validated against QMC sampling method and its robustness is tested for different aeroelastic random parameters and different Mach numbers [71]. The computational speedup compared to standard MC simulation is at least 2 orders of magnitude.

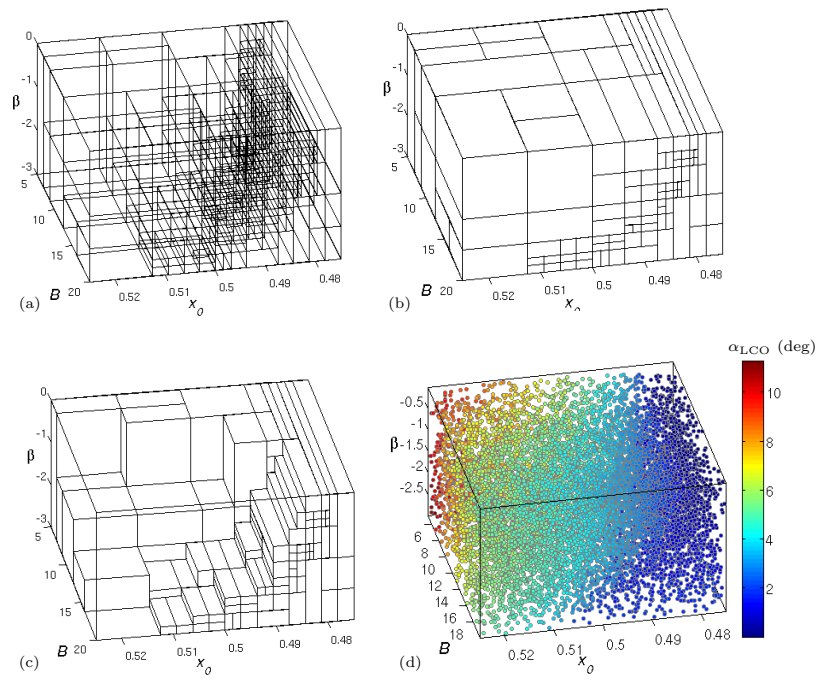


Figure IV.5 – Piecewise gPC LCO results at $M = 2.5$ with combined uncertainties in the elastic axis location x_0 , torsional stiffness B and flap angle β ($P = 4$) (a) wireframe rendering of the converged adaptive random space decomposition; (b) shaded-surface view; (c) cutaway view; (d) response surface of α_{LCO} obtained using 10,000 gPC samples.

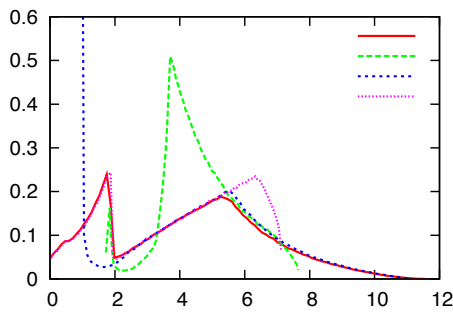


Figure IV.6 – Comparison of the α_{LCO} pdf profiles at $M = 2.5$

Flow-structure interactions of slender bodies subject to Vortex-Induced Vibrations

This vast topic addresses the numerical simulation and physical analysis of flow-structure interaction problems and more specifically the prediction of (free or forced) Vortex-Induced Vibrations (VIV) of slender bluff (rigid or flexible) bodies in a variety of incompressible incoming flows. This work has been communicated in the following publications [117, 278, 282, 283, 277, 280, 276, 529, 530, 118] with a more recent one [46].

Concluding remarks and some perspectives

This chapter first summarizes the main results obtained in the different studies presented in this manuscript. Some remarks and suggestions are proposed as a follow up guidance for ensuing works. Then, some midterm perspectives on new evolutions and topics of interest, in part impelled by recently started Ph.D. projects or collaborations, are exposed.

Summary

This manuscript considers probabilistic mechanics in the light of Computational Fluid Dynamics (CFD) that is a valuable predictive tool to analyze and simulate fluid flow problems but often fails when compared to experimental measurements. The question of the reliability and usefulness of computer predictions to practical applications demonstrates that confidence in CFD simulations must be quantitatively assessed. This can be done with Uncertainty Quantification (UQ) which aims at taking into account various system uncertainties in order to predict their impact onto the resulting stochastic model response. This work reports on parametric mechanical uncertainties defined by probability theory. It focus on UQ tackled by stochastic spectral methods that are grounded in strong mathematical bases and provide a rich probabilistic characterization of the system response. Even though spectral representations are applied to both random input data and model solution, it is mainly the propagation and quantification of this uncertainty that is addressed. The mathematical framework of the spectral representation of stochastic processes in numerical mechanics is introduced first. Some recent developments and possible improvements of those methods are then proposed and the numerical techniques are applied to the UQ of various fluid flows, with a particular emphasis on flows that have not been extensively investigated in the UQ literature: namely incompressible shear flows and shock-dominated compressible flows.

First, linear stability analysis of a plane Couette flow subject to an internal random perturbation – here added to the linearly sheared base flow – is carried out via a stochastic spectral projection based on the gPC theory. This approach probabilistically quantifies the stability properties of the system in a stochastic context. The computation of the sensitivity functions does not rely on any linear dependence assumptions of the response to the random perturbation nor it is restricted to small perturbation variations. A Gaussian random field with a Gaussian covariance kernel of prescribed correlation length Cl and variance is chosen to model the random fluctuations and is represented via a Karhunen-Loève expansion. We focus mainly on the sensitivity of the eigenspectrum as well as the maximum possible amplification of the transient growth; those quantities being computed thanks to a linear stability solver relying on a Chebyshev spectral collocation method. The eigenmodes close to the branch intersection of the eigenspectrum are shown to be the most sensitive to the uncertainty. Large variability in the normal velocity disturbance is obtained for correlation length lower than half of the channel height. The symmetric modes in the defects mainly influence the phase speed in the streamwise direction, while centrosymmetric components influence the stability of the system. Despite, this variance in the solution, the modal analysis shows that the flow remains linear stable for the range of correlation lengths and perturbation magnitudes investigated. This result may be attributed to the smoothness of the chosen random (Gaussian) perturbation and a correlation length too large to access a critical base flow wavelength of $\lambda/H \sim 1/2$, where H is the half-channel height.

Some preliminary results at $Cl/H \sim 1/3$ indicate that a few realizations, with low probability, did become unstable. In fact, the real computational challenge arises when a very short correlation length is considered. In this case, the level of noise induces a strong variation in closely spaced eigenvalues and it becomes difficult to accurately characterize the solution to the random eigenproblem [169]. Practically the difficulty appears in the form of mode switching whereby the eigenvalues of modes associated with particular physical behaviors do not maintain the same ordering across statistical realizations of the random system. The loss of convergence of the standard PC representation may be counterbalanced through basis enrichment [169]. We propose to test

the model refinement adaptive techniques described in Section 5.2 of Chapter 1 on this problem and release a report of our results in a near future.

Then, the effect of the inflow uncertainties on the growth of a forced two-dimensional plane mixing layer initiating from laminar conditions has been investigated. The stochastic analysis combines a stochastic spectral projection method with a spectral- hp element direct numerical solver. The amplitudes of the discrete forcing modes – composed of a fundamental plus one or two subharmonic modes – are treated as bounded random variables with amplitude amounting at most to 10% of the mean inflow. Uncertainties in the bi-modal and tri-modal perturbation magnitudes have significant effects on the spatial distribution of the mixing layer growth. The mixing layer is more sensitive during the vortex pairing phases. Moreover, the influence of uncertainty associated with fundamental or subharmonic forcing modes turns out to be stronger in specific downstream spatial areas. Probability density functions of the mixing layer thickness have shown large variations of the distributions leading to high level of uncertainty in the response. The growth of the layer thickness is not uniform and the most probable thickness evolves in a stepwise fashion along the downstream direction and almost doubles at each new pairing.

The flow structure in a three-dimensional plane mixing layer is largely two-dimensional [101] and the streamwise organization of vortices has a strong influence on the spanwise vortex structures [33, 318]. Indeed, we have seen that the principal mechanism of growth in the stochastic two-dimensional mixing layer simulation remains through pairing interactions. While, this mechanism dominates the pre-transition region of the three-dimensional plane mixing layer flow, it does not seem to be the case past the transition region. It is reported that self-similar plane mixing layers grow linearly, without preferred thickness levels, although at faster rate than two-dimensional layers, and therefore it is hard to speculate about their sensitivity to inflow perturbations. Because the transition to turbulence is triggered by the three-dimensional interaction between Kelvin-Helmholtz rollers and secondary streamwise structures, it is clear that UQ of three-dimensional mixing layer simulations is most relevant. Unfortunately, this is still out of reach for direct numerical solutions. One may resort to cheaper computational deterministic methods (e.g. LES) with the drawback of introducing unwanted numerical uncertainty (e.g. discretization/subgrid model errors,...). We propose a short-term simple UQ of a three-dimensional mixing layer LES with some one-dimensional stochastic perturbations along the spanwise direction in order to trigger the interaction of the primary vortex pairings with the secondary streamwise structures.

Stochastic spectral methods have been developed and adapted with success to ordinary differential, elliptic and parabolic equations subject to parametric uncertainties but their application to stochastic (nonlinear) hyperbolic problems is more challenging. Nonlinear hyperbolic systems of conservation laws promote discontinuous spatial solutions in finite time (i.e. shock waves). In a stochastic setting, discontinuous solutions develop in the stochastic space as well and severe Gibbs-like oscillations ineluctably appear close to the solution strong gradients. A new approach inspired by kinetic theory and akin to nonlinear Galerkin-type projection is proposed in this context. The idea is to expand an adjoint (entropic) variable related to the solution on the polynomial chaos basis, instead of the solution itself. This ensures the hyperbolicity of the obtained Galerkin system and the preservation of the physical invariants of the system. This makes the numerical method more stable and enables efficient control of the oscillations, that are drastically reduced in the vicinity of the shocks. Numerical and computational aspects of this approach compared to the classical one are theoretically discussed and put to perspectives when applied to simple inviscid Burgers' equation test case and to the more practical case of a two-dimensional Euler system with uncertain initial conditions.

The approach remains costly for high dimensional problems due to the additional optimization step, the CFL stability condition and the computation of some expectations of the fluxes via numerical quadratures. The use of sparse numerical cubatures to lower the computational cost of our applications has been quite inappropriate because of its impact on the accuracy of the scheme. It is therefore important to pursue this work and test *adaptive* sparse cubatures in order to capture and take advantage of the anisotropic behavior of the fluxes representation.

The prediction of transonic aerodynamics in the presence of external flow related uncertainties is of great interest for aerospace engineering related studies. The emphasis is put on the features of the Reynolds-averaged mean flow, which are the meaningful data, used for aerodynamic shape optimization for instance. For such analysis, global or oversimplified models are no longer relevant, and high fidelity Navier–Stokes simulations must be carried out. In our studies a stochastic spectral projection solver, based on gPC expansions, was applied to the uncertainty quantification of stochastic transonic flows around different airfoils due to random operating conditions. Simple stochastic models are considered in which the free-stream Mach number and the angle of attack are represented as independent random variables with bounded supports. The stochastic solver is coupled with a RANS deterministic solver to extract statistical informations of both the mean-flow and the anisotropic turbulent field. The stochastic/sensitivity analysis confirms that the free-stream Mach number uncertainty is the leading driving mechanism of the stochastic aerodynamic field. Nonetheless, once the mean-position of the

shock wave is constrained by the existence of the separated shear layer, the probability density function of the solution may exhibit a bifurcation corresponding to a jump in the solution with a most probable value quickly switching from a larger to a lower value.

For the parametric stochastic ranges of interest, the methodology does not suffer from any lack of robustness despite strong non-linearities (mainly due to the shock waves) present in the stochastic solution. An error analysis, based on the number of solution samples and the polynomial order at use depicts the coupling between aliasing error, finite-term projection error and the numerical error related to the intrinsic numerical approximation of the deterministic solver. It demonstrates that spatial distributions of solution statistics for this type of applications are smoother when deterministic and stochastic discretization errors are of comparable magnitude. Moreover, global aerodynamic quantities (e.g. lift and drag coefficients) and more local quantities such as the isentropic Mach number and pressure coefficients show fast convergence rates. Nonetheless, for other derived quantities more sensitive to numerical noise, such as the skin friction, the accuracy of the approximation remains acceptable.

In the following, we present some midterm additional perspectives that are in part impelled by recently started Ph.D projects or collaborations. Standard techniques for representing and quantifying the effect of uncertainty in the response of numerical simulations are now widespread. However, it becomes urgent to improve the representation of stochastic processes that describe the properties of random *inputs* to those simulations.

Parametric input identification, estimation and representation

An open question with enormous significance for UQ is the problem of realistic representation and description of input uncertainty (initial/operating/boundary conditions, model parameters, source terms,...). Most of the spectral UQ literature is frequently caricatural on this topic. This is because research in this area has been traditionally focus on other aspects of UQ, i.e. mainly related to the development of the UQ propagation stage and quantification of the response, with improvement on the efficiency, implementation, performance... The quantification of input uncertainty is often rudimentary, associating a random variable to each of the random parameter. Moreover, it is very common to make a choice *a priori* on the input distributions, relying for instance on “labeled” distributions, such as *uniform* distributions, due to a lack of knowledge. Another common weak assumption is random parameters *independence*. The “gold rush” for the development of suitable and efficient stochastic representations of ever increasing larger data sets (e.g. hundreds of random parameters) relies heavily on the assumption of independent random dimensions which is most of the time not justified for engineering systems. In fact the effective stochastic dimensionality of the system depends strongly on the appropriate representation of the correlations existing between the dependent random variables representing the inputs. This mathematical description is particularly difficult when data is gathered from different sources, let say from both experiments and simulations, or when direct observations/measurements are not possible or too costly. Several methodologies for the identification of representations of random variables/processes from *experimental* data for instance have been proposed, such as the method of moments [8], maximum likelihood [106, 165], maximum entropy [91] or Bayesian inference [501, 164].

The predictive accuracy of stochastic models depends also strongly on the availability of input data. For instance, a stochastic formulation is presented in [164] for the impact of data limitations associated with the calibration of parameters for these models, on their overall predictive accuracy. More specifically, the idea is to estimate gPC representations of these processes that are *consistent* with the data. The estimated polynomial chaos coefficients are themselves characterized as random variables with unknown probability density function, thus permitting the analysis of the dependence of their values on further experimental evidence. Others used the same idea together with a Bayesian approach to solve the inverse problem and infer on the gPC coefficients [9]. The use of the gPC methods for inverse problems seems promising to improve the acceleration of stochastic inverse problems and broaden their scope.

Inverse problems in science usually refer to the estimation of model parameters or inputs from *indirect* observations. While the resolution of a forward problem tries to predict the system outputs given the inputs by solving the governing equations, an inverse problem (IP) reverses this relationship by seeking to estimate uncertain inputs from measurements or observations. The IP is often formulated as a (large) *deterministic nonlinear* optimization problem that minimizes the discrepancy between the observed and predicted outputs in some appropriate norm while also minimizing a regularization term that penalizes unwanted features of the inputs [461, 215]. Following this procedure, a set of “best” inputs, i.e. fitting the data and minimizing the regularization penalty term, are obtained. However, in practice the observations are *limited* and often *noisy*. The forward model may also have limitations on its predictive value due to imperfections/errors in the model or the numerical scheme dedicated to its resolution (cf. V&V process in the Introduction Chapter). Moreover IP are often non-local and/or non-causal making their resolution ill-posed. For instance, no realistic physical

parameters may match the observed data (problem of existence), or a there is no unique solution (problem of uniqueness) or small measurement errors can lead to enormous changes in the estimated model (problem of stability). Therefore, it becomes more legitimate to seek a complete *statistical* description of the input values that is consistent with the data, instead of discrete estimates of the best-fit inputs.

The Bayesian inference (BI) approach follows this path by reformulating the IP as a problem of *statistical inference*, incorporating the forward model, prior information on the inputs, and uncertainties in the measurements. The solution is the *posterior* joint pdf of the inputs, which reflects the degree of confidence in their values [462, 215]. Thus, it becomes possible to quantify the resulting uncertainty in the inputs, taking into account the model, prior information, and uncertainties in the data. Some recent works have explored the use of forward metamodels to accelerate the convergence of BI [296, 137]. In particular, Marzouk et al. [296, 294, 295] was the first one to rely on the use of stochastic spectral methods, taking advantages of gPC representations for forward uncertainty propagation.

Efficient Bayesian inference for identification of dominant mixing zone parameters/scales in inertial confinement fusion

In the continuity of our studies on UQ of compressible gas dynamics with uncertain initial conditions, cf. the Richtmyer-Meshkov Instability (RMI) test case from Section 1.7.3 in Chapter III, we wish to apply the type of techniques previously described to the identification of the dominant parameters/scales of an initially perturbed material interface interacting with a shock wave to generate turbulent mixing. The RMI light-heavy fluid system under consideration is a very simplified version of an inertial confinement fusion (ICF) setup. The main idea is to *statistically* identify the critical defaults of the initial material interface shape that will eventually degenerate to an intricate turbulent mixing zone (TMZ) due to Rayleigh-Taylor instabilities. Indeed, ICF consists in heating and compressing a fuel target (pellet) in order to trigger nuclear fusion reactions and has more chance to succeed if instabilities are avoided. The energy delivered to the target outer layer by high energy beams of laser light induces inward propagating shock waves to the center of the domain. It is crucial for the fusion reactions to take place that the shock wave fronts remain spherical. This is why it is important to understand the effect of the form of the initial perturbation on the development of small-scale flow structures [191, 178].

We plan to apply Bayesian inference based on shock tube measurements [390, 488] and simulations [386] of mixing zone growth rates in order to recover the spatial scale statistics. The initial uncertain interface position will be modeled by a correlated random field and the forward model is the stochastic Euler system. The statistics of the uncertain interface position with respect to time will be estimated by building its gPC approximation similarly to the work produced in [386], permitting an computational acceleration of the CFD forward model. A preliminary study has been recently carried out, where we have described the uncertain initial interface position by a stochastic process of chosen correlation length and propagated the uncertainty via gPC techniques through the stochastic Euler system rather than relying on known turbulence models. After empirical calibration of the physical parameters defining the spatial random field, numerical results were compared to experimental ones and shown a good agreement. Besides, the stochastic model was predictive in the sense that calibrating one simulation with respect to one experiment allowed the prediction of the other experiments obtained with the same experimental dispositive.

Data assimilation addresses the problem of producing useful simulation predictions based on imperfect model equations and measurements. It has been used extensively in oceanic and atmospheric applications and other geoscience areas, marine technology, weather forecasting, hydrology... It involves the combination of observational data with the underlying dynamical principles governing the system under observation. Data assimilation techniques can be broadly categorized into methods based on control theory, stochastic approaches, direct minimization methods and estimation theory [408].

Direct methods simply minimize some appropriate cost function derived from inverse problems. For instance, genetic algorithms are based upon searches generated in analogy to the genetic evolution of natural organisms [95]. They are convenient as they avoid local minima. At each iteration or “generation” of the search, the algorithm keeps a population of approximate solutions. The population is evolved by manipulations in successive iterations such that the likelihood of producing better data-fitted generations increases for new populations.

The most widely adopted approach in estimation theory is the Kalman filter (KF) [82] that is a simplification of Bayesian estimation for the case of linear systems. KF is a mathematical tool using measurements observed over time and containing noise (random variations) and other inaccuracies, but producing values that tend to be closer to the true values of the measurements and their associated calculated values. KF is optimal for linear systems in a Gaussian framework. However, for nonlinear systems the KF requires a linearization of the state equations, resulting in the extended KF (EKF) [145], which may introduce significant error. Both KF and

EKF require calculations of the covariance function of the state variables. Although this covariance provides a good estimate of uncertainty in the solutions, its numerical handling can be inefficient for systems with large dimensions of the state variables. The ensemble Kalman filter (EnKF), first proposed by Evensen in [120], has become popular in a wide variety of application areas. EnKF is straightforward to implement, as it employs random ensembles to represent solution states, but introduces sampling errors that affect its accuracy. These errors may be reduced using larger number of samples. Nevertheless, this can be too time consuming in practice for large-scale problems. Li & Xiu propose an efficient EnKF implementation via gPC expansion [257]. The key ingredients of the proposed approach involve: – solving the system of stochastic state equations via the gPC methodology to gain efficiency; and – sampling the gPC approximation of the stochastic solution with an arbitrarily large number of samples, at virtually no additional computational cost, to drastically reduce the sampling errors. The resulting algorithm thus achieves a better accuracy at reduced computational cost.

Data assimilation in arterial hemodynamics: a coupled approach making use of simplified modeling dynamics and MRI experiments

The simulation of blood-flow and arterial pulse traveling in the human body is a very challenging task. It is in fact a strongly nonlinear coupled problem for large arteries like the aorta, as there is a substantial amount of energy exchanged between fluid and structure in each cardiac beat. An accurate model should account for the heart, the arterial and venous networks (including capillaries), as well as taking into account the non-Newtonian blood behavior and visco-elastic wall constitutive laws. This task is nowadays out of reach and several approximations must be employed: most of the time the blood is considered a Newtonian fluid, the heart and venous network are disregarded. Another approximation is to consider reduced models for the fluid-structure interaction (FSI) dynamics. The resulting model is a network of one-dimensional (1-D) models for the arterial system, which can be closed with zero-dimensional (0-D) “lumped” models to account for the neglected parts of the arterial tree. The tuning of the mechanical properties of the arterial wall of a specific patient as well as the calibration of the partially reflective outflow boundary conditions are crucial to an accurate and patient-specific prediction of cardiovascular risks.

With this topic, again we are interested by inverse problem of estimating the state and the parameters of the system given a set of measurements, typically provided by medical imaging (here MRI measurements along the descending aorta). We believe, this step is absolutely necessary to make numerical simulations personally tuned for every patient and usable in clinical practice.

Our goal is to estimate from artery wall displacements and fluid velocity and pressure the artery wall stiffness as well as proximal Windkessel resistance and compliance, which are a very important parameters for fluid boundary conditions in hemodynamics. Inspired by the work of Dumas [111] and Decoene [482], we propose to use direct minimization methods and more particularly genetic algorithms applied to one-dimensional fluid-structure interaction model discretized with a Discontinuous Galerkin method [399]. The volumetric flow rate inflow boundary condition is fed by MRI data measured on the patient. In a more elaborate stage, Bayesian inference or Kalman filtering will be combined with gPC response surface to infer on those physical quantities and predict accurately the arterial response on long varying cardiac cycles.

Appendix A

Spectral/*hp* element DNS solver for deterministic incompressible Navier-Stokes equations

Sommaire

1	Incompressible Navier-Stokes equations	147
2	Weak form, time integration splitting scheme and spatial discretization	147

Spectral methods in fluid dynamics are used in direct and large eddy simulations of turbulent flow. The spectral/*hp* element method, which incorporates both multi-domain spectral methods and high-order finite element methods, has been particularly successful when applied to complex geometries. We refer the reader to this monograph [218] for ample details on the method.

1 Incompressible Navier-Stokes equations

The governing equations are the incompressible Navier-Stokes equations, written here with a primitive-variable formulation and in convective form in a rectangular domain $\mathcal{D} \subset \mathbb{R}^2$ with boundary $\partial\mathcal{D} = \Gamma_d \cup \Gamma_n$. We refer to the diffusive time L^2/ν and normalize the pressure with respect to the viscous stress $\mu U/L$, in order to get the dimensionless form:

$$\frac{\partial \mathbf{u}}{\partial t} + (\mathbf{u} \cdot \nabla \mathbf{u}) = -\nabla p + Re^{-1} \nabla^2 \mathbf{u} + \mathbf{f} \quad \text{in } \mathcal{D}, \quad \text{and} \quad (\text{A.1})$$

$$\nabla \cdot \mathbf{u} = 0 \quad \text{in } \mathcal{D}, \quad \text{for } t \geq 0, \quad (\text{A.2})$$

where the Reynolds number is $Re = UL/\nu$ and \mathbf{f} is an external body force and $\mathbf{f} \in L^2(\mathcal{D})^2$. For simplicity, we consider homogeneous Dirichlet boundary condition over the domain boundary:

$$\mathbf{u} = 0 \quad \text{on } \mathcal{D}, \quad \text{for } t \geq 0. \quad (\text{A.3})$$

2 Weak form, time integration splitting scheme and spatial discretization

The weak formulation involves functional spaces that depends on the highest spatial derivatives in the system. Let us define the appropriate spaces:

$$H_0^1(\mathcal{D}) = \{v \in H^1(\mathcal{D}) \mid v = 0 \quad \text{on } \partial\mathcal{D}\} \quad (\text{A.4})$$

$$L_0^2(\mathcal{D}) = \{q \in L^2(\mathcal{D}) \mid \int_{\mathcal{D}} q \, d\mathbf{x} = 0\}. \quad (\text{A.5})$$

We seek a velocity field \mathbf{u} that belongs to the space $\mathcal{V} \equiv H_0^1(\mathcal{D})^2$ and a pressure p that belongs to the space

$\mathcal{Q} = L_0^2(\mathcal{D})$, i.e. we seek the couple $(\mathbf{u}(t), p(t)) \in \mathcal{V} \times \mathcal{Q}$ | for almost every $t \in [0, T]$:

$$\frac{d}{dt}(\mathbf{u}(t), \mathbf{v}) + \mathcal{A}(\mathbf{u}(t), \mathbf{v}) + \mathcal{B}(\mathbf{v}, p(t)) \quad (\text{A.6})$$

$$= Re^{-1} \mathcal{C}(\mathbf{u}(t); \mathbf{u}(t), \mathbf{v}) + (\mathbf{f}(t), \mathbf{v}) \quad \forall \mathbf{v} \in \mathcal{V}, \quad (\text{A.7})$$

$$\mathcal{B}(\mathbf{u}(t), q) = 0 \quad \forall q \in \mathcal{Q}, \quad (\text{A.8})$$

$$\mathbf{u}(0) = \mathbf{u}^0, \quad (\text{A.9})$$

where the continuous bilinear forms \mathcal{A} , \mathcal{B} are defined as:

$$\mathcal{A}: \mathcal{V} \times \mathcal{V} \longrightarrow \mathbb{R}, \quad \mathcal{A}(\mathbf{u}, \mathbf{v}) = (\nabla \mathbf{u}, \nabla \mathbf{v}), \quad (\text{A.10})$$

$$\mathcal{B}: \mathcal{V} \times \mathcal{Q} \longrightarrow \mathbb{R}, \quad \mathcal{B}(q, \mathbf{v}) = -(q, \nabla \cdot \mathbf{v}), \quad (\text{A.11})$$

and \mathcal{C} :

$$\mathcal{C}: \mathcal{V} \times \mathcal{V} \times \mathcal{V} \longrightarrow \mathbb{R}, \quad \mathcal{C}(\mathbf{u}; \mathbf{w}, \mathbf{v}) = \int_{\mathcal{D}} \mathbf{v} \cdot (\mathbf{u} \cdot \nabla \mathbf{w}) dx, \quad (\text{A.12})$$

where (\cdot, \cdot) denotes the inner product in the L^2 space.

The approach taken next is the one of splitting (or fractional-step) methods for the primitive variables. This approach does not usually require the use of staggered grids for high-order elements and is therefore quite efficient, especially for high Reynolds numbers for which $(\nu \Delta t)$ is small. The idea is to define an appropriate projection operator, so that we can solve for the velocity field without approximating the pressure field. Most projection methods compute first a tentative or intermediate velocity $\hat{\mathbf{u}}$, that is *not* divergence-free [76, 468]. This field is then projected on the subspace of solenoidal vectors functions.

In the following, the $L^2(\mathcal{D})$ space is decomposed into a divergence-free contribution: $\mathcal{F}(\mathcal{D}) = \{\mathbf{v} \mid \nabla \cdot \mathbf{v} = 0 \text{ in } \mathcal{D}, \mathbf{v} \cdot \mathbf{n} = 0 \text{ on } \delta \mathcal{D}\}$ and an irrotational contribution: $\mathcal{G}(\mathcal{D}) = \{\mathbf{w} \mid \mathbf{w} = \nabla \phi\}$. The functions from those two spaces are orthogonal. The Helmholtz decomposition for a general vector, \mathbf{q} , applies and we have $\mathbf{q} = \mathbf{v} + \mathbf{w}$ and $\mathbf{v} = \mathbb{P}_{\mathcal{F}} \mathbf{q}$ with the projection operator $\mathbb{P}_{\mathcal{F}}: L^2(\mathcal{D}) \rightarrow \mathcal{F}(\mathcal{D})$. The Navier-Stokes equations are now written:

$$\frac{\partial \mathbf{u}}{\partial t} = \mathbb{P}_{\mathcal{F}} [Re^{-1} \nabla^2 \mathbf{u} - \mathbf{u} \cdot \nabla \mathbf{u}], \quad (\text{A.13})$$

which is independent of pressure, and

$$\nabla^2 \phi = \nabla \cdot \mathbf{q}, \quad \text{and} \quad \frac{\partial \phi}{\partial n} = \mathbf{q} \cdot \mathbf{n}, \quad (\text{A.14})$$

with the compatibility condition for the Neumann problem being automatically satisfied. Then $\mathbf{w} = \nabla \phi$ and therefore $\mathbf{v} = \mathbf{q} - \mathbf{w}$.

The imposition of the correct Neumann pressure boundary condition, written in the *rotational form* is crucial in obtaining high-order accuracy. Karniadakis *et al.* use stiffly stable time integrators to extend the temporal accuracy of the dual splitting scheme to high orders. In the following, we assume an order of integration (J_e) for the advection terms, (J_i) for the diffusion terms and (J_p) for the pressure boundary condition. In practice, we often choose $J_e = J_i = J_p = J \subset \{1, 2, 3\}$. The semi-discrete system may be decomposed as [219]:

$$\frac{\hat{\mathbf{u}} - \sum_{q=0}^{J_i-1} \alpha_q \mathbf{u}^{n-q}}{\Delta t} = - \sum_{q=0}^{J_e-1} \beta_q [(\mathbf{u} \cdot \nabla) \mathbf{u}]^{n-q} \quad (\text{A.15})$$

$$\frac{\hat{\mathbf{u}} - \hat{\mathbf{u}}}{\Delta t} = - \nabla p^{n+1} \quad (\text{A.16})$$

$$\frac{\gamma_0 \mathbf{u}^{n+1} - \hat{\mathbf{u}}}{\Delta t} = Re^{-1} \nabla^2 \mathbf{u}^{n+1}. \quad (\text{A.17})$$

In the first stage, the non-linear terms are explicitly computed and extrapolated with a constant order, J_e , in time with time step Δt . The integration of the convective terms involves the α_q and β_q terms, that are the weights coefficients for the mixed explicit-implicit stiffly stable integration [217, 219]. The velocity field is in fact transformed into physical space and subsequently the nonlinear products are obtained at all quadrature points in a collocation fashion. Another transform is then performed to bring the results back to modal space.

In the second stage, assuming the intermediate field $\hat{\mathbf{u}}$ is *divergence-free* and taking the derivative of the second equation, the problem can be recast as an elliptic *Poisson* equation:

$$\nabla^2 p^{n+1} = \Delta t^{-1} \nabla \cdot \hat{\mathbf{u}}, \quad (\text{A.18})$$

with consistent Neumann boundary conditions derived from the normal component of the momentum equations:

$$\frac{\partial p^{n+1}}{\partial n} = - \left[\frac{\partial \mathbf{u}^{n+1}}{\partial t} + \sum_{q=0}^{J_e-1} \beta_q [(\mathbf{u} \cdot \nabla) \mathbf{u}]^{n-q} + \nu \sum_{q=0}^{J_p-1} \beta_q (\nabla \times \boldsymbol{\omega})^{n-q} \right] \cdot \mathbf{n}, \quad (\text{A.19})$$

where \mathbf{n} is the outward unit normal vector along the boundary, and $\boldsymbol{\omega} = \nabla \times \mathbf{u}$ is the vorticity. Once p^{n+1} is found, substitution into Eq. (A.16) immediately yields the second stage approximation to the velocity field.

In the third stage, the updated velocity field, \mathbf{u}^{n+1} is computed, cf. Eq. (A.17), and the problem can be recast as an Helmholtz equation:

$$\left(\nabla^2 - \frac{\gamma_0}{\nu \Delta t} \right) \mathbf{u}^{n+1} = - \frac{\hat{\mathbf{u}}}{\nu \Delta t}, \quad (\text{A.20})$$

with Dirichlet velocity boundary conditions (for instance: no-slip and stationary walls for a flow around a fixed body) and $\gamma_0 = \sum_{q=0}^{J_i-1} \alpha_q$, for consistency. In the classical splitting methods the velocity error scales linearly with $(\nu \Delta t)$ but in the presented version this error is of high-order of the form $\mathcal{O}((\nu \Delta t)^J)$, where $J \geq 2$ is the time-integration order. Note that with this scheme the end-of-step velocity \mathbf{u}^{n+1} satisfies the complete boundary conditions but is not divergence-free (unlike $\hat{\mathbf{u}}$).

Next, the spectral element discretization is conducted. We consider a decomposition $\mathcal{T} = \{\mathcal{D}^e\}$ of the global domain $\bar{\mathcal{D}} = \mathcal{D} \cup \partial\mathcal{D}$ into N_{el} non-overlapping elements (or subdomains), \mathcal{D}^e , $e = 1 \dots N_{el}$, that can be triangular or quadrilateral (or a mix of the two) elements. Each of these elements has a local boundary $\partial\mathcal{D}^e$ and is then mapped to a standard (or reference) region $\hat{\mathcal{D}}$ (with $\hat{\mathcal{D}} = \mathcal{S}^2 = \{(\xi_1, \xi_2) \mid -1 \leq \xi_1, \xi_2 \leq 1\}$ for a square or $\hat{\mathcal{D}} = \mathcal{T}^2 = \{(\xi_1, \xi_2) \mid -1 \leq \xi_1, \xi_2; \xi_1 + \xi_2 \leq 0\}$ for a triangle). Therefore, each \mathcal{D}^e is obtained from a transformation f_e from the reference element $\hat{\mathcal{D}}$ and f_e is bijective and differentiable with its inverse.

On the reference element, we introduce a polynomial space $\hat{\mathbb{P}}_P$, of degree P , in each coordinate. If one uses coupled methods, the choice of the same space of approximation for both the velocity and the pressure fields is not possible and a compatibility condition (cf. *inf-sup* condition) has to be imposed in order to restrict the pressure space and avoid spurious oscillations. On the contrary, for splitting methods, it was found by Karniadakis et al. [220] that an equal order polynomial interpolation for both the velocity and the pressure field leads to stable simulations. Indeed, it has been observed, in general, that in splitting schemes the *inf-sup* condition between the velocity and the pressure approximation spaces is not required.

We set $h_e = \text{diam } \mathcal{D}^e$ and $P_e \geq 1$ to be the polynomial degree we want to use in \mathcal{D}^e . We define the functions:

$$V_{P_e}(\mathcal{D}^e) = \{v \mid v = \hat{v} \circ f_e^{-1} \text{ for some } \hat{v} \in \hat{\mathbb{P}}_P\}, \quad (\text{A.21})$$

the functions of $V_{P_e}(\mathcal{D}^e)$ are images through f_e of polynomial functions $\hat{v} \in \hat{\mathbb{P}}_P$ chosen in $\hat{\mathcal{D}}$. Finally, we define the spectral/*hp* element space as:

$$\mathcal{X}^\delta = \{v \in C^0(\bar{\mathcal{D}}) \mid v|_{\mathcal{D}^e} \in V_{P_e}(\mathcal{D}^e), \forall \mathcal{D}^e \in \mathcal{T}\}, \quad (\text{A.22})$$

where the subindex δ is a short notation for ‘‘discrete’’ that accounts for both the local geometric sizes $\{h_e\}$ and the local polynomial degrees $\{P_e\}$. The actual space \mathcal{V}^δ that will be used is a subspace of \mathcal{X}^δ whose functions vanish on the Dirichlet portion (if any) of the boundary.

The most commonly used spectral/*hp* element bases are those which can be expanded into a globally C^0 continuous expansion. The general 2D expansion basis is formed of Jacobi polynomials of mixed weights and can be decomposed into the product of 1D modified principal functions. For quadrilateral elements, the most natural and straightforward way to construct the basis is by taking a product of the one-dimensional basis which can be thought of as one-dimensional *tensors*:

$$\phi_p(\xi) = \begin{cases} \psi_0^a(\xi) = \left(\frac{1+\xi}{2}\right), \\ \psi_p^a(\xi) = \left(\frac{1+\xi}{2}\right) \left(\frac{1-\xi}{2}\right) P_{p-1}^{1,1}(\xi), & 0 < p < P. \\ \psi_P^a(\xi) = \left(\frac{1+\xi}{2}\right), \end{cases} \quad (\text{A.23})$$

and $P_k^{1,1}$ are the Jacobi polynomials with $(\alpha = 1, \beta = 1)$ and ξ is the local cartesian coordinate. The two-dimensional modal bases can be constructed by a simple product of the one-dimensional tensors in each of the Cartesian coordinate directions and the modal expansion maintains a hierarchic form:

$$\phi_{pq}(\xi_1, \xi_2) = \phi_p(\xi_1) \phi_q(\xi_2), \quad 0 \leq p, q; p \leq P, q \leq P \quad (\text{A.24})$$

where p, q denote the different components of the tensorial expansion.

For every element of the partition, a suitably chosen boundary-adapted must be defined. A basis for the whole space \mathcal{X}^δ is then obtained by connecting together the elemental basis functions on each element \mathcal{D}^e in order to guarantee global continuity, as required in the Galerkin formulation for incompressible flows. The two-dimensional expansion is decomposed into boundary modes (vertex and edge modes) which have support along the boundary of the region, and interior modes which have zero support on all boundaries. Each bubble basis function within one element immediately generates a global basis function by extending it by zero outside the element. Vertex and edge basis functions living in contiguous elements are properly matched to generate global basis functions.

Finally, we write the approximate solution \mathbf{u}^δ (for instance the velocity field) within an element \mathcal{D}^e as:

$$\mathbf{u}^\delta(\mathbf{x}, t) = \sum_{p=0}^{p=P} \sum_{q=0}^{q=P} \tilde{\mathbf{u}}_{pq}(t) \phi_{pq}(\xi_1, \xi_2), \quad \mathbf{x} \in \mathcal{D}^e, \quad (\text{A.25})$$

where $\tilde{\mathbf{u}}_{pq}(t)$ contains the local degrees of freedom of expansion coefficients and the trial functions $\phi_{pq}(\xi_1, \xi_2)$ (as well as the test functions) are described by Eq. (A.23).

The expansions $\phi_{pq}(\xi_1, \xi_2)$ define the following polynomial space of tensor product expansions:

$$\phi_{pq}(\xi_1, \xi_2) \subseteq \hat{\mathbb{P}}_P(\mathcal{S}^2) = \text{span}\{\xi_1^p \xi_2^q\}_{(p,q) \in \mathcal{J}}, \quad (\text{A.26})$$

with $\mathcal{J} = \{(p, q) | 0 \leq p \leq P_1, 0 \leq q \leq P_2\}$. The definition of the set \mathcal{J} indicates the range over which the expansion modes must be assembled if they are to span the complete polynomial basis.

Remark A.1

In order to extend the tensor product expansion to unstructured grids, i.e. simplex regions such as triangular regions one needs to generalize the tensor product expansion concept. In practice, an appropriate change of coordinate system is necessary to map the triangular element to a reference quadrilateral element. Then orthogonal expansions are constructed using generalized products of orthogonal principal functions [441].

Appendix B

Multidimensional numerical integration

Sommaire

1	Stochastic integration techniques	153
1.1	Monte-Carlo	153
1.2	Some variance reduction techniques	154
1.3	Markov Chain Monte-Carlo	154
2	Deterministic integration techniques	155
2.1	Some univariate nested or non-nested quadrature formulas	155
2.2	Multivariate cubatures	160

We are interested in computing the N -dimensional integral of a functional ψ of the solution \mathbf{u} of our system represented by the model $\mathbf{u}(\omega) = h(\Theta(\omega))$ where ω is a random event from the Ω event space. Here, the probability space (Ω, \mathcal{F}, P) is characterized with N mutually *independent* random variables $\Theta = \{\Theta_j(\omega)\}_{j=1}^N$, $N \in \mathbb{N}$ with probability distribution $P_{\Theta}(d\theta)$. We note this finite-dimensional space $(\Omega^{(N)}, \mathcal{B}^{(N)}, P_{\Theta})$ where:

$$\Omega^{(N)} = \Omega_1 \times \dots \times \Omega_N \subset \mathbb{R}^N, \quad (\text{B.1})$$

with $\Omega_j := \text{range}(\Theta_j) = \Theta_j(\Omega)$, $\mathcal{B}^{(N)}$ is the Borel σ -algebra of $\Omega^{(N)}$ (cf. Section 1.3). We define the integral we seek as:

$$\mathcal{J}^N[\psi] = \int_{\Omega^{(N)}} \psi(\mathbf{u}) f_{\Theta}(\theta) d\theta. \quad (\text{B.2})$$

1 Stochastic integration techniques

1.1 Monte-Carlo

The Monte-Carlo (MC) method [129, 407, 265, 413] is the simplest approach where the integral is evaluated as an expectation $\mathcal{J}^N[\psi] = \mathbb{E}[\psi(\mathbf{u}(\Theta))]$. A set of n_{MC} simulations are carried out with n_{MC} *independent and identically distributed* (i.i.d) realizations $\Theta^{(1)}, \dots, \Theta^{(n_{\text{MC}})}$ generated using a pseudo random number generator. The empirical mean $\hat{\mathcal{J}}$ of the sequence is:

$$\hat{\mathcal{J}} \equiv \hat{\mathcal{J}}_{n_{\text{MC}}}^N = \frac{1}{n_{\text{MC}}} \sum_{k=1}^{n_{\text{MC}}} \psi(h(\Theta^{(k)})), \quad (\text{B.3})$$

where $(\Theta^{(k)})_{k=1 \dots n_{\text{MC}}}$ is a n_{MC} -sample Θ . From a statistical point of view, the MC estimator $\hat{\psi}_{n_{\text{MC}}}$ is random due to the randomness in the choice of the samples. The estimator is *unbiased*:

$$\mathbb{E}[\hat{\mathcal{J}}] = \mathbb{E}[\psi(\mathbf{u})], \quad (\text{B.4})$$

and its variance is given by:

$$\text{var}(\hat{\mathcal{J}}) = \frac{1}{n_{\text{MC}}} \text{var}(\psi(\mathbf{u})), \quad (\text{B.5})$$

According to the *central limit theorem* (CLT), we have *almost sure* convergence of the MC estimator:

$$\hat{\mathcal{J}} \xrightarrow[n_{\text{MC}} \rightarrow +\infty]{} \mathbb{E}[\psi(\mathbf{u})], \quad (\text{B.6})$$

with probability 1.

If $h(\Theta)$ is a second-order RA (i.e. $\sigma^2 = \mathbb{E}[\psi(h(\Theta))]^2 < \infty$ 1.4), then CLT provides the following convergence rate:

$$(\mathcal{J} - \hat{\mathcal{J}}) \xrightarrow[n_{\text{MC}} \rightarrow +\infty]{\mathcal{L}} \frac{1}{\sqrt{n_{\text{MC}}}} \mathcal{N}(0, \sigma^2), \quad (\text{B.7})$$

with a confidence interval of level $(1 - 2\alpha)$ for \mathcal{J} :

$$\left[\hat{\mathcal{J}} - F^{-1}(\alpha) \sqrt{\frac{\widehat{\text{var}}(h(\Theta))}{n_{\text{MC}}}}, \hat{\mathcal{J}} + F^{-1}(\alpha) \sqrt{\frac{\widehat{\text{var}}(h(\Theta))}{n_{\text{MC}}}} \right], \quad (\text{B.8})$$

$$\text{with } \widehat{\text{var}}(h(\Theta)) = \frac{1}{n_{\text{MC}} - 1} \sum_{k=1}^{n_{\text{MC}}} \left(h(\Theta^{(k)}) - \hat{\mathcal{J}} \right)^2.$$

The main advantages of the MC method are:

- no regularity condition on h and ψ excepting $\mathbb{E}[\psi(h(\Theta))]^2 < \infty$.
- the convergence rate $\mathcal{O}(\frac{1}{\sqrt{n_{\text{MC}}}})$, although slow, is not depending on the number of dimensions N .
- the method may be applied to any quantities that can be expressed as an expectation.
- trivial to parallelize.

On the other hand it depends heavily on the quality of the pseudo-random number generator. Inadequate random number generators produce biased results (e.g. due to artificial correlations between the generated numbers).

1.2 Some variance reduction techniques

Monte-Carlo methods may be speed up by various techniques for variance reduction (Antithetic Variables; Control Variates; Matching Moment Methods; Stratified sampling; Importance sampling).

The Latin Hypercube Sampling (LHS) method [306] aims at generating pseudo-random numbers that are more representative of the joint distribution of the input random vector than those generated by MC simulation.

The convergence rate of LHS is in general better (or at least not worse!) than the MC convergence [362]:

$$\text{var}(\hat{\mathcal{J}}_{n_{\text{LHS}}}^N) \leq \frac{n_{\text{LHS}}}{n_{\text{LHS}} - 1} \text{var}(\hat{\mathcal{J}}_{n_{\text{MC}}}^N). \quad (\text{B.9})$$

A drawback of the approach is that the sample set can not be randomly enriched with new points, otherwise loosing its LHS property.

The Quasi Monte-Carlo (QMC) method [344, 335] differs from the MC method in the choice of the sample positions. It evaluates the integrand at *correlated* quadrature points (not *randomly* chosen) that are generated from “low discrepancy series” $D_{n_{\text{QMC}}}$. A sequence $\{\Theta^{(1)}, \dots, \Theta^{(n_{\text{QMC}})}\}$ is called *quasi random* if its discrepancy obeys:

$$D_{n_{\text{QMC}}} \leq c (\log n_{\text{QMC}})^n n_{\text{QMC}}^{-1},$$

where c, n are constants.

Various quasi-random sequences have been developed in the literature: let us mention Van Der Corput, Halton, Faure, Hammersley, SQRT, Niederreiter, Lapeyre-Pagès and Sobol’ sequences [344]. Sobol’ sequences seem efficient to estimate moderately high-dimensional (say $N \geq 10$) integrals.

Often, we have $n = N$ and the typical QMC error is of the order of [335]:

$$\epsilon_{\text{QMC}} \approx \mathcal{O}(n_{\text{QMC}}^{-1} \cdot (\log n_{\text{QMC}})^N).$$

We see that the $\mathcal{O}(\log n_{\text{QMC}})^N$ dominates for large number of dimensions N but otherwise we get a $\mathcal{O}(n_{\text{QMC}}^{-1})$ convergence rate. So the advantage in the convergence rate compared to the MC method deteriorates for a large number of random dimensions.

1.3 Markov Chain Monte-Carlo

Markov Chain Monte-Carlo (MCMC) is a term used to cover a broad range of methods for numerically computing probabilities, or for optimization [319, 148, 146, 171, 407]. They are simulation methods, mostly used in complex stochastic systems where exact computation are not computationally feasible. The idea is to generate a sample from a distribution. This sample can then be used to estimate various characteristics of the

distribution such as moments, quantiles, modes, the density, or other statistics of interest. Methods that fall under this heading for integration include *Metropolis* sampling, *Hastings* sampling and *Gibbs* sampling. MCMC relies on a sequence of *dependent* observations $\{\theta_i\}$ generated from a Markov chain. The Markov chain generates observation that depends only on the previous observation, ie:

$$p(\theta_i|\theta_0, \dots, \theta_{i-1}) = p(\theta_i|\theta_{i-1}),$$

where is the $p(\theta_{i+1} \in A | \theta_i = \theta) \equiv T(\theta, A)$ is the *transition kernel*. Under some regularity conditions, when a Markov chain runs for long enough it will asymptotically settle down to a limiting or ergodic distribution close to the distribution f_Θ we seek. This is true regardless of the state in which it is started. The main condition that we need to ensure holds is called *irreducibility*. That is, the set of possible states of the Markov chain must not reduce into separate non-communicating classes.

In practice, the following steps have to be carried out:

- Create a Markov chain which has ergodic distribution f_Θ
- Show that the chain is irreducible
- Find an initial state θ_0 such $p(\theta_0) > 0$
- Run the chain for a while to allow it to reach the ergodic distribution
- Start harvesting simulations and computing the required functions

An important consideration with MCMC is whether or not the chain has converged to the desired distribution? Say the chain has been run for m_{MCMC} iterations, and we can assume that the sample points $\{\theta_i\}_{i=m_{\text{MCMC}}+1, \dots, n_{\text{MCMC}}}$ are distributed according to the *stationary* distribution. We can discard the first m_{MCMC} iterations and use the remaining $(n_{\text{MCMC}} - m_{\text{MCMC}})$ samples to get an estimate of the expectation as follows:

$$\hat{J} = \frac{1}{(n_{\text{MCMC}} - m_{\text{MCMC}})} \sum_{k=m_{\text{MCMC}}+1}^{n_{\text{MCMC}}} \psi(h(\theta_k)), \quad (\text{B.10})$$

The number of samples m_{MCMC} that are discarded is called the *burn-in*. The size of the burn-in period is the subject of current research in MCMC methods.

2 Deterministic integration techniques

Again, we are interested by the evaluation of $J^N[\psi]$, but we wish to use an approximation that takes the form of a discrete sum, i.e.

$$J^N[\psi] \approx Q_l^N[\psi] = \sum_{k=1}^{N_q} \psi(h(\mathbf{y}^{(k)})) \mathbf{W}^{(k)}, \quad (\text{B.11})$$

where $\mathbf{y}^{(k)}$ and $W^{(k)}$ are the nodes and weights of the so-called (N -dimensional) *cubature*. The $\mathbf{l} = (l_1, \dots, l_N) \in \mathbb{N}^N$ parameter represents the cubature level, i.e. it gives an indication on the accuracy of the quadrature (it is particularly useful in the case of adaptive approaches where successive layers of grid are used, i.e. nested quadratures).

With this technique, the quadrature points and corresponding weights are known *deterministic*¹ quantities inheriting properties from one-dimensional quadrature rules. The multi-dimensional grids are constructed as tensor products of one-dimensional integration rules or quadrature formulas—e.g. of Gaussian, Clenshaw-Curtis, or Fejer quadrature formulas.

2.1 Some univariate nested or non-nested quadrature formulas

We next briefly summarize a few important univariate quadrature rules, either for *uniform* integration in the bounded interval $[-1, 1]$ or for Gaussian integration on the real axis \mathbb{R} . Those quadratures will be the foundation of the multidimensional integration grids.

In the following, $\Lambda_l = \{y_l^{(i)}, \dots, y_l^{(n(l))}\}$ denotes the set of abscissas used by the quadrature rule of precision level l and total number of points given by the function $n(l)$. If the quadrature rule is nested, we have that $\Lambda_l \subset \Lambda_{l+1}$. This property will be essential to maintain the computational cost reasonable in large dimensions. We are interested by the performance of the different quadratures that we quantify by their polynomial exactness and some error bounds.

Definition B.1

Let \mathbb{P}_p^1 be the univariate space of polynomials of total degree at most p . A quadrature formula Q_l has a degree $\text{deg}(Q_l) = p$ of (polynomial) exactness if $J[f] = Q_l[f]$, $\forall f \in \mathbb{P}_p^1$.

1. This is the reason why the notation is slightly different and $\mathbf{y}^{(k)}$ are used instead of $\Theta^{(k)}$ for the realization samples.

Definition B.2

The quadrature error is defined as $\|\mathcal{J}[f] - \mathcal{Q}_l[f]\|$ and will be presented after assuming some regularity on the function to integrate (that we relate to derivatives bounds). In this framework, we will consider non-periodic functions f from the standard smoothness class:

$$\mathcal{C}^r := \{f : \Omega \rightarrow \mathbb{R}, \left\| \frac{\partial^s f}{\partial y^s} \right\| < \infty, s \leq r\}, \quad r \in \mathbb{N}, \quad (\text{B.12})$$

where r represents the smoothness parameter and the norm is defined as:

$$\|f\| = \max \{\|D^s f\|_\infty \mid s = 0, \dots, r\}. \quad (\text{B.13})$$

We consider a one-dimensional quadrature approximation $\mathcal{Q}_{l_k}^1$ (in dimension $\Omega^{(k)}$) of precision l_k with $n_k(l_k)$ points, $\{y_k^{(i)}, i = 1, \dots, n_k(l_k)\}$:

$$\mathcal{J}^1[\psi] = \int_\Omega \psi(\theta) f_\Theta(\theta) d\theta \approx \mathcal{Q}_{l_k}^1[\psi] \equiv \sum_{i=1}^{n_k(l_k)} \psi(h(y_k^{(i)})) w_{l_k}^{(i)}, \quad (\text{B.14})$$

where the strictly increasing function $n_k : \mathbb{N}_+ \rightarrow \mathbb{N}_+$, relating the precision level l_k for dimension k to the number of quadrature points at this level, is such that $n_k(0) = 0$, $n_k(1) = 1$ and $n_k(j) < n_k(j+1)$ for $j \geq 1$ and for $k = 1, \dots, N$.

Non-nested Gauss-type (e.g. Gauss-Legendre) quadrature rules will be presented first, then some nested quadratures will be also detailed (actually, trapezoidal and Newton-Cotes formulas [154] are examples of low-order nested quadrature rules but will not be described here).

2.1.1 Gaussian-type formula

A n -point Gaussian quadrature rule, named after Carl Friedrich Gauss, has the property to integrate *exactly* polynomials of degree $\mathcal{O}(2n)$ or less by a suitable choice of points $y_k^{(i)}$ and weights $w^{(i)}$, cf. Eq. B.14, [119][5]. The appropriate nodes are located within the integration interval and are in fact the roots of the family of polynomials *orthogonal* with respect to the weight function (here the probability distribution) involved in the integral, cf. Eq. B.14.

Practically, nodes and weights can be computed from the eigenvalues and eigenvectors of an associated linear algebra problem. This is usually named as the Golub–Welsch algorithm [170].

Here are some properties of any univariate Gaussian quadrature $\mathcal{Q}_l^{\text{GC}}$ of level l with total number of points $n(l)$:

- it has a degree of exactness $\text{deg}(\mathcal{Q}_l^{\text{GC}}) = 2n(l) - 1$, i.e. it integrates exactly any functional from the $\mathbb{P}_{2n(l)-1}^1$ space.

2.1.2 Clenshaw-Curtis and Fejér formula

The Clenshaw-Curtis (CC) quadrature points are non-equidistant abscissas given as the zeros or the extreme points of Chebyshev polynomials [81]. When the extrema are used, the grid becomes *nested*. The nested grid for a certain number of points $n(l)$ at level l is obtained from:

$$\begin{aligned} y_1^{(i)} &= 0, \quad \text{for } l = 1 \text{ and } n(l) = 1 \\ y_l^{(i)} &= -\cos\left(\frac{\pi(i-1)}{n(l)-1}\right), \quad i = 1, 2, \dots, n(l); n(l) > 1, \end{aligned} \quad (\text{B.15})$$

and the grid grows according to:

$$n(1) = 1 \quad \text{and} \quad n(l) = 2^{l-1} + 1, \quad \text{for } l > 1. \quad (\text{B.16})$$

The respective weights are given by:

$$\begin{aligned} w_l^{(i)} = w_l^{(n+1-i)} &= \frac{2}{n-1} \left(1 - \frac{\cos(\pi(i-1))}{n(n-2)} \right. \\ &\quad \left. - 2 \sum_{k=1}^{(n-3)/2} \frac{1}{4k^2-1} \cos\left(\frac{2\pi k(i-1)}{n-1}\right) \right), \quad \text{for } i = 2, \dots, n-1, \end{aligned}$$

and

$$w_l^{(1)} = w_l^{(n)} = \frac{1}{n(n-2)},$$

with $n \equiv n(l)$ in order to simplify the notations.

Remark B.3

It is important to choose $n(1) = 1$, in the case of large dimensions N , otherwise the initial number of points $n(1)^N$ is too large.

There exists more efficient computational strategies (e.g. involving DFT) to evaluate the nodes and corresponding weights [491] of CC and Fejér's quadrature rules.

Here are some properties of the univariate CC quadrature $\mathcal{Q}_l^{\text{CC}}$ of level l with total number of points $n(l)$:

- it has a degree of exactness $\text{deg}(\mathcal{Q}_l^{\text{CC}}) = n(l) - 1$, i.e. it integrates exactly any functional from the $\mathbb{P}_{n(l)-1}^1$ space².
- its error bound is:

$$\epsilon = \mathcal{O}((n(l))^{-r}) = \mathcal{O}(2^{-lr}),$$

where \mathcal{O} contains constant values depending on r , that can be obtained from known bounds for the respective Peano kernels, [50].

Remark B.4

So CC accuracy is only about $\sim 1/2$ of the one of Gauss-type quadrature (e.g. Gauss-Legendre quadrature in $[-1, 1]$) for the same number of points. In practice, it was shown that the supposed factor-of-2 of Gauss quadrature was rarely realized for non polynomial functions [477]. Moreover, it was shown that the error does not decay to zero evenly but does so in two distinct stages, when applied to certain analytic functions [504]. In conclusion, we can say that for the numerical integration of general functions, CC turns out to be a good compromise.

We notice that the CC grid includes the boundary nodes of the domain. Fejér's (F) rule (sometimes called Filippi formula) is the same as CC except for the boundary nodes that are omitted.

- the initial point is defined as $y_1^{(1)} = 0$, for $l = 1$ and $n(1) = 1$.
- its grid grows as $n(l) = 2^l - 1$ for $l > 1$.
- so, although nested, the grid grows faster than the CC rule due to this exclusion of the end points.

The weights are updated, compared to CC, to account for the missing end points. The polynomial degree of exactness is the same as the CC quadrature.

Fig. 2.1.2 compares the CC and F nodes up to level $l = 7$.

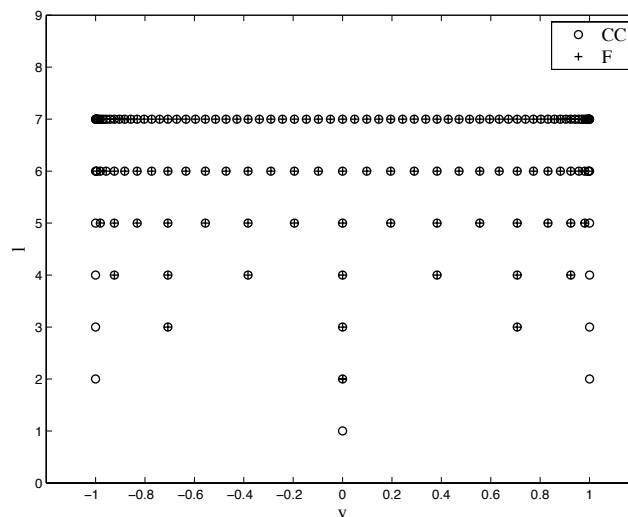


Figure B.1 – Clenshaw-Curtis (CC) & Fejér (F) quadrature nodes distribution for different integration level l . Because of the way the points are represented, the Fejér quadrature level corresponding to the distributions should read $l + 1$ on the left axis.

². Check if it's actually of degree $n(l)$ because of the odd number of points.

2.1.3 Kronrod-Patterson formula

Bounded support:

With this quadrature, the idea is to build a sequence of nested formulae whose degree of exactness increases faster than that of the CC sequence without using many more nodes. Kronrod [242] proposes to extend a $n(l)$ -points Gauss quadrature rule by interlacing $(n(l) + 1)$ additional points with positive weights, the degree of polynomial exactness becoming $\sim 3 \cdot n(l)$. For the Gauss-Legendre formula, the new abscissas are real, symmetric and inside the integration interval.

Patterson [367] generalizes this approach by a recursive expansion of Kronrod’s scheme and obtains a sequence with maximal degree of exactness. He constructs a sequence of polynomials $G_k(y)$ of degree $2^{k-1}(n + 1)$, $k \geq 1$, satisfying:

$$\int_{-1}^1 P_n(y) \left(\prod_{i=1}^{k-1} G_i(y) \right) G_k(y) y^j dy = 0, \quad \text{for } j = 0, 1, \dots, 2^{k-1}(n + 1) - 1,$$

where $P_n(y)$ is the n^{th} Legendre polynomial and $n \equiv n(l)$. In practice, the computation of the additional KP quadrature points location as well as the corresponding weights may be obtained via Laurie’s algorithm [245], cf. for instance Gautschi’s implementation [142].

Remark B.5

KP extension do not necessarily exist for all Gauss-Legendre formulas. For example, in the case of 2-point Gauss-Legendre formula, only four extensions are possible. For 3-point Gauss-Legendre formula, the existence of the extensions has been verified up to level $l = 9$, i.e. up to $n(9) = 511$ points.

Here are some properties of the univariate KP quadrature Q_l^{KP} of level l with total number of points $n(l)$, and constructed based on a 3-point Gauss-Legendre formula:

- the initial point is defined as $y_1^{(1)} = 0$, for $l = 1$ and $n(1) = 1$.
- its grid grows as $n(l) = 2^l - 1$ for $l > 1$.
- it has a degree of exactness $\text{deg}(Q_l^{\text{KP}}) = 3 \cdot 2^{l-1} - 1$ for $l > 1$, i.e. it integrates exactly any functional from the $\mathbb{P}_{3 \cdot 2^{l-1} - 1}^1$ space.
- its error bound is [154]:

$$\epsilon = \mathcal{O}((n(l))^{-r}) = \mathcal{O}(2^{-lr}),$$

and more accurate bounds are approximated in [370].

Fig. 2.1.3 shows the KP nodes up to level $l = 7$.

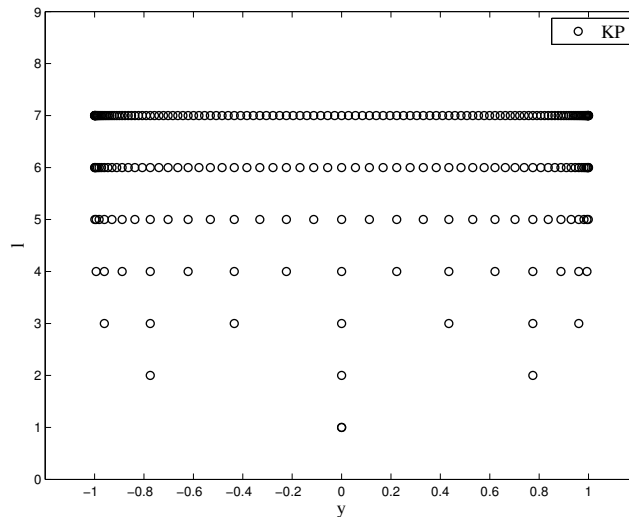


Figure B.2 – Kronrod-Patterson (KP) quadrature nodes distribution for bounded support for different integration level l .

Unbounded support:

In [149], the authors develop two families of fully symmetric interpolatory integration rules that can be used to numerically estimate multidimensional integrals over infinite regions with a Gaussian weight function. They show how to generalize Patterson’s method to produce successive extensions of the one point Gauss-Hermite

Table B.1 – Number of nested grid points n from the fully symmetric interpolatory rule [149] vs. quadrature level l for integration over unbounded support with a Gaussian weight function. The corresponding polynomial exactness p is presented in the last column. (a): $\mathcal{Q}_{[1+2+6+10+16]}^1$ rule; (b): $\mathcal{Q}_{[1+2+8+20]}^1$ rule. Bold numbers refer to valid solutions of the KP-type enrichment and italic numbers to intermediate stages with no valid enrichment. l^* is the level notation used in [149].

l	l^*	n	\mathbb{P}_p^1
1	1	1	1
2	2	(+2) 3	5
	<i>3</i>	<i>5</i>	
	<i>4</i>	<i>7</i>	
3	5	(+6) 9	15
	<i>6</i>	<i>11</i>	
	<i>7</i>	<i>13</i>	
	<i>8</i>	<i>15</i>	
	<i>9</i>	<i>17</i>	
4	10	(+10) 19	29
	<i>11</i>	<i>21</i>	
	<i>12</i>	<i>23</i>	
	<i>13</i>	<i>25</i>	
	<i>14</i>	<i>27</i>	
	<i>15</i>	<i>29</i>	
	<i>16</i>	<i>31</i>	
	<i>17</i>	<i>33</i>	
5	18	(+16) 35	51

l	l^*	n	\mathbb{P}_p^1
1	1	1	1
2	2	(+2) 3	5
	<i>3</i>	<i>5</i>	
	<i>4</i>	<i>7</i>	
	<i>5</i>	<i>9</i>	
3	6	(+8) 11	19
	<i>7</i>	<i>13</i>	
	<i>8</i>	<i>15</i>	
	<i>9</i>	<i>17</i>	
	<i>10</i>	<i>19</i>	
	<i>11</i>	<i>21</i>	
	<i>12</i>	<i>23</i>	
	<i>13</i>	<i>25</i>	
	<i>14</i>	<i>27</i>	
	<i>15</i>	<i>29</i>	
4	16	(+20) 31	51

rule.

Unfortunately, the rule enrichment process is not as stable as the one for bounded supports as some grid extension levels only provide invalid (i.e. imaginary) roots for the location of the nodes. They have derived two different extension sequences that do not have the same number of points n for the different grid levels l but have similar polynomial exactness p , cf. Table B.1. We notice that the progression is not as regular. These higher-degree rules are the most efficient rules known for polynomial accuracies and are only moderately unstable as the degree of polynomial precision increases [149].

Fig. 2.1.3 shows the KP nodes up to level $l = 7$.

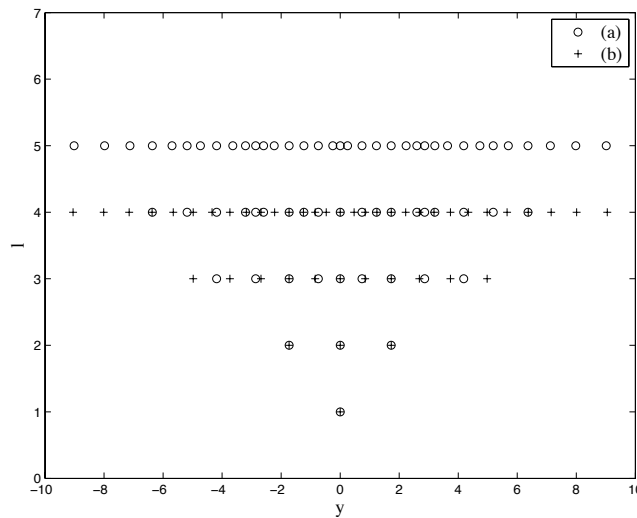


Figure B.3 – Fully symmetric interpolatory rule [149] vs. quadrature level l for integration over unbounded support with a Gaussian weight function. (a): $\mathcal{Q}_{[1+2+6+10+16]}^1$ rule; (b): $\mathcal{Q}_{[1+2+8+20]}^1$ rule.

2.2 Multivariate cubatures

Again, we need to introduce some special function class in order to produce integration error bounds depending on the class. For the quadrature error bounds, we will differentiate among functions from the standard smoothness class:

$$\mathcal{C}_N^r := \{f : \Omega^{(N)} \rightarrow \mathbb{R} : \max_{|\mathbf{s}| \leq r} \left\| \frac{\partial^{|\mathbf{s}|} f}{\partial y_j^{|\mathbf{s}|}} \right\|_\infty < \infty, \text{ for } j = 1, \dots, N\}, \quad (\text{B.17})$$

where $\mathbf{s} \in \mathbb{N}_0^N$ is used to denote a partial derivative of order $|\mathbf{s}| = s_1 + \dots + s_N$, and functions from the partially separable class with bounded *mixed* derivatives:

$$\mathcal{F}_N^r := \{f : \Omega^{(N)} \rightarrow \mathbb{R} : \max_{\mathbf{s} \leq r} \left\| \frac{\partial^{|\mathbf{s}|} f}{\partial y_1^{s_1} \dots \partial y_N^{s_N}} \right\|_\infty < \infty\}, \quad (\text{B.18})$$

where $\mathbf{s} \leq r$ means $s_j \leq r$ for every $i = 1, \dots, N$. We remark that the associated spaces, in the case of $[-1, 1]^N$ -periodicity, are the Korobov spaces [469].

2.2.1 Full tensor product-based grids

The N -dimensional cubature can be constructed from complete tensorization of one-dimensional quadrature rules B.14:

$$\mathcal{Q}_l^N[\psi] = (\mathcal{Q}_{l_1}^1 \otimes \dots \otimes \mathcal{Q}_{l_N}^1) \psi, \quad (\text{B.19})$$

with the multi-index notation $\mathbf{l} = (l_1, \dots, l_N) \in \mathbb{N}_+^N$. The grid points of the entire grid, represented by the ensemble Γ_l^N , are constructed based on tensor-products of the one-dimensional grid points:

$$\Gamma_l^N := \Lambda_{l_1}^1 \times \dots \times \Lambda_{l_N}^1, \quad (\text{B.20})$$

so that Eq. B.19 becomes:

$$\begin{aligned} \mathcal{Q}_l^N[\psi] &= (\mathcal{Q}_{l_1}^1 \otimes \dots \otimes \mathcal{Q}_{l_N}^1) \psi \\ &= \sum_{k_1=1}^{n_1(l_1)} \dots \sum_{k_N=1}^{n_N(l_N)} \psi(h(y_1^{(k_1)}, \dots, y_N^{(k_N)})) w_{l_1}^{(k_1)} \dots w_{l_N}^{(k_N)} \end{aligned} \quad (\text{B.21})$$

Eq. B.21 represents the most general case where different level of quadrature precision l_k , different number of quadrature points n_{l_k} and different type of quadrature may be employed along each k^{th} dimension. This is quite useful to treat the case where the independent random parameters have different distributions.

In fact, if $n_1(l_1) = n_2(l_2) = \dots = n_N(l_N) = n_l$, which means that precision level and corresponding number of grid points is the same for each dimension (i.e. isotropic formula), then the total number of cubature points becomes:

$$N_q = (n_l)^N. \quad (\text{B.22})$$

In this case, we observe an *exponential* growth of the number of points with N .

2.2.2 Sparse grids

When the number of grid points along each random dimension becomes too large, grids based on full tensor products are too costly. An alternative are sparse quadratures [351] which require less quadrature points and can overcome this curse of dimension to a certain extent. The sparse quadrature based on Smolyak algorithm [446] has the advantage of remaining accurate with a convergence rate depending weakly on N . In this way, the number of function evaluations and the numerical accuracy become independent of the dimension of the problem up to logarithmic factors. With this approach, the quadrature points and the weights are known and come from combinations of different rules in different dimensions.

One can imagine that if the tensor product of quadrature formulas combine high-order formulas in only a few random dimensions with low-order formulas in the other dimensions, then the resulting quadrature may be feasible in high dimensions. A good idea is to combine such quadratures by introducing quadrature differences:

$$\Delta \mathcal{Q}_{l_k}^1 := (\mathcal{Q}_{l_k}^1 - \mathcal{Q}_{l_k-1}^1), \quad k = 1, \dots, N,$$

where $\mathcal{Q}_{l_k}^1$ is defined in Eq. B.14 (and is not necessarily nested) and $\mathcal{Q}_0^1 := 0$. In general, the difference formulas are quadrature formulas on the union of the grids $\Lambda_{l_k}^1 \cup \Lambda_{l_k-1}^1$ (which becomes $\Lambda_{l_k}^1$ in the nested case). We note that for nested quadratures, the quadrature difference requires updating the set of nodes from $\mathcal{Q}_{l_k}^1$ that have weights equal to the difference of weights between level l_k and $l_k - 1$.

The goal is now to build a cubature for which only a few levels l_k are large. One possible choice is to use linear combinations of such quantities only for indices that fall within a *simplex* instead of an hypercube as in the classical simple product formula.

Given a *level* $\nu \in \mathbb{N}_+$, the sparse cubature formula in N dimensions is:

$$Q_\nu^N[\psi] = \sum_{\mathbf{k} \in \mathcal{J}(\nu, N)} (\Delta Q_{k_1}^1 \otimes \dots \otimes \Delta Q_{k_N}^1) \psi, \quad (\text{B.23})$$

or may also be expressed as [154]:

$$Q_\nu^N[\psi] = \sum_{\mathbf{k} \in \mathcal{K}(\nu, N)} (-1)^{\nu + N - |\mathbf{k}|_1 - 1} \binom{N-1}{|\mathbf{k}|_1 - \nu} \cdot (Q_{k_1}^1 \otimes \dots \otimes Q_{k_N}^1) \psi,$$

where the sets \mathcal{J} and \mathcal{K} are defined in the case of the Smolyak's construction as:

$$\begin{aligned} \mathcal{J}(\nu, N) &= \{\mathbf{k} \in \mathbb{N}_+^N, \mathbf{k} > 0 : g(\mathbf{k}) \leq \nu - 1\}, \\ \mathcal{K}(\nu, N) &= \{\mathbf{k} \in \mathbb{N}_+^N, \mathbf{k} > 0 : \nu - N \leq g(\mathbf{k}) \leq \nu - 1\}, \end{aligned}$$

where the strictly increasing function

$$g : \mathbb{N}_+^N \rightarrow \mathbb{N}_+ \mid g(\mathbf{k}) = \sum_{n=1}^N (k_n - 1),$$

characterizes the set of multi-indices used to construct the sparse approximation.

This time the cubature grid is based on union of grids:

$$\Gamma_\nu^N = \bigcup_{\mathbf{l} \in \mathcal{J}(\nu, N)} (\Lambda_{l_1}^1 \times \dots \times \Lambda_{l_N}^N).$$

As the sparse quadrature is enriched by increasing the quadrature level from l to $(l+1)$, the grid points used in the earlier levels are retained. Therefore, the sparse quadrature is always *embedded* regardless of the nature of the 1D basis quadrature rule used. If the one-dimensional quadrature rule is *nested*, i.e. if:

$$\Lambda_{l+1}^j \subseteq \Lambda_l^j \quad \text{then} \quad \Gamma_\nu^N \subset \Gamma_{\nu+1}^N, \quad (\text{B.24})$$

and this results in a much smaller number of collocation points compared to the non-nested formulas:

$$\Gamma_\nu^N = \bigcup_{\mathbf{l} \in \tilde{\mathcal{J}}(\nu, N)} (\Lambda_{l_1}^1 \times \dots \times \Lambda_{l_N}^N),$$

with $\tilde{\mathcal{J}}(\nu, N) = \{\mathbf{k} \in \mathbb{N}_+^N, \mathbf{k} > 0 : g(\mathbf{k}) = \nu - 1\}$.

It is important to notice that the Smolyak algorithm will perform his task of building a multi-dimensional grid for any family of one-dimensional quadrature rules. The latter will affect the total number of cubature points as well as the overall accuracy of the integration.

Figs. 2.2.2 show the KP nodes for unbounded support up to level $l = 7$.

Polynomial exactness:

In this paragraph the focus is on polynomial exactness. We refer to [351] for details.

— Let us first consider the general case with assumptions B.1 and I.22 and let us assume that the sparse grid is based on univariate quadrature formulas of degree $m(i) \geq 2i - 1$ for a number of nodes $n(i) \leq m(i) + 1$ (e.g. Gaussian quadrature formulas). Then the sparse cubature of level ν based on this univariate rule has certain properties:

Corollary B.6 ([351] p.9)

Q_ν^N B.23 has (at least) a polynomial degree of exactness:

$$\deg(Q_\nu^N) = 2\nu - 1. \quad (\text{B.25})$$

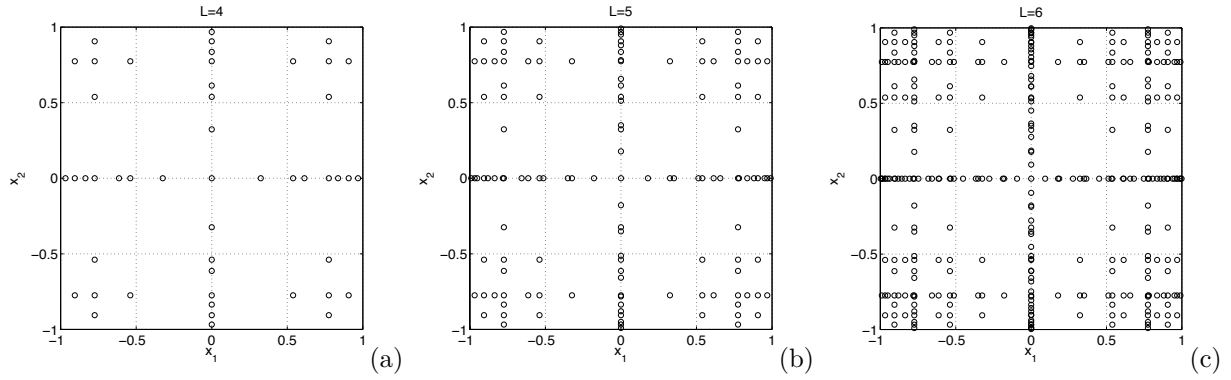


Figure B.4 – 2D Legendre collocation grids for different levels of resolution. (a): 4^2 grid points; (b): 5^2 grid points; (c): 6^2 grid points.

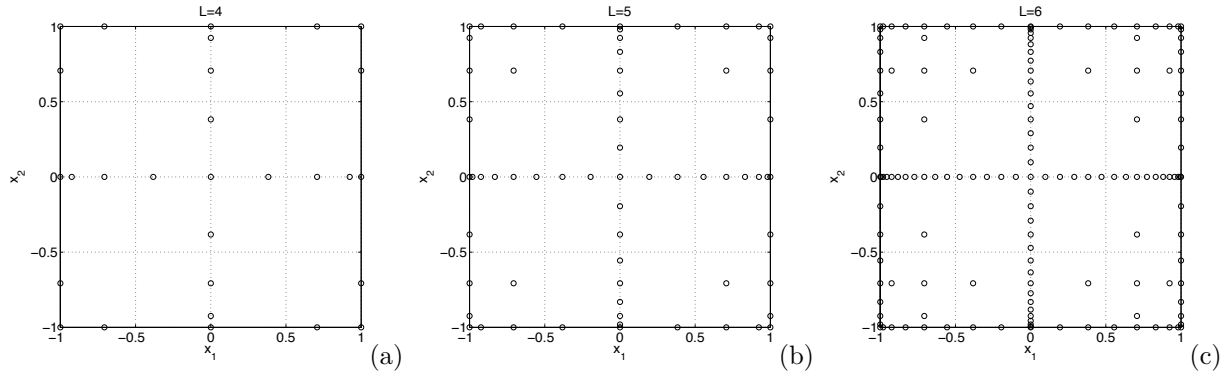


Figure B.5 – 2D Clenshaw-Curtis collocation grids for different levels of resolution. (a): 4^2 grid points; (b): 5^2 grid points; (c): 6^2 grid points.

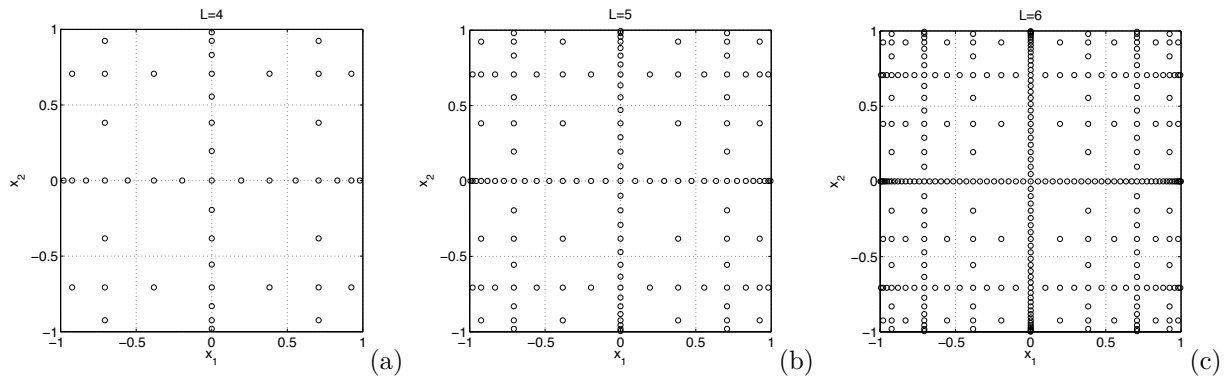


Figure B.6 – 2D Fejer-II collocation grids for different levels of resolution. (a): 4^2 grid points; (b): 5^2 grid points; (c): 6^2 grid points.

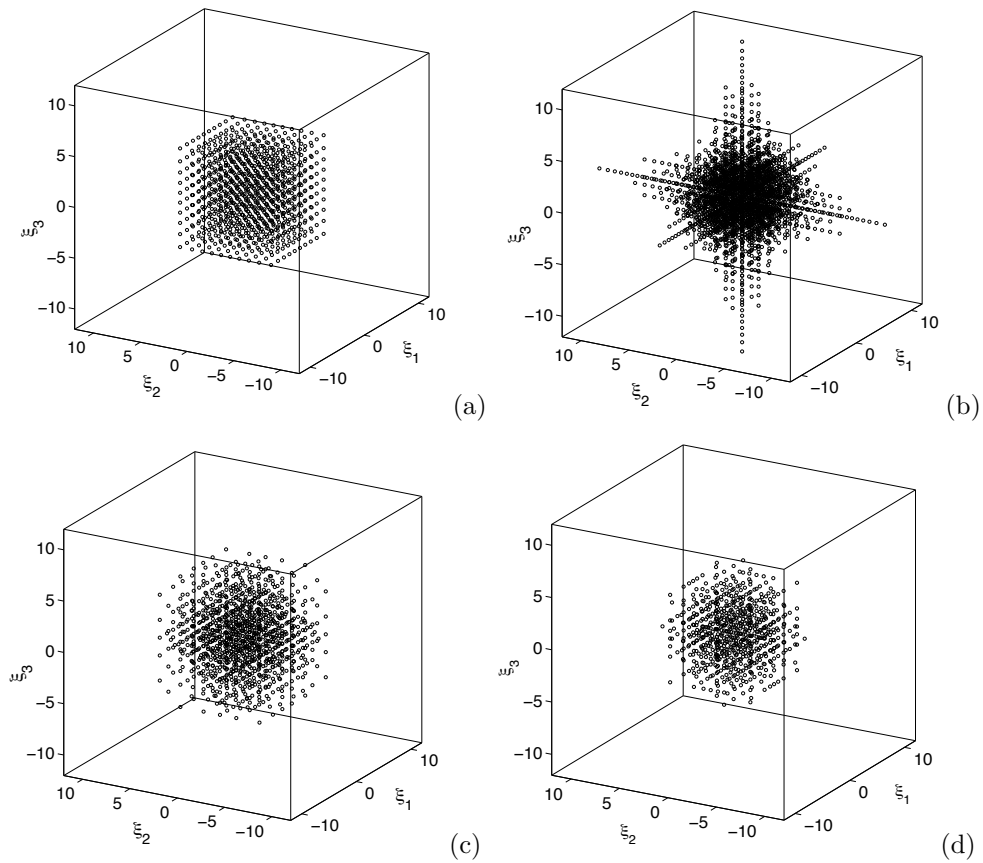


Figure B.7 – Different cubature grids for integration with Gaussian weight in three-dimensions. (a) Full tensor product-based Gauss-Hermite with $\deg(Q_{l=10}^{3\text{GH}}) = 19$, $N_q = 1000$; (b) Sparse Gauss-Hermite $\deg(Q_{\nu=3}^{3\text{GH}}) = 19$, $N_q = 2815$; (c) $\deg(Q_{\nu=3}^{3\text{GH}}) = 19$, $N_q = 1159$; (d) Sparse Kronrod-Patterson [149] $\deg(Q_{\nu=3}^{3\text{GK}}) = 15$, $N_q = 703$;

Corollary B.7 ([351] p.12)

An asymptotic upper bound for the total number of cubature points N_q of \mathcal{Q}_ν^N to reach this accuracy is:

$$N_q \approx \frac{2^\nu}{\nu!} \cdot N^\nu, \quad (\text{B.26})$$

when ν is fixed and $N \gg 1$.

Remark B.8

If we consider \mathbb{P}_ν^N the space of all polynomials in N variables of total degree at most ν , the dimension of this space is $\dim(\mathbb{P}_\nu^N) = \binom{\nu + N}{N} \approx \frac{1}{\nu!} \cdot N^\nu$. In fact, any method trying to integrate the space \mathbb{P}_ν^N will need at least $\dim(\mathbb{P}_\nu^N)$ function values. For large N , the sparse cubature method only uses about 2^ν as many function values. Since this factor is independent of N , the polynomial dependence on N is optimal. We conclude that the number of nodes grows fast but polynomially.

- If we assume now that $\Omega^{(N)}$ is a bounded hyperrectangle in \mathbb{R}^N , and we consider without loss of generality that $\Omega^{(N)} = [-1, 1]^N$, and if we assume that the weight functions are symmetric, and if we consider nested univariate quadrature formulas such as Clenshaw-Curtis rule B.15, then:

Corollary B.9 ([351] p.15)

\mathcal{Q}_ν^N B.23 has polynomial degree of exactness:

$$\deg(\mathcal{Q}_\nu^N) = \begin{cases} 2\nu - 1 & \text{if } \nu < 3N + 1, \\ 2^{\sigma-2}(N + \tau + 1) + 2N - 1 & \text{otherwise,} \end{cases} \quad (\text{B.27})$$

where $\tau = (\nu + N - 1) \bmod N$ and $\sigma = \text{floor}((\nu + N - 1)/N)$ ³.

The same upper bound for N_q as previously mentioned applies when ν is fixed and N is large.

Lemma B.10 ([337], Lemma 1)

the total number of cubature points N_q of \mathcal{Q}_ν^N to reach this accuracy is:

$$N_q = \mathcal{O}(2^\nu \cdot \nu^{N-1}), \quad (\text{B.28})$$

when ν is fixed and $N \gg 1$.

Corollary B.11 ([351] p.15)

An asymptotic upper bound for the total number of cubature points N_q of \mathcal{Q}_ν^N to reach this accuracy is $N_q \approx c_N \cdot \nu^N \cdot (\log \nu)^{N-1}$, when $\nu \rightarrow \infty$ and N is fixed.

- In section 6 of [351], the authors generalize the approach from [149] to the general case where the weight functions of the integration are fully symmetric, i.e. $f_{\Theta_i}(\theta_i) = f_{\Theta_i}(-\theta_i)$, $\forall i = 1, \dots, N$ on unbounded supports. In Fig. 2.2.2, we show the differences between full, sparse and fully symmetric grids with the same polynomial exactness for Gaussian distributions.

Delayed basis sequences:

If one is concerned with highest polynomial accuracy at low cost, it is possible to optimize the classical sparse grid construction with respect to its polynomial degree of exactness [371]. For instance, the author explored the effect of delayed Kronrod-Patterson sequences, where the growth of the number of points is much slower with the cubature level. Moreover, he shows that the sequence is almost asymptotically optimal and that this type of construction is very efficient provided smooth functions are integrated, since such functions are well approximated by polynomials.

Appendix C

Lagrangian-GAIA solver for deterministic Euler systems

Sommaire

1	Lagrange-remap schemes	167
1.1	Lagrangian step	168
1.2	Remapping step	168
2	Godunov Acoustic Invariant Advection (GAIA) numerical flux	169
2.1	Arbitrary high-order scheme for linear advection equation	169
2.2	GAIA numerical flux for the Lagrangian step	170
2.3	Numerical flux for the remapping step	170
3	Numerical flux limiters	170
3.1	Total Variation Diminishing (TVD) limiter	170
3.2	Monotonicity Preserving (MP) limiter	170
4	Directional splitting	171

1 Lagrange-remap schemes

We recall the 1D Euler system in cartesian coordinates:

$$\begin{cases} \partial_t \rho + \partial_x(\rho u) = 0, \\ \partial_t(\rho u) + \partial_x(\rho u^2 + p) = 0, \\ \partial_t(\rho e) + \partial_x(\rho u e + p u) = 0, \end{cases} \quad (\text{C.1})$$

where ρ is the mass density, u is the velocity and e is the total specific energy. The system is closed by a perfect gas equation of state $p = (\gamma - 1)\rho\epsilon$ where $\epsilon = e - \frac{u^2}{2}$ is the specific internal energy.

The Lagrange+remap scheme requires the resolution of the Euler system in *Lagrangian* coordinates. This is achieved by a change of variables:

$$\partial_t x = u \text{ with initial condition } x|_{t=0} = X, \quad (\text{C.2})$$

where X is called the Lagrangian coordinate and we introduce the *mass* coordinate m such that:

$$\partial m = \rho^0 \partial X = \rho \partial x,$$

with $\rho|_{t=0} = \rho^0$.

The Euler system in mass coordinates becomes:

$$\begin{cases} \partial_t \tau_L - \partial_m u_L = 0, \\ \partial_t u_L + \partial_m p_L = 0, \\ \partial_t e_L + \partial_m p_L u_L = 0, \end{cases} \quad (\text{C.3})$$

where $\tau_L = \frac{1}{\rho_L}$ is the specific volume in Lagrangian coordinates: for every function $\psi(x, t)$, the function $\psi_L(X, t)$ represents ψ in the Lagrangian coordinates, $\psi_L(X(x, t), t) = \psi(x, t)$. The jacobian of the transformation is given

by:

$$\begin{aligned} J_L(X(x, t), t) &= \frac{\partial x}{\partial X}(X(x, t), t) \\ &= \frac{\rho_L^0(X(x, t))}{\rho_L(X(x, t), t)} = \frac{\rho^0(x)}{\rho(x, t)} = J(x, t). \end{aligned} \quad (\text{C.4})$$

Time is discretized and we denote $\Delta t = t^{n+1} - t^n$ a time step. We consider the space \mathcal{D}_x discretized in N_x volumes of equal sizes $\Delta x = \Delta x_i = x_{i+\frac{1}{2}} - x_{i-\frac{1}{2}}$ where $x_{i-\frac{1}{2}}$ and $x_{i+\frac{1}{2}}$ are the boundaries of the cell i . At the beginning of the time step, $x_{i+\frac{1}{2}}^n = x_{i+\frac{1}{2}}$ and $x_{i-\frac{1}{2}}^n = x_{i-\frac{1}{2}}$ for all $i \in \{1, \dots, N_x\}$.

In Lagrangian coordinates, the spatial domain is also discretized in N_x *moving* cells¹: the position of the cell boundaries at time t^{n+1} is denoted $x(X_{i+\frac{1}{2}}, t^{n+1}) = x_{i+\frac{1}{2}}^{n+1}$ and is the solution of the equation

$$\partial_t x = u. \quad (\text{C.5})$$

By integrating this equation on $]t^n, t^{n+1}[$, we obtain:

$$x_{i+\frac{1}{2}}^{n+1} = x_{i+\frac{1}{2}}^n + \Delta t u_{i+\frac{1}{2}}^* = x_{i+\frac{1}{2}} + \Delta t u_{i+\frac{1}{2}}^*, \quad (\text{C.6})$$

so that the volume of the Lagrangian cell is given by:

$$x_{i+\frac{1}{2}}^{n+1} - x_{i-\frac{1}{2}}^{n+1} = \Delta x_i^{n+1} = \Delta x + \Delta t (u_{i+\frac{1}{2}}^* - u_{i-\frac{1}{2}}^*). \quad (\text{C.7})$$

In mass coordinates, we obtain:

$$\Delta m_i = \Delta x \rho_i = \Delta X_i \rho_i^0. \quad (\text{C.8})$$

1.1 Lagrangian step

The Lagrangian step corresponds to the integration of the Euler system in mass coordinates (C.3) on one time step. Integrating (C.3) on the control volume $]t^n, t^{n+1}[\times]m_{i-\frac{1}{2}}, m_{i+\frac{1}{2}}[$, we obtain

$$\begin{cases} \frac{(\tau_L)_i^{n+1} - (\tau_L)_i^n}{\Delta t} - \frac{(u_L)_{i+\frac{1}{2}}^* - (u_L)_{i-\frac{1}{2}}^*}{\Delta m_i} = 0, \\ \frac{(u_L)_i^{n+1} - (u_L)_i^n}{\Delta t} + \frac{(p_L)_{i+\frac{1}{2}}^* - (p_L)_{i-\frac{1}{2}}^*}{\Delta m_i} = 0, \\ \frac{(e_L)_i^{n+1} - (e_L)_i^n}{\Delta t} + \frac{(p_L u_L)_{i+\frac{1}{2}}^* - (p_L u_L)_{i-\frac{1}{2}}^*}{\Delta m_i} = 0, \end{cases} \quad (\text{C.9})$$

which is exact. The approximation begins with the discretization of the numerical fluxes $(u_L)_{i+\frac{1}{2}}^*$, $(p_L)_{i+\frac{1}{2}}^*$, $(p_L u_L)_{i+\frac{1}{2}}^*$. This is done in Section 2.2.

1.2 Remapping step

This step corresponds to a backward mapping from the Lagrangian quantities (calculated during the Lagrangian step) on the moving grid $((\tau_L)_i^{n+1}, (u_L)_i^{n+1}, (e_L)_i^{n+1})^t$ to the Eulerian quantities on the fixed initial grid $(\rho_i^{n+1}, (\rho u)_i^{n+1}, (\rho e)_i^{n+1})^t$. This is done again by introducing a change of variables in the integral:

$$\begin{aligned} &\int_{X_{i-\frac{1}{2}}}^{X_{i+\frac{1}{2}}} \rho^0(X) \psi_L(X, t^{n+1}) dX \\ &= \int_{x_{i-\frac{1}{2}}^{n+1}}^{x_{i+\frac{1}{2}}^{n+1}} \rho^0(x) \psi(x, t^{n+1}) J(x, t^{n+1}) dx, \\ &= \int_{x_{i-\frac{1}{2}}^{n+1}}^{x_{i+\frac{1}{2}}^{n+1}} \rho(x, t) \psi(x, t^{n+1}) dx. \end{aligned} \quad (\text{C.10})$$

Then, we have

$$\begin{aligned} \int_{X_{i-\frac{1}{2}}}^{X_{i+\frac{1}{2}}} \rho^0(X) \psi_L(X, t^{n+1}) dX &= \int_{x_{i-\frac{1}{2}}^n}^{x_{i+\frac{1}{2}}^n} \rho \psi(x, t^{n+1}) dx \\ &+ \int_{x_{i-\frac{1}{2}}^{n+1}}^{x_{i+\frac{1}{2}}^{n+1}} \rho \psi(x, t^{n+1}) dx + \int_{x_{i-\frac{1}{2}}^n}^{x_{i+\frac{1}{2}}^n} \rho \psi(x, t^{n+1}) dx. \end{aligned} \quad (\text{C.11})$$

1. moving with time in the Eulerian reference frame.

We recover both the expressions of the FV means in Lagrangian and Eulerian coordinates

$$(\rho\psi)_i^{n+1} = \rho_i^n (\psi_L)_i^{n+1} - \frac{1}{\Delta x} \left(\int_{x_{i+\frac{1}{2}}^n}^{x_{i-\frac{1}{2}}^{n+1}} \rho\psi(x, t^{n+1}) dx + \int_{x_{i-\frac{1}{2}}^n}^{x_{i+\frac{1}{2}}^{n+1}} \rho\psi(x, t^{n+1}) dx \right). \quad (\text{C.12})$$

Using the relations (C.6)-(C.7), we obtain the exact expression of the remapping step:

$$(\rho\psi)_i^{n+1} = \rho_i^n (\psi_L)_i^{n+1} - \frac{\Delta t}{\Delta x} \left(u_{i+\frac{1}{2}}^* (\rho\psi)_{i+\frac{1}{2}}^* - u_{i-\frac{1}{2}}^* (\rho\psi)_{i-\frac{1}{2}}^* \right), \quad (\text{C.13})$$

where $\psi \in \{1, u, e\}$ and where the flux is defined by

$$(\rho\psi)_{i+\frac{1}{2}}^* = \frac{1}{x_{i+\frac{1}{2}}^{n+1} - x_{i+\frac{1}{2}}^n} \int_{x_{i+\frac{1}{2}}^n}^{x_{i+\frac{1}{2}}^{n+1}} \rho\psi(x, t^{n+1}) dx. \quad (\text{C.14})$$

Once again, the previous expression is exact and the approximation will begin when discretizing the integrals in (C.14) for $\psi \in \{1, u, e\}$. This will be done in section 2.3.

2 Godunov Acoustic Invariant Advection (GAIA) numerical flux

We describe the numerical scheme used to approximate the fluxes in expressions (C.9) and (C.13). For more details we refer to [213, 183]. The GAIA numerical flux is a generalization of the arbitrary high-order scheme for the linear advection equation.

2.1 Arbitrary high-order scheme for linear advection equation

Let us consider the linear advection equation:

$$\partial_t u + a \partial_x u = 0, \quad (\text{C.15})$$

with $a \in \mathbb{R}$ constant. The integration of (C.15) on a control volume $]t^n, t^{n+1}[\times]x_{i-\frac{1}{2}}, x_{i+\frac{1}{2}}[$ leads to the exact formulation

$$\frac{u_i^{n+1} - u_i^n}{\Delta t} + a \frac{F_{i+\frac{1}{2}}^* - F_{i-\frac{1}{2}}^*}{\Delta x} = 0. \quad (\text{C.16})$$

The following fluxes, defined through recurrence formulae, are arbitrarily high-order fluxes of order N in space and time for solving (C.15), cf. [213]:

- If $a > 0$ and if $N = 1$ then $F_{j+1/2}^1 = u_j^n$, the exponent of F denotes the order of the numerical flux. If $a > 0$ and $N > 1$ then

$$F_{j+1/2}^N = F_{j+1/2}^{N-1} - \frac{1}{N!} \left(\prod_{i=-m, i \neq 0}^M (\nu + 1) \right) \left(\sum_{k=0}^{N-1} C_{N-1}^k u_{j+m-k}^n \right), \quad (\text{C.17})$$

with $m = \lfloor \frac{N}{2} \rfloor$, $M = \lfloor \frac{N-1}{2} \rfloor$ and $C_n^p = \frac{n!}{p!(n-p)!}$.

- If $a < 0$ and if $N = 1$ then $F_{j+1/2}^1 = u_{j+1}^n$. If $a < 0$ and $N > 1$ then

$$F_{j+1/2}^N = F_{j+1/2}^{N-1} - \frac{1}{N!} \left(\prod_{i=-M, i \neq 0}^m (\nu + 1) \right) \left(\sum_{k=0}^{N-1} C_{N-1}^k u_{j+M-k+1}^n \right), \quad (\text{C.18})$$

with $m = \lfloor \frac{N}{2} \rfloor$, $M = \lfloor \frac{N-1}{2} \rfloor$ and $C_n^p = \frac{n!}{p!(n-p)!}$.

2.2 GAIA numerical flux for the Lagrangian step

During the Lagrangian step, the idea is to apply the recurrence formulae of the numerical fluxes (C.17)-(C.18) to the Riemann invariants J_+ and J_- satisfying the non linear advection equations

$$\partial_t J_{\pm} + (\rho c) \partial_x J_{\pm} = 0, \quad (\text{C.19})$$

where c is the sound velocity and where $J_{\pm} = u \pm \int \frac{dp}{\rho c}$. In the expression of the numerical fluxes, for non uniform advection, upwinding with respect to (ρc) is applied on the boundaries of the cell j .

The numerical fluxes are then defined: they are conservative for all $N \in \mathbb{N}$. At order 1, we find back the classical acoustic Riemann solver [474], which is also entropic. For $N > 1$, the numerical fluxes are of prescribed order only in the linear advection limit of the Euler system in Lagrangian coordinates. For $N > 1$, in order to stabilize the scheme in the vicinity of shocks, some limiters of fluxes are used. They are briefly presented appendix 3.

2.3 Numerical flux for the remapping step

During the remapping step, the recurrence formulae for the numerical fluxes (C.17) are applied to the conservative quantities $\psi \in \{\rho, \rho u, \rho e\}$ with u as advection velocity. Indeed, $\psi \in \{\rho, \rho u, \rho e\}$ satisfy the equations (cf. [115])

$$\partial_t \psi_L(X(x, t), t) = \partial_t \psi(x, t) + u(x, t) \partial_x \psi(x, t), \quad (\text{C.20})$$

whose integration on a control volume is given by (C.13).

In the expression of the numerical fluxes, for non uniform advection, we glue u_j on the stencil of the considered cell j .

The numerical flux, after the Lagrangian and remapping steps, is conservative $\forall N \in \mathbb{N}$. It is of effective order N in the linear advection limit of the Euler system. For order 1, it is also entropic. For orders $N > 1$, in the vicinity of discontinuities, the scheme leads to the appearance of numerical oscillations. Some flux limiters are used in practice in order to stabilize the scheme. They are presented appendix 3.

3 Numerical flux limiters

The flux limiter is presented applied to equation (C.15) where a is the advection velocity. The efficiency of this limiter for the stabilization of high order schemes is discussed in [213]. The limiter forces the flux to a certain interval: we describe the form of this interval in the following. We denote by $[[\alpha, \beta]]$ the interval $[\min(\alpha, \beta), \max(\alpha, \beta)]$ and $\nu = a \frac{\Delta t}{\Delta x}$.

3.1 Total Variation Diminishing (TVD) limiter

— If $a < 0$ then

$$F_{j+1/2}^{TVD} \in [[u_j^n, u_{j+1}^n]] \cap [[u_{j+1}^{UL}, u_{j+1}^{UL}]] \quad (\text{C.21})$$

where $u_{j+1}^{UL} = u_{j+1}^n - \frac{(1+\nu)}{\nu} (u_{j+1}^n - u_{j+2}^n)$.

— If $a > 0$ then

$$F_{j+1/2}^{TVD} \in [[u_j^n, u_{j+1}^n]] \cap [[u_j^n, u_j^{UL}]] \quad (\text{C.22})$$

where $u_j^{UL} = u_j^n + \frac{(1-\nu)}{\nu} (u_j^n - u_{j-1}^n)$.

3.2 Monotonicity Preserving (MP) limiter

We define the curvature

$$d_j = f_{j+1}^n - 2f_j^n + f_{j-1}^n,$$

with

$$d_{j+1/2} = \text{minmod}(4d_j - d_{j+1}, 4d_{j+1} - d_j, d_j, d_{j+1}).$$

The fluxes are confined to the following intervals:

— If $a < 0$ then

$$F_{j+\frac{1}{2}}^{MP} \in [[u_j^n, u_{j+1}^n, u_{j+\frac{1}{2}}^{MD}]] \cap [[u_{j+1}^n, u_{j+1}^{UL}, u_{j+1}^{LC}]]. \quad (\text{C.23})$$

With

$$\begin{aligned}
u_{j+1}^{UL} &= u_{j+1}^n - \frac{(1+\nu)}{\nu}(u_{j+1}^n - u_{j+2}^n), \\
u_{j+1/2}^{MD} &= \frac{1}{2}(u_j^n + u_{j+1}^n) - \frac{1}{2}d_{j+1/2}, \\
u_{j+1}^{LC} &= u_{j+1}^n - \frac{1}{2}\frac{(1+\nu)}{\nu}(d_{j+3/2} + (u_{j+1}^n - u_{j+2}^n)).
\end{aligned} \tag{C.24}$$

— If $a > 0$ then

$$F_{j+1/2}^{MP} \in \left[[u_j^n, u_{j+1}^n, u_{j+1/2}^{MD}] \right] \cap \left[[u_j^n, u_j^{UL}, u_j^{LC}] \right]. \tag{C.25}$$

With

$$\begin{aligned}
u_j^{UL} &= u_j^n + \frac{(1-\nu)}{\nu}(u_j^n - u_{j-1}^n), \\
u_{j+1/2}^{MD} &= \frac{1}{2}(u_j^n + u_{j+1}^n) - \frac{1}{2}d_{j+1/2}, \\
u_j^{LC} &= u_j^n - \frac{1}{2}\frac{(-1+\nu)}{\nu}(d_{j-1/2} + (u_j^n - u_{j-1}^n)).
\end{aligned} \tag{C.26}$$

4 Directional splitting

In this section, we briefly describe the principles of directional splitting. It allows solving multidimensional systems thanks to one dimensional numerical schemes.

Let us consider the two dimensional system

$$\partial_t U + \partial_x f(U) + \partial_y h(U) = 0 \text{ with } U \in \mathcal{U} \subset \mathbb{R}^n. \tag{C.27}$$

A directional splitting scheme for the solution of system (C.27) consists of two steps during a time iteration $t^n \rightarrow t^{n+1}$:

— Step 1:

— If n even: solve $\partial_t U + \partial_x f(U) = 0$ on Δt with initial condition U_i^n . We denote \tilde{U}_i the obtained solution.

— If n odd: solve $\partial_t U + \partial_y h(U) = 0$ on Δt with initial condition U_i^n . We denote \tilde{U}_i the obtained solution.

— Step 2:

— If n even: solve $\partial_t U + \partial_y h(U) = 0$ on Δt with initial condition \tilde{U}_i . We denote \bar{U}_i the obtained solution.

— If n odd: solve $\partial_t U + \partial_x f(U) = 0$ on Δt with initial condition \tilde{U}_i . We denote \bar{U}_i the obtained solution.

The scheme is then closed supposing $\bar{U}_i = U_i^{n+1}$. When the time step Δt is constant in the different steps, such a splitting is called *Strang* splitting and is second order in time (see [457]).

Bibliography

- [1] R. Abgrall. On essentially non-oscillatory schemes on unstructured meshes: Analysis and implementation. *Journal of Computational Physics*, 114(1):45 – 58, 1994.
- [2] R. Abgrall, P. M. Congedo, C. Corre, and S. Galéra. A simple semi-intrusive method for uncertainty quantification of shocked flows, comparison with a non-intrusive Polynomial Chaos method. In *V European Conference on Computational Fluid Dynamics, ECCOMAS CFD 2010*, Lisbon, Portugal, 2010.
- [3] Remi Abgrall. A simple, flexible and generic deterministic approach to uncertainty quantifications in non linear problems: application to fluid flow problems. *Rapport de Recherche INRIA*, (00325315), 2008.
- [4] Remi Abgrall, Pietro Marco Congedo, Stéphane Galera, and Gianluca Geraci. Semi-intrusive and non-intrusive stochastic methods for aerospace applications. In *4TH EUROPEAN CONFERENCE FOR AEROSPACE SCIENCES*, Saint Petersburg, Russie, 2011.
- [5] M. Abramowitz and I. Stegun. *Handbook of Mathematical Functions with Formulas, Graphs, and Mathematical Tables*. Dover, New York, 1970.
- [6] S. Acharjee and N. Zabaras. A Concurrent Model Reduction Approach on Spatial and Random Domains for the Solution of Stochastic PDEs. *Int. J. Numer. Meth. Engrg.*, 2005.
- [7] Paul Andersson, Martin Berggren, and Dan S. Henningson. Optimal disturbances and bypass transition in boundary layers. *Phys. Fluids*, 11(1):134–150, 1999.
- [8] M. Arnst and R. Ghanem. Probabilistic equivalence and stochastic model reduction in multiscale analysis. *Computer Methods in Applied Mechanics and Engineering*, 197(43-44):3584 – 3592, 2008. <ce:title>Stochastic Modeling of Multiscale and Multiphysics Problems</ce:title>.
- [9] M. Arnst, R. Ghanem, and C. Soize. Identification of bayesian posteriors for coefficients of chaos expansions. *Journal of Computational Physics*, 229(9):3134–3154, 2010.
- [10] Badrinarayanan Velamur Asokan and Nicholas Zabaras. Using stochastic analysis to capture unstable equilibrium in natural convection. *Journal of Computational Physics*, 208:134–153, 2005.
- [11] Badrinarayanan Velamur Asokan and Nicholas Zabaras. Variational multiscale stabilized FEM formulations for transport equations: stochastic advection-diffusion and incompressible stochastic Navier-Stokes equations. *Journal of Computational Physics*, 205:94–133, 2005.
- [12] Badrinarayanan Velamur Asokan and Nicholas Zabaras. A stochastic variational multiscale method for diffusion in heterogeneous random media. *Journal of Computational Physics*, 218(2):654 – 676, 2006.
- [13] A. C. Atkinson and A. N. Donev. *Optimum experimental designs*, volume 8 of *Statistical Science Series*. Oxford Clarendon Press, 1992.
- [14] Kendall E. Atkinson. *The Numerical Solution of Integral Equations of the Second Kind*. Cambridge University Press, 1997.
- [15] I. Babuška, F. Nobile, and R. Tempone. A stochastic collocation method for elliptic partial differential equations with random input data. *SIAM J. Numer. Anal.*, 45(3):1005–1034, 2007.
- [16] I. Babuška, R. Tempone, and G.E. Zouraris. Galerkin finite element approximations of stochastic elliptic differential equations. Technical Report 02-38, TICAM, 2002.
- [17] I. Babuška, R. Tempone, and G.E. Zouraris. Galerkin finite element approximations of stochastic elliptic differential equations. *SIAM J. Numer. Anal.*, 42:800–825, 2004.
- [18] Ivo Babuška and Panagiotis Chatzipantelidis. On solving elliptic stochastic partial differential equations. *Computer Methods in Applied Mechanics and Engineering*, 191(37-38):4093 – 4122, 2002.
- [19] Ivo Babuska and J. Tinsley Oden. Verification and validation in computational engineering and science: basic concepts. *Computer Methods in Applied Mechanics and Engineering*, 193(36-38):4057 – 4066, 2004.
- [20] J. Bäck, F. Nobile, L. Tamellini, and R. Tempone. Stochastic spectral galerkin and collocation methods for pdes with random coefficients: A numerical comparison. In T. J. Barth, M. Griebel, D. E. Keyes, R. M. Nieminen, D. Roose, T. Schlick, J. S. Hesthaven, and E. M. Rønquist, editors, *Spectral and High Order Methods for Partial Differential Equations*, volume 76 of *Lecture Notes in Computational Science and Engineering*, pages 43–62. Springer Berlin Heidelberg, 2011.

- [21] B. Bamieh and M. Dahleh. Energy amplification in channel flows with stochastic excitation. *Phys. Fluids*, 13(11):3258–3269, 2001.
- [22] D. Barkley and L. S. Tuckerman. Stability analysis of perturbed plane Couette flow. *Physics of Fluids*, 11(5):1187–1195, 1999.
- [23] R. Bartels. Flow and turbulence modeling and computation of shock buffet onset for conventional and supercritical airfoils. NASA/TP-1998-206908, 1998.
- [24] T. Barth. On the propagation of statistical model parameter uncertainty in CFD calculations. *Theor. Comput. Fluid Dyn.*, 10.1007/s00162-011-0221-2:1–23, 2011.
- [25] T. Barth and P. O. Frederickson. Higher order solution of the euler equations on unstructured grids using quadratic reconstruction. In *Aerospace Sciences Meeting and Exhibit, Reno, NV*, pages 1–12, 1990.
- [26] V. Barthelmann, E. Novak, and K. Ritter. High dimensional polynomial interpolation on sparse grids. *Adv. Comput. Math.*, 12:273–288, 2000.
- [27] G.K. Batchelor. *The theory of homogeneous turbulence*. Cambridge, University Press, 1953. Cambridge.
- [28] I. Batchelor, G. K. & Proudman. The large-scale structure of homogeneous turbulence. *Phil. Trans. R. Soc. Lond. A*, 248:369–405, 1956.
- [29] J. B. Bell, J. Foo, and A. L. Garcia. Algorithm Refinement for the Stochastic Burgers’ Equation. *J. Comp. Phys.*, 223:451–468, 2007.
- [30] F.E. Benth and J. Gjerde. Convergence rates for finite element approximations of stochastic partial differential equations. *Stoch. & Stoch. Reports*, 63:313–326, 1998.
- [31] P.S. Beran and C.L. Pettit. A direct method for quantifying limit-cycle oscillation response characteristics in the presence of uncertainties. AIAA Paper 2004-1695, 2004.
- [32] P.S. Beran, C.L. Pettit, and D.R. Millman. Uncertainty quantification of limit-cycle oscillations. *Journal of Computational Physics*, 217:217–247, 2006.
- [33] L. P. Bernal and A. Roshko. Streamwise vortex structure in plane mixing layers. *Journal of Fluid Mechanics*, 170:499–525, 1986.
- [34] G. Berveiller. *Stochastic finite elements : intrusive and non-intrusive methods for reliability analysis*. PhD thesis, Université Blaise Pascal, Clermont-Ferrand, 2005.
- [35] M. Berveiller, B. Sudret, and M. Lemaire. Stochastic Finite Element: a Non Intrusive Approach by Regression. *Rev. Eur. Méc. Num.*, 15(1-2-3):81–92, 2006.
- [36] D. Biau and A. Bottaro. Transient growth and minimal defects: Two possible initial paths to transition to turbulence in plane shear flows. *Physics of Fluids*, 16(10):3515–3529, 2004.
- [37] C. Bishop. *Neural Networks for Pattern Recognition*. Clarendon Press, Oxford., 1995.
- [38] G. Blatman. *Adaptive sparse polynomial chaos expansions for uncertainty propagation and sensitivity analysis*. PhD thesis, Université Blaise Pascal, Clermont-Ferrand, 2009.
- [39] G. Blatman, B. Sudret, and M. Berveiller. Quasi-Random Numbers in Stochastic Finite Element Analysis. *Mech. Ind. proofs*, 8:289–297, 2007.
- [40] Géraud Blatman and Bruno Sudret. Sparse polynomial chaos expansions and adaptive stochastic finite elements using a regression approach. *Comptes Rendus Mécanique*, 336(6):518 – 523, 2008.
- [41] Géraud Blatman and Bruno Sudret. Efficient computation of global sensitivity indices using sparse polynomial chaos expansions. *Reliability Engineering & System Safety*, 95(11):1216 – 1229, 2010.
- [42] D. Bose, M. J. Wright, and G. E. Palmer. Uncertainty analysis of laminar aeroheating predictions for mars entries. *Journal of thermophysics and heat transfer*, 20(4):652–662, 2006.
- [43] A. Bottaro, P. Corbett, and P. Luchini. The effect of base flow variation on flow stability. *Journal of Fluid Mechanics*, 476:293–302, 2003.
- [44] S. Bottin, O. Dauchot, F. Daviaud, and P. Manneville. Experimental evidence of streamwise vortices as finite amplitude solutions in transitional plane couette flow. *Physics of Fluids*, 10(10):2597–2607, 1998.
- [45] F. Bouchut and F. James. One-Dimensional Transport Equations with Discontinuous Coefficients. *Non-linear Analysis, TMA*, 32(7):891–933, 1998.
- [46] R. Bourguet, D. Lucor, and M. S. Triantafyllou. Mono- and multi-frequency vortex-induced vibrations of a long tensioned beam in shear flow. *Journal of Fluids and Structures*, in press, 2011.
- [47] G. E. P. Box and N. R. Draper. *Empirical Model-Building and Response Surfaces*. Probability and mathematical statistics. Wiley, 1987.
- [48] S. Boyaval, C. Le Bris, T. Lelièvre, Y. Maday, N. Nguyen, and A. Patera. Reduced basis techniques for stochastic problems. *Archives of Computational Methods in Engineering*, 17:435–454, 2010. 10.1007/s11831-010-9056-z.

- [49] J. P. Boyd. *Chebyshev and Fourier Spectral Methods*. Dover, 2nd edition, 2001.
- [50] Helmut Brass. Bounds for Peano kernels. In H. Brass and G. Hammerlin, editors, *Numerical Integration IV*, volume 112 of *ISNM*, pages 39–55. 1993.
- [51] F. K. Browand and B. O. Latigo. Growth of the two-dimensional mixing layer from a turbulent and nonturbulent boundary layer. *Physics of Fluids*, 22(6):1011–1019, 1979.
- [52] G. L. Brown and A. Roshko. On density effects and large structure in turbulence mixing layer. *Journal of Fluid Mechanics*, 64:775–816, 1974.
- [53] L. Bruno, C. Canuto, and D. Fransos. Stochastic aerodynamics and aeroelasticity of a flat plate via generalised polynomial chaos. *Journal of Fluids and Structures*, 25:1158–1176, 2009.
- [54] H.-J. Bungartz and M. Griebel. Sparse grids. In *Acta Numerica*, volume 13, pages 147–270. Cambridge, University Press, 2004.
- [55] P. Burattini, P. Lavoie, A. Agrawal, L. Djenidi, and R.A. Antonia. Power law of decaying homogeneous isotropic turbulence at low reynolds number. *Phys. Rev. E*, 73:066304, 2006.
- [56] Kathryn M. Butler and Brian F. Farrell. Three-dimensional optimal perturbations in viscous shear flow. *Physics of Fluids A: Fluid Dynamics*, 4(8):1637–1650, 1992.
- [57] D. G. Cacuci. *Sensitivity and uncertainty analysis - Theory*. Chapman & Hall/CRC, 2003.
- [58] L. Cambier and J.-P. Veuillot. Status of the elsA software for flow simulation and multidisciplinary applications. In *AIAA Paper 2008-664*, Reno, USA, 2008. 46th AIAA Aerospace Sciences Meeting and Exhibit.
- [59] R.H. Cameron and W.T. Martin. The orthogonal development of nonlinear functionals in series of Fourier-Hermite functionals. *Annals of Mathematics*, 48:385, 1947.
- [60] R.H. Cameron and W.T. Martin. The orthogonal development of nonlinear functionals in series of Fourier-Hermite functionals. *Ann. Math.*, 48:385, 1947.
- [61] G.H. Canavan. Some properties of a Lagrangian Wiener-Hermite expansion. *Journal of Fluid Mechanics*, 41:405–412, 2001.
- [62] C. Canuto, M.Y. Hussaini, A. Quarteroni, and T.A. Zang. *Spectral methods in fluid dynamics*. Springer-Verlag, Berlin/Heidelberg, 1988.
- [63] Claudio Canuto and Davide Fransos. Numerical solution of partial differential equations in random domains: An application to wind engineering. *Communications in Computational Physics*, 5(2-4):515–531, 2009.
- [64] T. Chantrasmı, A. Doostan, and G. Iaccarino. Padé-Legendre approximants for uncertainty analysis with discontinuous response surfaces. *Journal of Computational Physics*, 228(19):7159 – 7180, 2009.
- [65] F. Charru. *Instabilités Hydrodynamiques*. EDP Sciences, 2007.
- [66] J.-C. Chassaing, G.A. Gerolymos, and I. Vallet. Efficient and robust computation of 3-d compressible flows with reynolds-stress closure. *AIAA Journal*, 41(5):763–773, 2003.
- [67] J.-C. Chassaing, G.A. Gerolymos, and I. Vallet. Reynolds-stress model dual-time-stepping computation of unsteady 3-d flows. *AIAA Journal*, 41(10):1882–1894, 2003.
- [68] J.-C. Chassaing and D. Lucor. Numerical investigation of airfoil performance at stochastic transonic flow regimes. 5th. European Congress on Computational Methods in Applied Sciences and Engineering, June 30-July 04 2008, Venice, Italy, 2008.
- [69] J.-C. Chassaing and D. Lucor. Stochastic investigation of flows about airfoils at transonic speeds. *AIAA J.*, 48(5):938–950, 2010.
- [70] J.-C. Chassaing and D. Lucor. Adaptive approaches for uncertainty quantification of airfoil LCO. International Forum on Aeroelasticity and Structural Dynamics, 26-30 June, Paris, France, 2011.
- [71] J.-C. Chassaing, D. Lucor, and J. Trégon. Stochastic nonlinear aeroelastic analysis of a supersonic lifting surface using an adaptive spectral method. *Journal of Sound and Vibration*, in press, 2011.
- [72] Qian-Yong Chen, David Gottlieb, and Jan S. Hesthaven. Uncertainty analysis for the steady-state flows in a dual throat nozzle. *Journal of Computational Physics*, 204(1):378 – 398, 2005.
- [73] Shikui Chen and Wei Chen. A new level-set based approach to shape and topology optimization under geometric uncertainty. *Structural and Multidisciplinary Optimization*, 44:1–18, 2011.
- [74] V. C. P. Chen, D. Ruppert, and C. A. Shoemaker. Applying experimental design and regression splines to high-dimensional continuous-state stochastic dynamic programming. *Operations Research*, 47(1):38–53, 1999.
- [75] S. Choi, R. V. Grandhi, R. A. Canfield, and C. L. Pettit. Polynomial chaos expansion with latin hypercube sampling for estimating response variability. *AIAA Journal*, 42(6):1191–1198, 2004.

- [76] A.J. Chorin. The numerical solution of the navier-stokes equations for an incompressible fluid. *Bull. Amer. Math. Soc.*, 73:928, 1967.
- [77] A.J. Chorin. Gaussian fields and random flow. *J. Fluid Mech.*, 85:325–347, 1974.
- [78] Mike Christie, Vasily Demyanov, and Demet Erbas. Uncertainty quantification for porous media flows. *Journal of Computational Physics*, 217(1):143 – 158, 2006. Uncertainty Quantification in Simulation Science.
- [79] H.-S. Chung and J. J. Alonson. Using gradients to construct cokriging approximation models for high-dimensional design optimization problems. In *40th AIAA Aerospace Sciences Meeting and Exhibit*, 2002.
- [80] C. Clark, T.T. & Zemach. Symmetries and the approach to statistical equilibrium in isotropic turbulence. *Phys. Fluids*, 10(11):2846–2858, 1998.
- [81] C. W. Clenshaw and A. R. Curtis. A method for numerical integration on an automatic computer. *Numer. Math.*, 2:197–205, 1960.
- [82] S.E. Cohn. An introduction to estimation theory. *J. Meteorol. Soc. Jpn.*, 75:257–288, 1997.
- [83] P. Comte, M. Lesieur, H. Laroche, and X. Normand. Numerical simulations of turbulent plane shear layers. In J.-C. André, J. Cousteix, F. Durst, B. E. Launder, F. W. Schmidt, and J. H. Whitelaw, editors, *Turbulent shear flows 6*, pages 361–380. Springer-Verlag, Berlin, 1989.
- [84] G. Comte-Bellot and S. Corrsin. The use of a contraction to improve the isotropy of grid-generated turbulence. *Journal of Fluid Mechanics*, 25:657 – 682, 1966.
- [85] P.M. Congedo, C. Corre, and J.-M. Martinez. Shape optimization of an airfoil in a bzt flow with multiple-source uncertainties. *Computer Methods in Applied Mechanics and Engineering*, 200(1-4):216 – 232, 2011.
- [86] Paul G. Constantine, Alireza Doostan, and Gianluca Iaccarino. A hybrid collocation/galerkin scheme for convective heat transfer problems with stochastic boundary conditions. *International Journal for Numerical Methods in Engineering*, 80(6-7):868–880, 2009.
- [87] G. M. Corcos and F. S. Sherman. Vorticity concentration and the dynamics of unstable free shear layers. *Journal of Fluid Mechanics*, 74:241, 1976.
- [88] N. Cressie. *Statistics for Spatial Data*. John Wiley & Sons, New York, NY, 1991.
- [89] Thierry Crestaux, Olivier Le Maître, and Jean-Marc Martinez. Polynomial chaos expansion for sensitivity analysis. *Reliability Engineering & System Safety*, 94(7):1161 – 1172, 2009. Special Issue on Sensitivity Analysis.
- [90] S.C. Crow and G.H. Canavan. Relationship between a wiener-hermite expansion and an energy cascade. *J. Fluid Mech.*, 41:387–403, 1970.
- [91] Sonjoy Das, Roger Ghanem, and James C. Spall. Asymptotic sampling distribution for polynomial chaos representation from data: A maximum entropy and fisher information approach. 30(5):2207–2234, 2008.
- [92] O. Dauchot and F. Daviaud. Streamwise vortex in plane Couette flow. *Physics of Fluids*, 7(5):901–903, 1995.
- [93] P. A. Davidson. *Turbulence. An introduction for scientists and engineers*. Oxford University Press, 2004.
- [94] R. W. Davis and E. F. Moore. A numerical study of vortex merging in mixing layers. *Physics of Fluids*, 28(6):1626–1635, 1985.
- [95] Goldberg D.E. *Genetic algorithms in search, optimization, and machine learning*. Addison-Wesley, 1989.
- [96] I. De Bruin. *Direct and Large-Eddy Simulation of the Spatial Turbulent Mixing Layer*. PhD thesis, University of Twente, Twente, the Netherlands, 2001.
- [97] M.K. Deb, I. Babuška, and J.T. Oden. Solution of stochastic partial differential equations using Galerkin finite element techniques. *Comput. Methods Appl. Mech. Engrg.*, 190:6359–6372, 2001.
- [98] Bert J. Debuschere, Habib N. Najm, Alain Matta, Omar M. Knio, Roger G. Ghanem, and Olivier P. Le Maître. Protein labeling reactions in electrochemical microchannel flow: Numerical simulation and uncertainty propagation. *Phys. Fluids*, 15(8):2238–2250, 2003.
- [99] Bert J. Debuschere, Habib N. Najm, Philippe P. Pébay, Omar M. Knio, Roger G. Ghanem, and Olivier P. Le Maître. Numerical Challenges in the Use of Polynomial Chaos Representations for Stochastic Processes. *J. Sci. Comp.*, 26:698–719, 2004.
- [100] S. Deck. Numerical simulation of transonic buffet over a supercritical airfoil. 43(11):1556–1566, 2005.
- [101] J. Delville, L. Ukeiley, L. Cordier, J. P. Bonnet, and M. Glauser. Examination of large-scale structures in a turbulent plane mixing layer. part 1. proper orthogonal decomposition. *Journal of Fluid Mechanics*, 391:91–122, 1999.
- [102] G. Deodatis. Weighted integral method. I: stochastic stiffness matrix. *J. Eng. Mech.*, 117(8):1851–1864, 1991.

- [103] G. Deodatis and M. Shinozuka. Weighted integral method. II: response variability and reliability. *J. Eng. Mech.*, 117(8):1865–1877, 1991.
- [104] Bruno Deprés. Propagation des incertitudes dans les lois de conservation. To appear, 2011.
- [105] A. Desai and S. Sarkar. Uncertainty quantification and bifurcation behavior of an aeroelastic system. ASME 2010, Paper FEDSM-ICNMM2010-30050, August 1-5, 2010 Montréal, Quebec, Canada, 2010.
- [106] C. Desceliers, R. Ghanem, and C. Soize. Maximum likelihood estimation of stochastic chaos representations from experimental data. *International Journal for Numerical Methods in Engineering*, 66(6):978–1001, 2006.
- [107] A. Doostan, R. Ghanem, and J. Red-Horse. Stochastic model reductions for chaos representations. *Computer Methods in Applied Mechanics and Engineering*, 196(37-40):3951–3966, 2007.
- [108] Alireza Doostan and Gianluca Iaccarino. A least-squares approximation of partial differential equations with high-dimensional random inputs. *Journal of Computational Physics*, 228(12):4332 – 4345, 2009.
- [109] F. Dubois and G. Mehlman. Nonparameterized entropy fix for roe’s method. *AIAA Journal*, 31(1):199–200, 1993.
- [110] B. Dubrulle and J.-P. Zahn. Nonlinear instability of viscous plane couette flow part 1. analytical approach to a necessary condition. *Journal of Fluid Mechanics*, 231:561–573, 1991.
- [111] L. Dumas. Inverse problems for blood flow simulations. In *EngOpt 2008 - International Conference on Engineering Optimization*. Rio de Janeiro, Brazil, 01-05 June 2008, 2008.
- [112] R. Duvigneau. Robust design of a transonic wing with uncertain mach number. In *EUROGEN 2007 Evolutionary Methods for Design, Optimization and Control, 11–13 June 2007, Jyväskylä, Finland*, 2007.
- [113] R. P. Dwight and Z.-H. Han. Efficient uncertainty quantification using gradient-enhanced Kriging. In *50th AIAA/ASME/ASCE/AHS/ASC Structures, Structural Dynamics, and Materials Conference*, Palm Springs, California, 2009.
- [114] B. Efron and C. Stein. The jackknife estimate of variance. *The Annals of Statistics*, 9(3):586–596, 1981.
- [115] C. Enaux. *Analyse Mathématique et Numérique d’un Modèle Multifluide Multivitesse pour l’Interpénétration de Fluides Miscibles*. Thèse de doctorat, École Centrale Paris, 2007.
- [116] O. Ernst, C. Powell, D. Silvester, and E. Ullmann. Efficient solvers for a linear stochastic galerkin mixed formulation of diffusion problems with random data. *SIAM J. Sci. Comput.*, 31(2):1424–1447, 2009.
- [117] C. Evangelinos, D. Lucor, and G.E. Karniadakis. DNS-derived force distribution on flexible cylinders subject to VIV. *Journal of Fluids and Structures*, 14(3):429, 2000.
- [118] C. Evangelinos, D. Lucor, C.-H. Su, and G.E. Karniadakis. Flow-induced vibrations of non-linear cables. Part 1: Models and algorithms. *International Journal for Numerical Methods in Engineering*, 55(5):535–556, 2002.
- [119] G. Evans. *Practical Numerical Integration*. John Wiley & Sons, Chichester, 1993.
- [120] G. Evensen. Sequential data assimilation with a nonlinear quasi-geostrophic model using monte carlo methods to forecast error statistics. *J. Geophys. Res.*, 99:10143–10162, 1994.
- [121] R. Eymard, T. Gallouet, and R. Herbin. *Finite Volume Methods, in Handbook of Numerical Analysis*, volume 7. P.G. Ciarlet, J. L. Lions eds, 2006.
- [122] T.D. Fadale and A.F. Emery. Transient effects of uncertainties on the sensitivities of temperatures and heat fluxes using stochastic finite elements. *J. Heat Trans.*, 116:808–814, 1994.
- [123] K. Fang, Run ze Li, and Agus Sudjianto. *Design and modeling for computer experiments*. Computer science and data analysis series. Chapman & Hall/CRC, 2006.
- [124] B. F. Farrell and P. J. Ioannou. Optimal perturbation of uncertain systems. *Stochastics and Dynamics*, 2(3):395–402, 2002.
- [125] Brian F. Farrell and Petros J. Ioannou. Stochastic forcing of the linearized navier–stokes equations. *Physics of Fluids A: Fluid Dynamics*, 5(11):2600–2609, 1993.
- [126] W. Feller. *An Introduction to Probability Theory and Its Applications*, volume 1 of *Probability and mathematical statistics*. Wiley, 3rd edition, 1971.
- [127] Scott Ferson, William L. Oberkampf, and Lev Ginzburg. Model validation and predictive capability for the thermal challenge problem. *Computer Methods in Applied Mechanics and Engineering*, 197(29-32):2408 – 2430, 2008. Validation Challenge Workshop.
- [128] R. Field. Numerical methods to estimate the coefficients of the Polynomial Chaos expansion. In *Proc. 15th ASCE Engineering Mechanics Division Conference*, New York, USA, 2002. Columbia University.
- [129] G.S. Fishman. *Monte Carlo: Concepts, Algorithms, and Applications*. Springer-Verlag, 1996.

- [130] J. Foo, X. Wan, and G.E. Karniadakis. The multi-element probabilistic collocation method: Error analysis and applications. *Journal of Computational Physics*, 227(22):9572–9595, 2008.
- [131] Jasmine Foo, Zohar Yosibash, and George Em Karniadakis. Stochastic simulation of riser-sections with uncertain measured pressure loads and/or uncertain material properties. *Computer Methods in Applied Mechanics and Engineering*, 196(41-44):4250 – 4271, 2007.
- [132] Alexander I.J Forrester, Neil W Bressloff, and Andy J Keane. Optimization using surrogate models and partially converged computational fluid dynamics simulations. *Proceedings of the Royal Society A: Mathematical, Physical and Engineering Science*, 462(2071):2177–2204, 2006.
- [133] Paul D Frank and Gregory R Shubin. A comparison of optimization-based approaches for a model computational aerodynamics design problem. *Journal of Computational Physics*, 98(1):74 – 89, 1992.
- [134] P. Frauenfelder, C. Schwab, and R.A. Todor. Finite elements for elliptic problems with stochastic coefficients. *Comput. Methods Appl. Mech. Engrg.*, 193:205–228, 2005.
- [135] P. Frauenfelder, C. Schwab, and R. A. Tudor. Finite elements for elliptic problems with stochastic coefficients. *Computer methods in applied mechanics and engineering*, 19:205–228, 2005.
- [136] Batt R. G. Some measurements on the effect of tripping the two-dimensional shear layer. *AIAA Paper*, 13:245–247, 1975.
- [137] D. Galbally, K. Fidkowski, K. Willcox, and O. Ghattas. Non-linear model reduction for uncertainty quantification in large-scale inverse problems. *International Journal for Numerical Methods in Engineering*, 81(12):1581–1608, 2010.
- [138] B. Ganapathysubramanian and N. Zabarar. Sparse grid collocation schemes for stochastic natural convection problems. *Journal of Computational Physics*, 225(1):652 – 685, 2007.
- [139] B. Ganapathysubramanian and N. Zabarar. A non-linear dimension reduction methodology for generating data-driven stochastic input models. *Journal of Computational Physics*, 227(13):6612 – 6637, 2008.
- [140] B. Ganapathysubramanian and N. Zabarar. A stochastic multiscale framework for modeling flow through random heterogeneous porous media. *Journal of Computational Physics*, 228(2):591 – 618, 2009.
- [141] V. E. Garzon. *Probabilistic Aerothermal Design of Compressor Airfoils*. PhD thesis, MIT, 2003.
- [142] Walter Gautschi. *Orthogonal Polynomials: Computation and Approximation*. Numerical Mathematics and Scientific Computation. Oxford University Press, 2004.
- [143] M. I. Gavarini, A. Bottaro, and F. T. M. Nieuwstadt. The initial stage of transition in pipe flow: role of optimal base-flow distortions. *Journal of Fluid Mechanics*, 517:131–165, 2004.
- [144] D. F. Gayme, B. J. McKeon, A. Papachristodoulou, B. Bamieh, and J. C. Doyle. A streamwise constant model of turbulence in plane couette flow. *Journal of Fluid Mechanics*, 665:99–119, 2010.
- [145] A. Gelb. *Applied Optimal Estimation*. MIT Press, 1975.
- [146] Alan E. Gelfand and Adrian F. M. Smith. Sampling-based approaches to calculating marginal densities. *Journal of the American Statistical Association*, 85(410):398–409, 1990.
- [147] J. B. Gelman, A. Carlin, H.S. Stern, and D.B. Rubin. *Bayesian data analysis*. Texts in statistical science. Chapman and Hall/CRC, 2nd edition, 2003.
- [148] Stuart Geman and Donald Geman. Stochastic relaxation, Gibbs distributions, and the Bayesian restoration of images. 6:721–741, 1984.
- [149] A. Genz and B. D. Keister. Fully symmetric interpolatory rules for multiple integrals over infinite regions with Gaussian weight. *Journal of Computational and Applied Mathematics*, 71(299-309), 1996.
- [150] W.K. George. The decay of homogeneous isotropic turbulence. *Phys. Fluids A*, 4(7):1492–1509, 1992.
- [151] G.A. Gerolymos, E. Sauret, and I. Vallet. Contribution to the single-point-closure reynolds-stress modelling of inhomogeneous flow. *Theor. Comput. Fluid Dyn.*, 17:407–431, 2004.
- [152] G.A. Gerolymos and I. Vallet. Wall-normal-free near-wall reynolds-stress closure for 3-d compressible separated flows. *AIAA Journal*, 39:1833–1842, 2001.
- [153] Marc Gerritsma, Jan-Bart van der Steen, Peter Vos, and George Karniadakis. Time-dependent generalized polynomial chaos. *Journal of Computational Physics*, 229(22):8333 – 8363, 2010.
- [154] T. Gerstner and M. Griebel. Numerical integration using sparse grids. *Numerical Algorithms*, 18(3):209–232, 1998.
- [155] T. Gerstner and M. Griebel. Dimension-Adaptative Tensor-Product Quadrature. *Computing*, 71(1):65–87, 2003.
- [156] B. J. Geurts and J. Fröhlich. A framework for predicting accuracy limitations in Large Eddy Simulations. *Physics of Fluids*, 14(6):L41–L44, June 2002.

- [157] R. Ghanem. Higher-order sensitivity of heat conduction problems to random data using the spectral stochastic finite element method. *Journal of Heat Transfer*, 121(2):290–299, 1999.
- [158] R. Ghanem and S. Dham. Stochastic finite element analysis for multiphase flow in heterogeneous porous media. *Transp. Porous Media*, 32:239–262, 1998.
- [159] R. Ghanem and D. Ghosh. Efficient characterization of the random eigenvalue problem in a polynomial chaos decomposition. *International Journal for Numerical Methods in Engineering*, 72(4):486–504, 2007.
- [160] R. G. Ghanem and P. Spanos. Spectral techniques for stochastic finite elements. *Arch. Comput. Methods Eng.*, 4:63–100, 1997.
- [161] R.G. Ghanem and R.M. Kruger. Numerical solution of spectral stochastic finite element systems. *Comput. Methods Appl. Mech. Engrg.*, 129:289–303, 1996.
- [162] R.G. Ghanem and P. Spanos. *Stochastic Finite Elements: a Spectral Approach (revised edition)*. Springer-Verlag, 2003.
- [163] Roger Ghanem. Probabilistic characterization of transport in heterogeneous media. *Computer Methods in Applied Mechanics and Engineering*, 158(3-4):199 – 220, 1998.
- [164] Roger G. Ghanem and Alireza Doostan. On the construction and analysis of stochastic models: Characterization and propagation of the errors associated with limited data. *Journal of Computational Physics*, 217(1):63 – 81, 2006.
- [165] Roger G. Ghanem, Alireza Doostan, and John Red-Horse. A probabilistic construction of model validation. *Computer Methods in Applied Mechanics and Engineering*, 197(29-32):2585 – 2595, 2008.
- [166] D. Ghiocel and R. Ghanem. Stochastic finite-element analysis of seismic soil-structure interaction. *ASCE Journal Engrg. Mech.*, 128(1):66–77, 2002.
- [167] Sandip Ghosal. An analysis of numerical errors in large-eddy simulations of turbulence. *Journal of Computational Physics*, 125:187–206, 1996.
- [168] D. Ghosh, R. Ghanem, and J. Red-Horse. Analysis of eigenvalues and modal interaction of stochastic systems. *AIAA J.*, 43(10):2196–2201, 2005.
- [169] Debraj Ghosh and Roger Ghanem. Stochastic convergence acceleration through basis enrichment of polynomial chaos expansions. *International Journal for Numerical Methods in Engineering*, 73(2):162–184, 2007.
- [170] A. Gil, J. Segura, and N. M. Temme. *Numerical methods for special functions*, chapter 5.3. SIAM, 2007.
- [171] W.R. Gilks, S. Richardson, and D.J. Spiegelhalter. *Markov Chain Monte Carlo in practice*. Chapman & Hall, 1995.
- [172] A. Girard. *Approximate methods for propagation of uncertainty with Gaussian Process models*. PhD thesis, University of Glasgow, 2004.
- [173] A. Girard, C. E. Rasmussen, J. Quinero-Candela, and R. Murray-Smith. Gaussian process priors with uncertain inputs – application to multiple-step ahead time series forecasting. In *Advances in neural information processing systems*, pages 529–536. MIT Press, 2003.
- [174] J. Glimm and D.H. Sharp. Prediction and the quantification of uncertainty. *Physica D*, 133:152–170, 1999.
- [175] E. Godlevski and P.A. Raviart. *Hyperbolic systems of conservation laws*. Ellipse, 1991. Paris.
- [176] David Gottlieb and Dongbin Xiu. Galerkin method for wave equations with uncertain coefficients. *Communications in Computational Physics*, 3(2):505–518, 2008.
- [177] M. Gunzburger. Sensitivities, adjoints, and flow optimization. *Int. J. Num. Meth. Fluids*, 31:53–78, 1999.
- [178] M. Hahn, D. Drikakis, D. L. Youngs, and R. J. R. Williams. Richtmyer-Meshkov turbulent mixing arising from an inclined material interface with realistic surface perturbations and reshocked flow. *Phys. of Fluids*, 23:046101, 2011.
- [179] Kenneth M. Hanson. A framework for assessing uncertainties in simulation predictions. *Physica D: Nonlinear Phenomena*, 133(1-4):179 – 188, 1999.
- [180] Ami Harten, Bjorn Engquist, Stanley Osher, and Sukumar R Chakravarthy. Uniformly high order accurate essentially non-oscillatory schemes, III. *Journal of Computational Physics*, 71(2):231 – 303, 1987.
- [181] T. Hastie, R. Tibshirani, and J. Friedman. *The elements of statistical learning: data mining, inference and prediction*. Statistics. Springer, 2nd edition, 2009.
- [182] M. Hegland. Adaptive sparse grids. *Proceedings of CTAC, Brisbane*, pages 16–18, 2001.
- [183] O. Heuzé, S. Jaouen, and H. Jourden. Dissipative Issue of High-Order Shock Capturing Schemes with Non-Convex Equations of State. *J. Comp. Phys.*, 228(3):833–860, 2009.

- [184] Tran Duong Hien and Michal Kleiber. Stochastic finite element modelling in linear transient heat transfer. *Computer Methods in Applied Mechanics and Engineering*, 144(1-2):111 – 124, 1997.
- [185] J. O. Hinze. *Turbulence*. McGraw-Hill Series in Mechanical Engineering, 1975.
- [186] C.-M. Ho and L. S. Huang. Subharmonics and vortex merging in mixing layers. *Journal of Fluid Mechanics*, 119:443–473, 1982.
- [187] C.-M. Ho and P. Huerre. Perturbed free shear layers. *Annual Review of Fluid Mechanics*, 16:365–424, 1984.
- [188] C.-M. Ho and Y.-Q. Zhang. On the manipulation of spreading rates of forced mixing layers. In *Proceedings of 3rd International Symposium on Turbulent Flows*, pages 75–81, UC Davis, 1981.
- [189] C.-M. Ho, Y. Zohar, J. K. Foss, and J. C. Buell. Phase decorrelation of coherent structures in a free shear layer. *Journal of Fluid Mechanics*, 230:319–337, 1991.
- [190] H. Holden, Oksendal, J. Uboe, and T. Zhang. *Stochastic partial differential equations: a modeling, white noise functional approach*. Birkhäuser Boston, 1996.
- [191] R. L. Holmes, G. Dimonte, B. Fryxell, M. L. Gittings, J. W. Grove, M. Schneider, D. H. Sharp, A. L. Velikovich, R. P. Weaver, and Q. Zhang. Richtmyer-Meshkov instability growth: experiment, simulation and theory. *J. Fluid Mech.*, 389:55–79, 1999.
- [192] T. Homma and A. Saltelli. Importance measures in global sensitivity analysis of nonlinear models. *Reliability Engineering and System Safety*, 52(1):1–17, 1996.
- [193] S. Hosder, R.W. Walters, and M. Balch. Efficient sampling for non-intrusive polynomial chaos applications with multiple uncertain input variables. AIAA Paper 2007–1939, 2007.
- [194] S. Hosder, R.W. Walters, and R. Perez. A non-intrusive polynomial chaos method for uncertainty propagation in cfd simulations. AIAA Paper 2006–891, 2006.
- [195] Thomas Y. Hou, Wuan Luo, Boris Rozovskii, and Hao-Min Zhou. Wiener chaos expansions and numerical solutions of randomly forced equations of fluid mechanics. *Journal of Computational Physics*, 216:687–706, 2006.
- [196] S. P. Huang, S. T. Quek, and K. K. Phoon. Convergence study of the truncated Karhunen-Loeve expansion for simulation of stochastic processes. *International Journal for Numerical Methods in Engineering*, 52(9):1029–1043, 2001.
- [197] L. Huyse and R.W. Walters. Random field solutions including boundary condition uncertainty for the steady-state generalized Burgers equation. Technical Report 2001-35, ICASE, 2001.
- [198] Gianluca Iaccarino, Rene Pecnik, James Glimm, and David Sharp. A QMU approach for characterizing the operability limits of air-breathing hypersonic vehicles. *Reliability Engineering & System Safety*, 96(9):1150 – 1160, 2011.
- [199] O. Inoue. Double-frequency forcing on spatially growing mixing layers. *Journal of Fluid Mechanics*, 234:553, 1992.
- [200] O. Inoue. Note on multiple-frequency forcing on mixing layers. *Fluid Dynamics Research*, 16:161–172, 1995.
- [201] T. Ishida, P. A. Davidson, and Y. Kaneda. On the decay of isotropic turbulence. *Journal of Fluid Mechanics*, 564:455 – 475, 2006.
- [202] C. Webster J. Burkardt, M.D. Gunzburger. Reduced order modeling of some nonlinear stochastic partial differential equations. *Int. J. Numer. Anal. Model.*, 4(3-4):368–391, 2007.
- [203] L. Jacquín, P. Molton, S. Deck, B. Maury, and D. Soulevant. An experimental study of shock oscillation over a transonic supercritical profile. In *AIAA Paper 2005-4902*, Toronto, Canada, 2005.
- [204] A. Jameson. Aerodynamic design via control theory. *Journal of Scientific Computing*, 3:233–260, 1988. 10.1007/BF01061285.
- [205] A. Jameson, L. Martinelli, and N.A. Pierce. Optimum aerodynamic design using the Navier–Stokes equations. *Theoretical and Computational Fluid Dynamics*, 10:213–237, 1998.
- [206] Rebekka Kopmann Jan Riehme and Uwe Naumann. Uncertainty quantification based on forward sensitivity analysis in sisyphé. In *ECCOMAS CFD 2010*, Lisbon, Portugal, 2010.
- [207] J. Janusevskis and R. Le Riche. Simultaneous kriging-based sampling for optimization and uncertainty propagation. Technical Report hal-00506957, 2010.
- [208] M. Jardak, C.-H. Su, and G.E. Karniadakis. Spectral polynomial chaos solutions of the stochastic advection equation. *J. Sci. Comput.*, 17:319–338, 2002.
- [209] E. Jaynes. Information theory and statistical mechanics. *Phys. Rev.*, 106:620–630, 1957.

- [210] Javier Jiménez and Robert D. Moser. Large-eddy simulations: where are we and what can we expect? *AIAA Journal*, 38(4):605–612, April 2000.
- [211] D. R. Jones, M. Schonlau, and W. J. Welch. Efficient global optimization of expensive black-box functions. *Journal of Global Optimization*, 13:455–492, 1998.
- [212] J.-C. Jouhaud, P. Sagaut, M. Montagnac, and J. Laurenceau. A surrogate-model based multidisciplinary shape optimization method with application to a 2d subsonic airfoil. *Computers & Fluids*, 36(3):520 – 529, 2007.
- [213] H. Jourdain and S. Del Pino. Arbitrary High-Order Schemes for the Linear Advection and Wave Equations: Application to Hydrodynamics and Aeroacoustics. *C.R. Acad. Sci. paris, Ser. I*, 342:441–446, 2006.
- [214] Chang-Yeol Jung. Evolution of probability distribution in time for solutions of hyperbolic equations. *Journal of Scientific Computing*, 41(1):13–48, 10 2009.
- [215] J. Kaipio and E. Somersalo. *Statistical and computational inverse problems*, volume 160 of *Applied Mathematical Sciences*. Springer, 2005.
- [216] K. Karhunen. Zur spektral theorie stochastischer prozesse. *Annales Academiae Scientiarum Fennicae*, 37, 1946.
- [217] G. E. Karniadakis, M. Israeli, , and S. A. Orszag. High-order splitting methods for the incompressible Naviers-Stokes equations. *Journal of Computational Physics*, 97:414–443, 1991.
- [218] G. E. Karniadakis and S. J. Sherwin. *Spectral/hp Element Methods for CFD*. Oxford University Press, New York, 2005.
- [219] G.E. Karniadakis and S.J. Sherwin. *Spectral/hp Element Methods for CFD*. Oxford University Press, 2nd edition, 2005.
- [220] George Em Karniadakis, Moshe Israeli, and Steven A Orszag. High-order splitting methods for the incompressible navier-stokes equations. *Journal of Computational Physics*, 97(2):414 – 443, 1991.
- [221] A. Keese. A review of recent developments in the numerical solution of stochastic partial differential equations (stochastic finite elements). Technical Report Informatikbericht Nr.: 2003-06, Technical University Braunschweig, Brunswick, Germany, 2003.
- [222] A. Keese and H. G. Matthies. Hierarchical parallelisation for the solution of stochastic finite element equations. *Computers & Structures*, 83(14):1033 – 1047, 2005.
- [223] Andreas Keese. *Numerical solution of systems with stochastic uncertainties: a general purpose framework for stochastic finite elements*. PhD thesis, Technische Universität Braunschweig, Mechanik-Zentrum, 2005.
- [224] R. E. Kelly. On the stability of an inviscid shear layer which is periodic in space and time. *Journal of Fluid Mechanics*, 27(4):657–689, 1967.
- [225] G. Khujadze, M. Oberlack, and G. Chagelishvili. Direct numerical simulation of stochastically forced laminar plane couette flow: Peculiarities of hydrodynamic fluctuations. *Phys. Rev. Lett.*, 97(3):034501, Jul 2006.
- [226] A. Khuri and J. Cornell. *Response Surfaces : Designs and Analyses*. Marcel Dekker, New York, 1987.
- [227] R. D. Kirkman and M. Metzger. Sensitivity analysis of low reynolds number channel flow using the finite volume method. *International Journal for Numerical Methods in Fluids*, 57(8):1023–1045, 2008.
- [228] M. Kleiber and T.D. Hien. *The stochastic finite element method*. John Wiley & Sons Ltd, 1992.
- [229] W. A. Klimke. *Uncertainty Modeling using Fuzzy Arithmetic and Sparse Grids*. Ph. d. thesis, Von der Fakultat Mathematik und physik der univeritat Stuttgart, 2005.
- [230] O. M. Knio and O. P. Le Maître. Uncertainty propagation in CFD using polynomial chaos decomposition. *Fluid Dynamics Research*, 38(9):616–640, 2006.
- [231] O. M. Knio, M. T. Reagan, H. N. Najm, and R.G. Ghanem. Uncertainty Quantification in Reacting Flow Simulations through Non-Intrusive Spectral Projection. *Combust. Flame*, 132:545–555, 2003.
- [232] J. Ko. *Application des Polynômes de Chaos à la Simulation d’Ecoulements Convectifs Incertains*. PhD thesis, Université Pierre et Marie Curie, Paris, France, 2009.
- [233] J. Ko, D. Lucor, and P. Sagaut. Uncertainty quantification of plane mixing layers using the polynomial chaos approach. 6th EUROMECH Fluid Mechanics Conference, KTH Mechanics, June 2006, Stockholm, Sweden, 2006.
- [234] J. Ko, D. Lucor, and P. Sagaut. Effect of base flow uncertainty on couette flow stability. 5th. European Congress on Computational Methods in Applied Sciences and Engineering, June 30-July 04 2008, Venice, Italy, 2008.

- [235] J. Ko, D. Lucor, and P. Sagaut. Sensitivity of two-dimensional mixing layer growth to the phase differences between the perturbation modes. Saskatoon, Canada, 2008. 16th Annual Conference of the CFD Society of Canada, June 2008.
- [236] J. Ko, D. Lucor, and P. Sagaut. Sensitivity of two-dimensional spatially developing mixing layers with respect to uncertain inflow conditions. *Physics of Fluids*, 20(7):077102–077120, 2008.
- [237] J. Ko, D. Lucor, and P. Sagaut. Effects of base flow uncertainty on couette flow stability. *Computers & Fluids*, 43(1):82 – 89, 2011.
- [238] A. N. Kolmogorov. On the degeneration of isotropic turbulence in an incompressible viscous fluid. *Dokl. Akad. Nauk. SSSR*, 31(6):538 – 541, 1941.
- [239] H. König. *Eigenvalue Distribution of Compact Operators*. Birkhäuser Verlag, 1986.
- [240] S. G. Krige. A statistical approach to some basic mine valuation problems on the witwatersrand. *J. Chem. Metal. and Mining Soc. of South Africa*, 52(6):119–139, 1951.
- [241] P. A. Krogstad, P.-Å. & Davidson. Is grid turbulence Saffman turbulence? *Journal of Fluid Mechanics*, 642:373 – 394, 2010.
- [242] A.S. Kronrod. Nodes and weights of quadrature formulas. *Consultants bureau*, MR 32 #597:Authorized translation from the Russian, 1965.
- [243] Jeffrey C. Lagarias, James A. Reeds, Margaret H. Wright, and Paul E. Wright. Convergence properties of the nelder–mead simplex method in low dimensions. *SIAM J. Optimization*, 9(1):112–147, 1998.
- [244] Pui-Man Lam and Diola Bagayoko. Spatiotemporal correlation of colored noise. *Phys. Rev. E*, 48(5):3267–3270, Nov 1993.
- [245] D.P. Laurie. Calculation of gauss-kronrod quadrature rules. *Mathematics of Computation*, 66:1133–1145, 1997.
- [246] P. Lavoie and R. A. Djenedi, L. & Antonia. Effects of initial conditions in decaying turbulence generated by passive grids. *Journal of Fluid Mechanics*, 585:395 – 420, 2007.
- [247] O. Le Maitre, O. Knio, H. Najm, and R. Ghanem. A stochastic projection method for fluid flow. i. basic formulation. *J. Comput. Phys.*, 173:481–511, 2001.
- [248] O. Le Maitre, O. Knio, H. Najm, and R. Ghanem. Uncertainty propagation using Wiener-Haar expansions. *J. Comput. Phys.*, 197:28–57, 2004.
- [249] O. Le Maitre, M. Reagan, H. Najm, R. Ghanem, and O. Knio. A stochastic projection method for fluid flow. ii. random process. *J. Comput. Phys.*, 181:9–44, 2002.
- [250] O. P. Le Maître and Omar M. Knio. *Spectral Methods for Uncertainty Quantification with applications to Computational Fluid Dynamics*. Scientific Computation. Springer Netherlands, 2010.
- [251] J. Le Meitour, D. Lucor, and J.-C. Chassaing. Adaptive piecewise polynomial chaos approaches: application to nonlinear aeroelastic flutter. In *ASME 2010 3rd Joint US-European Fluids Engineering Summer Meeting: Volume 1, Symposia – Parts A, B, and C*, number FEDSM-ICNMM2010-31292, pages 2957–2968. August 1-5 2010, Montreal, Canada, 2010.
- [252] B.H.K. Lee, S.J. Price, and Y.S. Wong. Nonlinear aeroelastic analysis of airfoils : bifurcation and chaos. *Progress in Aerospace Sciences*, 35:205–334, 1999.
- [253] E. Leinov, G. Malamud, Y. Elbaz, L.A. Levin, G. Ben-Dor, D. Shvarts, and O. Sadot. Experimental and Numerical Investigation of the Richtmyer-Meshkov Instability under Re-Shock Conditions. *J. Fluid Mech.*, 626:449–475, 2009.
- [254] J. Lerner and E. Knobloch. The long-wave instability of a defect in a uniform parallel shear. *Journal of Fluid Mechanics*, 189:117–134, 1988.
- [255] A. Levy and J. Rubinstein. Some properties of smoothed principal component analysis for functional data. *Journal of the Optical Society of America*, 16(1):28–35, 1999.
- [256] R. M. Lewis. Using sensitivity information in the construction of kriging models for design optimization. *AIAA Journal*, 28(4799):730–737, 1998.
- [257] J. Li and D. Xiu. A generalized polynomial chaos based ensemble kalman filter with high accuracy. *Journal of Computational Physics*, 228:5454–5469, 2009.
- [258] R. Li and R. Ghanem. Adaptive polynomial chaos expansions applied to statistics of extremes in nonlinear random vibration. *Prob. Engng. Mech.*, 13(2):125–136, 1998.
- [259] L. Librescu, G. Chiochia, and P. Marzocca. Implications of cubic physical/aerodynamic non-linearities on the character of the flutter instability boundary. *International Journal of Non-Linear Mechanics*, 38:173–199, 2003.

- [260] G. Lin, C.-H. Su, and G. E. Karniadakis. The Stochastic Piston Problem. *PNAS*, 101(45):15840–15845, 2004.
- [261] G. Lin, C.-H. Su, and G.E. Karniadakis. Stochastic Modeling of Random Roughness in Shock Scattering Problems: Theory and Simulations. *Comp. Meth. Appl. Mech. Engrg.*, 2008.
- [262] G. Lin, S.-H. Su, and G.E. Karniadakis. Predicting shock dynamics in the presence of uncertainties. *Journal of Computational Physics*, 217:260–276, 2006.
- [263] G. Lin and A. Tartakovsky. Numerical studies of three-dimensional stochastic darcy’s equation and stochastic advection-diffusion-dispersion equation. *Journal of Scientific Computing*, 43:92–117, 2010. 10.1007/s10915-010-9346-5.
- [264] Guang Lin, Chau-Hsing Su, and George Em Karniadakis. Random roughness enhances lift in supersonic flow. *Phys. Rev. Lett.*, 99(10):104501, Sep 2007.
- [265] J. S. Liu. *Monte Carlo Strategies in Scientific Computing*. Statistics. Springer, 2001.
- [266] L. Liu and E.H. Dowell. The secondary bifurcation of an aeroelastic airfoil motion: effect of high harmonics. *Nonlinear Dynamics*, 37:31–49, 2005.
- [267] P.-L. Liu and A. Der Kiureghian. Finite element reliability of geometrically nonlinear uncertain structures. *J. Eng. Mech.*, 117:1806–1825, 1991.
- [268] W.K. Liu, T. Belytschko, and A. Mani. Probabilistic finite elements for nonlinear structural dynamics. *Comput. Methods Appl. Mech. Engrg.*, 56:61–81, 1986.
- [269] M. Loève. *Probability Theory, Fourth edition*. Springer-Verlag, 1977.
- [270] G.J. Loeven, J.A.S. Witteven, and H. Bijl. Probabilistic collocation: an efficient non-intrusive approach for arbitrarily distributed parametric uncertainties. AIAA Paper 2007–317, 2007.
- [271] P. S. Lowery and W. C. Reynolds. Numerical simulation of a spatially-developing, forced, plane mixing layer. Technical Report Report TF-26, Mechanical Engineering Department, Stanford University, 1986.
- [272] Z. Lu and D. Zhang. A comparative study on uncertainty quantification for flow in randomly heterogeneous media using monte carlo simulations and conventional and KL-based moment-equation approaches. *SIAM J. Sci. Comput.*, 26(2):558–577, 2004.
- [273] P. Luchini. Reynolds-number-independent instability of the boundary layer over a flat surface: optimal perturbations. *Journal of Fluid Mechanics*, 404:289–309, 2000.
- [274] D. Lucor. *Generalized Polynomial Chaos: Applications to Random Oscillators and Flow-Structure Interactions*. PhD thesis, Brown University, RI, USA, 2004.
- [275] D. Lucor, C. Enaux, H. Jourdain, and P. Sagaut. Stochastic design optimization: Application to reacting flows and detonation. *Comp. Meth. Appl. Mech. Eng.*, 196(49-52):5047–5062, 2007.
- [276] D. Lucor, L. Imas, and G.E. Karniadakis. Vortex dislocations and force distribution of long flexible cylinders subjected to sheared flows. *Journal of Fluids and Structures*, 15(3-4):641–650, 2001.
- [277] D. Lucor and G.E. Karniadakis. Stochastic Flow-Structure Interactions. In K.J. Bathe, editor, *Computational Fluid and Solid Mechanics*, volume 1-2, pages 1426–1429. 2nd MIT Conference, Cambridge, MA, USA, June 17-20, 2003, Elsevier Press, 2003.
- [278] D. Lucor and G.E. Karniadakis. Adaptive generalized polynomial chaos for nonlinear random oscillators. *SIAM J. Sci. Comput.*, 26(2):720–735, 2004.
- [279] D. Lucor and G.E. Karniadakis. Noisy inflows cause a shedding-mode switching in flow past an oscillating cylinder. *Phys. Rev. Lett.*, 92(15):154501–1; 154501–4, 2004.
- [280] D. Lucor and G.E. Karniadakis. Predictability and uncertainty in flow-structure interactions. *European Journal of Mechanics / B Fluids*, 23(1):41–49, 2004.
- [281] D. Lucor, J. Meyers, and P. Sagaut. Sensitivity analysis of LES to subgrid-scale-model parametric uncertainty using Polynomial Chaos. *Journal of Fluid Mechanics*, 585:255–279, 2007.
- [282] D. Lucor, C.-H. Su, and G.E. Karniadakis. Generalized polynomial chaos and random oscillators. *Int. J. Numer. Meth. Engrg.*, 60(3):571–596, 2004.
- [283] D. Lucor and M.S. Triantafyllou. Parametric study of a two degree-of-freedom cylinder subject to vortex-induced vibrations. *Journal of Fluids and Structures*, 24(8):1284 – 1293, 2008. Unsteady Separated Flows and their Control.
- [284] D. Lucor, D. Xiu, Su. C.-H., and G. E. Karniadakis. Predictability and uncertainty in CFD. *International Journal for Numerical Methods in Fluids*, 43:483–505, 2003.
- [285] D. Lucor, D. Xiu, and G.E. Karniadakis. Spectral representations of uncertainty in simulations: Algorithms and applications. In *Proceedings of the Fifth International Conference on Spectral and High Order Methods*, volume 17. ICOSAHOM-01, June 11-15 2001, Uppsala, Sweden, 2002.

- [286] D. Lucor, D. Xiu, C.-H. Su, and G.E. Karniadakis. Predictability and uncertainty in CFD. *Int. J. Numer. Methods Fluids*, 43(5):483–505, 2003.
- [287] John L. Lumley. *Stochastic tools in turbulence*. Academic Press, New York., 1970.
- [288] Xiang Ma and Nicholas Zabarar. A stabilized stochastic finite element second-order projection method for modeling natural convection in random porous media. *Journal of Computational Physics*, 227(18):8448 – 8471, 2008.
- [289] Xiang Ma and Nicholas Zabarar. An adaptive hierarchical sparse grid collocation algorithm for the solution of stochastic differential equations. *Journal of Computational Physics*, 228(8):3084 – 3113, 2009.
- [290] O. Le Maître. A newton method for the resolution of steady stochastic navier-stokes equations. *Computers & Fluids*, 38(8):1566–1579, 2009.
- [291] Olivier Le Maître, M. T. Reagan, B. Debusschere, H. N. Najm, R. G. Ghanem, and O. M. Knio. Natural convection in a closed cavity under stochastic non-boussinesq conditions. *SIAM J. Sci. Comput.*, 26(2):375–394, 2004.
- [292] O.P. Le Maître, O.M. Knio, B.J. Debusschere, H.N. Najm, and R.G. Ghanem. A multigrid solver for two-dimensional stochastic diffusion equations. *Computer Methods in Applied Mechanics and Engineering*, 192(41-42):4723 – 4744, 2003.
- [293] M. Martinelli. *Sensitivity Evaluation in Aerodynamic Optimal Design*. PhD thesis, Université de Nice - Sophia Antipolis, 2007.
- [294] Youssef Marzouk and Dongbin Xiu. A stochastic collocation approach to Bayesian inference in inverse problems. *Communications in Computational Physics*, 6(4):826–847, 2009.
- [295] Youssef M. Marzouk and Habib N. Najm. Dimensionality Reduction and Polynomial Chaos Acceleration of Bayesian Inference in Inverse Problems. *J. Comp. Phys.*, 228(6):1862–1902, 2009.
- [296] Youssef M. Marzouk, Habib N. Najm, and Larry A. Rahn. Stochastic Spectral Methods for Efficient Bayesian Solution of Inverse Problems. *J. Comp. Phys.*, 224(2):560–586, 2007.
- [297] L. Mathelin and M.Y. Hussaini. A stochastic collocation algorithm for uncertainty analysis. Technical Report NASA/CR-2003-212153, NASA Langley Research Center, 2003.
- [298] L. Mathelin, M.Y. Hussaini, and T.A. Zang. Stochastic approaches to uncertainty quantification in CFD simulations. *Numer. Algo.*, 38:209–236, 2005.
- [299] L. Mathelin and O. P. Le Maître. A Posteriori Error Analysis for Stochastic Finite Element Solutions of Fluid Flows with Parametric Uncertainties. *ECCOMAS CFD*, 2006.
- [300] H. Matthies and A. Keese. Galerkin methods for linear and nonlinear elliptic stochastic partial differential equations. *Comput. Meth. Appl. Mech. Eng.*, 192(12-16):1295–1331, 2005.
- [301] H.G. Matthies. Computational aspects of probability in non-linear mechanics. Technical report, Institute of Scientific Computing, TU Braunschweig, Brunswick, Germany, 2003.
- [302] H.G. Matthies and C. Bucher. Finite elements for stochastic media problems. *Comput. Methods Appl. Mech. Engrg.*, 168:3–17, 1999.
- [303] H.G. Matthies and A. Keese. Multilevel solvers for the analysis of stochastic system. In K.J. Bathe, editor, *Computational Fluid and Solid Mechanics*, volume 2, pages 1620–1622. 1st MIT Conference, Cambridge, MA, USA, June 12-15, 2001, Elsevier Press, 2001.
- [304] W. D. McComb, A. Hunter, and C. Johnston. Conditional mode elimination and the subgrid modeling problem for isotropic turbulence. *Phys. Fluids*, 13(7):2030–2044, 2001.
- [305] Dale B. McDonald, Walter J. Grantham, Wayne L. Tabor, and Michael J. Murphy. Global and local optimization using radial basis function response surface models. *Applied Mathematical Modelling*, 31(10):2095 – 2110, 2007.
- [306] M. McKay, W. Conover, and R. Beckman. A comparison of three methods for selecting values of input variables in the analysis of output from a computer code. *Technometrics*, 21:239–245, 1979.
- [307] W. A. McMullan, S. Gao, and C. M. Coats. A comparative study of inflow conditions for two- and three-dimensional spatially developing mixing layers using large eddy simulation. *International Journal for Numerical Methods in Fluids*, 55(6):589–610, 2007.
- [308] L. R. Mead and N. Papanicolaou. Maximum Entropy in the Problem of Moments. *J. Math. Phys.*, 25(8), 1984.
- [309] W.C. Meecham and D.T. Jeng. Use of the wiener-hermite expansion for nearly normal turbulence. *J. Fluid Mech.*, 32:225–249, 1968.
- [310] W.C. Meecham and A. Siegel. Wiener-hermite expansion in model turbulence at large reynolds numbers. *Phys. Fluids*, 7:1178–1190, 1964.

- [311] U. B. Mehta. Some aspects of uncertainty in computational fluid dynamics results. *Journal of Fluids Engineering*, 113(4):538–543, 1991.
- [312] J. Le Meitour, D. Lucor, and J.-C. Chassaing. Stochastic aeroelastic analysis of a pitching and plunging airfoil in an incompressible flow. International Forum on Aeroelasticity and Structural Dynamics, June 21-25 2009, Seattle, WA, USA, 2009.
- [313] J. Le Meitour, D. Lucor, and J.-C. Chassaing. Prediction of stochastic limit cycle oscillations using an adaptive polynomial chaos method. *Aeroelasticity and Structural Dynamics Journal*, 2:3–22, 2010.
- [314] M. Meldi. *Quantification of the effects of uncertainties in turbulent flows: towards the assessment of LES results for industrial applications*. PhD thesis, DIMeC, Università degli studi di Modena e Reggio Emilia, Modena, Italy, 2011.
- [315] M. Meldi, D. Lucor, and P. Sagaut. Is the Smagorinsky coefficient sensitive to uncertainty in the form of the energy spectrum? *Phys. Fluids*, accepted, 2011.
- [316] M. Meldi, P. Sagaut, and D. Lucor. A stochastic view of isotropic turbulence decay. *Journal of Fluid Mechanics*, 668:351–362, 2011.
- [317] C. Meneveau. Statistics of turbulence subgrid-scale stresses: Necessary conditions and experimental tests. *Physics of Fluids*, 6(2):815–833, 1994.
- [318] R. W. Metcalfe, S. A. Orszag, M. E. Brachet, S. Menon, and J. J. Riley. Secondary instability of a temporally growing mixing layer. *Journal of Fluid Mechanics*, 184:207–243, 1987.
- [319] N. Metropolis, A. W. Rosenbluth, M. N. Rosenbluth, A. H. Teller, and E. Teller. Equation of state calculations by fast computing machines. *J. Chem. Phys.*, 21:1087–1092, 1953.
- [320] M. Meyer and H.G. Matthies. Efficient model reduction in non-linear dynamics using the Karhunen-Loève expansion and dual-weighted-residual methods. *Comp. Meth. Appl. Mech. Eng.*, Informatikbericht 2003-08, TU Braunschweig, Germany, 2004.
- [321] J. Meyers and P. Sagaut. On the model coefficients for the standard and the variational multi-scale Smagorinsky model. *Journal of Fluid Mechanics*, 569:287–319, 2006.
- [322] Johan Meyers, Bernard J. Geurts, and Martine Baelmans. Database-analysis of errors in large-eddy simulation. *Physics of Fluids*, 15(9):2740–2755, September 2003.
- [323] Johan Meyers and Charles Meneveau. A functional form for the energy spectrum parametrizing bottleneck and intermittency effects. *Phys. Fluids*, 20(6):065109, 2008.
- [324] A. Michalke. On the inviscid instability of the hyperbolic-tangent velocity profile. *Journal of Fluid Mechanics*, 19(4):543–556, 1964.
- [325] A. Michalke. On spatially growing disturbances in an inviscid shear layer. *Journal of Fluid Mechanics*, 23(3):521–544, 1965.
- [326] R. Mikulevicius and B. Rozovskii. Linear parabolic stochastic PDEs and Wiener chaos. *SIAM J. Math. Anal.*, 29:452–480, March 1998.
- [327] R. Mikulevicius and B. L. Rozovskii. Stochastic Navier–Stokes equations for turbulent flows. 35(5):1250–1310, 2004.
- [328] D.R. Millman. Quantifying initial conditions and parametric uncertainties in a nonlinear aeroelastic system with an efficient stochastic algorithm. Technical report, PhD. Dissertation, Air Force Institute of Technology, september 2004.
- [329] D.R. Millman, P.I. King, and P.S. Beran. A stochastic approach for predicting bifurcation of a pitch and plunge airfoil. AIAA Paper 2003-3515, 2003.
- [330] D.R. Millman, P.I. King, and P.S. Beran. Airfoil pitch-and-plunge bifurcation behavior with Fourier chaos expansions. *Journal of Aircraft*, 42(2):376–384, 2005.
- [331] D.R. Millman, P.I. King, R.C. Maple, and P.S. Beran. Predicting uncertainty propagation in a highly nonlinear system with a stochastic projection method. AIAA Paper 2004-1613, 2004.
- [332] J. C. Mohamed, M. S. & LaRue. The decay power law in grid-generated turbulence. *Journal of Fluid Mechanics*, 219:195 – 214, 1990.
- [333] P. Surya Mohan, Prasanth B. Nair, and Andy J. Keane. Stochastic projection schemes for deterministic linear elliptic partial differential equations on random domains. *International Journal for Numerical Methods in Engineering*, 85(7):874–895, 2011.
- [334] P. A. Monkewitz and P. Huerre. Influence of the velocity ratio on the spatial instability of mixing layers. *Physics of Fluids*, 25(7):1137–1143, July 1982.
- [335] William J. Morokoff and Russel E. Caflisch. Quasi-monte carlo integration. *Journal of Computational Physics*, 122(2):218 – 230, 1995.

- [336] I. Müller and T. Ruggeri. *Rational Extended thermodynamics, 2nd ed.* Springer. Tracts in Natural Philosophy, Volume 37, 1998. Springer-Verlag, New York.
- [337] T. Müller-Gronbach. Hyperbolic cross designs for approximation of random fields. *J. Statist. Planning Inf.*, 49:371–385, 1997.
- [338] R. H. Myers, D. C. Montgomery, and C. M. Anderson-Cook. *Response Surface Methodology: Process and Product Optimization Using Designed Experiments.* Probability and statistics. John Wiley and Sons, New York, 3rd edition, 2009.
- [339] P. Nair and A. Keane. Stochastic reduced basis methods. *AIAA J.*, 40:1653–1664, 2002.
- [340] H. N. Najm, B. J. Debusschere, Y. M. Marzouk, S. Widmer, and O. P. Le Maître. Uncertainty quantification in chemical systems. *International Journal for Numerical Methods in Engineering*, 80(6-7):789–814, 2009.
- [341] Habib N. Najm. Uncertainty quantification and polynomial chaos techniques in computational fluid dynamics. *Annual Review of Fluid Mechanics*, 41(1):35–52, 2009.
- [342] J.C. Newman, P.A. Newman, A.C. Taylor, and G.J.-W. Hou. Efficient nonlinear static aeroelastic wing analysis. *Computers and Fluids*, 28:615–628, 1999.
- [343] James C. Newman III, Arthur C. Taylor III, Richard W. Barnwell, Perry A. Newman, and Gene J.-W. Hou. Overview of sensitivity analysis and shape optimization for complex aerodynamic configurations. *Journal of Aircraft*, 36(1):87–96, 1999.
- [344] H. Niederreiter. *Random Number Generation and Quasi-Monte Carlo Methods.* SIAM: Philadelphia, PA, USA, 1992.
- [345] F. Nobile, R. Tempone, and C. Webster. A Sparse Grid Stochastic Collocation Method for Partial Differential Equations with Random Input Data. *SIAM J. Numer. Anal.*, 46(5):2309–2345, 2008.
- [346] F. Nobile, R. Tempone, and C. G. Webster. An anisotropic sparse grid stochastic collocation method for partial differential equations with random input data. *SIAM J. Numer. Anal.*, 46(5):2411–2442, 2008.
- [347] A. Nouy. Recent developments in spectral stochastic methods for the numerical solution of stochastic partial differential equations. *Archives of Computational Methods in Engineering*, 16(3):251–285, 2009.
- [348] A. Nouy and A. Clément. extended stochastic finite element method for the numerical simulation of heterogeneous materials with random material interfaces. *International Journal for Numerical Methods in Engineering*, 83(10):1312–1344, 2010.
- [349] Anthony Nouy. Generalized spectral decomposition method for solving stochastic finite element equations: Invariant subspace problem and dedicated algorithms. *Computer Methods in Applied Mechanics and Engineering*, 197(51-52):4718 – 4736, 2008.
- [350] Anthony Nouy. A priori model reduction through proper generalized decomposition for solving time-dependent partial differential equations. *Computer Methods in Applied Mechanics and Engineering*, 199(23-24):1603 – 1626, 2010.
- [351] Erich Novak and Klaus Ritter. Simple cubature formulas with high polynomial exactness. *Constructive Approximation*, 15:499–522, 1999.
- [352] Jeremy Oakley. Estimating percentiles of uncertain computer code outputs. *Journal of the Royal Statistical Society: Series C (Applied Statistics)*, 53(1):83–93, 2004.
- [353] W. L. Oberkampf and C. J. Roy. *Verification and Validation in Scientific Computing.* Cambridge University Press, 2010.
- [354] W.L. Oberkampf and M. F. Barone. Measures of agreement between computation and experiment: validation metrics. Technical Report SAND2005-4302, Sandia National Laboratories, 2005.
- [355] W.L. Oberkampf and T.G. Trucano. Validation Methodology in Computational Fluid Dynamics. Technical Report AIAA 2000-2549, Sandia National Laboratories, Albuquerque, New Mexico, 2000.
- [356] M. Oberlack. On the decay exponent of isotropic turbulence. *Proc. Appl. Math. Mech.*, 1(1):294–297, 2002.
- [357] H. Ogura. Orthogonal functionals of the Poisson process. *IEEE Trans. Info. Theory*, IT-18:473–481, 1972.
- [358] B. Oksendal. *Stochastic differential equations. An introduction with applications.* Springer-Verlag, fifth edition, 1998.
- [359] M. J. L. Orr. Recent advances in Radial Basis Function networks. Technical report, Institute for Adaptive and Neural Computation, Edinburgh, Scotland, UK, 1999.
- [360] S.A. Orszag and L.R. Bissonnette. Dynamical properties of truncated Wiener-Hermite expansions. *Phys. Fluids*, 10:2603, 1967.

- [361] D. Oster and I. Wygnanski. The forced mixing layer between parallel streams. *Journal of Fluid Mechanics*, 123:91–130, 1982.
- [362] A. Owen. A Central Limite Theorem for Latin Hypercube Sampling. *Journal of the Royal Statistical Society: Series B*, 54:541–551, 1992.
- [363] R. Palacios and C.E.S. Cesnik. Static nonlinear aeroelasticity of flexible slender wings in compressible flow. AIAA Paper 2005–1945, 2005.
- [364] L. Parussini, V. Pediroda, and S. Obayashi. Efficient nonlinear static aeroelastic wing analysis. *JSME International Journal, Series B*, 48(2):218–223, 2005.
- [365] Lucia Parussini, Valentino Pediroda, and Carlo Poloni. Prediction of geometric uncertainty effects on fluid dynamics by polynomial chaos and fictitious domain method. *Computers & Fluids*, 39(1):137 – 151, 2010.
- [366] P. C. Patnaik, F. S. Sherman, and G. M. Corcos. A numerical simulation of Kelvin-Helmholtz wave of finite amplitude. *Journal of Fluid Mechanics*, 73(2):215–240, 1976.
- [367] T.N.L. Patterson. The optimum addition of points to quadrature formulae. *Math. Comput.*, 22:847–856, 1968.
- [368] M. F. Pellissetti and R. G. Ghanem. Iterative solution of systems of linear equations arising in the context of stochastic finite elements. *Adv. Engrg. Software*, 31:607–616, 1999.
- [369] Jacques E.V. Peter and Richard P. Dwight. Numerical sensitivity analysis for aerodynamic optimization: A survey of approaches. *Computers & Fluids*, 39(3):373 – 391, 2010.
- [370] K. Petras. On the Smolyak cubature error for analytic functions. *Advances in Computational Mathematics*, 12:7193, 2000.
- [371] K. Petras. Smolyak cubature of given polynomial degree with few nodes for increasing dimension. *Numerische Mathematik*, 93:729–753, 2003.
- [372] Per Pettersson, Gianluca Iaccarino, and Jan Nordström. Numerical analysis of the Burgers’ equation in the presence of uncertainty. *Journal of Computational Physics*, 228(22):8394 – 8412, 2009.
- [373] Per Pettersson, Jan Nordström, and Gianluca Iaccarino. Boundary procedures for the time-dependent Burgers’ equation under uncertainty. *Acta Mathematica Scientia*, 30B(2):539–550, 2010.
- [374] C.L. Pettit. Uncertainty quantification in aeroelasticity: recent results and research challenges. *Journal of Aircraft*, 41(5):1217–1229, 2003.
- [375] C.L. Pettit. Uncertainty quantification in aeroelasticity: recent results and research challenges. *Journal of Aircraft*, 41(5):1217–1229, 2003.
- [376] C.L. Pettit and P.S. Beran. Polynomial chaos expansion applied to airfoil limit cycle oscillations. AIAA Paper 2004-1691, 2004.
- [377] C.L. Pettit and P.S. Beran. Spectral and multiresolution Wiener expansions of oscillatory stochastic processes. *Journal of Sound and Vibration*, 294(4-5):752 – 779, 2006.
- [378] Brian D. Phenix, Joanna L. Dinero, Menner A. Tatang, Jefferson W. Tester, Jack B. Howard, and Gregory J. McRae. Incorporation of parametric uncertainty into complex kinetic mechanisms: Application to hydrogen oxidation in supercritical water. *Combustion and Flame*, 112(1-2):132 – 146, 1998.
- [379] K. K. Phoon, S. P. Huang, and S. T. Quek. Implementation of Karhunen-Loeve expansion for simulation using a wavelet-Galerkin scheme. *Probabilistic Engineering Mechanics*, 17:293–303, 2002.
- [380] K.K. Phoon, H.W. Huang, and S.T. Quek. Simulation of strongly non-gaussian processes using karhunen-loeve expansion. *Probabilistic Engineering Mechanics*, 20(2):188 – 198, 2005.
- [381] O. Pironneau. On optimum design in fluid mechanics. *Journal of Fluid Mechanics*, 64(01):97–110, 1974.
- [382] G. Poëtte. *Propagation d’Incertitudes pour les Systèmes de Lois de Conservation, Méthodes Spectrales Stochastiques*. Phd thesis, Université Pierre et Marie Curie, Institut Jean Le Rond D’Alembert, 2009.
- [383] G. Poëtte, B. Després, and D. Lucor. Uncertainty quantification and propagation for systems of conservation laws. 5th. European Congress on Computational Methods in Applied Sciences and Engineering, June 30-July 04 2008, Venice, Italy, 2008.
- [384] G. Poëtte, B. Després, and D. Lucor. Uncertainty quantification for systems of conservation laws. *Journal of Computational Physics*, 228(7):2443–2467, 2009.
- [385] G. Poëtte, B. Després, and D. Lucor. Adaptive hybrid spectral methods for stochastic systems of conservation laws. In A. Sequeira J. C. F. Pereira and J. M. C. Pereira, editors, *ECCOMAS CFD 2010 Proceedings of the V European Conference on Computational Fluid Dynamics*, Lisbon, Portugal, 2010.
- [386] G. Poëtte, B. Després, and D. Lucor. Treatment of uncertain interfaces in compressible flows. *Comp. Meth. Appl. Math. Engrg.*, 200(1-4):284–308, 2011.

- [387] G. Poëtte, B. Després, and D. Lucor. Uncertainty Propagation for Systems of Conservation Laws, High-Order Stochastic Spectral Methods. In Jan S. Hesthaven and Einar M. Rønquist, editors, *Spectral and High Order Methods for Partial Differential Equations*, Lecture Notes in Computational Science and Engineering, pages 293–307. ICOSAHOM '09 conference, June 22–26 2009, Trondheim, Norway, 2011.
- [388] G. Poëtte and D. Lucor. Iterative galerkin-based spectral projection method with application to compressible gas dynamics. *Journal of Computational Physics*, submitted, 2011.
- [389] G. Poëtte, D. Lucor, and B. Després. A numerical method for uncertain compressible flows. In *ASME 2010 3rd Joint US-European Fluids Engineering Summer Meeting: Volume 1, Symposia – Parts A, B, and C*, number FEDSM-ICNMM2010-30939, pages 2923–2939. August 1–5 2010, Montreal, Canada, 2010.
- [390] Poggi, Thorembey, and Rodriguez. Velocity Measurements in turbulent gaseous mixtures induced by Richtmyer-Meshkov instability. *Physics of Fluids*, 10:11, 1998.
- [391] Stephen B. Pope. *Turbulent Flows*. Cambridge University Press, 2000.
- [392] M. J. D. Powell. *Radial basis functions for multivariable interpolation: a review*, pages 143–167. Clarendon Press, New York, NY, USA, 1987.
- [393] Michele M. Putko, Arthur C. Taylor, Perry A. Newman, and Lawrence L. Green. Approach for input uncertainty propagation and robust design in cfd using sensitivity derivatives. *Journal of Fluids Engineering*, 124(1):60–69, 2002.
- [394] Herschel Rabitz, Ömer F. Alis, Jeffrey Shorter, and Kyurhee Shim. Efficient input–output model representations. *Computer Physics Communications*, 117(1–2):11 – 20, 1999.
- [395] V.M. Rao, A. Behal, P. Marzocca, and C.M. Rubillo. Adaptive aeroelastic vibration suppression of a supersonic airfoil with flap. 10:309–315, 2006.
- [396] C. E. Rasmussen and C. K. I. Williams. *Gaussian Processes for Machine Learning*. The MIT Press, 2006.
- [397] M T Reagan, H N Najm, B J Debusschere, O P Le Maître, O M Knio, and R G Ghanem. Spectral stochastic uncertainty quantification in chemical systems. *Combustion Theory and Modelling*, 8(3):607–632, 2004.
- [398] M. T. Reagan, H. N. Najm, P. P. Pébay, O. M. Knio, and R. G. Ghanem. Quantifying uncertainty in chemical systems modeling. *International Journal of Chemical Kinetics*, 37(6):368–382, 2005.
- [399] P. Récho. Modélisation de l’écoulement sanguin dans le réseau artériel par un système hyperbolique de loi de conservation. Master’s thesis, Ecole Centrale de Lyon, 2008.
- [400] S. C. Reddy, P. J. Schmid, and D. S. Henningson. Pseudospectra of the Orr-Sommerfeld Operator. *SIAM Journal of Applied Mathematics*, 53(1):15–47, February 1993.
- [401] J. Reuther, S. E. Cliff, and R. M. Hicks. Practical design optimization of wing/body configurations using the euler equations. In *AIAA Applied Aerodynamics Conference*, AIAA paper series, pages 330–342, 1992.
- [402] J. Reuther, A. Jameson, J. Farmer, L. Martinelli, and D. Saunders. Aerodynamic shape optimization of complex aircraft configurations via an adjoint formulation. In *Aerospace Sciences Meeting and Exhibit*, number AIAA-1996-94, Reno, NV, 1996.
- [403] J. J. Riley and R. W. Metcalfe. Direct numerical simulation of a perturbed, turbulent mixing layer. *AIAA Paper*, 80-0274, 1980.
- [404] A. Rinnooy Kan and G. Timmer. Stochastic global optimization methods part ii: Multi level methods. *Mathematical Programming*, 39:57–78, 1987. 10.1007/BF02592071.
- [405] B. D. Ripley. *Pattern Recognition and Neural Networks*. Cambridge University Press, 1996.
- [406] P.J. Roache. Quantification of uncertainty in Computational Fluid Dynamics. *Annu. Rev. Fluid. Mech.*, 29:123–160, 1997.
- [407] C. P. Robert and G. Casella. *Monte Carlo Statistical Methods*. Springer-Verlag, New York, 2nd edition edition, 2004.
- [408] A. R. Robinson and P. F. J. Lermusiaux. Overview of data assimilation. Technical Report 62, The division of engineering and applied sciences, Harvard University, Cambridge, Massachusetts, 2000.
- [409] Robert S. Rogallo and Rarviz Moin. Numerical simulations of turbulent flows. *Annual Review in Fluid Mechanics*, 16:99–137, 1984.
- [410] M. M. Rogers and R. D. Moser. Direct simulation of self-similar turbulent mixing layer. *Physics of Fluids*, 6(2):903–923, 1994.
- [411] C. J. Roy and W. L. Oberkampf. A comprehensive framework for verification, validation, and uncertainty quantification in scientific computing. *Comp. Meth. Appl. Math. Engrg.*, 200:2131–2144, 2011.
- [412] Christopher J. Roy. Review of code and solution verification procedures for computational simulation. *Journal of Computational Physics*, 205(1):131 – 156, 2005.

- [413] R. Y. Rubinstein and D. P. Kroese. *Simulation and the Monte Carlo Method*. Wiley Series in Probability and Statistics. Wiley, 2nd edition, 2008.
- [414] Leonid Ryzhik, George Papanicolaou, and Joseph B. Keller. Transport equations for elastic and other waves in random media. *Wave Motion*, 24(4):327 – 370, 1996.
- [415] S. K. Sachdeva, P. B. Nair, and A. J. Keane. Hybridization of stochastic reduced basis methods with polynomial chaos expansions. *Prob. Eng. Mech.*, 21(2):182–192, 2006.
- [416] J. Sacks, W. J. Welch, T. J. Mitchell, and H. P. Wynn. Design and analysis of computer experiments. *Stat. Sci.*, 4(4):409–423, 1989.
- [417] P. J. Saffman. The large-scale structure of homogeneous turbulence. *Journal of Fluid Mechanics*, 27:581 – 593, 1967.
- [418] P. J. Saffman. A note on decay of homogeneous turbulence. *Phys. Fluids*, 10(1349), 1967.
- [419] C. Sagaut, P. & Cambon. *Homogenous Turbulence Dynamics*. Cambridge University Press, 2008.
- [420] J. Laurenceau; P. Sagaut. Building efficient response surfaces of aerodynamic functions with kriging and cokriging. *AIAA J.*, 46(2):498–507, 2008.
- [421] Pierre Sagaut. *Large Eddy Simulations for Incompressible flows*. Scientific Computation. Springer-Verlag, third edition, 2006.
- [422] S. Sakamoto and R. Ghanem. Polynomial chaos decomposition for the simulation of non-gaussian non-stationary stochastic processes. *J. Eng. Mech.*, 128(2):190–201, 2002.
- [423] A. Saltelli and Sobol I.M. About the use of rank transformation in sensitivity analysis of model output. *Reliability Engineering and System Safety*, 50:225–239, 1995.
- [424] N. D. Sandham and W. C. Reynolds. Some inlet-plane effects on the numerically simulated spatially-developing mixing layer. In J.-C. André, J. Cousteix, F. Durst, B. E. Launder, F. W. Schmidt, and J. H. Whitelaw, editors, *Turbulent shear flows 6*, pages 441–454. Springer-Verlag, Berlin, 1989.
- [425] T. J. Santner, B. J. Williams, and W. I. Notz. *The design and analysis of computer experiments*. Statistics. Springer, 2003.
- [426] L.T. Santos, F.A. Dorini, and M.C.C. Cunha. The probability density function to the random linear transport equation. *Applied Mathematics and Computation*, 216(5):1524 – 1530, 2010.
- [427] T. P. Sapsis and P. F. J. Lermusiaux. Dynamically Orthogonal Field Equations for Continuous Stochastic Dynamical Systems. *Physica D*, 238:2347–2360, 2009.
- [428] C. Scheidt and I. Zabalza-Mezghani. Assessing uncertainty and optimizing production schemes: Experimental designs for non-linear production response modeling. an application to early water breakthrough prevention. In *ECMOR IX*, Cannes, France, 2004.
- [429] P. J. Schmid. Nonmodal stability theory. *Annual review of Fluid Mechanics*, 39:129–162, 2007.
- [430] P. J. Schmid and D. S. Henningson. *Stability and Transition in Shear Flows*. Springer, 2001.
- [431] W. Schoutens. *Stochastic processes in the Askey scheme*. PhD thesis, K.U. Leuven, 1999.
- [432] W. Schoutens. *Stochastic Processes and orthogonal polynomials*. Springer-Verlag, New York, 2000.
- [433] G. I. Schüeller. Computational stochastic mechanics - recent advances. *Computers & Structures*, 79(22-25):2225–2234, 2001.
- [434] G.I. Schüeller. A State-of-the-Art Report on Computational Stochastic Mechanics. *Probabilistic Engineering Mechanics*, 12(4):197–321, 1997.
- [435] A. Segall and T. Kailath. Orthogonal functions of independent-increment processes. *IEEE Trans. Info. Theory*, 22(3):287–298, 1976.
- [436] D. Serre. *Systèmes Hyperboliques de Lois de Conservation, partie I*. Diderot, 1996. Paris.
- [437] D. Serre. *Systèmes hyperboliques de lois de conservation, parties I et II*. Diderot, 1996. Paris.
- [438] Glenn Shafer. *A mathematical theory of evidence*. Princeton Univ. Press, Princeton, New Jersey, 1976.
- [439] Jie Shen and Li-Lian Wang. Sparse spectral approximations of high-dimensional problems based on hyperbolic cross. *SIAM Journal on Numerical Analysis*, 48(3):1087–1109, 2010.
- [440] Laura L. Sherman, Arthur C. Taylor III, Larry L. Green, Perry A. Newman, Gene W. Hou, and Vamshi Mohan Korivi. First- and second-order aerodynamic sensitivity derivatives via automatic differentiation with incremental iterative methods. *Journal of Computational Physics*, 129(2):307 – 331, 1996.
- [441] S.J. Sherwin. Hierarchical hp finite elements in hybrid domains. *Finite Elements in Analysis and Design*, 27:109–119, 1997.

- [442] M. Shinozuka and G. Deodatis. Response variability of stochastic finite element systems. *J. Eng. Mech.*, 114(3):499–519, 1988.
- [443] F. Simon, P. Guillen, P. Sagaut, and D. Lucor. A gPC-based approach to uncertain transonic aerodynamics. *Computer Methods in Applied Mechanics and Engineering*, 199(17-20):1091–1099, 2010.
- [444] J. Smagorinsky. General circulation experiments with the primitive equations: I. The basic experiment. *Monthly Weather Review*, 91(3):99–165, 1963.
- [445] A. J. Smola and B. Schölkopf. A tutorial on Support Vector Regression. Technical Report TR-98-030, NeuroCOLT, 1998.
- [446] S.A. Smolyak. Quadrature and interpolation formulas for tensor products of certain classes of functions. *Soviet Mathematics, Doklady*, 4:240–243, 1963.
- [447] J. Sobieszcanski-Sobieski. The case for aerodynamic sensitivity analysis. Technical Report CP 2457, NASA, 1987.
- [448] I. M. Sobol. Sensitivity analysis for non-linear mathematical models. *Math. Modeling Comp. Experiment*, 1:407–414, 1993.
- [449] C. Soize and R. Ghanem. Physical systems with random uncertainties: chaos representations with arbitrary probability measure. *SIAM J. Sci. Comput.*, 26(2):395–410, 2004.
- [450] P. Spanos and R.G. Ghanem. Stochastic finite element expansion for random media. *ASCE Journal of Engineering Mechanics*, 115(5):1035–1053, 1989.
- [451] AIAA standards. Guide for verification and validation of computational fluid dynamics simulations. Technical Report AIAA G-077-1998, American Institute of Aeronautics and Astronautics, 1998.
- [452] S. Stanley and S. Sarkar. Simulations of spatially developing two-dimensional shear layers and jets. *Theoretical computational fluid dynamics*, 9:121–147, 1997.
- [453] G. Stefanou and M. Papadrakakis. Assessment of spectral representation and Karhunen-Loève expansion methods for the simulation of Gaussian stochastic fields. *Computer Methods in Applied Mechanics and Engineering*, 196:2465–2477, 2007.
- [454] M. L. Stein. *Interpolation of Spatial Data*. Statistics. Springer, 1999.
- [455] F. Stern, R. Wilson, H.W. Coleman, and E.G Paterson. Comprehensive approach to verification and validation of CFD simulations - part 1 : Methodologies and procedures. *Journal of Fluids Engineering*, 123:803–810, 2001.
- [456] G.W. Stewart and Ji-Guang Sun. *Matrix perturbation theory*. Academic Press, Boston, 1990.
- [457] G. Strang. On the construction and the comparison of difference schemes. *SIAM, Journal on Numerical Analysis*, 5(3):506–517, 1968.
- [458] C. H. Su and D. Lucor. Covariance kernel representations of multidimensional second-order stochastic processes. *Journal of Computational Physics*, 217(1):82–99, 2006.
- [459] G. Szego. *Orthogonal polynomials*, volume 23. American Mathematical Society, colloquium publications, 1939.
- [460] Tao Tang and Tao Zhou. Convergence analysis for stochastic collocation methods to scalar hyperbolic equations with a random wave speed. *Communications in Computational Physics*, 8(1):226–248, 2010.
- [461] A. Tarantola. *Inverse Problem Theory - Methods for Data Fitting and Model Parameter Estimation*. Elsevier, 1987.
- [462] A. Tarantola. *Inverse Problem Theory and Methods for Model Parameter Estimation*. SIAM: Philadelphia, 2005.
- [463] D. M. Tartakovsky and D. Xiu. Stochastic Analysis of Transport in Tubes with Rough Walls. *J. Comp. Phys.*, 217:248–259, 2006.
- [464] M. Tatang, W. Pan, R. Prinn, and G. McRae. An efficient method for parametric uncertainty analysis of numerical geophysical models. *Journal of Geophysical Research*, 102:21925–21932, 1997.
- [465] M.A. Tatang. *Direct incorporation of uncertainty in chemical and environmental engineering systems*. PhD thesis, MIT, Massachusetts, USA, 1995.
- [466] A. C. Taylor, L. L. Green, P. A. Newman, and M. M. Putko. Some advanced concepts in discrete aerodynamic sensitivity analysis. *AIAA J.*, 41(7):1224–1229, 2003.
- [467] G. I. Taylor. Statistical theory of turbulence. *Proc. R. Soc. Lond. A*, 151:421–444, 1935.
- [468] R. Temam. Sur l’approximation de la solution des equations de navier-stokes par la methode des fractionnaires ii. *Arch. Rational Mech. Anal.*, 33:377, 1969.
- [469] V.N. Temlyakov. *Approximation of periodic functions*. Nova Science, New York, 1994.

- [470] N. Tillmark. On the Spreading Mechanisms of a Turbulent Spot in Plane Couette Flow. *Europhysics Letters*, 32:481–485, 1995.
- [471] N. Tillmark and P. H. Alfredsson. Experiments on transition in plane couette flow. *Journal of Fluid Mechanics*, 235:89–102, 1992.
- [472] Berlin) Tino Weinkauff (ZIB, Bernd R. Noack (TU Berlin), Pierre Comte (U Strasbourg), Andreas Dillmann (DLR Göttingen), and Berlin) Hans-Christian Hege (ZIB. Coherent-structure skeleton of a turbulent mixing layer. In *Gallery of Fluid Motion*, 2004.
- [473] R. A. Todor and C. Schwab. Convergence rates for sparse chaos approximations of elliptic problems with stochastic coefficients. *IMA Journal of Numerical Analysis*, 27(2):232–261, 2007.
- [474] E. F. Toro. *Riemann Solvers and Numerical Methods for Fluid Dynamics: a Practical Introduction*. Springer, Berlin, 2nd edition, 1999.
- [475] L. N. Trefethen. Spectral Methods in Matlab. Technical report, SIAM, 2000.
- [476] L. N. Trefethen, A. E. Trefethen, S. C. Reddy, and T. A. Driscoll. Hydrodynamic stability without eigenvalues. *Science*, 261:578–584, 1993.
- [477] Lloyd N. Trefethen. Is Gauss Quadrature Better than Clenshaw-Curtis? *SIAM rev.*, 50(1):67 – 87, 2008.
- [478] J. Tryoen. Adaptive anisotropic stochastic discretization schemes for uncertain conservation laws. In *ASME-FEDSM Proceedings*, Montreal, Canada, 2010.
- [479] J. Tryoen, O. Le Maitre, M. Ndjinga, and A. Ern. Intrusive galerkin methods with upwinding for uncertain nonlinear hyperbolic systems. *Journal of Computational Physics*, 229:6485–6511, 2010.
- [480] J. Tryoen, O. Le Maître, M. Ndjinga, and A. Ern. Roe solver with entropy corrector for uncertain hyperbolic systems. *Journal of Computational and Applied Mathematics*, 235(2):491 – 506, 2010. Special Issue on Advanced Computational Algorithms.
- [481] E. Turgeon, D. Pelletier, and J. Borggaard. A general continuous sensitivity equation formulation for the kappa-epsilon model of turbulence. *International Journal of Computational Fluid Dynamics*, 18(1):29–46, 2004.
- [482] A. Decoene V. Martin, F. Clément and J.F. Gerbeau. Parameter identification for a one-dimensional blood flow model. In *ESAIM Proc.*, 2005.
- [483] E.H. Vanmarcke and M. Grigoriu. Stochastic finite element analysis of simple beams. *J. Eng. Mech*, 109:1203–1214, 1983.
- [484] V. Vapnik. *The nature of statistical learning theory*. Springer, New York, 1995.
- [485] D. Venturi, X. Wan, and G. E. Karniadakis. Stochastic low-dimensional modelling of a random laminar wake past a circular cylinder. *Journal of Fluid Mechanics*, 606:339–367, 2008.
- [486] D. Venturi, X. Wan, and G. E. Karniadakis. Stochastic bifurcation analysis of rayleigh-bénard convection. *Journal of Fluid Mechanics*, 650:391–413, 2010.
- [487] Daniele Venturi. A fully symmetric nonlinear biorthogonal decomposition theory for random fields. *Physica D: Nonlinear Phenomena*, 240(4-5):415 – 425, 2011.
- [488] Vetter and Sturtevant. Experiments on the Richtmyer-Meshkov instability of an air/SF6 interface. *Shock Waves*, 4:247–252, 1995.
- [489] V. Volterra. *Leçons sur les équations intégrales: et les équations intégrales-différentielles*. Gauthier-Villars, 1913.
- [490] Peter E.J. Vos, Spencer J. Sherwin, and Robert M. Kirby. From h to p efficiency: Implementing finite and spectral/hp element methods to achieve optimal performance for low- and high-order discretisations. *Journal of Computational Physics*, 229(13):5161 – 5181, 2010.
- [491] J. Waldvogel. Fast construction of the fejer and clenshaw-curtis quadrature rules. *BIT Numerical Mathematics*, 43(1):1–18, 2003.
- [492] R.W. Walters. Towards stochastic fluid mechanics via polynomial chaos. AIAA Paper 2003–413, 2003.
- [493] X. Wan. *Adaptive Multi-Element Generalized Polynomial Chaos: Algorithms and Applications*. PhD thesis, Brown University, RI, USA, 2007.
- [494] X. Wan and G.E. Karniadakis. An adaptive multi-element generalized polynomial chaos method for stochastic differential equations. *Journal of Computational Physics*, 209:617–642, 2005.
- [495] X. Wan and G.E. Karniadakis. Long-term behavior of polynomial chaos in stochastic flow simulations. *Computer Methods in Applied Mechanics and Engineering*, 195:5582–5596, 2006.
- [496] X. Wan and G.E. Karniadakis. Multi-element generalized polynomial chaos for arbitrary probability measures. *SIAM Journal of Scientific Computing*, 28(3):901–928, 2006.

- [497] X. Wan and G.E. Karniadakis. Stochastic heat transfer enhancement in a grooved channel. *Journal of Fluid Mechanics*, 565:255–278, 2006.
- [498] Xiaoliang Wan and George Karniadakis. Multi-element generalized polynomial chaos for arbitrary probability measures. *SIAM Journal on Scientific Computing*, 28(3):901–928, 2006.
- [499] Xiaoliang Wan and George Em Karniadakis. Error Control in Multi-Element Generalized Polynomial Chaos Method for Elliptic Problems with Random Coefficients. *Commun. Comp. Phys.*, 5(2-4):793–820, 2009.
- [500] M.P. Wand and M.C. Jones. *Kernel smoothing*. Monographs on Statistics and Applied Probability 60. Chapman and Hall/CRC, 1995.
- [501] Jingbo Wang and Nicholas Zabaras. Hierarchical bayesian models for inverse problems in heat conduction. *Inverse Problems*, 21:183–206, 2005.
- [502] Q. Wang. *Uncertainty quantification for unsteady fluid flow using adjoint-based approaches*. PhD thesis, Stanford University, 2008.
- [503] W.K. Wang, H. & George. The integral scale in homogeneous isotropic turbulence. *Journal of Fluid Mechanics*, 459(429-443), 2002.
- [504] J. A. C. Weideman and Lloyd N. Trefethen. The kink phenomenon in Fejér and Clenshaw-Curtis quadrature. *Numer. Math.*, 107:707–727, 2007.
- [505] I. Weisbrot and I. Wygnanski. On coherent structures in a highly excited mixing layer. *Journal of Fluid Mechanics*, 195:137–159, 1988.
- [506] W. J. Welch, R. R. Buck, J. Sacks, H. P. Wynn, T. J. Mitchell, and M. D. Morris. Screening, predicting and computer experiments. *Technometrics*, 34(1):15–25, 1992.
- [507] P. Whittle. On stationary processes in the plane. *Biometrika*, 41:434–449, 1954.
- [508] N. Wiener. The homogeneous chaos. *Amer. J. Math.*, 60:897–936, 1938.
- [509] R. V. Wilson and A. O. Demuren. Numerical simulation of two-dimensional spatially-developing mixing layer. Technical Report NAS1-19480, NASA Langley Research Center, 1994.
- [510] C. D. Winant and F. K. Browand. Vortex pairing: the mechanism of turbulent mixing layer growth at moderate Reynolds number. *Journal of Fluid Mechanics*, 63:237–255, 1974.
- [511] C.L. Winter and D.M. Tartakovsky. Groundwater flow in heterogeneous composite aquifers. *Water Resour. Res.*, 38:23, 2002.
- [512] J.A.S. Witteveen and H. Bijl. An alternative unsteady adaptive stochastic finite elements formulation based on interpolation at constant phase. *Computer Methods in Applied Mechanics and Engineering*, 198(3-4):578–591, 2008.
- [513] J.A.S. Witteveen and H. Bijl. An unsteady adaptive stochastic finite elements formulation for rigid-body fluid-structure interaction. *Computers and Structures*, 86:2123–2140, 2008.
- [514] J.A.S. Witteveen and H. Bijl. Higher period stochastic bifurcation of nonlinear airfoil fluid-structure interaction. *Mathematical Problems in Engineering*, 2009:1–26, 2009.
- [515] J.A.S. Witteveen and H. Bijl. A tvd uncertainty quantification method with bounded error applied to transonic airfoil flutter. *Communications in Computational Physics*, 6:406–432, 2009.
- [516] J.A.S. Witteveen, A. Loeven, S. Sarkar, and H. Bijl. Probabilistic collocation for period-1 limit cycle oscillations. *Journal of Sound and Vibration*, 311(311):421–439, 2008.
- [517] J.A.S. Witteveen, S. Sarkar, and H. Bijl. Modeling physical uncertainties in dynamic stall induced fluid-structure interaction of turbine blades using arbitrary polynomial chaos. *Computers and Structures*, 85:866–878, 2007.
- [518] M. Wolf. *Analyse Mathématique et Numérique du système de la magnétohydrodynamique résistive avec termes de champ magnétique auto-généré*. PhD thesis, Institut de Recherche Mathématique Avancée, Université de Strasbourg, 2011.
- [519] M. J. Wright, D. Bose, and Y.-K. Chen. Probabilistic modeling of aerothermal and thermal protection material response uncertainties. *AIAA J.*, 45(2):399–410, 2007.
- [520] C. Wu, H. Zhang, and T. Fang. Flutter analysis of an airfoil with bounded random parameters in compressible flows via Gegenbauer polynomial approximation. *Aerospace Science and Technology*, 11:518–526, 2007.
- [521] I. Wygnanski and H. E. Fiedler. The two-dimensional mixing region. *Journal of Fluid Mechanics*, 41:327–361, 1970.
- [522] D. Xiu and G.E. Karniadakis. Modeling uncertainty in steady state diffusion problems via generalized polynomial chaos. *Comput. Methods Appl. Math. Engrg.*, 191:4927–4948, 2002.

- [523] D. Xiu and G.E. Karniadakis. The Wiener-Askey polynomial chaos for stochastic differential equations. *SIAM Journal on Scientific Computing*, 24(2):619–644, 2002.
- [524] D. Xiu and G.E. Karniadakis. The Wiener-Askey polynomial chaos for stochastic differential equations. *SIAM J. Sci. Comput.*, 24(2):619–644, 2002.
- [525] D. Xiu and G.E. Karniadakis. Modeling uncertainty in flow simulations via generalized polynomial chaos. *J. Comput. Phys.*, 187:137–167, 2003.
- [526] D. Xiu and G.E. Karniadakis. A new stochastic approach to transient heat conduction modeling with uncertainty. *Inter. J. Heat Mass Trans.*, 46:4681–4693, 2003.
- [527] D. Xiu and G.E. Karniadakis. Supersensitivity due to uncertain boundary conditions. *Int. J. Numer. Meth. Engng.*, submitted, 2003.
- [528] D. Xiu and G.E. Karniadakis. Uncertainty modeling of Burgers’ equation by generalized polynomial chaos. In P.D. Spanos and G. Deodatis, editors, *Computational Stochastic Mechanics. Proceedings of the fourth International Conference on Computational Stochastic Mechanics, Corfu, Greece, June 9-12, 2002*, pages 655–661. Millpress Rotterdam, 2003.
- [529] D. Xiu, D. Lucor, and G.E. Karniadakis. Modeling uncertainty in flow-structure interactions. In K.J. Bathe, editor, *Computational Fluid and Solid Mechanics*, volume 2, pages 1420–1423. 1st MIT Conference, Cambridge, MA, USA, June 12-15, 2001, Elsevier Press, 2001.
- [530] D. Xiu, D. Lucor, C.-H. Su, and G.E. Karniadakis. Stochastic modeling of flow-structure interactions using generalized polynomial chaos. *J. Fluid Eng.*, 124(1):51–59, 2002.
- [531] D. Xiu and A. Tartakovsky. Numerical methods for differential equations in random domains. *SIAM J. Sci. Comput.*, 28(3), 2006.
- [532] Dongbin Xiu. *Numerical Methods for Stochastic Computations: A Spectral Method Approach*. Princeton Univ. Press, 2010.
- [533] Dongbin Xiu and Jan S. Hesthaven. High-order collocation methods for differential equations with random inputs. *J. Sci. Comput.*, 27(3):1118–1139, 2005.
- [534] F. Yamazaki, M. Shinozuka, and G. Dasgupta. Neumann expansion for stochastic finite element analysis. Technical report, Dept. Civil Eng., Columbia University, 1985.
- [535] Y. Yu, M. Zhao, T. Lee, N. Pestieau, W. Bo, J. Glimm, and J.W. Grove. Uncertainty quantification for chaotic computational fluid dynamics. *Journal of Computational Physics*, 217:200–216, 2006.
- [536] D. Zhang. *Stochastic methods for flow in porous media*. Academic Press, 2002.
- [537] Dongxiao Zhang and Zhiming Lu. An efficient, high-order perturbation approach for flow in random porous media via Karhunen-Loeve and polynomial expansions. *Journal of Computational Physics*, 194:773–794, 2004.
- [538] Y.-Q. Zhang, C.-M. Ho, and P. Monkewitz. The mixing layer forced by fundamental and subharmonic. In V. V. Kozlov, editor, *IUTAM Symposium*, pages 385–395, Novosibirsk, USSR, July 1984. Springer-Verlag.
- [539] M. D. Zhou and I. Wygnanski. The response of a mixing layer formed between parallel streams to a concomitant excitation at two frequencies. *Journal of Fluid Mechanics*, 441:139–168, 2001.
- [540] W.Q. Zhu, Y.J. Ren, and W.Q. Wu. Stochastic FEM based on local average of random vector fields. *J. Eng. Mech.*, 118(3):496–511, 1992.
- [541] W.Q. Zhu and W.Q. Wu. A stochastic finite element method for real eigenvalue problems. *Prob. Eng. Mech.*, 6:228–232, 1991.
- [542] H.-J. Zimmermann. *Fuzzy set theory and its applications*. Kluwer Academic Publishers, Boston/Dordrecht/London, fourth edition edition, 1996.